Development of Metamaterials Based Electromagnetic Structures

A Thesis

Submitted in Fulfillment of the Requirement for the Award of the Degree of

DOCTOR OF PHILOSOPHY

in

Electronics and Communication Engineering Department

Submitted by

Atipriya Sharma

Roll No: 901606007

Under the guidance of

Dr. Ravi Panwar
Assistant Professor, ECED
Indian Institute of Information Technology,
Design & Manufacturing Jabalpur,
Madhya Pradesh

Dr. Rajesh Khanna
Professor, ECED
Thapar Institute of Engineering
and Technology, Patiala
Punjab

THAPAR INSTITUTE
OF ENGINEERING & TECHNOLOGY
(Deemed to be University)

Electronics & Communication Engineering Department

Thapar Institute of Engineering and Technology (TIET),

Patiala- 147004, Punjab, India

June 2021

CERTIFICATE

I, **Atipriya,** hereby certify that the proposed work in this thesis entitled "**Development of Metamaterials Based Electromagnetic Structures**" being submitted by me to **Department of Electronics and Communication Engineering, Thapar Institute of Engineering and Technology, Patiala** in fulfillment of the requirement for the award of the degree of "Doctor of Philosophy" is record of bonafide research works carried under the guidance and supervision of **Dr. Rajesh Khanna and Dr. Ravi Panwar.**

The work embodied in this thesis has not been submitted in any other Institute/ University for the award of any diploma or degree.

Date:

Atipriya Sharma

(901606007)

This is to certify that the above statement made by the candidate is correct to the best of our knowledge.

16/6/21

(Dr. Rajesh Khanna)
Professor
Department of Electronics &
Communication Engineering
TIET, Patiala
Punjab. India
Dated:

(Dr. Ravi Panwar)
Assistant professor
Department of Electronics &
Communication Engineering
IIITDM, Jabalpur
Madhya Pardesh. India
Dated:

ABSTRACT

Metamaterials (MM) are artificial or synthetic structures which possess unique properties such as negative permittivity (ε), permeability (μ), and refractive index, etc. The unique and useful properties of MM are offered by the shape, size, and arrangements of the unit cell, rather than the composition of the material. Conventional absorbers having larger thickness resulting in bulky, expensive, and narrow bandwidth that are replaced by the MM based absorbers (MMA). By considering the disadvantage of the conventional absorbers, in this thesis, MM based absorbers and low radar cross-section (RCS) antennas have been investigated. First of all, in this thesis, two distinct MM-based absorbers are designed, simulated, and measured in the range of 2 to 18 GHz. The first MMA is a hybrid structure that comprises of a cross-loaded split ring. The other proposed structure comprises eight sectors loaded circle inside the square. The first MMA show the reflection coefficient (RC) is less than -10 dB from 8.5 to 16 GHz for the hybrid structure, which covers 7.5 GHz bandwidth. The other proposed structure exhibits the four RC resonant peaks of -25.9 dB, -18.9 dB, -16.1 dB, and -21.3 dB are noticed at 4.4 GHz, 6.0 GHz, 14.1 GHz, and 16.0 GHz, respectively. To evaluate the optimized values of the distinct dimensions the parametric studies have been performed on both the structures. Further, an effort has been made to determine the angular stability and polarization sensitivity of the proposed structures. The frequency-dependent EM properties of both structures are also demonstrated in this chapter. Further, the surface current, electric (**E**) field, and magnetic (**H**) field distributions are also found. Finally, the proposed prototypes have been fabricated to evaluate the measured results. The free-space microwave measurement setup is used for the performance evaluation of the fabricated prototypes.

Next, an efficient tunable absorber based on an active frequency selective surfaces (AFSS) utilizing p-i-n diode is presented. Initially, the AFSS has been designed, simulated, and analyzed using the CST studio. Further, the design of the active absorber which is based on AFSS is also presented. Another study is executed on AFSS loaded absorber with diode and without diode, to know its effect on the absorption characteristics. A single-layered, tunable, wideband AFSS based absorber is presented, which demonstrates the tunability in the range of 9.2 GHz to 11.2 GHz. To obtain the tunability AFSS loaded absorber with

different values of resistance has been evaluated. The normalized impedance, surface current, **E** field, and **H** field distributions are also presented. Finally, the proposed prototype has been fabricated to evaluate the measured result.

Further, two low RCS antennas are developed, which are based on MM techniques. The first one is MM inspired antenna and the second one is flexible MM-based superstrate coupled MPA, which enhances the gain along with RCS reduction (RCSR) of the MPA. The proposed MM impinged MPA it can be concluded that the structure provides RCSR, without affecting the other radiation properties and volume of the antenna. The reflection coefficient bandwidth of the second proposed MPA is the 800MHz, though the RCS bandwidth of the primary antenna is 1.7 GHz and the RCS bandwidth of the proposed antenna is 8.1 GHz. The increment in gain is observed in the proposed antenna. It can be observed that the maximum gain attained by the primary antenna is equal to 6.6 dB, whereas the maximum gain of the proposed antenna is equal to 7.2 dB. To evaluate the optimized values of the distinct dimensions, parametric studies have been performed on both the structures. Finally, the proposed prototypes have been fabricated to evaluate the measured results. The performance evaluation of the fabricated antennas has been carried out using a microwave measurement setup. A good agreement has been observed between the simulated and measured results of all the prototypes.

ACKNOWLEDGMENT

First and foremost, I am extremely thankful to Lord Shiva, for giving me an opportunity and strength to accomplish my PhD work. From the bottom of my heart, I would like to say a big thanks to my supervisor Dr. Rajesh Khanna (Professor, ECED, Thapar Institute of engineering and technology, Patiala) for his expert advice and constant encouragement during the whole research period and for being available despite his busy schedule. Many thanks to my supervisor Dr. Ravi Panwar (Associate Professor, ECED, IIITDM, Jabalpur) for his precious guidance, support and feedback throughout this successful journey. He taught me the correct methodology of research and how to manifest the work. I am grateful that they have spared valuable time for constructive criticism, too.

In addition, I would like to express my thanks to my doctoral committee members: Dr. Alpana Aggarwal, Dr. Kulvir Singh, Dr. Mohit Agarwal and Dr. Ashutosh Kumar for their encouragement and insightful comments. I cannot leave Thapar without mentioning Er. Naveen and Er. Manvi Sharma for their positive attitude, valuable suggestions and to create the best environment in the lab. Many thanks to the administration and staff of the TIET for their consistent help. I am also grateful to all my friends and colleagues for their support and encouragement.

I am blessed, to have a loving in-laws who support me and have faith in me all the time. I am extremely grateful to my beloved parents, who encouraged me to do pursue PhD and for their support and invaluable love throughout the years.

The most importantly, I would also like to extend my gratitude to Mr. Manish Kansal, my husband, for his patience, encouragement, support and love. The love and affection of my daughter Kayra is a great inspiration for me. Without their infinite support, patience and love, I would not be able to finish my PhD work.

(Atipriya Sharma)

TABLE OF CONTENT

Content

CHAPTER 1 (INTRODUCTION)

CHAPTER 2 (LITERATURE SURVEY)

CHAPTER 3 (DEVELOPMENT OF NEW HYBRID METAMATERIAL BASED MICROWAVE ABSORBING STRUCTURE)

CHAPTER 4 (DESIGN AND DEVELOPMENT OF ACTIVE MICROWAVE ABSORBING STRUCTURE)

CHAPTER 5 (DEVELOPMENT OF A MM INSPIRED ANTENNA WITH LOW RCS)

CHAPTER 6 (CONCLUSION AND FUTURE SCOPE)

LIST OF TABLES

LIST OF FIGURES

LIST OF ACORNYMS

MM	Metamaterial
SRR	Split Ring Resonator
DPS	Double Positive
EPS	Epsilion Negative
DNG	Double Negative
MNG	Mu Negative
SNG	Single Negative
LHM	Left-Handed Media
Mm	Millimeter
THz	Terahertz
EMI	Electromagnetic Interference
EM	Electromagnetic
E	Electric
H	Magnetic
MIMO	Multiple Input and Multiple Output
RAM	Radar Absorbing Material
RC	Reflection Coefficient
RCS	Radar Cross Section
LO	Low Observable
RCSR	Radar Cross Section Reduction

MPA	Microstrip Patch Antenna
GHz	Gigahertz
TE	Transverse Electric
TM	Transverse Magnetic
FSS	Frequency selective surfaces
CST	Computer Simulation Technology
HFSS	High-Frequency Structure Simulator
MMA	Metamaterial Absorber
SCR	Split-Coin Resonators
ELC	Electric-Field-coupled-LC
SRRs	Split-Ring Resonators
AIS	Artificial Impedance Surface
TL	Transmission Line
AMC	Artificial Magnetic Conductor
PEC	Perfect Electric Conductor
AFSS	Active FSS
PMM	Periodic Method of Moments
CP	Circularly Polarized
EBG	Electromagnetic Band Gap
RAS	Radar Absorbing Structure
HIGP	High Impedance Ground Plane

MEMS	Micro-electro-mechanical system
MEFSS	Miniaturized-element Frequency Selective Surfaces
NARR	Nano-absorptive Reducer
PCM	Polarization Conversion Material
MAS	Metamaterial Absorbing Structure
CMAs	Conventional Microwave Absorbers
3D	3 Dimensional
RC	Reflection Coefficient
TC	Transmission Coefficient
VNA	Vector Network Analyzer
SMA	Sub-Miniature Version A
MMS	Metamaterial Structure
S-parameters	Scattering Parameters
PCB	Printed Circuit Board
RF	Radio Frequency
MMAs	Microwave Absorbers
SC	Surface Current
RFID	Radio Frequency Identification Systems

LIST OF SYMBOLS

E	Permittivity
M	Permeability
Z	Normalized Impedance
N	Refractive index
Z_M	Impedance of material
Z_O	Impedance of free space
R	Radar range
S_r	Scattered power density
S_t	Power density intercepted by target
ε_r	Complex dielectric permittivity
μ_r	Complex magnetic permeability
A	Attenuation constant
Σ	Conductivity
tan δ	Loss tangent
Θ	Angle of incidence
Φ	Polarization angle
ε'	Real part of permittivity
ε''	Imaginary part of permittivity
μ'	Real part of permeability
μ''	Imaginary part of permeability
z'	Real part of impedance
z''	Imaginary part of impedance

LIST OF SCI PUBLICATIONS

- Atipriya Sharma, Ravi Panwar, Rajesh Khanna, "Experimental Validation of a Frequency-Selective Surface-Loaded Hybrid Metamaterial Absorber with Wide Bandwidth," IEEE Magnetics Letters, vol. 10, pp.1-5, 11 Feb 2019.
- Atipriya Sharma, Ravi Panwar, Rajesh Khanna, "Design and development of low radar cross section antenna using hybrid metamaterial absorber," Microwave and Optical Technology Letters, vol. 61, no.11, pp. 2491-9, Nov 2019.
- Atipriya Sharma, Ravi Panwar, Rajesh Khanna, "Microwave non-destructive testing of active frequency selective surface embedded tunable radar absorber," IET Electronics Letters, pp. 1-2, June 2020.

CHAPTER 1

INTRODUCTION TO METAMATERIALS

1.1 INTRODUCTION

Metamaterials are artificial or synthetic structures that provide unique properties such as negative permittivity (ε), permeability (μ) and refractive index. The unique and useful properties of MM are offered by the shape, size, and arrangements of the unit cell, rather than the composition of the material [1-5]. MM can be classified into 1-Dimensional, 2- Dimensional, and 3- Dimensional. The most commonly used shape of the MM is split-ring resonator (SRR), S-shaped resonator, mushroom shape structure, etc. Foremost, in 1967 Veselago invented the material with negative ε and/or negative μ in nature [6]. MMs are allocated in four different quadrants owing to the value of ε and μ as illustrated in Figure 1.1. The materials having positive values of 'ε' and 'μ' lie in the first quadrant, also called double-positive (DPS) [7]. Material having 'ε' negative found in the second quadrant, that indicates the direction of the incident field is opposite to the direction of the electric field induced in the material. This quadrant material is called epsilon negative (ENG) media. The third quadrant consists of the substances having a negative value of 'ε' and 'μ' both, also called double negative (DNG) media. If the value of 'μ' is negative of the material, this type of material lies in the fourth quadrant, which is also called mu negative (MNG). Single negative (SNG) media having a negative value of only one parameter, either ENG or MNG media, some authors also called left-handed media (LHM).

To understand the basic phenomenon of MM, need to recall the basic law of electromagnetism. The refractive index of the material is defined as

$$n=\sqrt{\varepsilon\,\mu} \tag{1.1}$$

Specifically, the refractive index depends upon ε and μ. The refractive index of the medium can be negative because of the negative value of ε and/or μ. Now, it is clearly shown that if $\mu < 0$ and $\varepsilon < 0$, then the substance is LHM. The existence of LHM brings the concept of negative refractive index, negative group velocity. The filtering characteristics and frequency response of the MM depend upon the geometrical and physical parameters listed below are:

- the ε and the thickness (th) of the MM substrate.

- the geometry i.e. the dimension, thickness, and shape of the conductor.
- the conductivity of the MM elements.
- the spacing between the elements of the MM
- the number of dielectric substrate layers in the case of multilayered MM.
- the different polarization angles.
- the different incident angles of the (electromagnetic) EM field.

In the designing of MM, the choice of MM element geometry is vitally important. Based on the bandwidth, sensitivity, resonant frequency, and angle of incidence, the elements have to be selective.

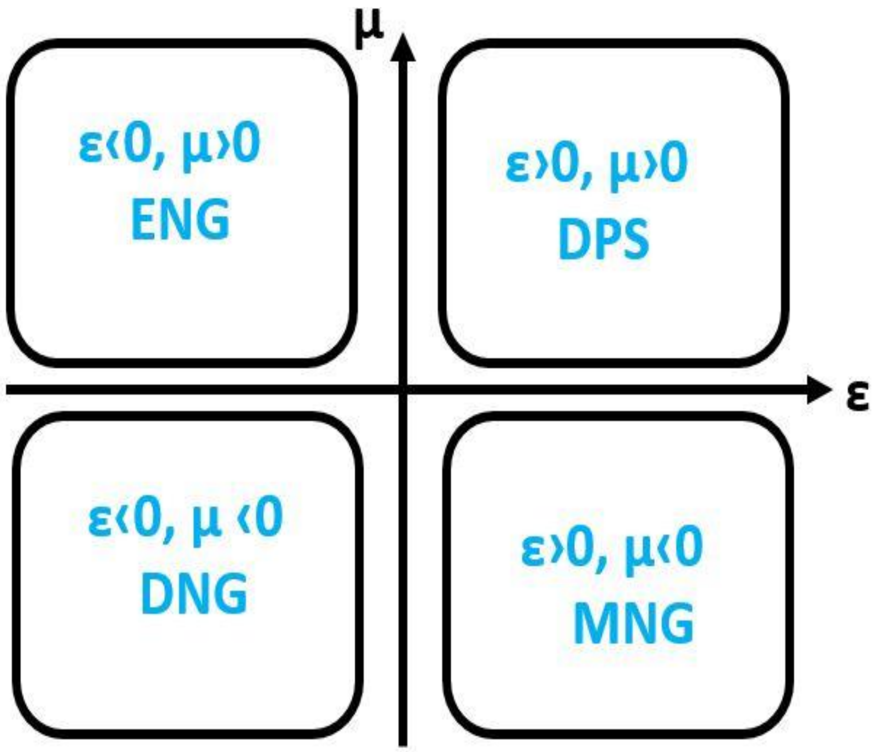

Figure 1.1. Classifications of MM based on the value of epsilon (ε) and mu (μ).

1.2 Application of MM

Metamaterials are practically implemented to give a positive impact across all range of technologies, where EM radiations are used. Especially, LHM has gained popularity in microwaves, because of its unique properties. MM coatings are used to magnify the radiation properties of the structures in the frequency range from Millimeter (mm) to Terahertz (THz). MM can be utilized to magnify the antenna characteristics like gain, directivity, etc. The basic requirement of the antenna in modern wireless communication is multiband response along with the reduction in the size of the antenna. The conventional techniques used to obtain the multiband response are bandgap structures, via, slots and parasitic patches, etc. All these techniques either enhance the volume of the antenna or introduce complexity. In this respect, the utilization of the MM of different shape plays an important role to reduce the volume and complexity of the antenna. To enhance the channel capacity in the wireless communication system, Multiple-Input and Multiple-Output (MIMO) antenna systems are used. For the MIMO antenna system design, two critical factors, the total size of the antenna system with limited space and isolation between the elements of the antenna are very important. Due to the less space between radiating elements of the antenna, the coupling coefficient is very high, which reduces the efficiency of MIMO antenna. To reduce the coupling between MIMO antenna, MM can be used.

RCS plays a crucial role in the field of stealth and low observable (LO) technology [1]. Mainly, there are two methods to reduce RCS, first, one is the shaping technique, in which the target configuration is modified for RCS reduction and the other is the application of radar absorbing material (RAM) [2]. Recently, one another method use of MM structures has been reported to reduce the RCS [3-6]. The other way to achieve the property of stealth technology is microwave absorbers. MM can also be used in microwave absorbers to enhance its characteristics like bandwidth and absorptivity. It can be used to enhance the absorption and reduce the reflected wave of the absorber. MM is also used to reduce the thickness of the absorber and also helps to improve the impedance matching property of the absorber. The other applications of MM are shielding, radome, superlens, and cloaking, etc. MM can be used as cloaks as well. Cloaking can be obtained by the cancellation of the electric (**E**) and magnetic (**H**) field generated by an object. Overall MM enhances the efficiency of all the microwave structures differently. MM adds an advantage of reconfigurability and multiband operation of the antenna and microwave structures. The most popularly known applications of MM are: MM inspired absorbers and MM based antennas.

1.2.1 MM inspired Absorber

RAM structures are used, to obtain the invisibility of target objects. Absorbers are the prototype which used to absorb the impinged EM wave, rather than transmit or reflect it. After that, the absorber transforms the absorbed energy into heat. Distinct shapes and structures of absorbers are available in the literature. The examples of absorbers are Dallenbach, Salisbury, and Jaumann layers. The configuration of these layers is illustrated in figure 1.2. The Dallenbach layer is the composition of a conducting substrate, on which lossy material is stacked. To obtain the minimum reflection for a particular wavelength, the permittivity, permeability, and thickness of the Dallenbach absorber can be adjusted. The principle of the Dallenbach layer relies on destructive interference between the incident wave and the reflected wave. To achieve the broadband response of the absorber, various layers are stacked on each other, because a single layer does not lead to broadband absorption.

The Salisbury screen is made up of a resistive layer on the conducting plane or metal plate, which is usually separated by a honeycomb dielectric spacer or air gap. The thickness of the air gap plays a crucial role in impedance matching. Therefore, the thickness of the spacer must be the odd multiple of the quarter wavelength. The demerit of the Salisbury screen that it can resonant only at a single frequency, therefore it restricts the practical usage of this screen. To overcome the demerit of the Salisbury screen, Jaumann layers have been introduced. Jaumann layers are the revamp structure of the Salisbury screen, to enhance the bandwidth with thin, multiple layers and with an air gap between the resistive sheets. Simultaneously, the cost of the prototype is increased due to the multilayering structure. Optimization of Jaumann prototype is complicated because of the numerous parameters involved in the designing, further, more number of layers leads to more complexity in optimization.

The Dallenbach, Salisbury, and Jaumann layers are conventional absorbers, which have demerits like high thickness heavyweight and expensive. To overcome the demerits of conventional absorbers, MM based absorbers are recommended nowadays. Microwave MM based absorbers minimize the reflection with different structures, shapes and because of variation in the values of ε and μ of the material used for fabrication. To achieve the minimum reflection the MM based absorbers, they must fulfill the conditions which are listed below.

- $Z_M = Z_O$

  where, Z_M is the impedance of material and Z_O is the impedance of free space.
- Electric permittivity should be equal to magnetic permeability.
- The attenuation of the wave is directly proportional to the distance.

The reflection coefficient (RC) can be expressed as:

$$RC = Z_M - Z_O / Z_M + Z_O \quad (1.2)$$

It can be observed from equation (1.2) that to reduce the reflection Z_M should be equal to Z_O. In other words, it can be said that the surface impedance should be matched to the incident medium. The intrinsic impedance can be expressed as:

$$Z_M/Z_o = \sqrt{\mu_R/\varepsilon_R} \quad (1.3)$$

where μ_R and ε_R are complex identities. Here real part permittivity and permeability indicate storage of the EM wave. Whereas, imaginary part permittivity and permeability describe losses in the form of heat. If μ_R becomes equal to ε_R, then reflection becomes zero as shown from (1.2) equation. Absorption potential of the material can be expressed as:

$$A = \frac{1}{2}\,\sigma\,\mathbf{E}^2 + \frac{1}{2}\omega\,\varepsilon_0\,\varepsilon_R\,\mathbf{E}^2 + \frac{1}{2}\,\omega\,\mu_0\,\mu_R\,\mathbf{H}^2 \quad (1.4)$$

where **E** and **H** are electric field and magnetic field strength**,** respectively. Whereas, σ is the conductivity of the material and ω is the angular speed of the EM wave. ε_0 and μ_0 are the dielectric permittivity and magnetic permeability respectively of the vacuum. Absorption and attenuation of the EM wave is dependent on conductivity, magnetic loss, and/ or dielectric loss of the material. The power of the EM wave deteriorates exponentially with distance (x), with the factor $e^{-\alpha x}$. The attenuation constant of the material can be written in terms of a = $(\varepsilon_R\mu_R - \varepsilon_i\mu_i)$ and b = $(\varepsilon_R\mu_i - \varepsilon_i\mu_r)$ as:

$$\alpha = -(\mu_0\,\varepsilon_0)^{1/2}\,\omega\,(a^2 + b^2)^{1/4}\,\text{Sin}\,[(1/2)\,tan^{-1}\,(\text{-a/b})] \quad (1.5)$$

To obtain the maximum attenuation, within a small thickness, α must be large, which means μ_R and ε_R must be large, which may resultant in poor impedance matching. Because, as we know

$$Z_o = (\mu_0/\varepsilon_0)^{1/2} \approx 377 \text{ ohms} \quad (1.6)$$

Therefore, it is necessary to obtain maximum absorption and attenuation of the EM wave, with a small thickness of the substrate and the substrate medium must be lossy. The other principle of absorption is the destructive interference of the EM wave.

The transmission or reflection characteristics of passive FSS, cannot be altered without the process of geometry redesigning. This is the main disadvantage of passive FSSs and also limits certain practical applications. More bandwidth and freedom to operate simultaneously at different frequencies are provided by active FSS. In recent years, compared to the conventional microwave absorbers (CMAs) active absorbers have attracted a great deal of attention. CMA offers no versatility after manufacturing, whereas with the help of external biasing circuits the active absorber offers tunability over a wide frequency range. The other advantages of non-linear active devices are it provides broad bandwidth and polarization-insensitive behavior of absorber.

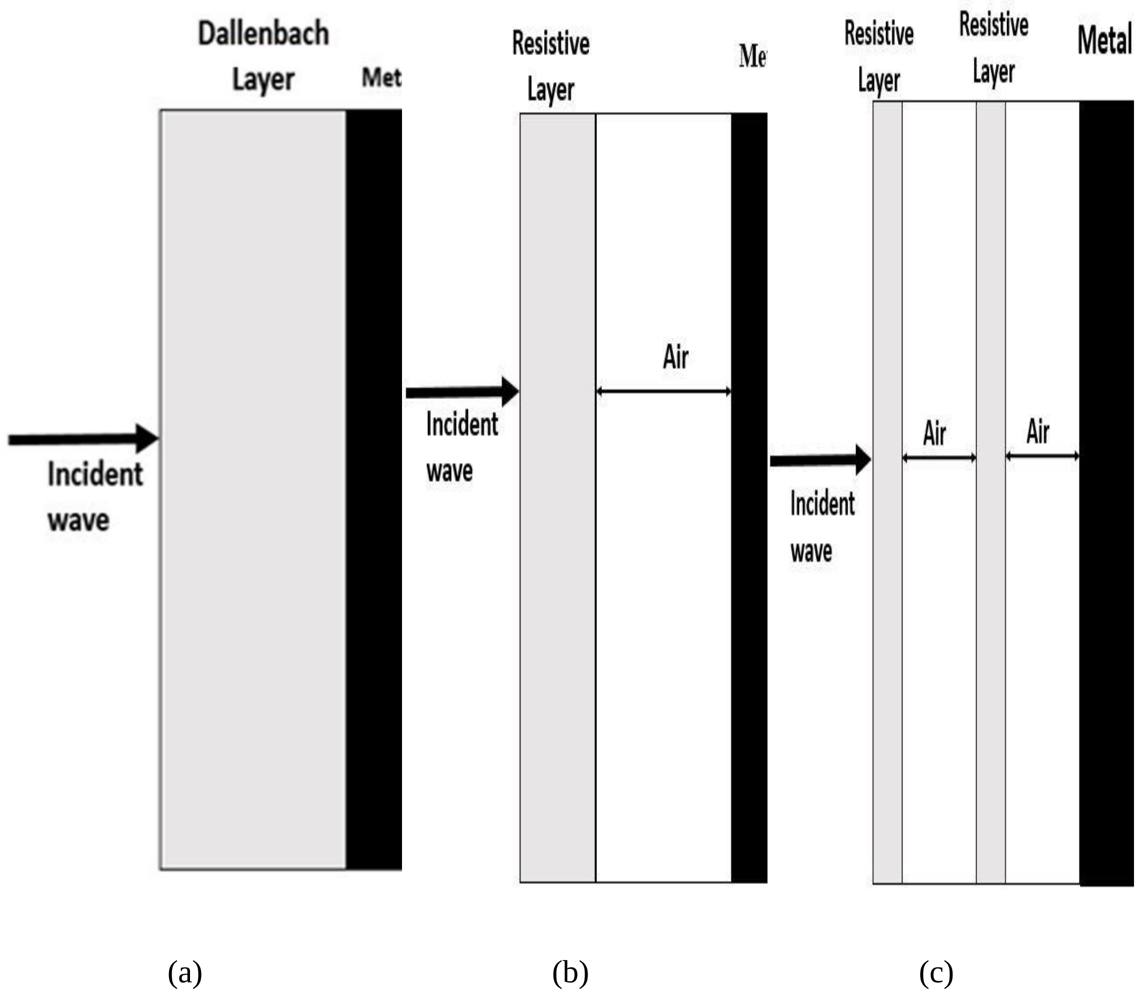

Figure 1.2. Configurations of conventional absorbers (a) Dallenbach, (b) Salisbury and (c) Jaumann.

1.2.2 MM inspired Antenna

The foremost parameter to be evaluated for the stealth or low observable (LO) technology is radar cross-section reduction (RCS) of the antenna. The stealth technology is to work/operate without giving enemy forces any indications about its presence. LO or stealth technology is one of the major parts of military tactics. LO technology concept is based on making sensitive targets like airborne vehicles and naval ships invisible to different detection devices such as sonar, radar, etc. RCS is described as the fictitious area that would act as a reflector, which reflects a similar amount of the EM radiation to the receiving radar antenna system to that from the target. According to the IEEE dictionary, RCS can be represented as an evaluation of the strength of the reflective signal of the target.

The equation of the RCS can be written as:

$$\text{RCS}=\frac{4\pi R^2 S_r}{S_t} \tag{1.7}$$

where;

R is a range of radar;

S_r is scattered power density (w/ m^2)

S_t is power density intercepted by target (w/ m^2).

Various ways are presented in the literature to reduce RCS. The most common methods which are implementing nowadays are:

- Absorber structures/ material
- Shaping

- ***Absorber structures/ material***

RAM can be used where shaping is not effective alone. The remarkable radar cross-section reduction (RCSR) has been achieved with the help of RAM structures, but it has also some drawbacks such as high maintenance, cost, and heavyweight.

- ***Shaping***

Shaping technique can be implemented in the design stage. The size of the object is directly proportional to the RCS. The larger an object, the stronger its reflection on the radar, and hence the greater its RCS. So, it becomes a mandate to provide shaping to the structure in this way so that it cannot reflect the signal towards the Radar. In stealth technology, the antenna plays the dominant role, as it is a part of the communication system, which transmits and receives EM wave. Therefore, stealth property could be reduced because of the high RCS of an antenna. Overall RCS of target objects like airborne vehicles and naval ships depend upon antennas.

Consequently, to reduce the RCS of the objects, need to reduce the RCS of an antenna.

1.3 Thesis Motivation

Stealth technology is considered as sophisticated and modern technology. However, there are so many examples of stealth that exist in nature. One of the best and simplest example is the change in color of reptiles and insects, with respect to their backgrounds. Without a question, humans were motivated to use deception to deal with fighting in wars, resultant in stealth technology. Stealth technology is based on RCSR of the target object. By considering the practical details it is necessary to resolve the following issues:

- There is a strong trade-off between bandwidth and thickness of the absorber. A broadband absorption can be achieved at the expense of higher absorbing layer coating thickness, which is not desirable for practical EM applications. Moreover, the thickness of the absorber cannot be increased beyond some specified limit.
- Reduce the RCS of an antenna without degrading other radiation characteristics like gain, directivity, reflection coefficient, and bandwidth of an antenna.
- The fabrication and measurement complexities are another important issue in the development of MM based absorber and antenna structures.

1.4 Contribution of the Thesis

Based on the motivations, the main contribution of the thesis is to design lightweight, compact, broadband MM based absorbers, and low RCS antennas. Frequency-dependent EM properties are also extracted from the proposed absorbers. The parametric study of different parameters of the proposed structure is also analyzed. The contribution of the thesis are listed below:

Contribution 1:

- Design of a new MM based microwave absorbing structure with wide absorption bandwidth.
    - Fabrication and measurement of the optimized MM based microwave absorbing structure.
    - Comparison of simulated and measured results.

In this contribution, two different MM based microwave absorbers have been designed and simulated.

The first one is a cross-loaded split ring-shaped FSS frequency-selective surface (FSS), single-substrate-layer, broadband MM absorber. A miniaturized structure, single-substrate layer, simple geometry, and wide bandwidth are some of the key features of the proposed MM absorber. The other one is comprised of eight sectors loaded circle inside the square-shaped FSS frequency-selective surface (FSS), single-substrate-layer multiband absorber. The key features of this absorber are multi-band absorption, polarization-insensitivity, and angular stability. This contribution is analyzed the surface current distribution, **E** field, and **H** field distribution. Frequency-based EM properties have been also extracted from S_{11} parameter. Additionally, the proposed structure is fabricated and measured in an anechoic chamber, and finally simulated and measured results are compared with each other.

Contribution 2:

- Design and analysis of a MM based active microwave absorber structure with variable frequency response.

There is no flexibility of microwave absorbing frequency range after fabrication of a particular absorber. To overcome this drawback, in this contribution an active microwave absorbed structure is designed and simulated. There are various methods to vary the frequency response of the structure. In this contribution to obtain the variable frequency response, p-i-n diode has been used in one method. Moreover, the simulated and measured results of the fabricated prototype are estimated.

Contribution 3:

- Development of a MM inspired antenna with low RCS.
    - Fabrication and measurement of the optimized MM inspired antenna.
    - Comparison of simulated and measured results.

This contribution devotes to MM inspired antenna to reduce its RCS. Two distinct MM-inspired antenna are designed, simulated, and finally fabricated to investigate their feasibility. The first one is a split square and ring-shaped based hybrid MM-inspired antenna and the second one is a flexible MM-based superstrate coupled microstrip patch antenna (MPA), which enhances the gain along with radar cross-section reduction (RCSR) of the MPA. In the first MM inspired antenna to reduce the complexity, split ring resonator (SRR) based two distinct MM unit cells are designed and simulated. Finally, the designed unit cells are distributed around the radiating patch to achieve the low RCS of an antenna. This research work is analyzed in the terms of RC and RCS characteristics. Simulated outcomes are validated by measured results. The second antenna devotes to reduce the RCS as well as increase the gain of an antenna. This contribution is analyzed different configurations of MM layer in terms of RCSR. In this contribution, the RC, RCS, and the gain of an antenna is well studied and analyzed. The radiation pattern of the proposed structure is also simulated and measured. Measured results are well-matched with the simulated ones.

1.5 Thesis Organization

This thesis is organized into six chapters. The detailed content of each chapter of the thesis are as follows:

CHAPTER 1 devotes to the introduction of MM and its classifications. Furthermore, this chapter gives the introduction to stealth technology and the techniques to reduce the RCS. The motivation for the research, contribution of the thesis, and thesis organization are also described in this chapter.

CHAPTER 2 deals with the available literature based on MM based absorbers, active absorbers, and MM based low RCS.

CHAPTER 3 illustrates the two distinct MM based absorber. Under the first design, the designing, optimization, and modelling of the hybrid structure, comprised of a cross-loaded split ring absorber is illustrated. The critical analysis of the proposed structure is also described. Frequency-dependent EM characteristics and current distribution are also illustrated. Besides, the comparison between simulated and measured results is described, which are quite well-matched with each other.

Secondly, the designing, optimization, and modelling of the eight sectors loaded circle inside the square-shaped FSS frequency-selective surface (FSS), single-substrate-layer multiband absorber. It also describes the Critical analysis and numerical demonstration of the proposed structure. Frequency-dependent EM characteristics and current distribution are also elucidated. Also, the comparison between simulated and measured results is described. Finally, comparison of the proposed structures with other reported work is given in this chapter.

CHAPTER 4 demonstrates the tunable absorber based on an active frequency selective surface (AFSS). A tunable, single layer, and wideband AFSS based absorber is presented, which demonstrates the tunability in the range of 9.2 to 11.2 GHz. A similar design of AFSS has been used to construct an efficient tunable microwave absorber, in which the bandwidth with forward resistance of 30Ω has been achieved.

Additionally, the critical analysis has also been investigated to know the effect of dimensions on AFSS loaded tunable absorber. Finally, the prototype is fabricated and measured for the validation of simulated results.

CHAPTER 5 presents the two distinct MM inspired antennas with low RCS. This chapter is divided into two subparts. The first one is splitted square and ring-shaped based hybrid MM inspired antenna and the second one is flexible MM based superstrate coupled MPA.

In the first antenna, the design of MM unit cell, design of reference, and proposed antennas are discussed. It also explains three different configurations based on MM unit cell. It analyzes the simulated and measured results of the proposed antennas, along with a comparison between both results.

The second part describes the flexible MM based superstrate antenna with high gain and low RCS. The two distinct MM unit cells are designed and simulated in the range of 2 to 12 gigahertz (GHz). The EM properties of these structures are estimated to reflect their MM nature. Five different configurations loaded with MM structures are designed and compared in terms of their RCSR. The design of primary and proposed antennas are also described. Finally, the primary and proposed antennas are fabricated and measured to authenticate the accuracy of the simulation.

CHAPTER 6 gives the conclusion of the research work and defines future work for further research.

CHAPTER 2

LITERATURE SURVEY

2.1 INTRODUCTION

MM based absorbers and antennas plays a significant role in distinct practical EM applications, having great potential to be commercialized. Typical MM based absorbers includes single layered, multilayered, active element, and polarization insensitive based structures. Each EM structure has its own advantages and disadvantages based on the frequency range and applications. MM inspired antennas are well known for the RCSR and enhance the gain of an antenna. This chapter discuss the critical review of such advanced EM structures. This chapter is divided into three sub parts, first part include the literature review based on MM based microwave absorbing structure. In second part the literature survey over MM based smart microwave absorbing structure is explored.

Finally, the literature review of MM inspired antenna with low RCS is presented in the third part.

2.2 LITERATURE SURVEY ON MM BASED ABSORBER

Design, theoretical discussion and test results are introduced for a multi ring shaped multiband FSS in [8]. Double ring element of the single screen structure is act as a low pass that reflects the signal of Ka-band but passes the signals of S, X, and Ku-band. A tri-ring element of the structure reflects the signal of X-band although transmits the signal for S and Ku band. Further, the two single screens which are mentioned above are cascaded to make the double screen non-similar double ring structure. Finally the testing has been performed and it is realized that the simulated and computed results are good in agreement with each other.

A tree like fractal based FSS structure is introduced for multiband frequency range in [9]. The benefits of the structure is that it covers multiband and its frequency response is same for both transverse electric (TE) and transverse magnetic (TM) polarizations. Further, it is also concluded that operation frequency of the individual band can be controlled by the similarity or scaling factor of the FSS elements.

A novel shape of FSS has been designed, simulated and fabricated for closely spaced bands in [10]. For the designing purpose equivalent circuit modelling is proposed to find out the optimal values of the parameters, and for its design multi-stage procedure is introduced. Further, an analytical technique (approximate) is used to decide the values of the equivalent circuit parameters of the structure, which is also used to determine the bandwidth of each band and the center frequency. For the verification of this procedure full-wave EM simulations have been used and finally, the testing has been performed on the fabricated prototype. It is concluded that with compact dimension of unit cell and with thin substrate thickness of the structure a stable frequency response for both TE and TM polarizations is achieved.

A radome based on Frequency selective surfaces (FSS), which act as a pass band filter for some particular frequency range and act as a absorber for transmission range is designed in [11]. The pass band behavior and a large rejection band is obtained because of closely packed interlinked Jerusalem cross shaped FSS, which is used as a ground plane. To analyze the behavior of the composite structure a thorough study on different parameters of the structure is performed. Further, an equivalent circuit modelling has been also introduced, and to verify the results of equivalent circuit approach. The full-wave numerical simulation has been done by using high-frequency structure simulator (HFSS) and computer simulation technology (CST) softwares.

Costa et al. proposed a thin absorbers based on high-impedance surfaces, which includes lossy frequency selective surface and large numbers of lumped resistors incorporated with resistive inks placed above a thin dielectric slab backed by a ground sheet. The optimal value of the structure depends on the substrate parameters and the FSS shape. With the same shape of FSS element, absorber can be used for narrowband and for wideband application [12].

A broadband metamaterial absorber (MMA) with octave bandwidth is introduced by Bhattacharyya et al. [13]. Two simple patches are deposited diagonally on the thin grounded substrate layer which gives 8.30 GHz absorption response from 6.86 to 15.16 GHz with 90% absorptivity. The analysis on the geometric parameters is also carried out to know the effect of parameters on the absorptivity. This structure is polarization sensitive due to two-fold symmetrical geometry. At 0° and 90° the maximum absorption take place and structure exhibits no absorption at 45°.

Chaurasiya et al. presented a polarization-insensitive ultrathin penta-band MMA which consists of a tetra arrow with closed ring resonator [14]. Because of four-fold symmetry geometry the structure is polarization insensitive upto 45° for both TE and

TM polarizations. This structure shows five different absorptivity peaks of 98.6%, 96.6%, 90.1%, 97.8%, and 93.1% at 3.4, 8.34, 9.46, 14.44, and 16.62 GHz respectively. The fabricated and simulated structures responses are in good agreement with each other. Therefore, it proves the reliability of the structure for many practical applications.

A broadband and thin absorber based on resistive FSS and magnetic sheets is reported by Wan et al [15]. The three layer structure contains a resistive FSS layer placed between two magnetic sheet layers. After simulation sample has been fabricated, and measurement result exhibits the 10.1 GHz absorption bandwidth from 7.9 to 18 GHz. The comparison between non resistive and resistive FSS is also shown and it is concluded that due to presence of resistors the power loss occur which results in enhancement in absorption and bandwidth.

A research is done by the Ghosh et al. based on ulta-thin, multi-band, wide-angle absorptive and polarization-insensitive metamaterial absorber [16]. The proposed structure consist of two centered copper rings etched on upper side of dielectric substrate layer. Due to four-fold symmetry design the absorber is polarization insensitive. Moreover, measured and simulated results are agree well with each other. Under normal incidence, the proposed structure shows four different absorptivity peaks of 98.81, 99.68, 99.98 and 99.34% absorption peaks at 4.11, 7.91, 10.13 and 11.51 GHz respectively .

Chaurasiya et al. presented a triple-band ultra-thin microwave MMA comprising of tetra-arrow ring shaped FSS printed on 1mm substrate thickness, whose one side is completely grounded [17] Simulated results reveals three different absorptivity peaks of 95.27%, 98.35%, and 97.96% at 4 GHz, 6.54 GHz, and 11.15 GHz respectively. The absorption mechanism satisfy the condition of multi-reflection interference theory. Moreover, the proposed MMA is highly absorptive and polarization-insensitive for both TM and TE polarizations. Finally for the verification of the proposed MMA, the fabricated prototype is tested and compared with simulated results, which coincide well with each other.

A triple band MMA using electric field-driven LC resonators is proposed by Srivastava et al. [18]. The proposed structure is polarization-independent over wide angle of incidence, it gives good absorption upto $60^{\circ}$for TM and TE polarizations. The unit cell is designed and simulated to provide the absorption in C-band. The real and imaginary parts of the complex dielectric permittivity (ε_r), complex magnetic permeability (μ_r) are also extracted from the simulated results, which satisfies the absorption conditions at all the resonant frequencies. Finally the optimal structure is fabricated to verify the simulated results. The measured results and simulated results are matched with each other.

Panwar et al. presented a thin microwave absorber, which is based on the Sierpinski gasket fractal FSS placed on the double substrate layer [19]. The overall thickness of the structure is less than 1.5 mm. Optimization of composite selection, thickness of layer, as well as layer preferences has been done by using a genetic algorithm. The structure comprises of double-layer coating with a FSS exhibits a Return loss of 35.57 dB at 9.5 GHz with bandwidth of 4.2 GHz from 8.2 to 12.4 GHz. To extract the values of ε_r and μ_r waveguide measurements are performed, the values are further used for the designing of composite absorber.

A wideband double U- shaped MMA with lumped resistor is introduced by Zhi et al. [20]. The structure consists of double U-shaped magnetic resonators with lumped resistors on a grounded dielectric substrate. The simulation has been done in the range of 2 to 18 GHz, which shows RL below -10 dB from 7.7 -18 GHz with peak value about -25 dB under normal incidence. Simulated surface current and power loss density distribution is also illustrated in this article, which indicate that use of the lumped resistors in the magnetic resonator is responsible for the wideband absorption of the MMA.

Zhong et al. investigated an ultrathin and broadband MMA, which composed of multilayered structure [21]. In this structure teflon with permittivity of 2.1 is used as a top layer substrate and rogers substrate is used at the bottom three layers of the structure. The structure is composed of three copper films in square shape and the last layer of the substrate is backed by a copper plate to reflect EM wave. Result shows that more than 90% absorption is achieved in the frequency range from 8.3 GHz to 21 GHz with a thickness of 3.65 mm. Moreover, the verification of the physical mechanism of the MMA is also presented in this work.

Cheng et al. presented a broadband MMA with lumped elements, which consists of the substrate sandwiched with continuous copper plate and split-coin resonators (SCR) shaped copper with lumped elements [22]. Authors have compared the single SCR MMA, with the composite MMA with lumped elements, and concluded that composite MMA with lumped elements has a wider absorptivity. Thereafter, parametric studies are also performed on the lumped resistance and capacitance values to know the optimized values for which maximum absorption is achieved.

An ultrathin multiband MMA is designed, analyzed, fabricated and measured by Cui et al. [23]. The structure composed of dielectric substrate with 1mm thickness sandwiched with periodic array of electric-field-coupled-LC (ELC) resonators of different dimensions and a metallic ground plane. Experimental results illustrates that excellent absorption has been obtained in the designed frequency bands with different angle of incidence under TE and TM polarizations. Thereafter in the form of surface current, the verification of the physical mechanism of the multiband MMA is also introduced in this article.

A novel shaped, dual-band FSS is introduced, designed, simulated and fabricated in [24]. In each FSS unit cell two-dimensional closed packed U-shaped slot resonators are used to obtain the absorption frequencies of 8.80 and 9.54 GHz. Also, each U-shaped slot resonator is consist of straight slot at the centre connected to two U-shaped arms. The parametric studies are also performed to optimize the dimensions of the slot resonators using CST Microwave Solver. The introduced FSS structure is polarization independent because of 90° rotation of FSS structure in the unit cell. Measured results are well in agreement with simulated ones.

The multi-band SRRs used as FSS unit cell is proposed in [25]. The equivalent circuit modelling is also introduced in this article, which reveals that, additional dip present in the transmission and reflection spectrums of structure. Because of the coupling effect between the periodic arrays of SRRs, the multiband properties are realized. Finally, the effect of SRR’s geometrical parameters are also investigated to know its effect on the resonance frequencies.

Sekar et al. presented a compact, ultra-thin MMA which composed of two circular rings inside the rectangular split ring [26]. The benefits of the introduced absorber is its wideband absorption with small unit cell size (8 mm × 8 mm size) and low thickness of substrate (1 mm thick) structure as compared to other reported microwave MMAs. While the drawback of this structure is that it is a polarization sensitive, with variation in angle of incidence the absorptivity will reduce. In order to realize the absorption mechanism surface current distribution is also presented which conclude that rectangular and circular rings are the responsible for low frequency resonance, while at higher frequency partially rectangle and the inner circular ring are responsible for absorption.

A broadband prefect MMA based on circular and fractal structure is introduced by Fan et al. in [27]. The top surface is of metallic patch which is stacked on a grounded dielectric substrate with 1.6 mm thickness. Because of the use of fractal and circular structure simultaneously, bandwidth is upgraded without affecting the dimension of the unit cell. To describe the absorption phenomenon the surface current density of the structure is also shown in the work. One more step, a equivalent circuit modelling has been introduced to predict the absorption frequency of the proposed structure. Due to four-fold geometry the structure is also polarization insensitive. Further, the testing is performed on the fabricated prototype which shows that computed results are in good agreement with simulated ones.

A wide-angle, seven band MMA is designed and simulated in [28]. An absorber is comprises of the single closed-meander-wire shape structure placed over a grounded dielectric substrate. It has been observed that 90% absorption has been achieved by the structure at seven different frequencies. Because of the symmetrical geometry the absorber is polarization insensitive, also gives the similar absorption response for both TM and TE polarizations under distinct angles. Thereafter, parametric studies are also performed to investigate the influence of the structure parameters on absorption property. Finally the structure is fabricated and measured results coincide well with the simulated ones.

A broadband MMA with two interlaced fishnet layers is proposed by Tan et al. in [29], which works in terahertz frequency range. The designed absorber composed of two distinct square shape fishnet layer with different thickness which is stacked on a ground plane to stop the transmission. The ground plane is composed of aluminum film with 200 nm thickness deposited on a silicon wafer. Two different polyimide spacers are used for two different fishnet layers. The individually fishnet layer is patterned on the corresponding polyimide spacers with photolithography process. The simulated results reveal that the three absorption peaks are obtained at 1.596, 1.791 and 1.989 THz and because of four-fold geometry the structure is polarization insensitive.

A FR-4 substrate based broadband MMA is proposed in [30], which composed of metallic patch on the top of the substrate backed by the ground plane. The diagonal corners of the patch are defected to obtain the broadband absorbance. The simulated results reveals that the more than 90% absorption has been achieved in the range of 4.0-6.0 GHz. Due to asymmetrical structure the absorber is sensitive to the different polarization angles. Optimization of the structure parameters are also performed to investigate the optimal value where broad bandwidth and the higher absorption can be achieved. E field distribution and surface current of the top and bottom of the absorber is also shown to understand the mechanism of the absorption.

An ultra-thin, single layer FR-4 substrate based broadband MMA is reported in [31], which is used for C-band applications. The reported MMA covers the whole C- band ranging from 4.0 GHz to 8.0 GHz. It is observed that more than 90% absorption has been achieved with this structure and upto 40° incident angle almost 80% absorption take place for both TM and TE polarizations. To realize the absorption mechanism, the E field distribution and surface current at three resonant peaks are also illustrated in this work. The electromagnetic parameters are also retrieved by S_{11} results. The comparison table is also given with respect to thickness, bandwidth and insensitivity angle with other reported structure and it conclude that the proposed structure is feasible for practical application because of its numerous advantages over other reported structure.

Beeharry et al. introduced a dual-layer, broadband and thin FSS based absorber to reduce EMI in radomes [32]. The proposed absorber composed of two different circular shape pattern on the two different dielectric substrate with different thickness, which is isolated by an air gap. Parametric studies are also performed on different parameters of the structure to investigate where the maximum absorption and wider bandwidth can be obtain. The remarkable bandwidth has been achieved with 89.7% absorption in the range of 4.8GHz to 11.1GHz for TM and TE polarizations. It is noted that the structure is polarization sensitive, upto 30° angle of incidence bandwidth get reduced at the upper frequency but at lower frequency the absorption remains almost constant. After the fabrication of the structure, the measured results are well matched with the simulated results.

A ultrawideband, polarization-independent MMA is introduced by Yoo et al. for X-band application. An ultrawide spectrum has been obtained with high absorptivity with the fusion of artificial impedance surface (AIS) and resistor-capacitor layer. The RC layer is stacked on the AIS layer with 4mm air gap. The structure is polarization insensitive because of hexagonal configuration of both layers, which also makes it unique. Transmission line (TL) modelling has been introduced to analyze the circuit and the structure designing is based on TL model. Further, to verify the results of TL modelling the full-wave simulation has been carried out. The TL analysis and simulated results are in good agreement with each other. Further, the fabrication has been performed on FR4 substrate and the fabricated prototype is tested and it is concluded that the simulated and computed results well coincide with each other. The -10 dB bandwidth ranging from 6.79 to 14.96 GHz has been obtained with 150Ω resistor value and 0.1pF capacitor value.

A compact, ultra-thin and wideband MMA has been presented by Tripathi et al [34]. The FR4 dielectric substrate is sandwiched between grounded plane and periodic pattern of microstrip bend shaped structure. The parametric studies are performed on the strip length and width to investigate the influence of there parameters on absorption and bandwidth of the structure. The -10 dB absorption bandwidth has been achieved from 8.60 to 12.35 GHz for normal incidence. E-field. H-field and surface current are also studied in this work to figure out the behavior of the absorber. Finally, the structure is fabricated and tested to verify the simulated results. Due to asymmetrical shape the structure is polarization sensitive which is proved by simulated and measured results.

2.3 LITERATURE SURVEY ON SMART ABSORBER

Bakir et al. studied the U shape FSS for absorber and sensor configuration [35]. The three configurations i.e. single, double and quad U-shaped FSS structures are discussed. A single frequency band-stop filter property is obtained by the quad and single U-shaped FSS elements, whereas the dual-frequency band-stop filter behavior acquired by the double U-shaped FSS. The single and double configuration of U-shaped FSS absorber exhibits maximum 90% absorbance. The optimal samples have been fabricated in order to verify the simulated results, which are in close agreement with each other.

Zhou et al. designed and simulated a composite RAM composed of gradient and spiral square shaped FSS along with resistor [36]. The operation bandwidth is significantly increased by the use of resistor in FSS as compared to single magnetic RAM. Under normal incidence outstanding absorptive performance with -10 dB below reflectivity is observed in the range of 6 to 18 GHz with 2.0 mm thickness of the substrate. Furthermore, the proposed structure shows high angular stability from 0° to 30°. To represent the influence of the resistors, nonresistor FSS structure is also fabricated and compared with composite RAM structure. For the validation, measured results are compared with simulated ones, which are well agreed with each other.

Costa and Monorchio [37] reveal a design, which consists of single resistive sheet mounted on a reactive surface at some fixed distance. At lower frequency, the structure acts as an artificial magnetic conductor (AMC), because of its composition which includes FSS layer on a grounded dielectric substrate, while at higher frequencies it acts as a perfect electric conductor (PEC). The distance between the resistive sheet and reactive surface should be maintained in such a way so that it can fulfil the condition of Salisbury screen for high-frequency regime, and for lower band it acts as an absorber. To analytically explain the behavior of the structure circuit modelling is also proposed. Measurement of the fabricated structure is also illustrated to verify the simulated results, which are well matched with each other.

A switchable reflector/absorber comprises active FSS (AFSS) for broadband as well as for single application is investigated by Ghosh et al. [38]. The AFSS composed of periodic square loops patterns, which are connected via p-i-n diodes resulting in switchable performance. Due to the symmetric configuration polarization insensitive structure is obtained, and the novelty is also obtained in the biasing network. A wideband switchable reflector/absorber characteristics has been obtained in C-band because of the resistors mounted on the surface. One step further, to validate the simulation results, fabricated samples have been measured in anechoic chamber. Under normal incidence and for distinct polarization angles simulated and measured results agree with each other.

A tunable broadband microwave absorber is designed, simulated and fabricated by Zeng et al. [39] A tunable characteristic is obtained because of AFSS structure. The unit cell of the AFSS comprises of PIN diode and two reverse anchor patches. To investigate the influence of biasing over the reflection coefficient, the biasing voltage is changed from 0.6 to 0.78V. It is observed that less than -10dB reflection coefficient is achieved from 7 to 13 GHz. Because of change in biasing voltage the absorbing frequency band can be also tuned from 7 to 13 GHz. The fabricated AFSS absorber is thin, light in weight and attains a broad bandwidth. Further, the fabricated sample is tested to justify the simulated results, which shows good agreement with each other.

A new MM active absorber is presented by Fan et al. [40] using non-Foster loads to make MMA active. Author also studied the performance of active MMA for TE and

TM polarizations, along with its analytical circuit modelling which included material losses also. To attain the wide-angle and wideband, active element is used, which is comprises of two port non-foster circuit, based on tunneling diodes. To verify the analytical results, an active MMA design is simulated, which illustrates good agreement with analytical results for TM and TE polarizations. Prototype fabrication and measurement can be done in the future to make it practically realizable.

[41] A slotted ground based tunable FSS is proposed. Metallic MEMS based bridge over the slot is used to tune the resonant frequency. The resonating frequency of FSS is depending upon the equivalent capacitive load of the bridge. As equivalent capacitive increases the resonance frequency decreases. The designed FSS is investigated using electromechanical and electromagnetic simulations. The FSS unit cell is simulated in a waveguide simulator to measure the S-parameter. The result shows that MEMS bridge shifts the frequency more than 1.7 GHz in the X-band. At resonance frequency i.e. 9.59 GHz, bandwidth of 400 MHz is obtained. The final FSS has 3.2 dB loss at 9.2GHz resonant frequency and low loss at high frequency. This is achieved by using MEMS bridge advantage over using SU-8 as the sacrificial layer. The MEMS bridges are fabricated with different height to study the change in the resonance frequency, whereas the fabricated prototype was tested at fixed heights. Simulated and measured results show excellent agreement. An FSS array is designed based on the FSS unit cell results. The design procedure to maximize the quality factor and controllable frequency range, and improve the radiation characteristics of the FSS array is discussed. Further simulations are performed to examine the performance of the FSS array with regards to grating lobes, oblique incidence and tunability.

[42] The author investigated angular stable, ultra-thin and low cost absorber at low frequencies. The proposed ultra-thin absorber comprising of metallic HIS and has been manufactured by low cost fabrication process. Therefore, it proves the reliability of the structure for many practical applications, such as to magnify the performance of wireless systems e.g., radio frequency identification systems (RFID). A common cardboard panel has been utilized as a substrate, aluminum foil is used as metallic part and shielding is provided by a spray paint. The final prototype has been tested in waveguide environment and free space at 5GHz and 868MHz respectively.

[43] For high-resolution measurements of thickness of a superstrate layer and variations in the dielectric constant a novel shaped MM sensor, integrated with an X-

band waveguide, is considered. The shift in the resonance frequency of the MM sensor is correlated with variations in superstrate parameters. These variations are caused by chemical, biological or physical factors. For 10 MHz shift in resonant frequency, the simulated results reveal the good resolution levels upto 0.023 absolute change in relative permittivity and 1.1 μm change in thickness of the sensing layer. A fabricated prototype has been verified experimentally and demonstrates good agreement with simulated results.

2.4 LITERATURE SURVEY ON RCSR ANTENNA

In this study RCSR of a microstrip antenna is achieved by replacing the normal substrate with ferrite based substrate with biasing [44]. RCS has been reduced over a wide frequency range with ferrite based substrate which works in cutoff state. When there is no biasing, antenna provides large RCS peaks at different resonance frequencies. When proper biasing is provided to the antenna, the elements of an antenna become short circuited, which results in reduction of RCS around 20-40 dB. This technique can also be implement to the array of an antenna. To acquire the simulated results a full-wave moment method has been employed.

Paquay et al. designed a thin AMC based structure for RCSR application [45]. The structure is composed of AMC and PEC elements which are placed in a chessboard fashion. Full copper plate with particular dimension constitutes the PEC part, while the AMC part is formed by Sievenpiper's mushrooms. For theoretical analysis and designing of the structure, Ansoft-HFSS software has been employed. The opposite phase reflection of PEC and AMC has been noticed at the resonant frequency, resulting in cancelation of reflecting waves and leading to RCSR. Further, fabricated prototype is tested to obtain the computed results, which proves the validation of this approach.

Y. Li et al. presented a technique to reduce the RCS of a microstrip antenna by cutting slots on ground [46]. Because of this simple technique antenna size and resonance frequency are reduced. The RCS is also reduced in the whole band of 2-8 GHz as compared to rectangular patch antenna. Radiation performance is preserved with this technique, while a negligible 0.9 dB gain reduction is also observed which is negligible. The in band RCSR has also been achieved from 2-4 GHz. To check the feasibility of this technique the structure has been fabricated, and it is concluded that the simulated results coincide with measured results.

A thin AMC structure for RCSR application has been designed and fabricated by Cos et al. [47]. The structure composed of AMC elements in chessboard fashion. To obtain the 180˚phase shift between two waves, causing destructive interference and thereby reduce the scattering level. Two different configurations of structure are designed, and fabricated. A comparison between these configurations in terms of measured RCSR is also present, which proves that AMC#1 gives better result as compared to other configurations. To know the behavior of the structure, it is also studied for different azimuth incident angles, which proves that the structure is polarization insensitive.

RCS of 2 × 2 array antenna is reduced by using the band- stop miniaturized FSS, composed of compact square loop elements [48]. The resonance frequency of an antenna and the FSS band is similar that is 3.3 to 3.4 GHz. Conventional ground plane of the array antenna is replaced by miniaturized square shape FSS except underneath the patch region. For the stop band FSS behaves as a ground plane, while for other frequencies it act as a transparent. Simulated results shows that wideband RCSR from 4 to 9.5 GHz is achieved, without affecting the various radiation characteristics like gain, impedance bandwidth and antenna pattern of an antenna in comparison with the typical array antenna. Finally, the structure is fabricated and tested, to verify the simulated results. Simulated and measured results are coincide well with each other, showing the importance of the structure for distinct practical applications.

In this study a novel technique is proposed by Genovesi et al. to reduce the RCS of an array of a microstrip antenna by using FSS [49]. The goal is achieved by replace the metallic ground plane of an array of a microstrip antenna with a hybrid geometry of FSS. The performance of hybrid ground which is based on FSS is realized by a periodic method of moments (PMM), and the designing of the structure is based on TL modelling. Simulation is also performed by using CST software to verify the results of analytical techniques. The results show that proposed antenna gives substantially out of band RCSR without affecting the in-band radiation characteristics of an array of a microstrip antenna. The fabricated structure has been measured, it is found that simulated and measured results are well coincide with each other.

A novel approach has been developed by Lee et al. to reduce the RCS of a microstrip patch antenna which can be used for communication purpose in aircrafts, fighter jets and other vehicles [50]. The electromagnetic band gap (EBG) structure of conducting polymer with square shaped pattern is printed on the grounded dielectric substrate. EBG structure is designed in this manner so that it can absorb 90% EM wave in X-band, thus reducing its RCS. Finally, the EBG structure is implemented around an antenna to reduce its RCS. It has been concluded that this approach is reduced around 83% RCS of an antenna, without disturbing its radiation properties. The maximum reduction 95% in RCS is obtained at 10.0 GHz. The fabricated prototype is further tested to verify the simulated results, they are good agreement with each other.

In this work in-band RCS of the array antennas has been reduced by using square patch element loaded with lumped resistor radar absorbing structure [51]. A 4×1 array of an antenna is designed, simulated and fabricated to investigate the performance of an antenna. Comparison between conventional antenna array and antenna array with RAS is also illustrated. It is shown that with RAS antenna array RCS is reduced and RAS is not disturbing the other radiation characteristics of the array. Finally, the measured result of fabricated prototype are formed to be well matched with the simulated results.

The hexagon shape quasi-fractal based FSS is introduced to reduce the out-of-band RCS of the 4×2 dipole array antenna in [52]. To reduce the RCS ground plate of an array antenna is replaced with this FSS providing the remarkable bandstop characteristics. This technique reduces the RCS while preserves the radiation characteristics of an antenna. FSS provides high angular stability, thus RCS peak up to 60°can be controlled. The measured results of the fabricated prototype are matched well with simulated ones.

In this study instead of using lossy FSS sheet, Turpin et al. used magnetically loaded RAM sheet [53]. This technique improved the absorption characteristics of the structure and also simplified the designing process. Stochastic optimizer is used to optimize the different parameters of the structure. There is a tradeoff has been observed by author, between absorption bandwidth and other parameters of the structure. The analytical approach has been utilized to optimize the different dimensions. This structure is used in patch antenna to improve the RCS of an antenna, but this structure can also be used for other practical applications.

Zhang et al. designed, simulated and fabricated two primary antennas namely antenna 1 and antenna 2. An antenna 2 is loaded with hexagonal shaped LHM to reduce the RCS [54]. Both primary antennas and modified antenna are resonating at 1.1 6 GHz. The remarkable out of band RCS is reduced of the modified antenna while preserving the radiation characteristics of the primary antennas. Surface current distribution and volume current distribution is also given in this study, which proves that the significant RCS reduction is achieved because of LHM. Meanwhile, both primary and modified antennas are fabricated and tested to find out the measured results, which coincide well with the simulated ones.

An AMC ground structure is used rather than copper grounded sheet to reduce the RCS of a microstrip array antenna in [55]. The operating band of antenna array is S-band, while the AMC cells operate in X band. The AMC ground composed of two distinct shapes, based on passive cancellation principle. Firstly, two unique AMC unit cells are simulated, namely AMC1 and AMC2, then they are merged to replace the traditional metallic ground of the primary antenna. AMC1 unit cell is made up of Jerusalem crosses shape metallic patch and AMC2 contains patch and square ring with gaps. It is observed that the RCS of the primary antenna array is reduced from 6 to 13.4 GHz. The fabrication has been done to verify the simulated results, it is concluded that simulated results are in good agreement with the measured ones.

Zhao et al. designed, simulated and fabricated a low RCS circularly polarized antenna [56]. In this work RCS has been reduced with the use of metasurface based array. The metasurface consist of 4×4 rectangular patches with linear-polarization. The proposed structure gives anti-phase reflections under orthogonal polarized incident wave resulting in scattering of the wave. To fulfill this condition antenna 2×2 sub array are arranged orthogonally and arrays are fed with 90° phase shift. Because of this arrangement, broadband circularly polarization and low RCS feature have been achieved simultaneously. To validate the simulated results, finally the fabrication has been done.

Liu et al. investigates the cross shaped MMA to reduce the RCS of the waveguide slot antenna [57]. The ultra-thin MMA is used as a ground plane of the slot antenna, instead of PEC ground plane. It is observed that with this configuration the monostatic and the bistatic RCS of a slot antenna are noticeably reduced, and the performance, characteristics of the antenna are preserved. Finally the fabricated prototype has been measured for the validation of simulated results, and it is concluded that the both results are in good agreement with each other, which shows the value of the antenna for stealth application.

Fu et al. presented composite AMC based surface for wide band RCSR [58]. The structure consist of two unique shaped AMC cells, with distinct resonance frequencies. The phase difference between both cells is within a range close to ±π over bandwidth. Because of ±π phase difference, the reflected wave from these two cells cancel each other. On the basis of this basic principle RCS has been reduced over a wide range of frequency. To check the feasibility and validation of the simulated results fabrication has been done. Finally, the fabricated prototype has been measured in anechoic chamber, and it is observed that RCSR has been obtained within 32% bandwidth from 5.1 to 7.5 GHz.

A thin AMC structure is designed, simulated and fabricated for RCSR by Paquay et al. [59]. The advantage of this structure is its simplicity, reduction in overall thickness along with RCS reduction. The structure is based on a cheeseboard configuration which consist of PEC and AMC cells. The AMC part consist of an array of Sievenpiper's mushrooms, whereas the full metallic patches have been used as a PEC cells in this configuration. At the operation frequency of the structure, the reflection of both cells have opposite phase, thereby cancelling each other, resultant in RCSR. Simulation and thorough analysis has been done with Ansoft-HFSS software. Monostatic and Bistatic measurements have been performed to confirm this approach.

A circle shaped patch novel dual layer broadband chessboard based configuration structure is presented to reduce the RCS [60]. Chessboard configuration consist of two different shapes of AMC cells, one is designed on rogers RO4003 substrate and the other one of only rogers RO4003 substrate with no copper on top of the substrate. It is observed that with this structure 73% bandwidth of -10 dB RCSR has been achieved as compared to metallic plate. As bandwidth so dependent on thickness of the structure, so an air gap is introduced to enhance the bandwidth with low cost. Finally, simulated and measured results are in good correspondence.

Zheng et al. investigated an ultra-thin RAM using high impedance ground plane (HIGP) for reduction of RCS of waveguide slot antenna [61]. As HIGP has high impedance property, therefore the thickness of the RAM is very thin, as compared to conventional absorbers. Moreover, lumped resistors are placed between the patches of HIGP. The ground plane of the waveguide slot antenna is also shielded by this new kind of RAM. Because of this technique it is observed that RCS of slot antenna is reduced significantly, as compared to the primary antenna (slot antenna with proper metallic ground plane). To validate the simulation, structure has been fabricated and it is concluded that the measured and simulated results are in good agreement.

A novel technique is presented to reduce the RCS of a circularly polarized (CP) 2×2 slot antenna array. In this feeding network is rotated sequentially to feed the elements of antenna array [62]. A staircase shaped MM structure is designed and manufactured due to the polarization conversion nature of the structure, CP radiation is obtained. A 180° phase difference has been observed between two MM cells, which ensures RCSR. The fabricated prototype is tested to validate the simulated results, which are in good agreement with each other.

Liu et al. presented a novel approach to reduce the monostatic RCS and to preserve the radiation properties, like realized boresight gains, impedance bandwidth and radiation patterns of a slot array antenna by using polarization conversion material (PCM) [63]. Fishbone-shaped element shape is used as a PCM in chessboard configuration, which is placed on the surface of an antenna. The analysis of RCSR mechanism and characterization is also done. Monostatic RCSR of antenna using PCM is observed from 6.0 to 18.0 GHz for both x and y polarization. To validate the results of simulations, the prototype is fabricated and tested and it is observed that the measured and simulated results are well matched with each other.

A wideband and thin nanobsorptive reducer (NARR) layer, capable of RCSR over a wide range of incident angles is proposed in [64]. The structure is comprises of two miniaturized-element frequency selective surfaces (MEFSS), which are placed on the dielectric substrate backed by a thin grounded plate. Two different MEFSS configurations are developed to achieve 180° phase difference over a broad frequency range. To reduce the bistatic RCS at both polarizations two MEFSS structures are arranged in aperiodic and periodic style. It is perceived that aperiodic NARR reduces the bistatic RCS more as compared to the periodic structure, while the monostatic RCSR level remains same for both configurations. For the validation both structures are fabricated and monostatic RCSR is presented experimentally. The simulated results are well matched with the corresponding measurments.

Liu et al. investigated a new method aimed at RCSR for both x and y polarizations of incident waves [65]. The goal is achieved with the help of PCM, which satisfies the principle of passive cancellation. A primary and proposed antennas are designed, simulated and finally fabricated to verify the reliability of the simulated structure. Primary antenna composed of conventional MPA while proposed antenna consists of MPA along with PCM. Simulated result of proposed antenna shows that 16 dB in-band and 14 dB out of band RCSR has been achieved, without affecting the radiation performance with compared to the primary antenna. Fabricated prototype is finally tested to verify the simulated results, which are well harmonized with each other.

Jha et al. proposed a new MM absorber to obtain the in-band RCSR of a planar patch antenna [66]. A hexagonal ring with six arms shaped MM is designed and simulated in such a way to operate in the C band. Firstly, the different parameters of MM structure have been optimized with the help of numerical simulator and finally the structure is fabricated and tested to verify the simulated results. Further, to reduce the in-band RCS MM absorber is loaded on a planar patch antenna. 99% absorption is achieved at 6.35 GHz in simulated results. Finally fabricated structure is tested and it shows that simulated results are in accordance with the measured results.

Wang et al. used microstrip resonators to obtain the in-band monostatic RCSR of a patch array antenna [67]. First author designed and simulated reference antenna which consist of patch array antenna, working at 4.5 GHz. Then author designed and simulated proposed antenna consiting of reference antenna and microstrip resonator, resonating at same frequency as reference antenna. Compared with reference antenna, the simulated results of proposed array antenna shows that the monostatic RCS for phi (ϕ) and theta (θ) polarized incident wave has been reduced at least by 10 dB. The proposed structure was fabricated and measurements were done.

EBG structure with RAM is used by the authors to reduce the backward RCS of asymmetric waveguide slot array antenna [68]. The proposed structure composed of mushroom-like EBG loaded with lumped resistance. First, author deigned and simulated basic antenna which is waveguide slot array antenna with 4×10 elements with full ground plane, to reduce the backward RCS. Then author replaced the ground plane of the array with EBG RAM. Because of this technique RCS gets reduced, while other radiation performance of the primary antenna is preserved. Measurment on fabricated structure exhibits well coincide with the simulated ones, which proves the reliability of the proposed structure.

Mushroom-like EBG structure is implemented to obtain the RCSR of patch array antenna [69]. The primary antenna is designed in this way, so that it can resonate at 5.0 GHz. The advanced antenna whose ground plane is replaced by mushroom-like EBG surface is also resonating at same frequency as primary antenna. The frequency band of the RCSR of the patch antenna array can be tuned by customising the parameters of the EBG. Finally, the structure is being fabricated and tested to validate the simulated results and it is concluded that the measured results are coincide well with simulated results.

Machado et al. investigated a novel technique to reduce out-of-band RCS of a dipole antenna [70]. The primary dipole antenna is designed and simulated, which resonates at 4.2 GHz. Further, thin copper layer at the back of dipole antenna is replaced by square shape FSS. With this technique out-band RCSR and improvement in gain is achieved. To validate the simulation, structure is fabricated and when simulated results are compared with experimental results, it is found that they are in good agreement with each other.

This Chapter gives insight into the MM inspired structures including MM inspired absorber and MM inspired antenna. Motivated by the above discussion, we design, analyze and fabricate the MM based absorber, MM smart absorber and MM inspired antenna to reduce RCS of the antenna.

CHAPTER 3

DEVELOPMENT OF NEW HYBRID METAMATERIAL BASED MICROWAVE ABSORBING STRUCTURE

In this chapter, two distinct MM-based absorbers are designed, simulated and measured in the range of 2 to 18 GHz. The first MMA is a hybrid structure that comprises of a cross-loaded split ring. The other proposed structure comprises eight sectors loaded circle inside the square. To evaluate the optimized values of the distinct dimensions the parametric studies have been performed on both the structures. Further, an effort has been made to determine the angular stability and polarization sensitivity of the proposed structures. The frequency-dependent EM properties of both structures are also demonstrated in this chapter. Further, the surface current, **E** field, and **H** field distributions are also represented. Finally, the proposed prototypes have been fabricated to evaluate the measured results. The free-space microwave measurement setup is used for the performance evaluation of the fabricated prototypes.

3.1 INTRODUCTION AND MOTIVATION

Microwave absorbers have been widely exploited by radio frequency (RF) & microwave scientists for distinct practical applications, like stealth & radomes, filters, electromagnetic interference (EMI) shields, cloaks, and lenses, etc. in the microwave, millimeter, and terahertz regimes [19], [71-73]. Various microwave absorbing materials and structures are available in the open literature, based on targeted operating frequency [74-75]. MM inspired microwave absorbers (MMAs) are one of the alternating solutions to reduce the thickness and weight of the structure. The concept of a perfect MMA has been first introduced by Landy et al. [76]. MMs are artificial or synthetic materials, engineered to achieve the customized EM properties, which are not found in nature [6] The condition of impedance matching can be obtained, by just manipulating the resonances of the equivalent material parameters, i.e., complex dielectric permittivity (ε_r) and complex magnetic permeability (μ_r) independently. Such a MM technology plays a significant role at higher frequencies as compared to the conventional materials. The development of MMA with wide bandwidth has been always one of the challenging aspects in front of the scientific community. Other important issues are related to the electrical thickness, polarization insensitivity, fabrication, and performance evaluation of such kinds of structures. Motivated by the above discussions, in this chapter two distinct MM-based absorbers are discussed in two sections. The first MMA is a hybrid structure that comprises of a cross-loaded split ring. In the first section FSS based broadband MMAs have been designed, optimized, fabricated, and measured in the range of 2 to 18 GHz. The main contribution of the hybrid FSS based EM structures is the broad absorption bandwidth with a smaller thickness. The other proposed structure is designed, simulated, and discussed in another part of this chapter. The proposed structure comprises eight sectors loaded circle inside the square. This proposed structure shows multiband absorption and polarization-insensitive behaviour in the range of 2 to 18 GHz.

3.2 DESIGN OF HYBRID METAMATERIAL ABSORBER

The unit cell geometry of the proposed MMA comprises a periodic FSS layer stacked with a dielectric substrate backed by a ground plane. The standard FR4 material has been selected as a dielectric substrate (relative permittivity, ε_r=4.3, and dielectric loss tangent, tan δ= 0.025) with a substrate layer thickness of 2.0 mm. The metallic layer and ground plane are made of copper (conductivity, σ = 5.8 × 107 S/m) with a layer thickness of 0.035 mm. Initially, a basic unit cell of a SRR is designed and simulated as shown in figure 3.1, whereas figure 3.2 illustrates the unit cell of a cross without SRR. Finally, the unit cell of the metamaterial absorbing structure (MAS) is shown in figure 3.3 which is a hybrid structure, comprised of a cross-loaded split ring. Here, the metallic FSS layer (made of copper) is represented by a yellow color, and the rest of the portion illustrates the dielectric substrate.

Table 3.1. Dimension of variables used in cross-loaded split ring MM.

Variable	Dimension (mm)	Variable	Dimension (mm)
P	8.0	L1	1.7
S	0.25	L2	1.5
W	0.9	W1	1.6
G	0.8	W2	1.6
R	3.14	-	-

These structures have been designed using CST Microwave Studio. The Floquet port has been employed to excite incident wave propagating in the z-direction, using the periodic boundary conditions along the x and y directions. The optimized value of the cross-loaded split ring MM followed by a critical parametric analysis is shown in table 3.1.

3.2.1 SIMULATED RESULTS AND NUMERICAL ANALYSIS

Figure 3.4 illustrates the simulated RC-frequency graph of the split ring, cross, and cross-loaded split ring FSS based absorbers in the range of 2 to 18 GHz. It is noticed that the absorption bandwidth corresponding to -10 dB RC for split ring FSS is 3.7 GHz (8.5 to 9.8 GHz and 11.4 to 13.8 GHz). A split ring FSS with a radius of 3.14 mm and two split ends contributes to three RC peaks of -20.7 dB, -15.5 dB, and -27.5 dB, at 8.8 GHz, 9.3 GHz, and 12.7 GHz, respectively, whereas alone cross exhibits no RC characteristics property below -10 dB. A remarkable enhancement is observed in -10 dB absorption bandwidth with the application of hybrid FSS geometry, i.e., cross-loaded split ring FSS as shown in Figure 3.4. The results show the RC is less than -10 dB from 8.5 to 16 GHz for the hybrid structure, which covers 7.5 GHz bandwidth. The peak RC values of the hybrid geometry are -20.2 dB, -17.5 dB, -29.0 dB, and -21.0 dB at 8.9, 9.3, 12.2, and 15.5 GHz, respectively. The cross-loaded split ring hybrid geometry has been chosen for further studies, due to its exceptional microwave absorbing performance as compared to the individual split ring, cross, and Jerusalem cross-loaded split ring FSS geometries.

It is well known that microwave absorption characteristics are strongly influenced by the substrate thickness [3]. Therefore, an effort has been made to study the effect of substrate layer thickness over RC characteristics of the hybrid structure. The corresponding results with varied substrate layer thickness are presented in Figure 3.5 (a). The substrate thickness has been varied from 1.4 to 2.4 mm while keeping the other parameters (i.e., FSS dimensions, etc.) constant. The degree of resonance matching is greatly affected by the corresponding variation in the substrate thickness. A similar effect has been observed by Fan et al. [77]. As the substrate thickness increases, more attenuation of the wave takes place. At 1.4, 1.6, and 1.8 mm substrate thickness the overall bandwidth is reduced, at higher frequency bandwidth is less than -10 dB is observed but at the lower frequency, it shows more than -10dB response. Similarly, at 2.2 and 2.4 mm thickness of the substrate, it shows less overall bandwidth as compared to the optimal substrate layer. At 2.2 and 2.4 mm substrate thickness the bandwidth is reduced, because of the higher frequency side, it exhibits more than -10 dB response.

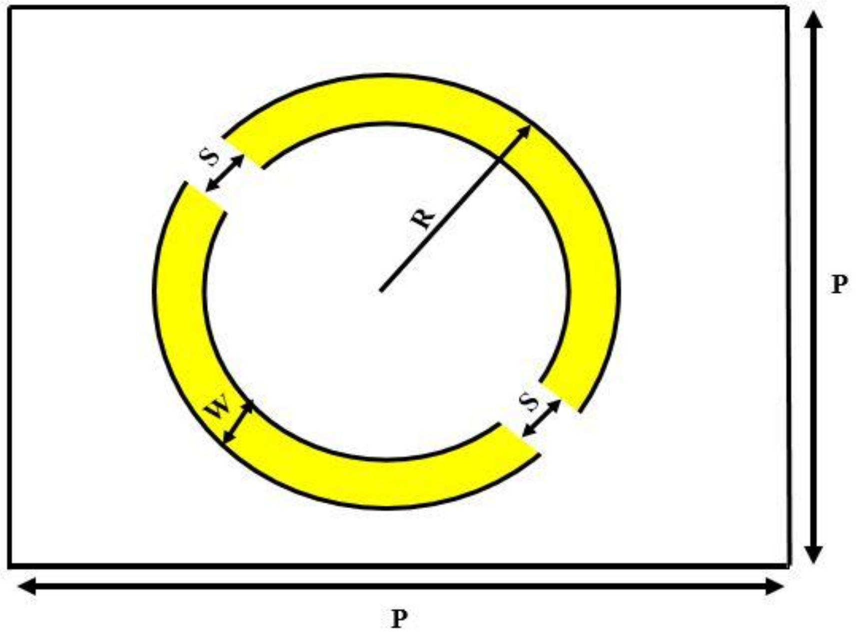

Figure 3.1. Front view of the Split ring resonator.

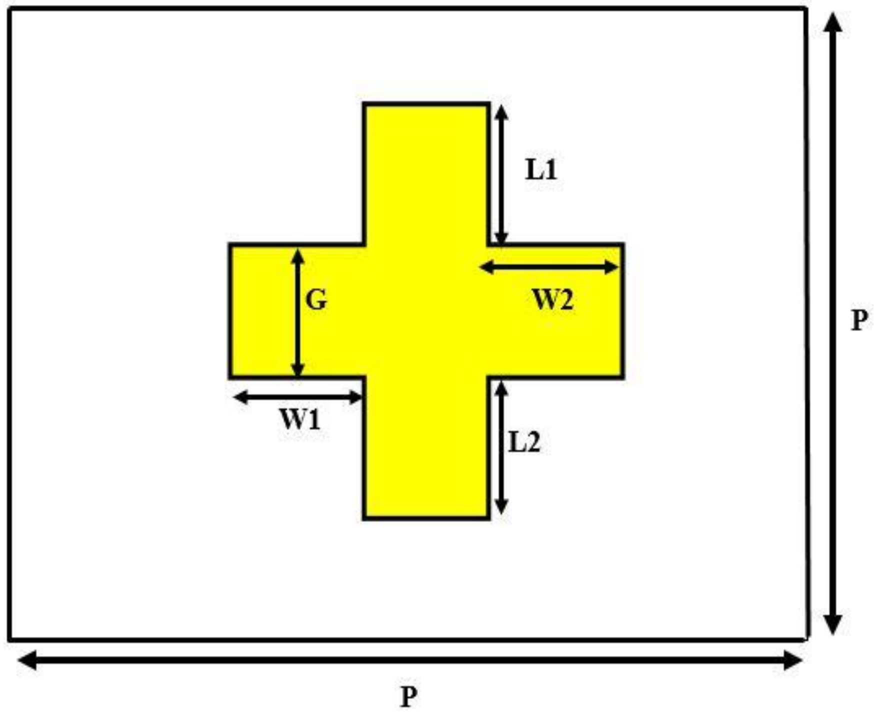

Figure 3.2. Front view of the cross shape structure.

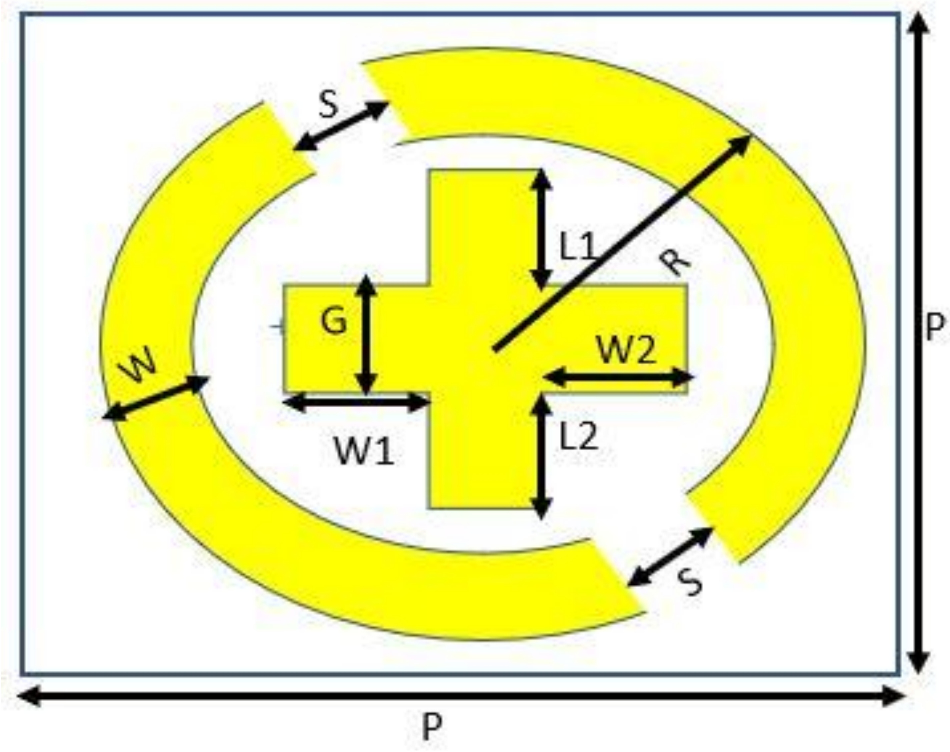

Figure 3.3. Front view of the proposed cross-loaded split ring MAS unit cell.

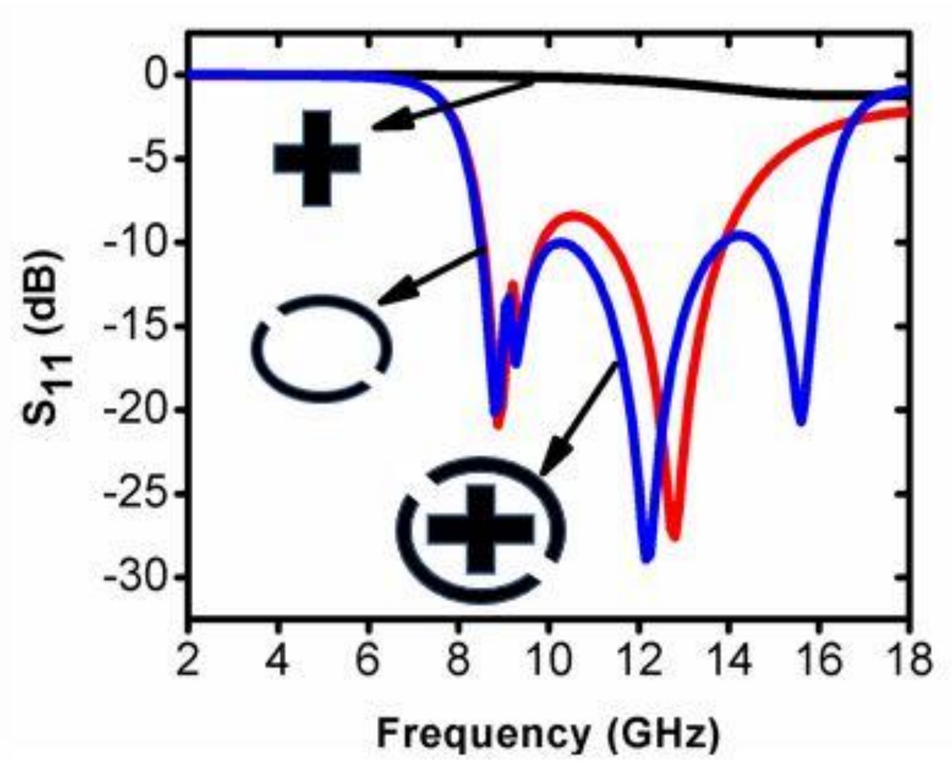

Figure 3.4. Frequency dependent RC characteristics of the split ring, cross, and cross-loaded split ring MMA.

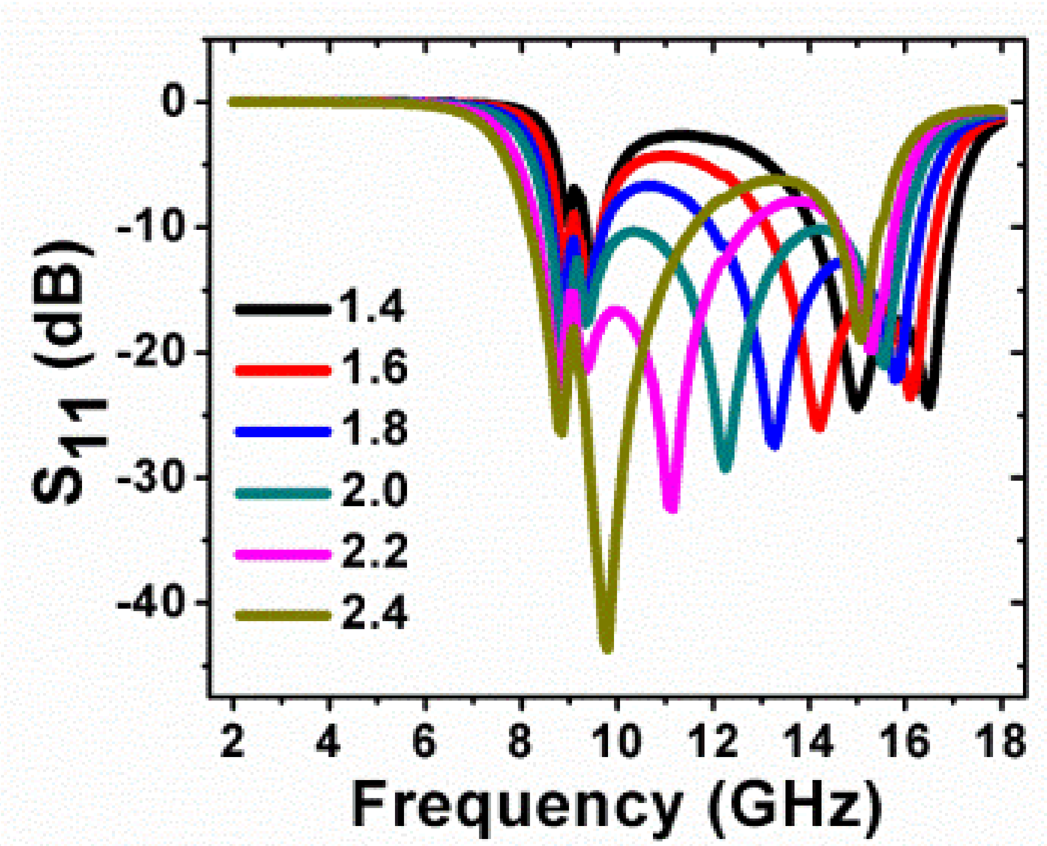

S11 (dB)
0
-10
-20
-30
-40
1.4
1.6
1.8
2.0
2.2
2.4
2
4
6
8
10
12
14
16
18
Frequency (GHz)

(a)

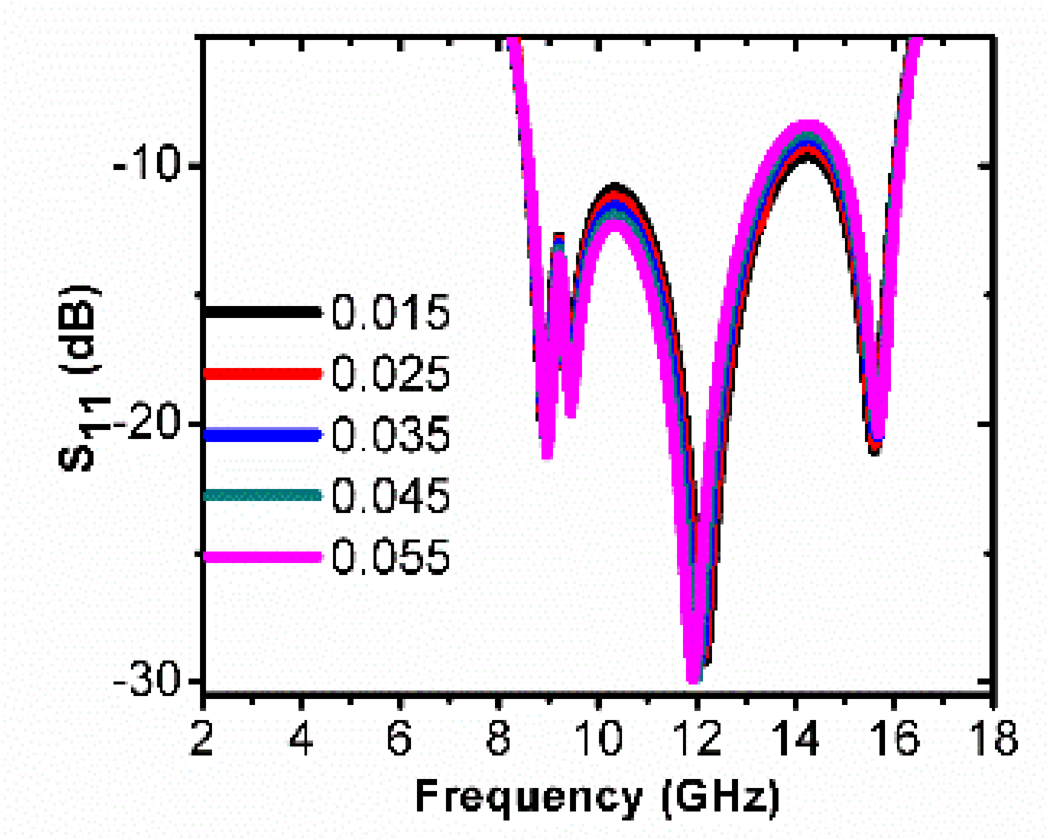

S11 (dB)
-10
-20
-30
0.015
0.025
0.035
0.045
0.055
2
4
6
8
10
12
14
16
18
Frequency (GHz)

(b)

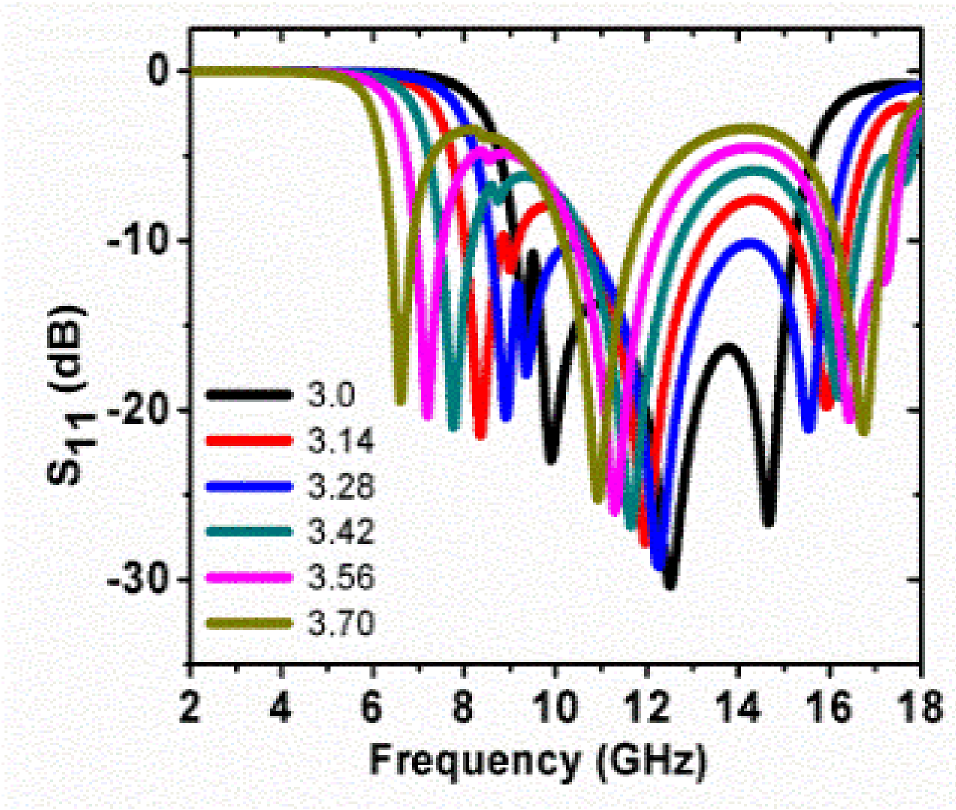

(c)

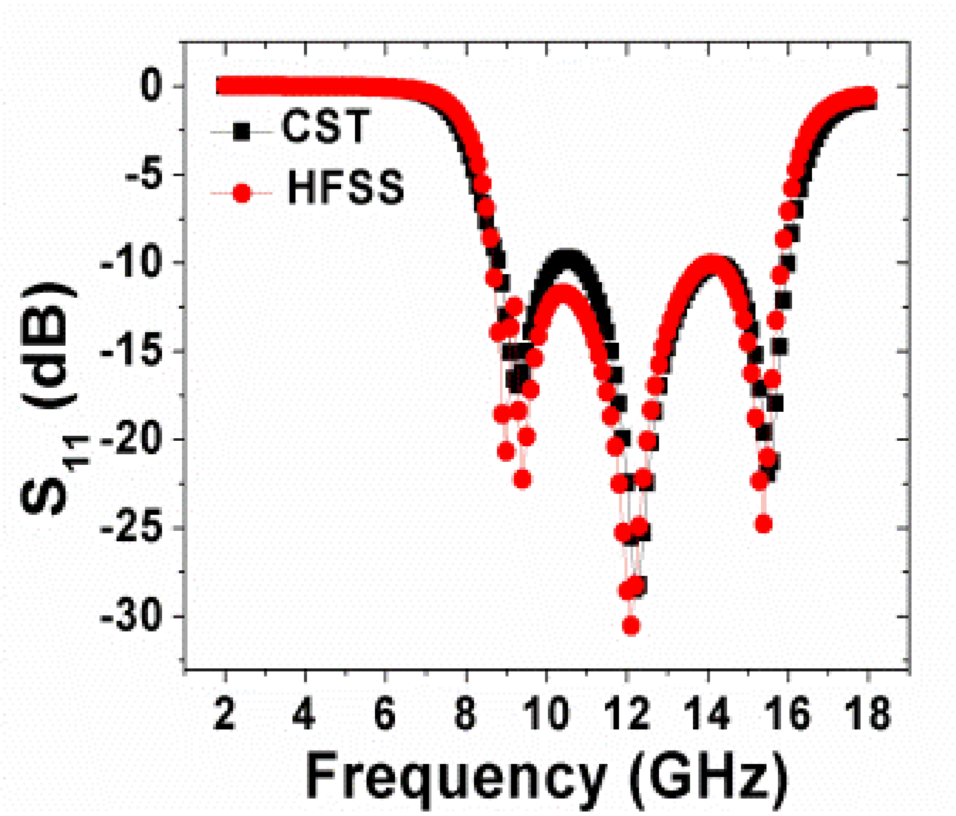

(d)

Figure 3.5. Effect of design variables (a), (b), (c) ring radius, and (d) comparison of CST and HFSS data.

At higher frequency, more than -10 dB response of RC is observed at 3.0 and 3.28 mm radius, therefore the overall bandwidth is reduced. The better microwave absorption properties in terms of wide absorption bandwidth of 7.5 GHz and minimum RC of -29.0 dB are noticed with an optimal value of r2, i.e., 3.14 mm, as clear from Figure 3.5 (c). Above 3.28 mm value of radius (3.42, 3.56, and 3.70 mm), the better higher frequency RC characteristics are obtained, but almost from 12 GHz to 16 GHz RC characteristics are shifted more than -10 dB. The results obtained from CST have been validated using HFSS, before the actual fabrication of the absorber. A perfect match among both HFSS and CST data is observed, as clear from Fig. 3.5 (d). The optimal structure is found to possess a maximum absorption of -29.0 dB at 12.2 GHz. The structure is studied under distinct polarization angles in the range of 0^o to 30^o at the normal incidence to examine its polarization sensitivity. Figure 3.6 (a) shows that absorption decreases gradually with a corresponding increase in the polarization angle, which may be due to the non-symmetrical geometry of the structure.

The significant microwave absorption properties have been obtained for the substrate thickness of 2.0 mm. Therefore, 2.0 mm is considered as an optimal substrate layer thickness of the proposed absorber. To further investigate the effect of FSS thickness over RC characteristics, conducting geometry thickness has been varied from 0.015 mm to 0.055 mm for an optimal substrate layer thickness, i.e., 2.0 mm. Figure 3.5 (b) shows the FSS thickness-dependent RC characteristics of MMA structure in the range of 2 to 18 GHz. The simulation results reveal the FSS thickness independent RC characteristics of proposed MMA. Similarly, the outer radius (r2) of the circle is varied from 3.0 to 3.7 mm, while making the other parameters constant. When r2 increases, the gap between the outer circle and inner geometry, i.e., cross sign increases, which affects the mutual coupling [78]. Further, an effort has been made to determine the angular stability of the proposed structure. Figures 3.6 (b), 3.6 (c) present the simulated RC graph of the proposed absorber with different angles of incidence under TE and TM polarization respectively. It is observed in figure 3.6 (b) that with an increase of incident angle, the higher resonance frequency shifts up under TE polarization, while lower resonance frequency shifts down as the incident angle increases. Whereas under TM polarization, no such major changes are observed in the range of 0^o to 30^o. The return loss level is improving with the increase in the value of angle as illustrated in figure 3.6 (c).

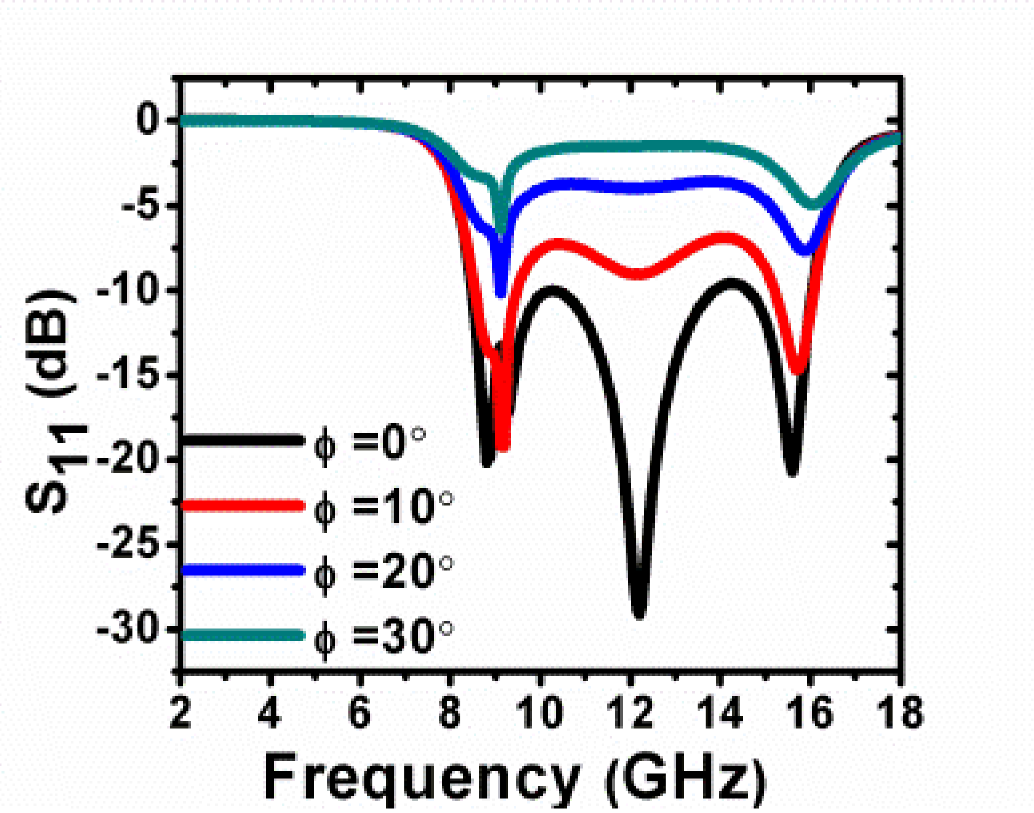
0
-5
-10
-15
-20
-25
-30
S11 (dB)
φ =0°
φ =10°
φ =20°
φ =30°
2
4
6
8
10
12
14
16
18
Frequency (GHz)

(a)

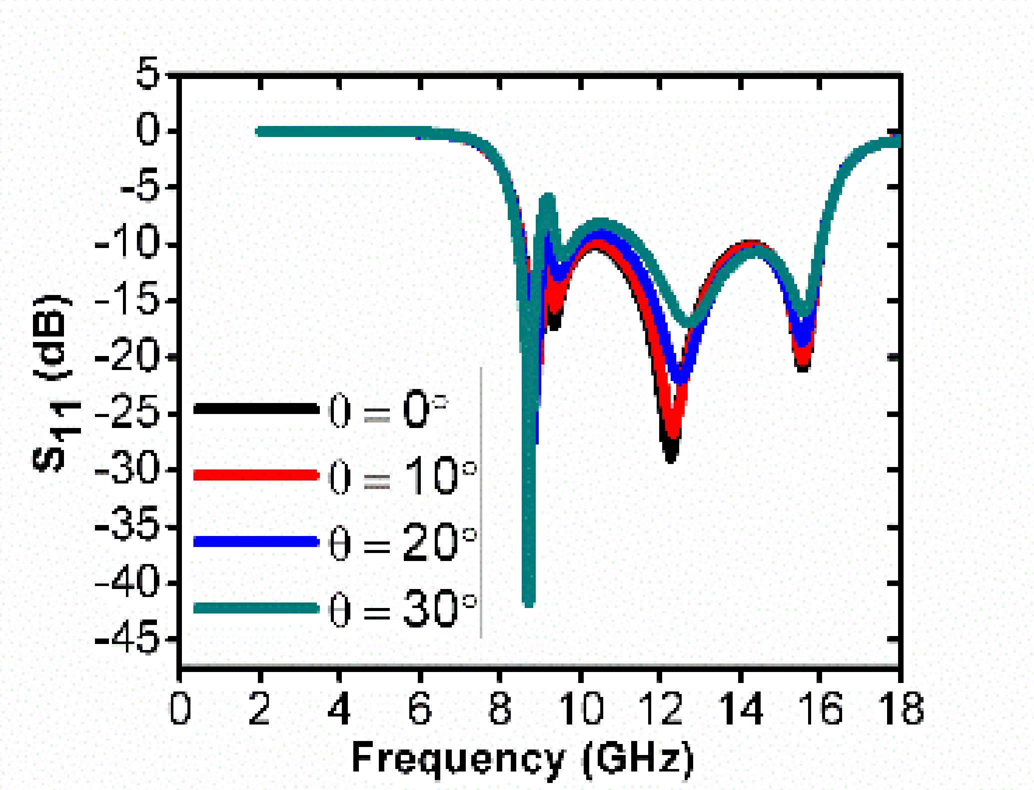
5
0
-5
-10
-15
-20
-25
-30
-35
-40
-45
S11 (dB)
θ = 0°
θ = 10°
θ = 20°
θ = 30°
0
2
4
6
8
10
12
14
16
18
Frequency (GHz)

(b)

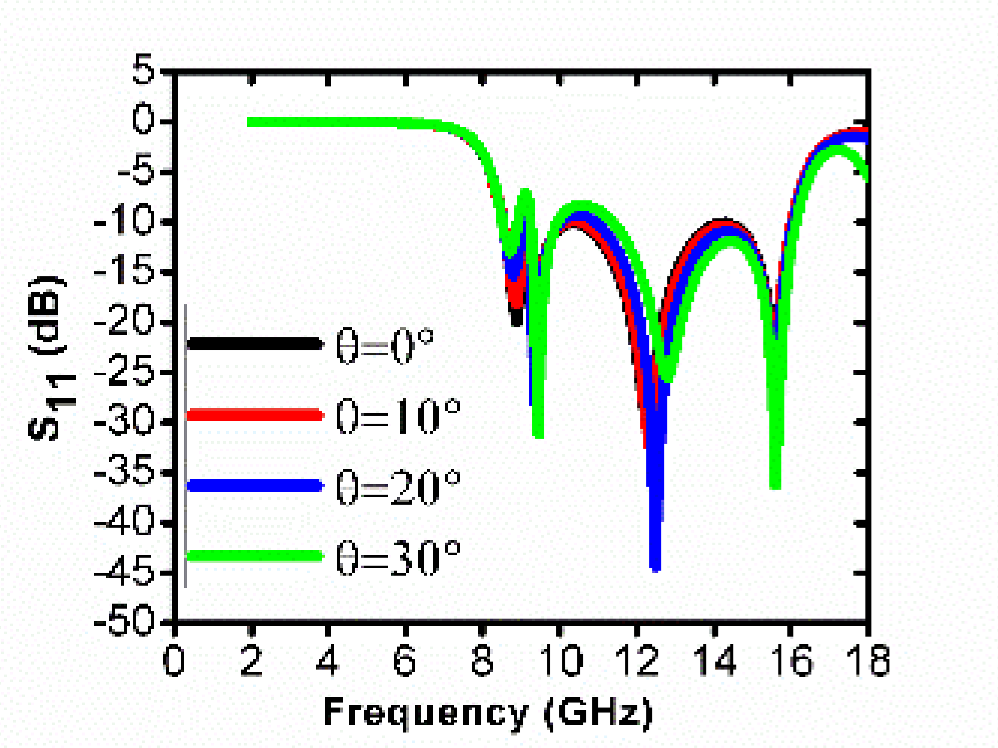

(c)

Figure 3.6. Simulated RC of proposed absorber with (a) different polarization angles under normal incidence,

(b) different angle of incidence under TE polarization. (c) different angle of incidence under TM polarization.

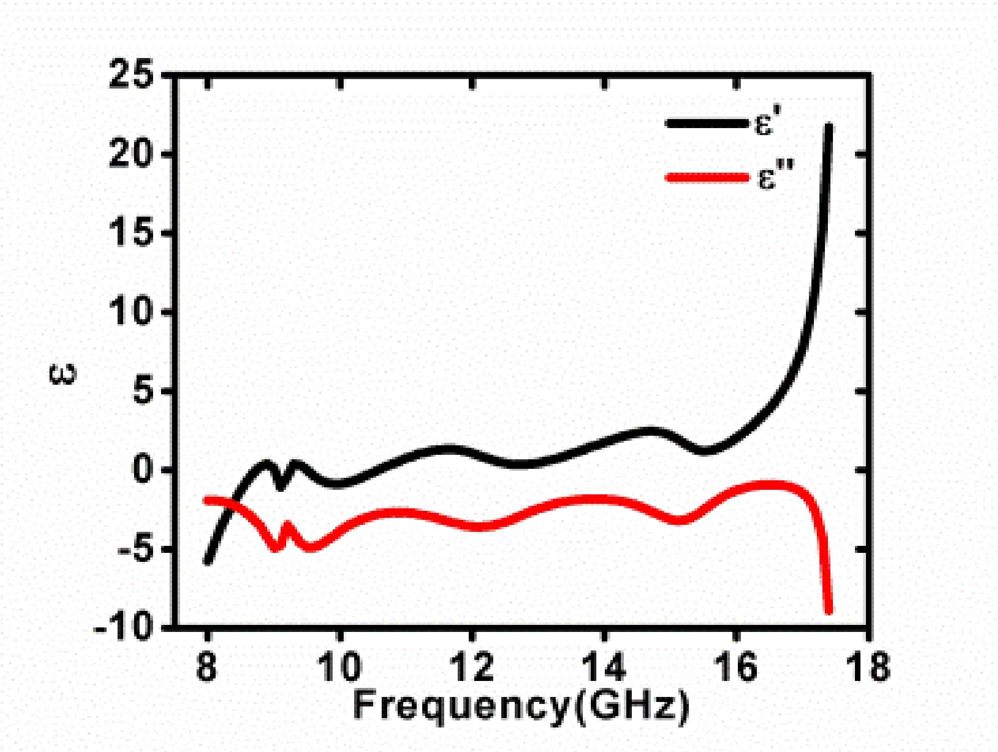

(a)

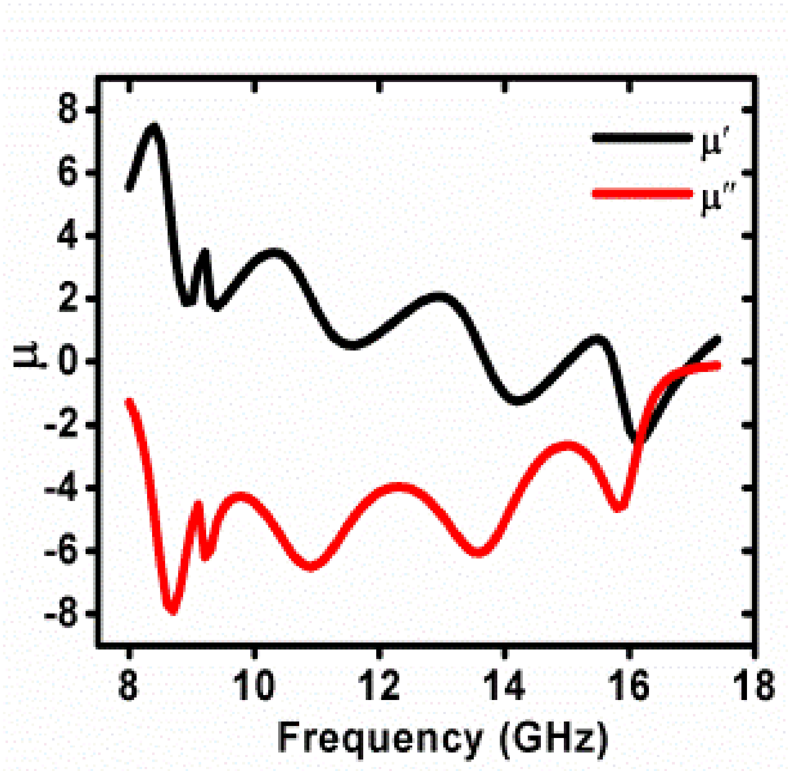

(b)

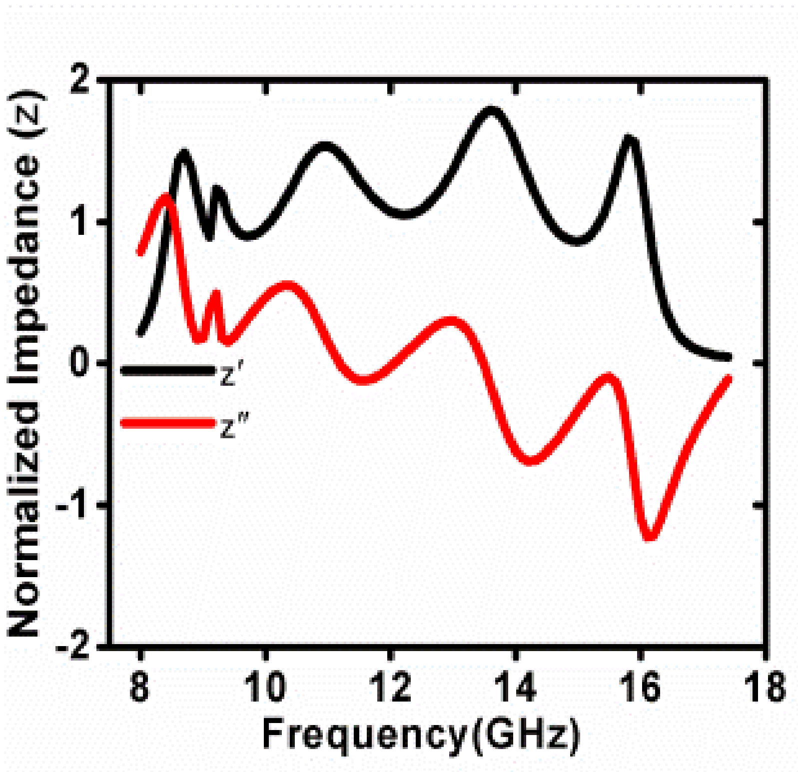

(c)

Figure 3.7. Frequency dependent EM properties (a) complex dielectric permittivity, (b) complex magnetic permeability, and (c) normalized impedance for an optimal sample.

Overall, the simulation results indicate that for any chosen dielectric material and FSS, there is always an optimal substrate thickness, and optimal FSS design variables, where the reflection becomes zero, i.e., maximum absorption. The negative values are clearly depicting the metamaterial nature of the proposed structure which are responsible for maximum absorption of the wave. The normalized impedance value of the proposed structure is almost equal to 1 in the range of 8 to 18 GHz, which justified the condition of an absorber. Figures 3.8 (a)-(f) illustrate the electric and magnetic field distributions at three resonant peaks (viz. 8.9 GHz, 12.2 GHz, and 15.5 GHz) to understand the absorption mechanism. After analyzing the result, it is noticed that hybrid geometry is the primary contributor to the more localized field. The contribution of the split ring is more at a lower frequency, on the other hand, at a higher frequency, fields are more influenced by the cross geometry. The top surface current distributions of the proposed structure at the resonant frequencies, i.e., 8.9 GHz, 12.2 GHz, and 15.5 GHz is illustrated in Figure 3.9. It is shown that at the lower resonant frequency, i.e., 8.9 GHz, the surface current distribution is more in the outer ring, whereas a small amount of current flows in the cross. Quite good matching of surface current is noticed for both the split ring as well as cross at 12.2 GHz. The major contribution of the surface current at 15.5 GHz is due to the cross, however, the outer ring is also found to be contributing to the same. At the resonant frequencies, high absorption has been observed, because with the top metallic patch the electrical resonance is coupled and the surface current makes the circulating loops around the incident magnetic field, therefore creating strong magnetic resonance. The absorption mechanism in MMAs can also be explained based on interference theory [79].

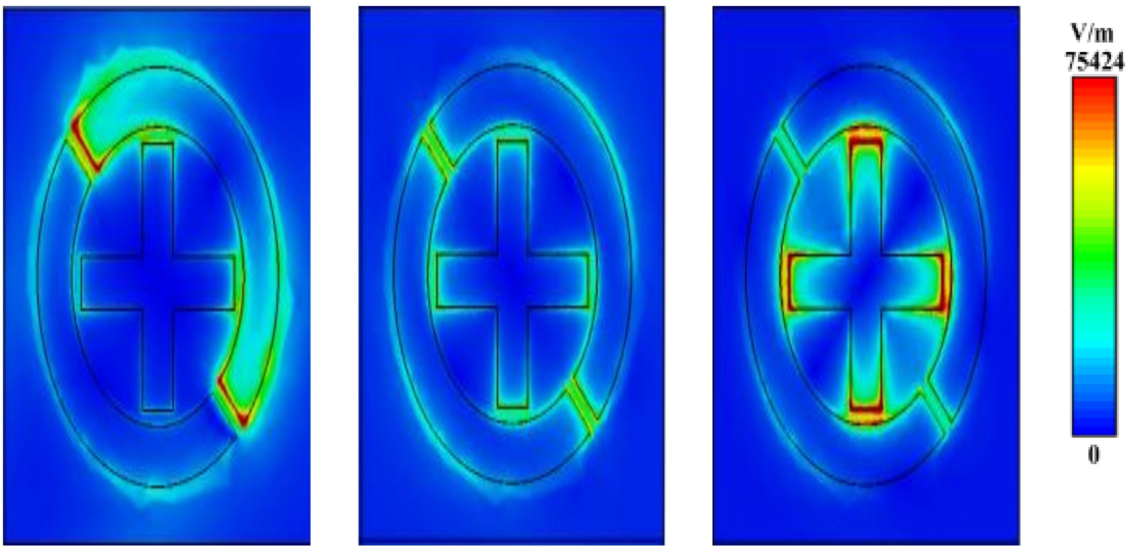

(a) **(b)** **(c)**

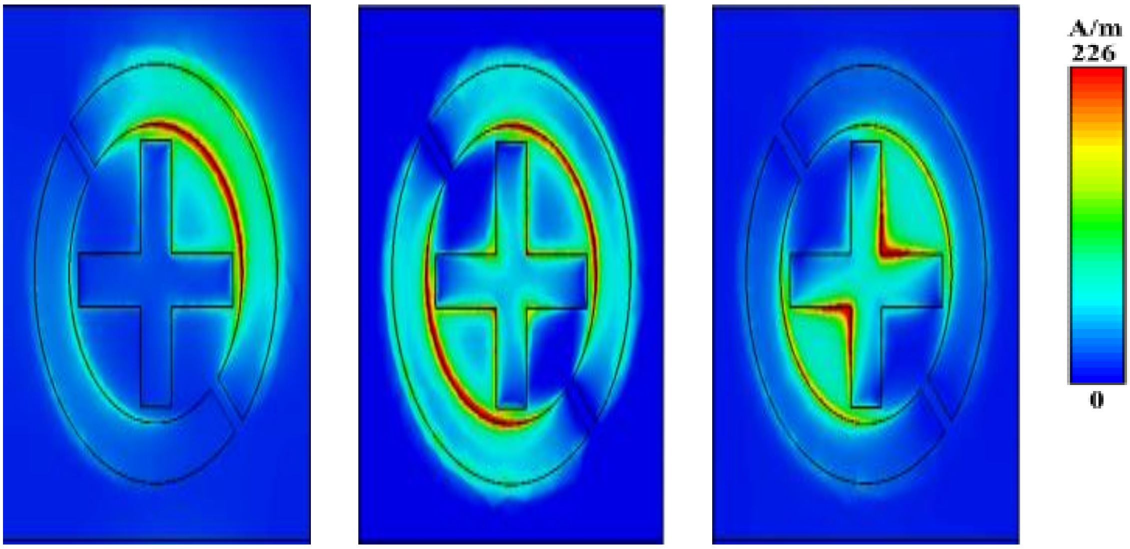

(d) (e) (f)

Figure 3.8. Electric field distributions at (a) 8.9 GHz, (b) 12.2 GHz, and (c) 15.5 GHz, magnetic field distributions at (d) 8.9 GHz, (e) 12.2 GHz, and (f) 15.5 GHz.

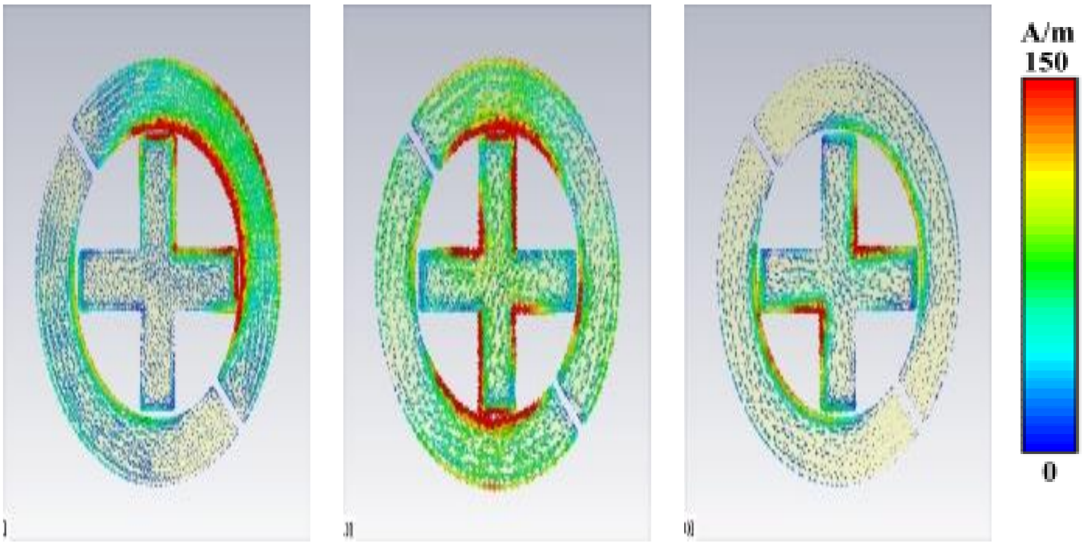

(a) (b) (c)

Figure 3.9. Surface current distribution of the proposed structure at (a) 8.9 GHz, (b) 12.2 GHz, and (c) 15.5 GHz.

3.2.2 FABRICATION AND EXPERIMENTAL VERIFICATION

An optimal sample of the cross-loaded split ring with an overall size of 200 × 200 mm^2 has been fabricated using standard printed circuit board (PCB) technology, to verify the simulated results. The performance evaluation of the fabricated structure has been carried out in an anechoic chamber using a single port free space, microwave measurement setup, comprising of a vector network analyzer (Keysight E5063A) and a broadband horn antenna as depicted in Figure 3.10 (a). The more details of single port free space measurement setup are provided in [4]. Figure 3.10 (b) presents the fabricated prototype of a cross-loaded split ring and a corresponding enlarged view of the unit cell is depicted in the inset. There are 25 unit cells in each row. The results obtained from CST are validated using both HFSS and experimental measurements.

(a)

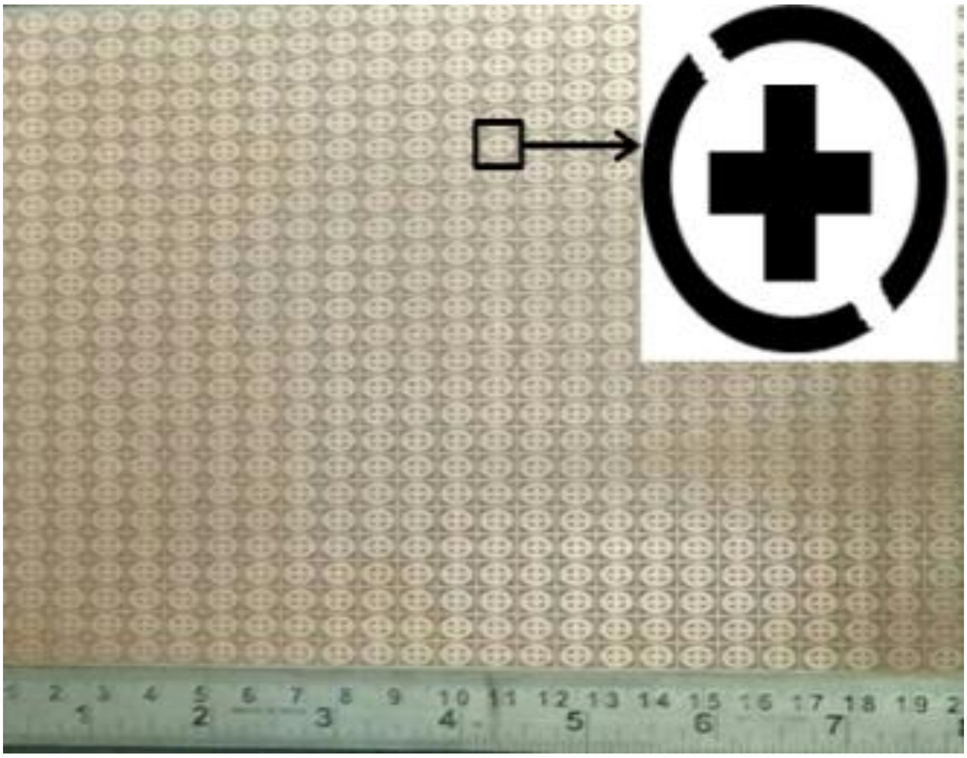

(b)

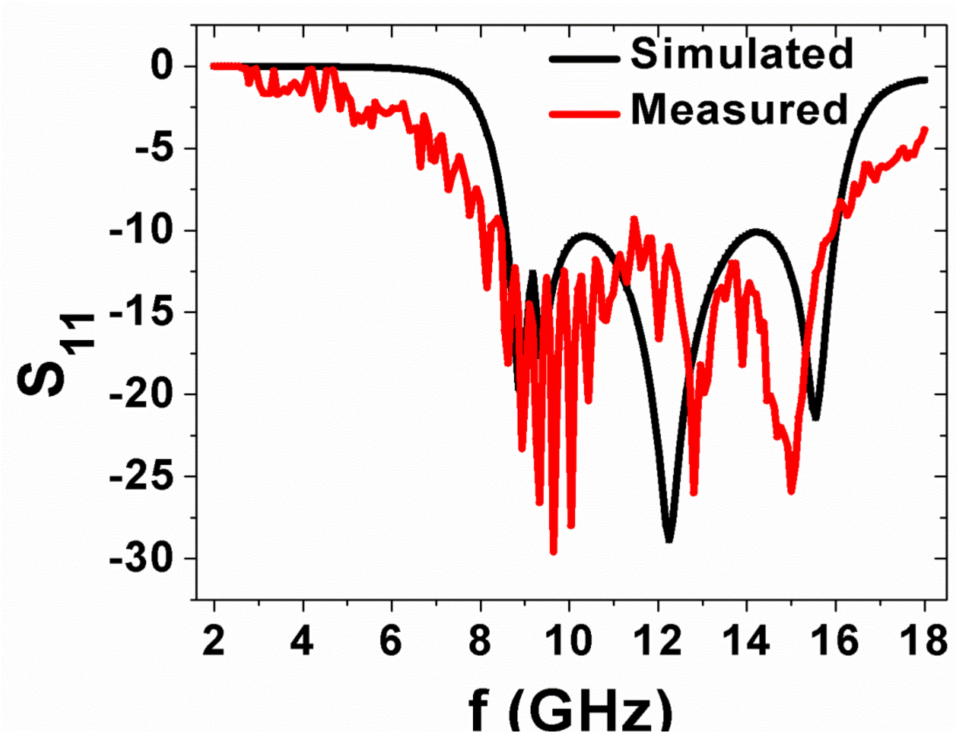

(c)

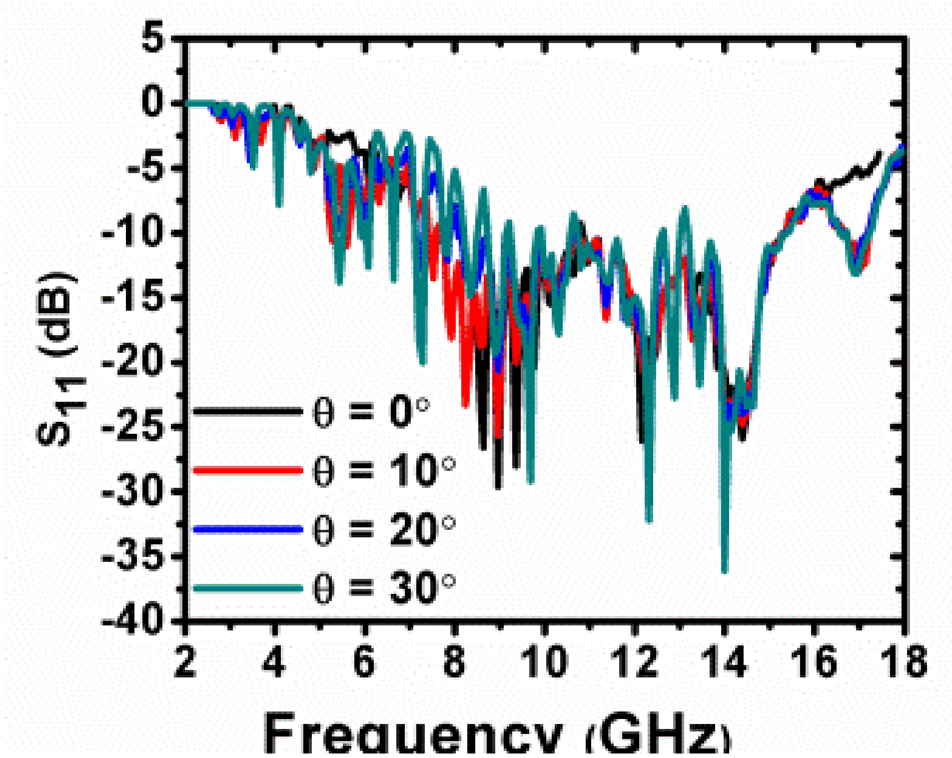

(d)

Figure 3.10. Performance evaluation based on experimental validation and verification (a). Free space, microwave measurement setup, (b) Fabricated prototype of cross-loaded split ring MMA and (c) measured and simulated graph (d) measured graph at distinct incidence angles.

Figure 3.10 (c) shows both the simulated and measured RC-frequency graph of the proposed structure under normal incidence in the range of 2 to 18 GHz. Figure 3.10

(d) presents the measured RC-frequency graph of the proposed absorber with different incidence angles. A close agreement has been observed among simulated and measured data. It has been noticed that the proposed absorber shows minimum RC from 8 to 16 GHz both in simulated and measured plots. Moreover, the -10 dB absorption bandwidth is 7GHz in the range of 8.5 GHz to 16 GHz. There is a slight difference in simulated and measured results, which might be due to finite prototype dimensions, and fabrication tolerances.

3.3 DESIGN OF MULTI BAND AND POLARIZATION INSENSITIVE ABSORBER

3.3.1 DESIGN OF UNIT CELL

A multiband and polarization-insensitive MM microwave absorber is presented in this part. The proposed structure consists of FSS layer stacked with a dielectric substrate backed by a ground plane. The standard FR4 material has been selected as a dielectric substrate (relative permittivity, εr=4.3, and dielectric loss tangent, tan δ= 0.025) with a substrate layer thickness of 1.6 mm.

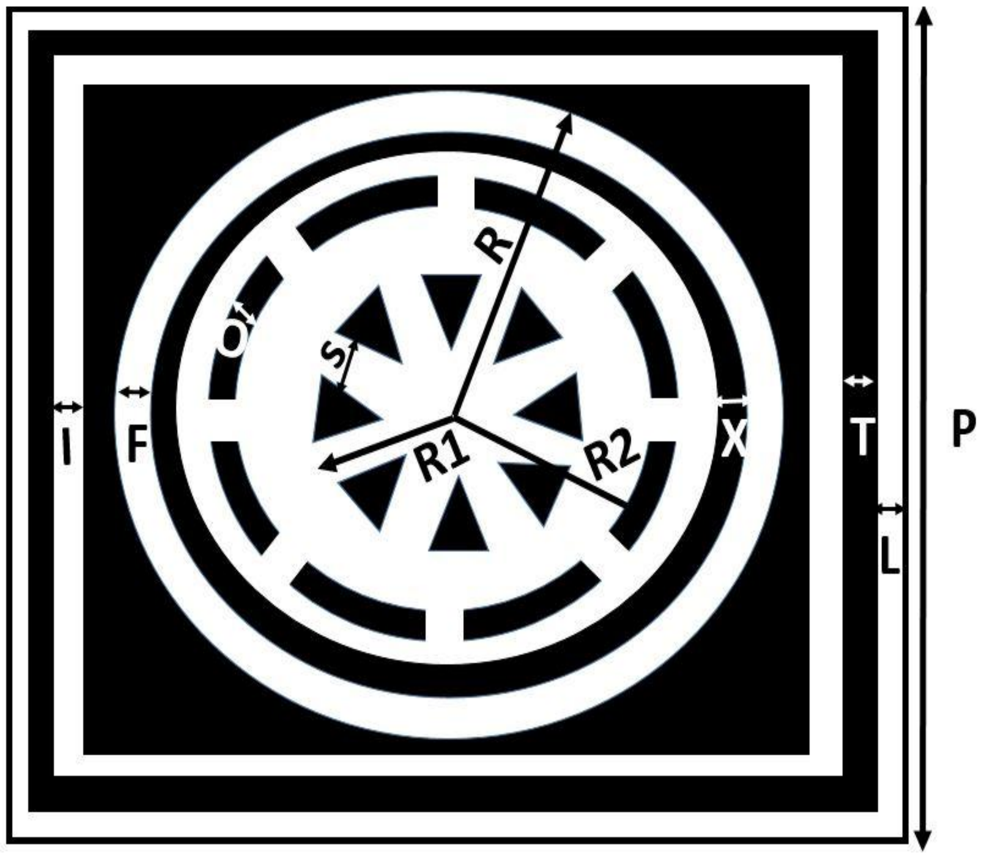

Figure 3.11. Front view of the proposed unit cell.

The proposed unit cell comprises eight sectors loaded circle inside the square as shown in Figure 3.11. The optimized value of the cross-loaded split ring is illustrated in Table 3.2. The structure has been designed and simulated using the CST software in frequency domain solver.

Table 3.2. Dimension of variables used in the proposed structure.

Parameter	Dimension (mm)	Parameter	Dimension (mm)
P	10	I	0.3
L	0.15	R	4.3
T	0.3	R1	2.4
O	0.3	R2	3.2
S	0.9	F	0.3
X	0.3	-	-

3.3.2 SIMULATED RESULTS AND NUMERICAL ANALYSIS

The simulated RC frequency graph of the proposed structure are investigated and demonstrated in Figure 3.12. The four resonant peaks of -25.9 dB, -18.9 dB, -16.1 dB, and -21.3 dB are noticed at 4.4 GHz, 6.0 GHz, 14.1 GHz, and 16.0 GHz, respectively. The significant result acquired from the RC graph is absorption characteristics, which are illustrated in Figure 3.13. It has been observed that at resonant frequencies the maximum absorption has been achieved in the range of 2 to 18 GHz. As the bottom surface of the structure is perfectly metal laminated, resultant in no transmission. It can be concluded from Figure 3.13, that at the resonance the maximum absorption has been achieved. The maximum absorption is observed of 94% and 92% at 4.4 GHz and 16.0 GHz, respectively. The absorption frequencies depend upon the geometric parameters of the absorber, as the change in dimensions leads to a corresponding change in the absorption response. The parametric studies are performed to discover the influence of the distinct geometrical design variables on the absorption. The first study is performed on the gap between the sectors which is denoted by ‘S’. With the decrease in the gap between the sectors, the value of capacitance also decreases, hence the higher resonating frequency-shifted towards left. It has been observed in Figure 3.14 (a) that the optimal value of ‘S’ is 0.9 mm. There is no difference is observed in lower frequency with change in ‘S’ parameter because it is majorly due to the excitation of the outer square and outer circle. With the further increase in the value of

‘S’, the four resonating peaks are observed with upwards shifting in the graph. The next study is performed on substrate thickness ‘h’ and illustrated in Figure 3.14 (b). It has been perceived that as the thickness of the substrate increases, the resonating frequency-shifted towards the left. The optimal value of the ‘h’ is 1.6mm. As the value of thickness approaches 2.0 mm, the higher absorption frequency diminished.

Further, the study is performed on the substrate permittivity as illustrated in Figure 3.14 (c). The proposed absorber is realized using an FR4 substrate with relative permittivity ‘εr’ of 4.2. Foremost, simulated RC graph of the proposed absorber with different angles of incidence under TE and TM polarization are studied and illuminated in Figures 3.15 (a) and 3.15 (b), respectively. For TE polarization a slight variation is observed in lower frequency with an increase of incident angle as portrayed in Figure 3.15 (a). In a higher frequency band, the structure shows different behavior for a distinct angle of incidence. A similar effect is observed for TM polarization as shown in Figure 3.15(b).

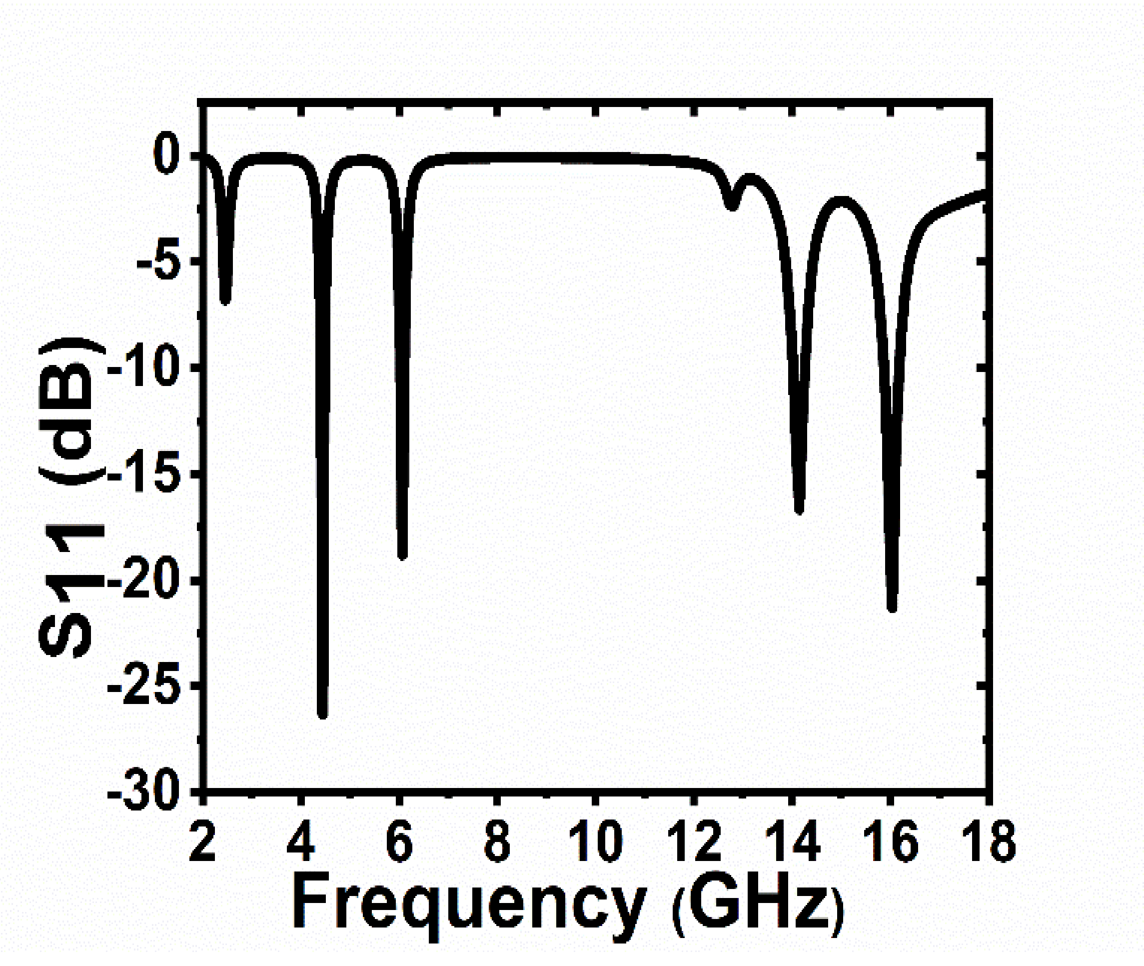

Figure 3.12. Simulated RC graph of proposed absorber

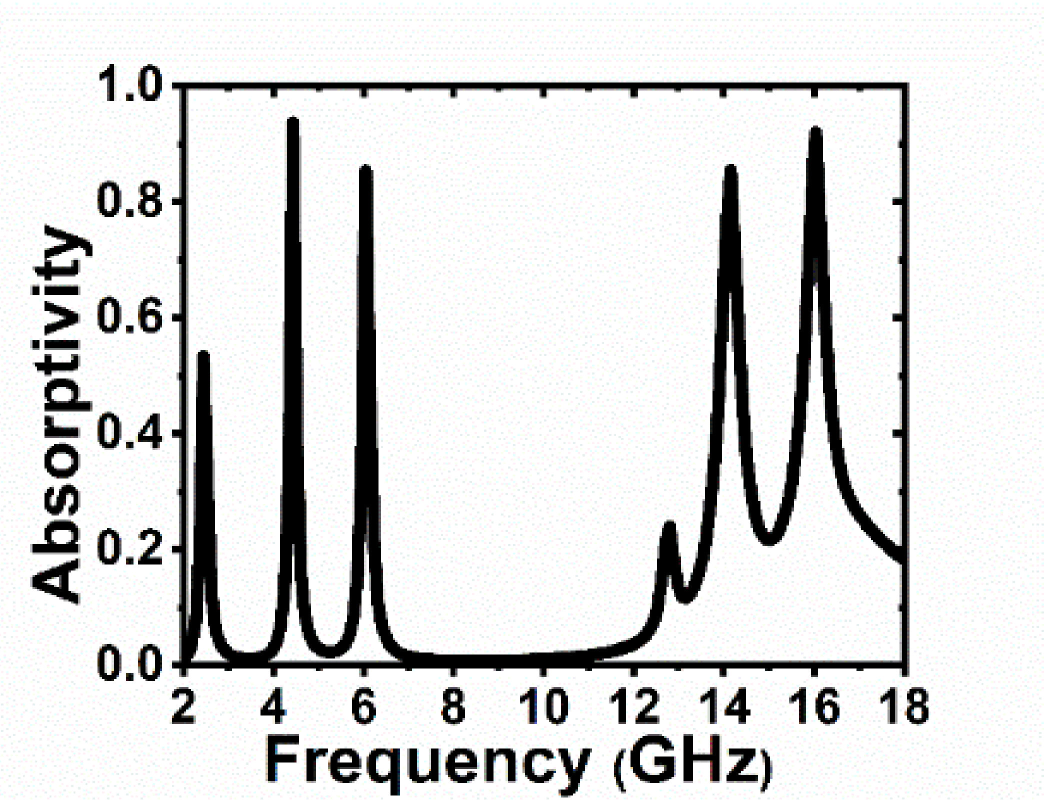

Figure 3.13 Simulated absorption characteristics of the proposed absorber in the range of 2 to 18 GHz.

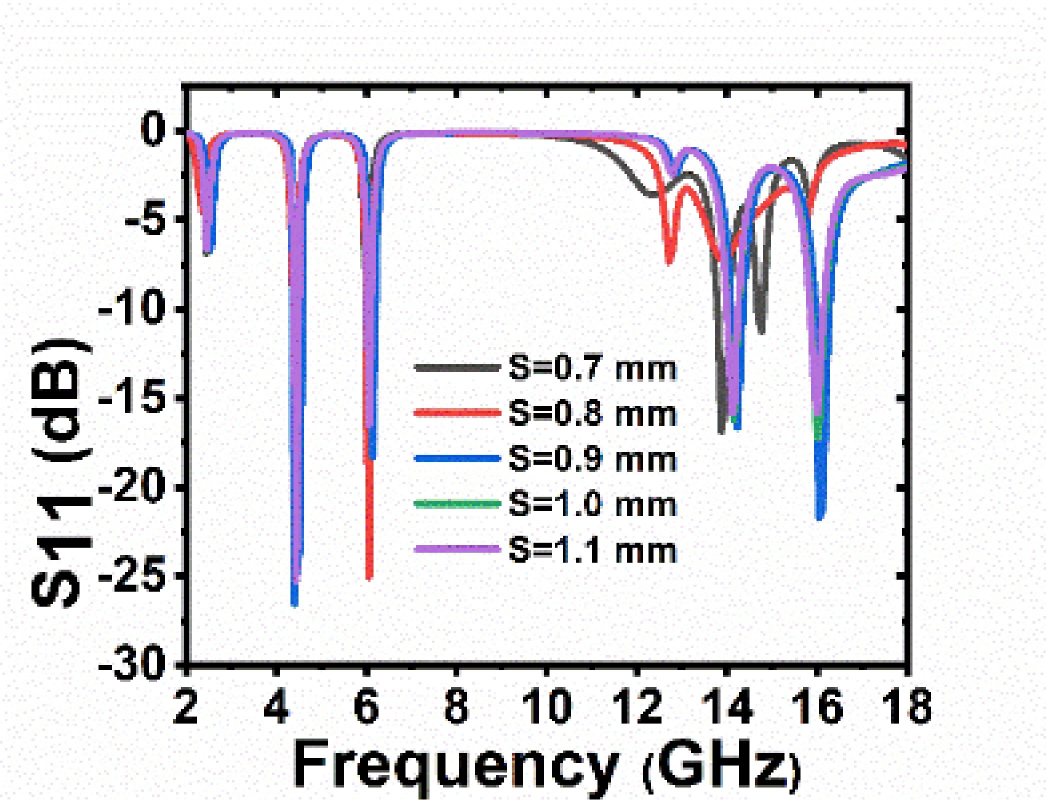

(a)

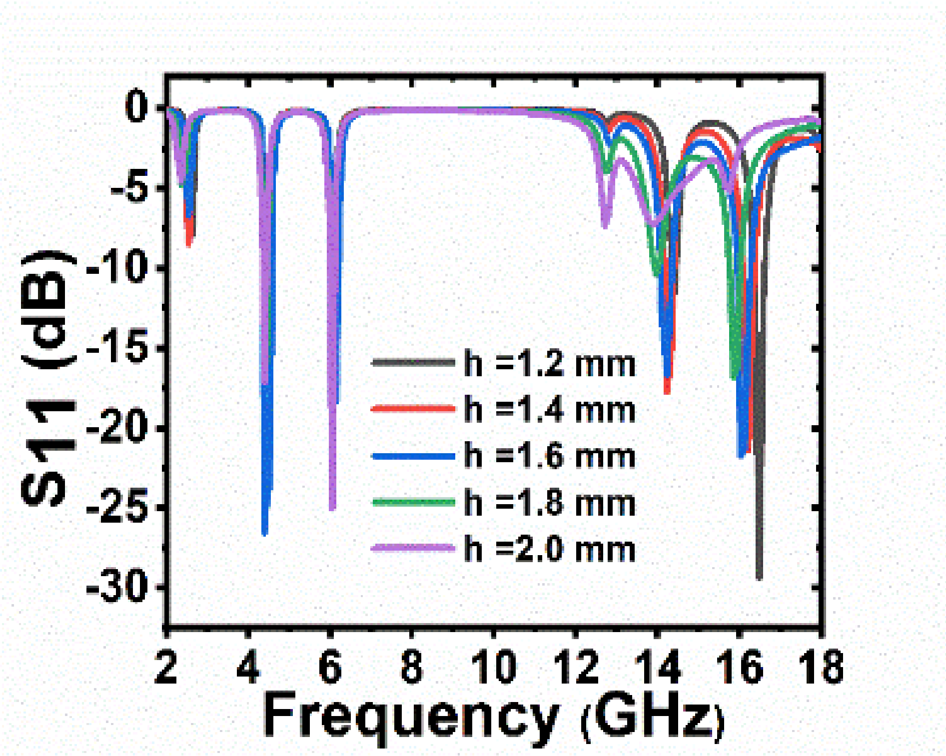

(b)

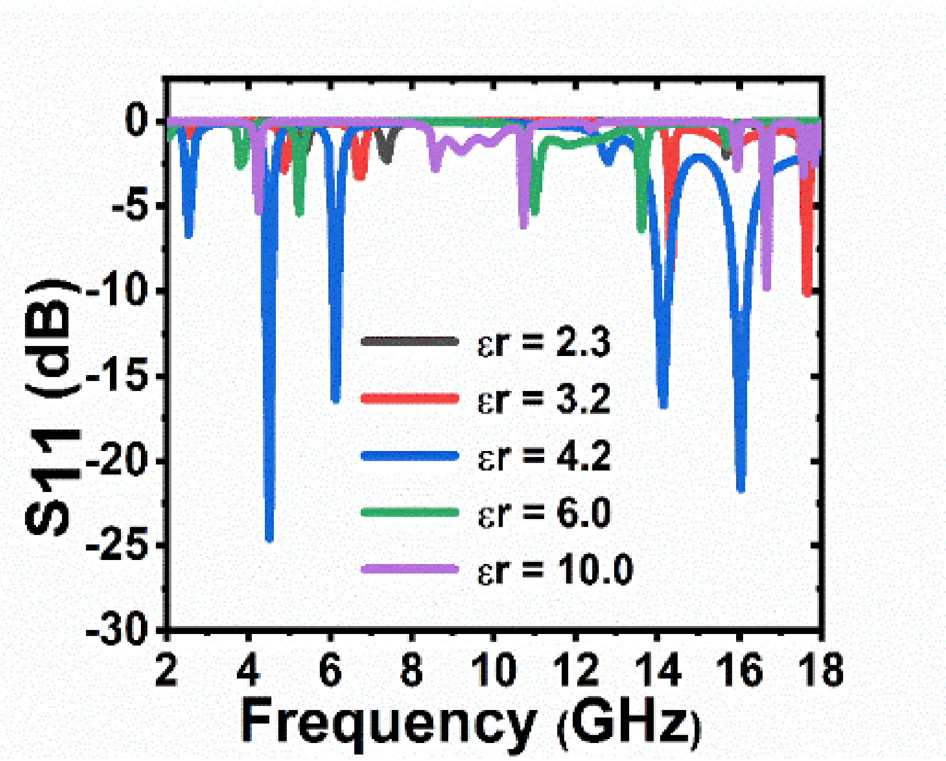

(c)

Figure 3.14. Effect of variation of geometrical design variables (a) ‘S’, (b) ‘h’, and (c) ‘εr’ on the RC.

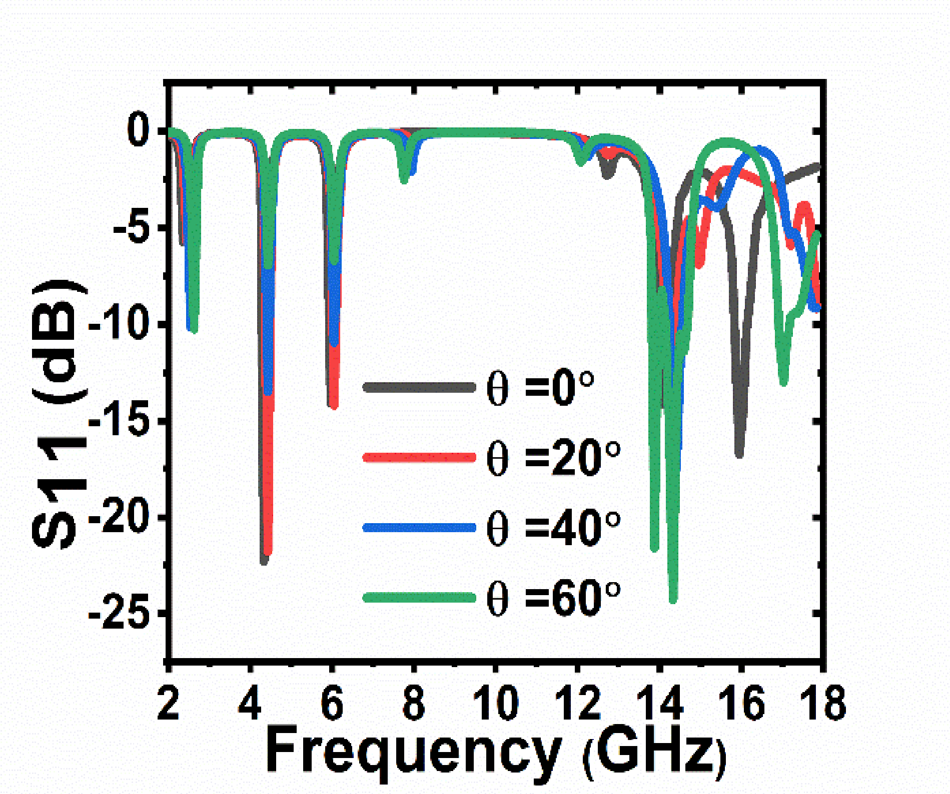
S11 (dB)
0
-5
-10
-15
-20
-25
2
4
6
8
10
12
14
16
18
Frequency (GHz)
θ =0°
θ =20°
θ =40°
θ =60°

(a)

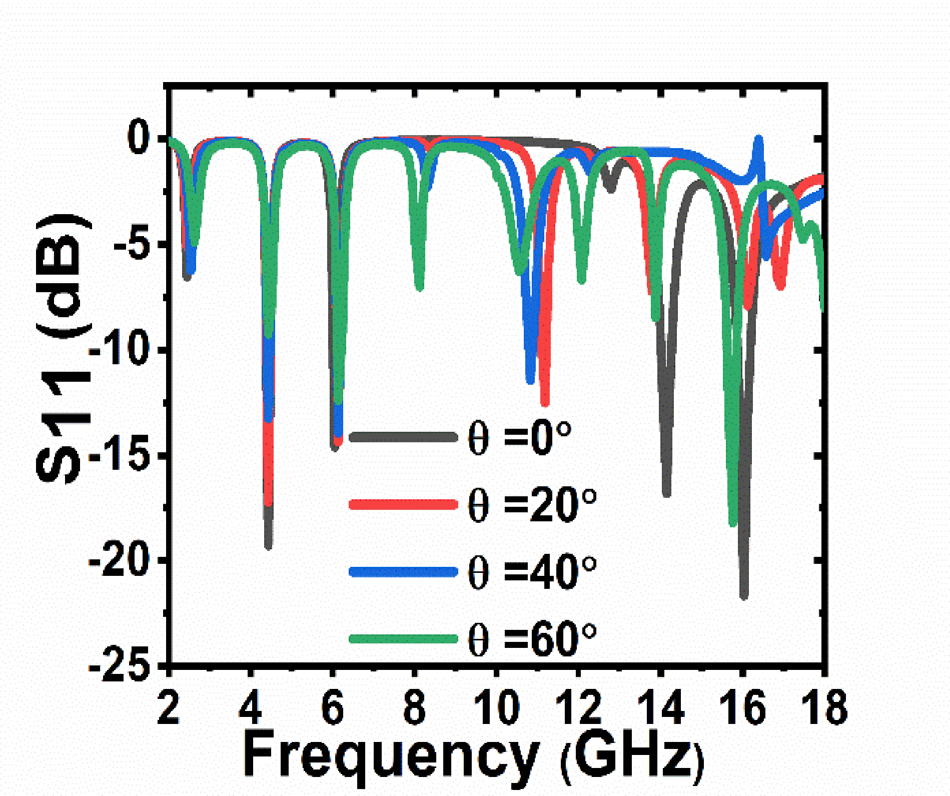
S11 (dB)
0
-5
-10
-15
-20
-25
2
4
6
8
10
12
14
16
18
Frequency (GHz)
θ =0°
θ =20°
θ =40°
θ =60°

(b)

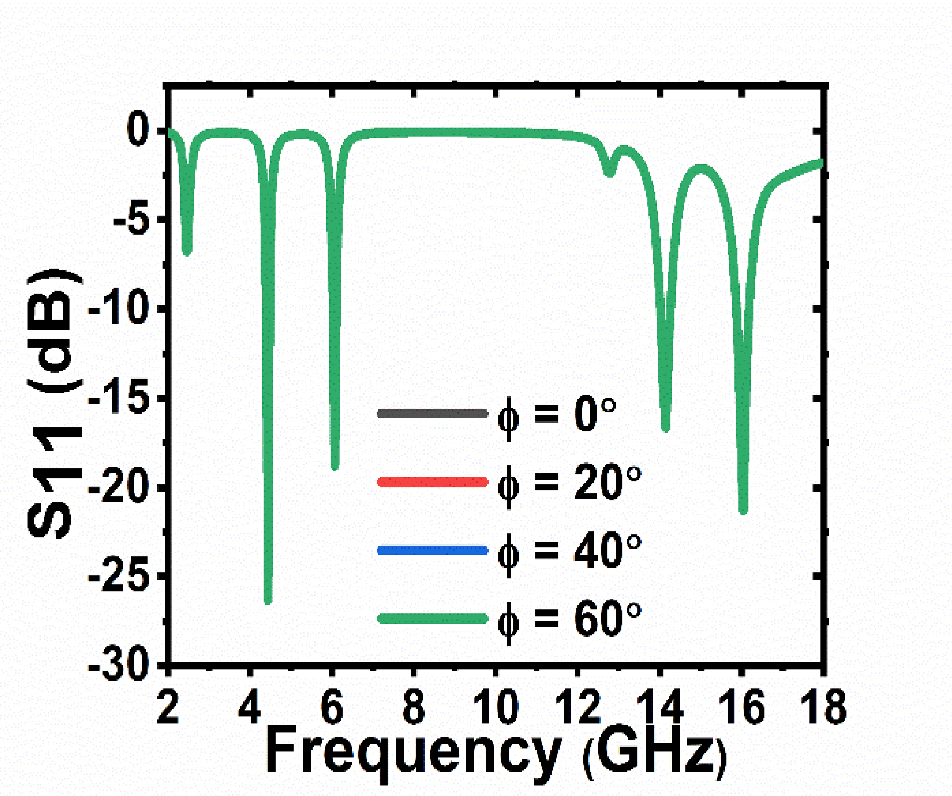

(c)

Figure 3.15. Simulated RC of proposed absorber with (a) different angle of incidence for TE polarization, (b) for TM polarization (c) different polarization angles under normal incidence.

The structure is studied under distinct polarization angles in the range of $0^{\circ}$to 60° at the normal incidence to examine its polarization sensitivity. It is analyzed from Figure 3.15 (c) that the structure exhibit polarization-insensitive characteristics from 2 to 18 GHz. The proposed MM absorber is a fourfold symmetric structure, as a result, it shows high absorption peaks under normal incidence for distinct polarization angles. The complex EM properties are extracted from scattering parameters using MATLAB coding [18]. The frequency response of the EM properties in terms of permittivity, permeability, and normalized impedance is reported in Figures 3.16 (a)-(c), respectively. The values of real and imaginary permittivity and permeability with respect to the resonant frequencies are summarized in Table 3.3. The negative values are responsible for maximum absorption and also indicate the nature of MMA. It is observed that at the peak frequencies the normalized impedance value of the structure is almost equal to 1, which satisfies the condition of impedance matching.

To have a comprehensible picture of the absorption behavior and to understand the absorption mechanism, we have represented the SC, E, and H field distributions of the proposed structure. Figures 3.17 (a)-(d) are manifested the surface current (SC) distributions at 4.4 GHz, 6.0 GHz, 14.1 GHz, and 16.0 GHz discretely. It is observed that over the lower frequencies (i.e., at 4.4 GHz and 6.0 GHz) absorption is predominantly because of the square and circle portion of the structure. Similarly, at the higher resonances (i.e., at 14.1GHz and 16.0 GHz) the eight sectors are also energetic along with other parts, with a strong current. **E** field distributions at the resonating frequencies are illustrated in Figures 3.18 (a)-(d). It is well being matched with SC distributions. E-field is concentrated on the outer square and outer circle portion at lower frequencies. While at higher frequencies the major **E-**field is also concentrated on the sectors of the proposed structure. Ergo, a strong magnetic resonance is observed because SC generates the circulating loops, resultant in high absorption achieved at the resonant frequencies [11]. Figures 3.19 (a)-(d) represent the **H**-field distribution at the resonating frequencies, which are well-matched with surface current and **E**- field distributions.

Table 3.3. Complex EM properties at resonance frequencies.

Frequency (GHz)	ε'	ε''	µ'	µ''
4.4	0.55	-7.4	2.4	-24.6
6.0	0.26	-4.0	5.2	-23.5
14.1	1.0	-4.3	0.9	-4.1
16.0	0.9	-3.0	1.0	-4.5

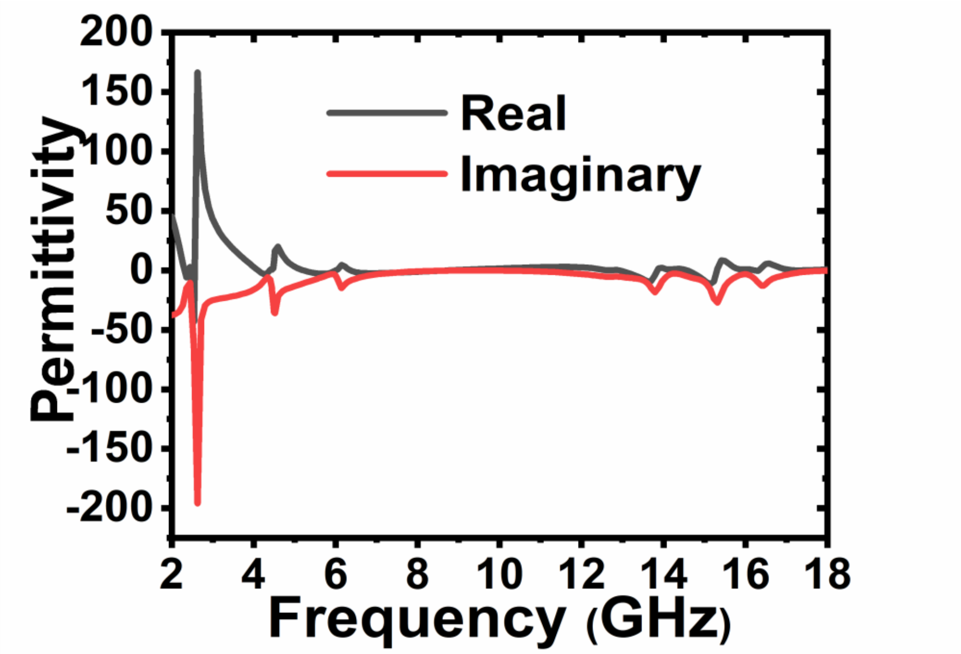

(a)

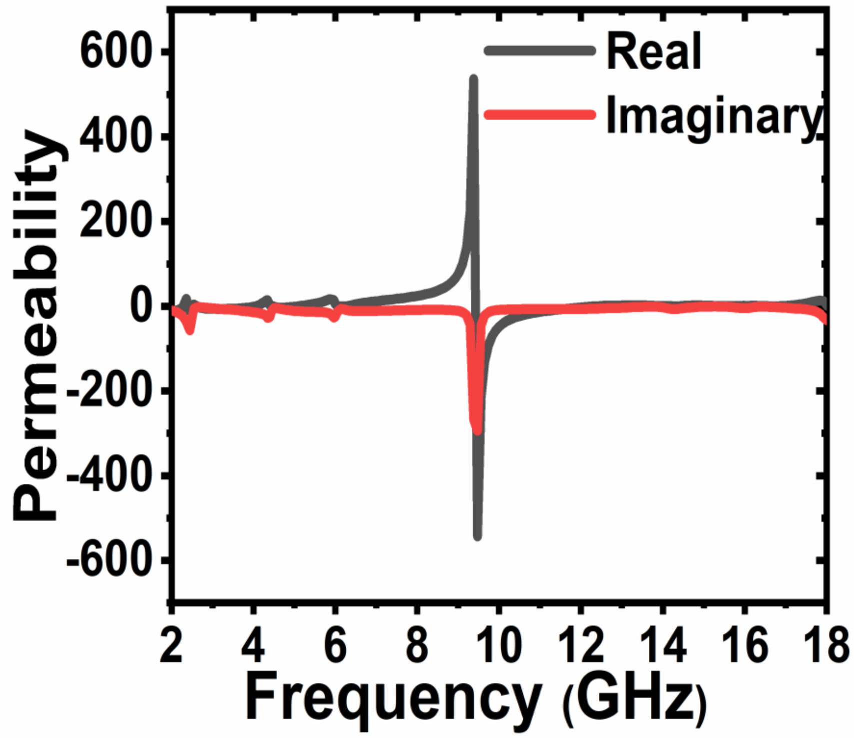

(b)

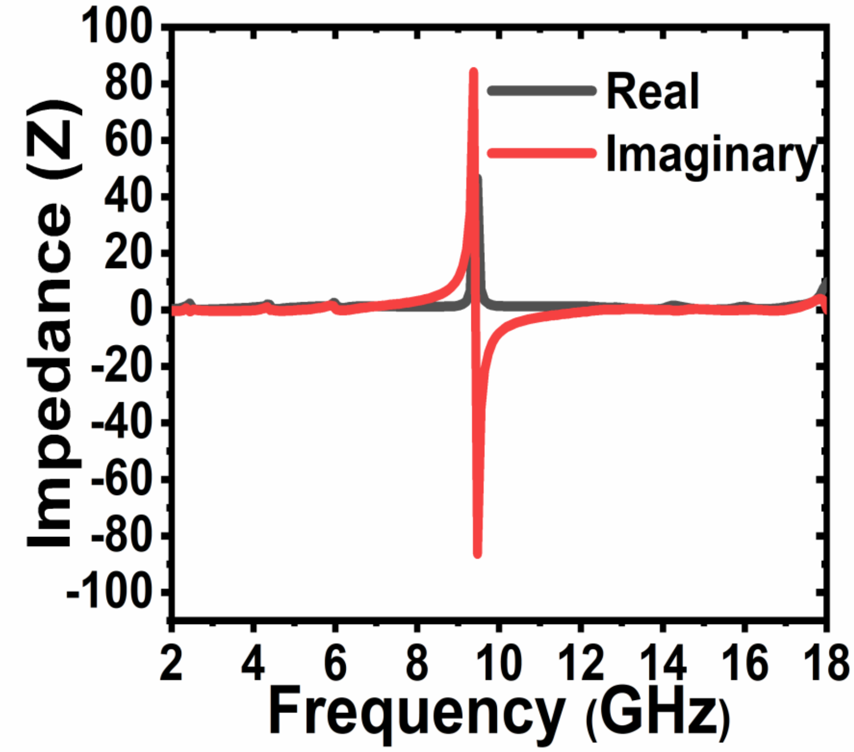

(c)

Figure 3.16. Complex electromagnetic properties (a) dielectric permittivity, (b) dielectric permeability, and (c) normalized impedance.

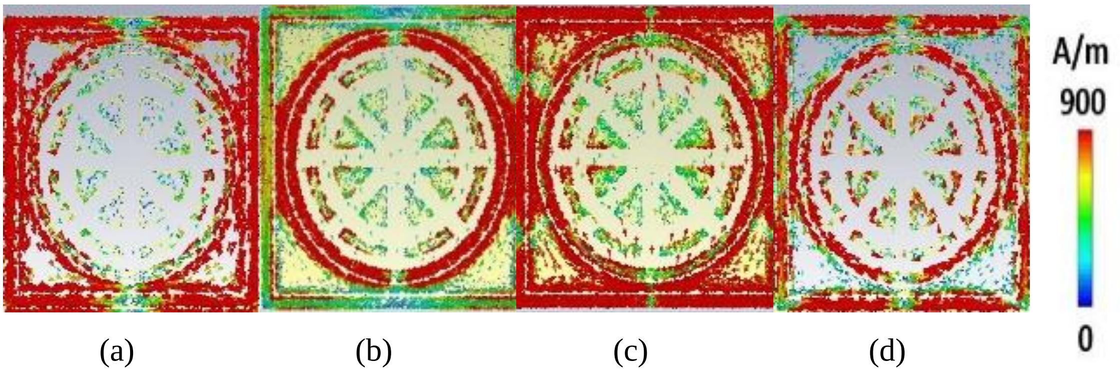

Figure 3.17. SC Distributions at (a) 4.4GHz, (b) 6.0 GHz, (c) 14.1GHz, and (d) 16.0 GHz.

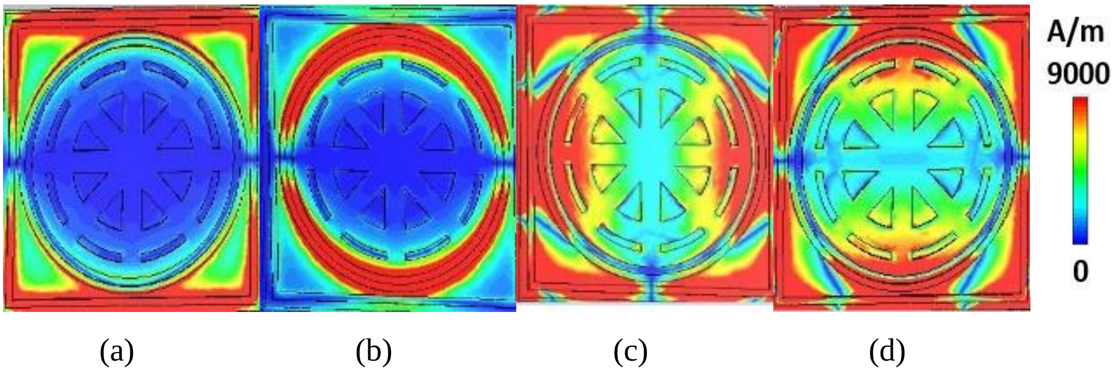

Figure 3.18. E-field distributions at (a) 4.4 GHz, (b) 6.0 GHz, (c) 14.1 GHz, and (d) 16.0 GHz.

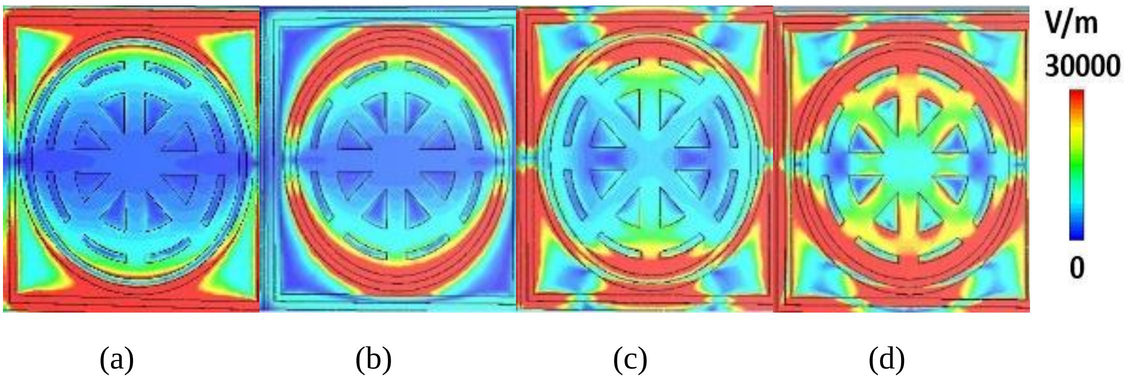

Figure 3.19. H-field distributions at (a) 4.4GHz, (b) 6.0 GHz, (c) 14.1GHz, and (d) 16.0 GHz.

3.3.3 FABRICATION AND EXPERIMENTAL VERIFICATION

To validate the simulated results, a prototype of size 200 × 200 mm^2 has been fabricated using a standard PCB technology as shown in Fig. 3.20 (a). A free space measurement setup has been employed to measure the frequency-dependent RC characteristics of the fabricated sample in the range of 2 to 18 GHz. The measurement has been performed in an anechoic chamber consist of a Keysight vector network analyzer (VNA) 35063A and broadband horn antennas.

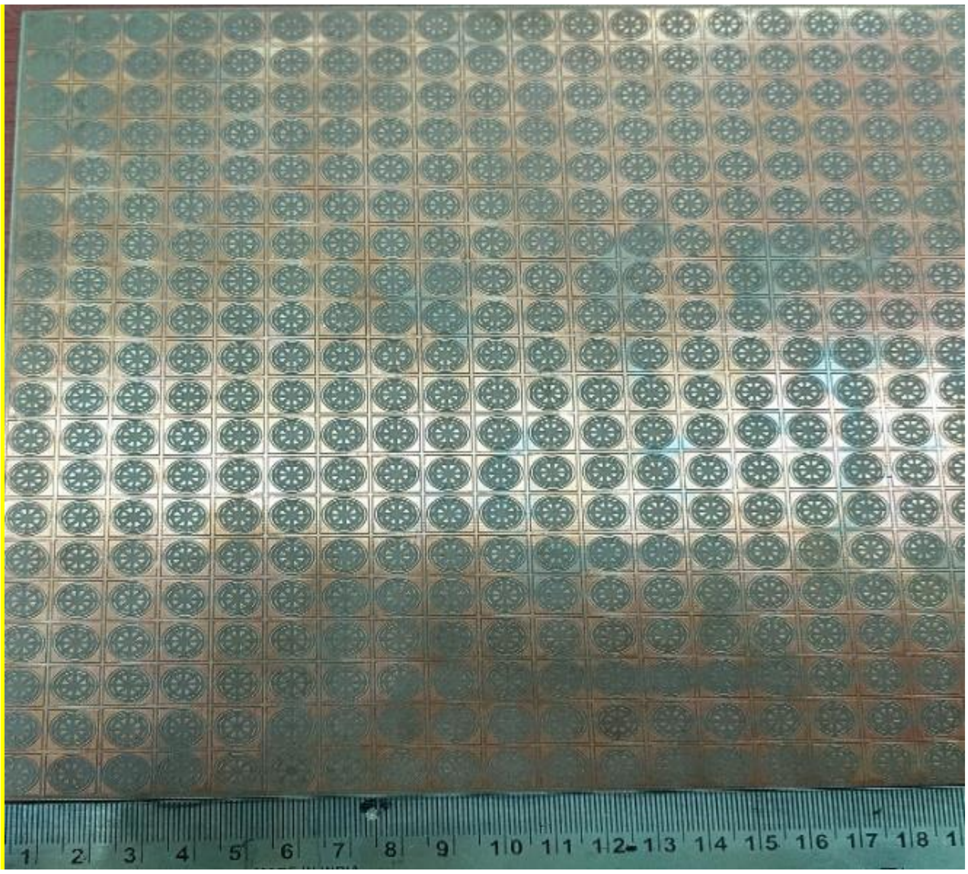
1
2
3
4
5
6
7
8
9
10
11
12
13
14
15
16
17
18

(a)

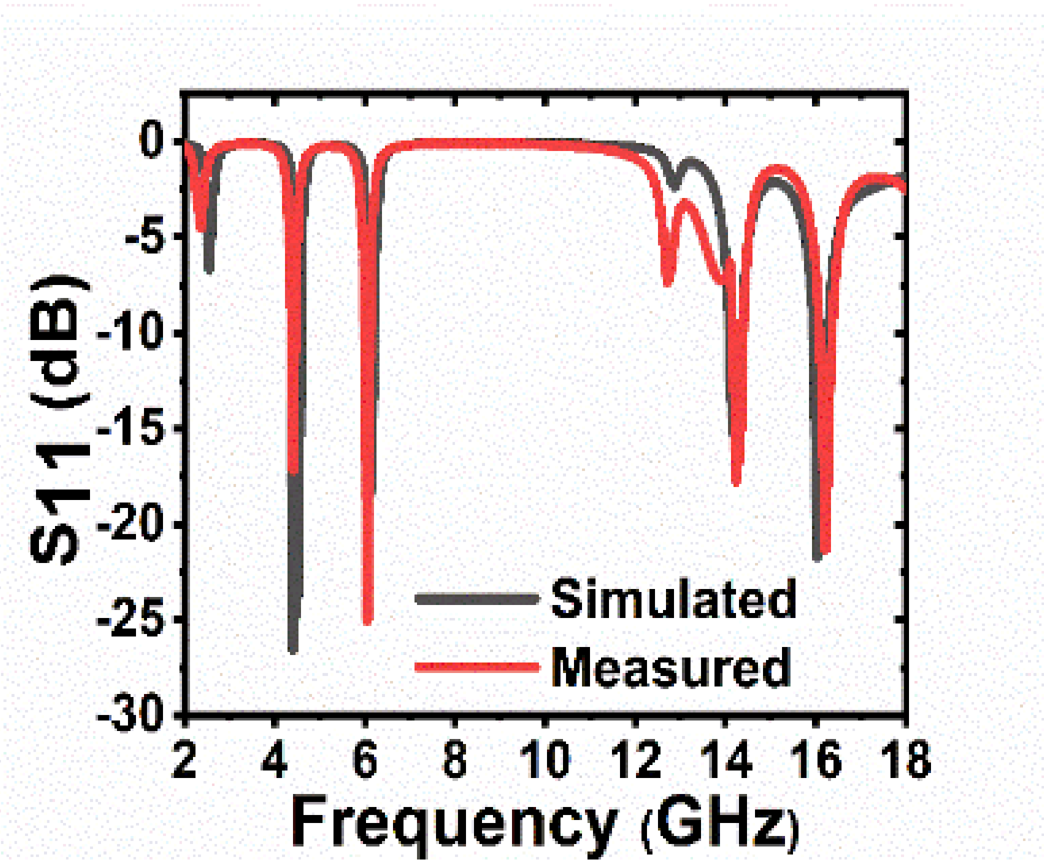
S11 (dB)
Frequency (GHz)
Simulated
Measured
0
-5
-10
-15
-20
-25
-30
2
4
6
8
10
12
14
16
18

(b)

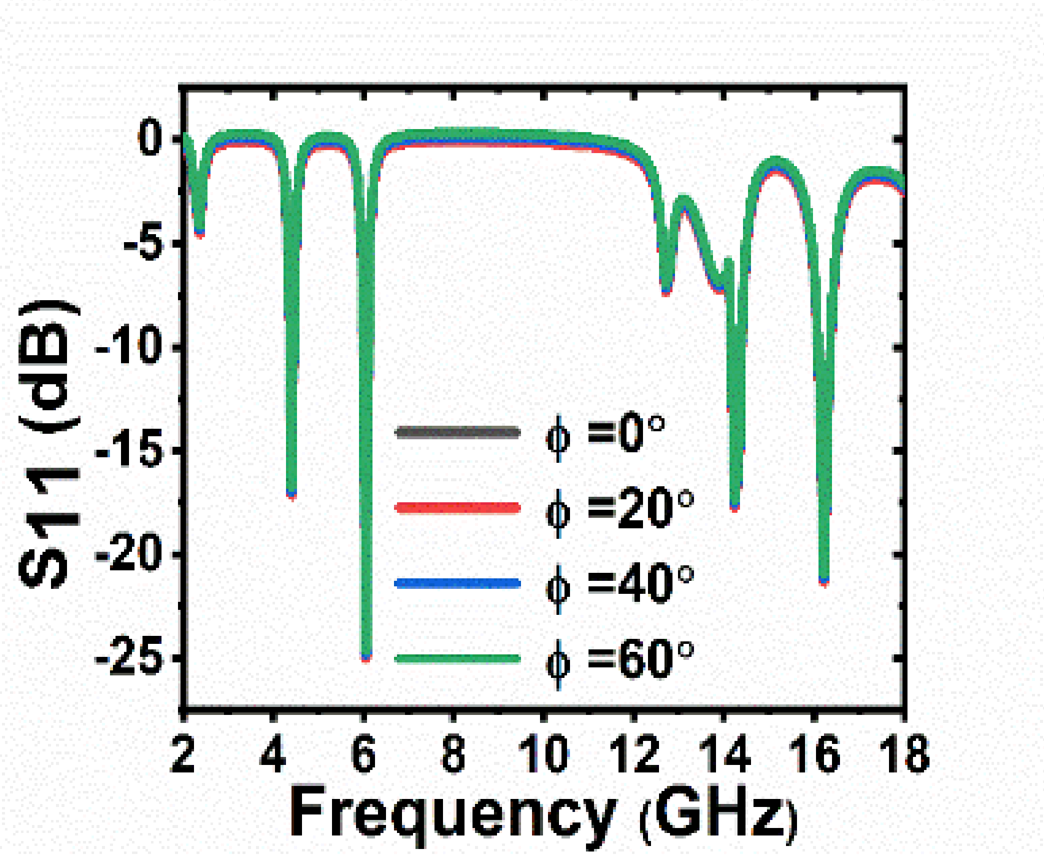
S11 (dB)
0
-5
-10
-15
-20
-25
2
4
6
8
10
12
14
16
18
Frequency (GHz)
ϕ =0°
ϕ =20°
ϕ =40°
ϕ =60°

(c)

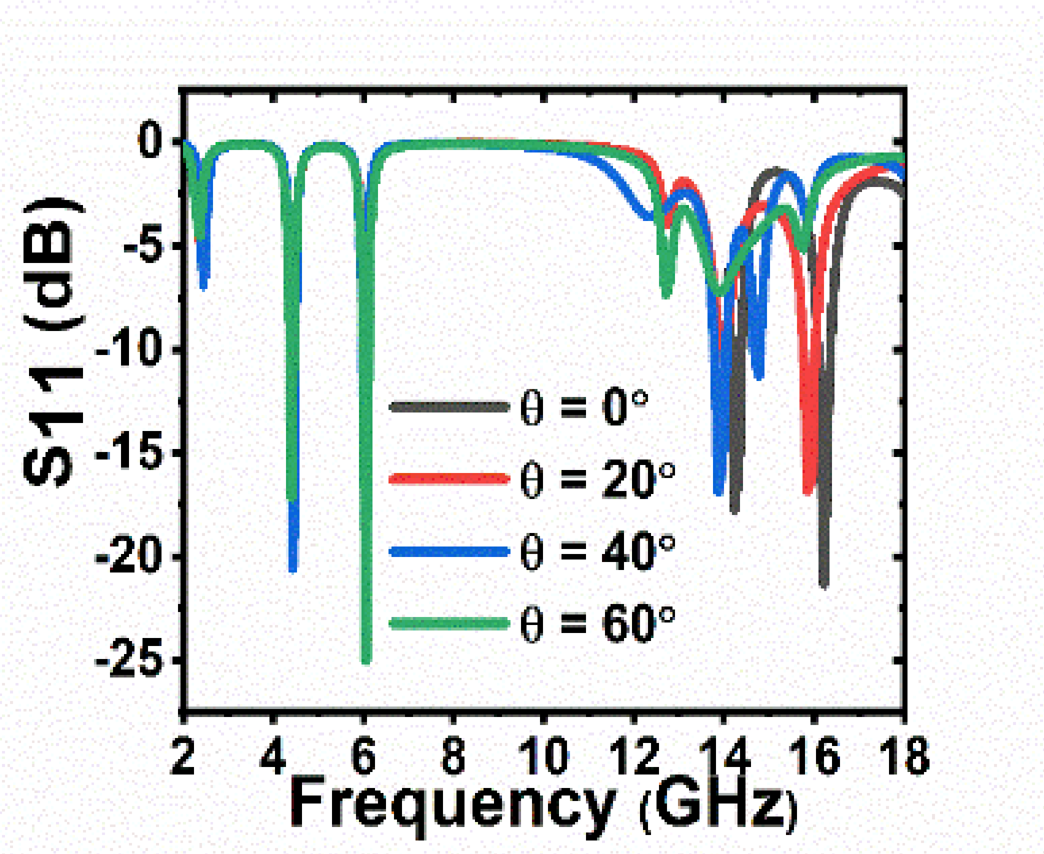
S11 (dB)
0
-5
-10
-15
-20
-25
2
4
6
8
10
12
14
16
18
Frequency (GHz)
θ = 0°
θ = 20°
θ = 40°
θ = 60°

(d)

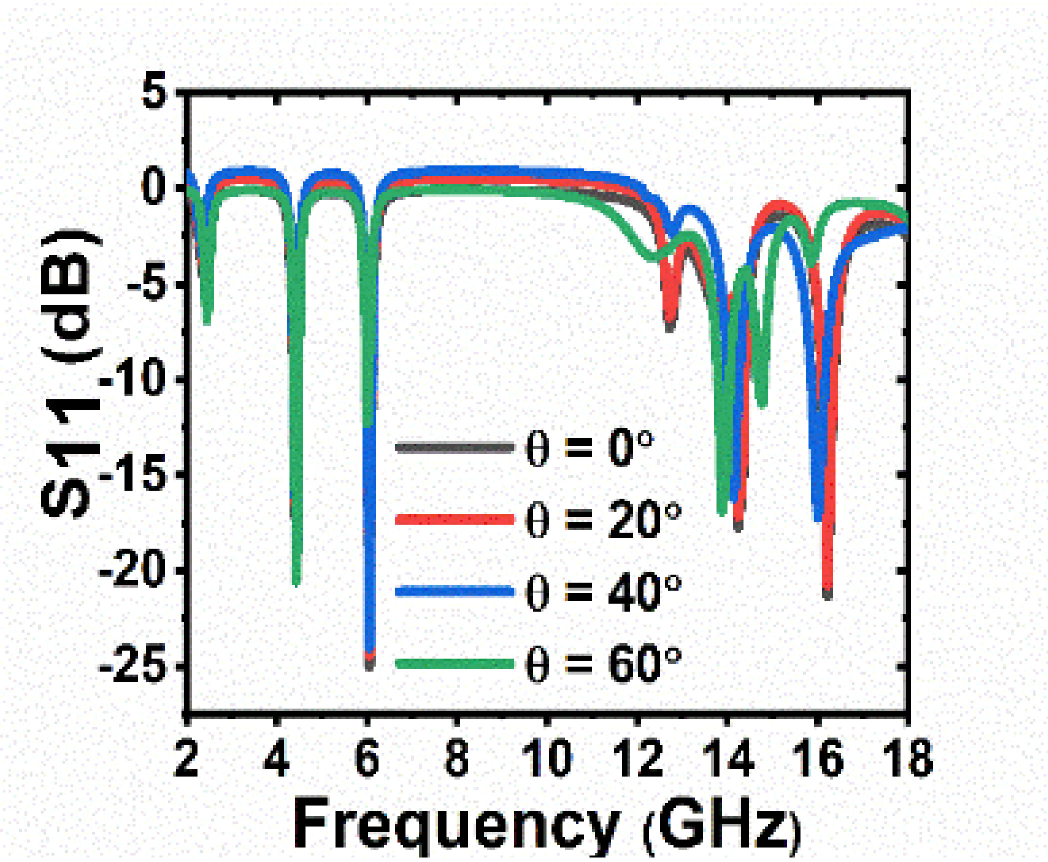

(e)

Figure 3.20. Measured RC characteristics (a) fabricated sample, (b) under normal incidence (c) with different polarization angles under normal incidence, (d) with different angles of incidence for TE polarization, and (e) for TM polarization.

The descriptive details of a free space microwave measurement setup are provided in [4]. The simulated and measured RC characteristics under normal incidence are shown in Figure 3.20 (b). A quite good agreement is noticed among simulated and measured results, except slight discrepancies which might be due to finite dimensions of sample, and fabrication tolerances. The polarization insensitive response is also investigated experimentally and illustrated in Figure 3.20 (c), which illustrates the same RC response with variation in polarization angle 'θ'from 0^{o} to 60^{o}. It has been observed in Figure 3.20 (c) that the prototype exhibits polarization-insensitive behavior in the range of 2 to 18 GHz. The measured RC response of the proposed fabricated sample with a distinct incidence angle under TE and TM are portrayed in Figures 3.20 (d) and 3.20 (e), respectively. The measured results show the variation in higher frequencies under TE and TM polarizations. More or less identical results are procured in lower frequencies under TE and TM polarizations as illustrated in Figures .20 (d) and 3.20 (e), respectively.

3.4 COMPARISON WITH OTHER REPORTED WORKS

Table 3.4 presents a systematic comparison of microwave absorption properties of the proposed absorber with other reported works. The comparison has been made based on absorber geometry, unit cell dimensions, absorber layer thickness, and relative bandwidth. The absorption properties of the proposed structure are in good agreement with the other reported works. It has been observed that cross-loaded split ring MAS shows 60% bandwidth with 2 mm thickness. Multi-layered absorber configuration has 3.65 mm thickness achieved 95.2% bandwidth, whereas the other structures have shown lesser bandwidth than cross-loaded split ring MAS. The other reported structure covers dual-band with multiple peaks with 1.6 mm thickness only.

Table 3.4. Comparison of proposed structure with earlier reported structures.

Absorber configurations	f_c (GHz)	Unit cell size (mm)	t (mm)	Relative BW (%)	Refs.
Metamaterial absorber	10	14.2	0.6	11%	Lee et al.(2011)
Ultra-thin broadband absorber	11.11	40	0.8	20%	Liu et al. (2012)
Multi- layered	15.13	6.4	3.65	95.2%	Xiong et al. (2013)
Artificial impedance surface-based absorber	10.15	13.8	5.6	45%	Yoo et al. (2014)
Hybrid cross-loaded split ring MAS	12.2	8	2	60%	Cross loaded split ring MAS
Eight sectors loaded circle inside the square	-	10	1.6	Multiple resonant peaks	Multiband and polarization-insensitive absorber

3.5 CONCLUSION

In this chapter, two distinct MM-based absorbers are demonstrated in the range of 2 to 18 GHz. The first MMA is a hybrid structure that comprises of a cross-loaded split ring. The key features of the first absorber are broadband absorption in the range of 8.5 to 16 GHz, covering the entire X-band. The other proposed structure comprises eight sectors loaded circle inside the square. A multiband and polarization-insensitive response are the main attributes of the second proposed structure. A critical analysis of both structures has been carried out to study the effect of design variables on the absorber characteristics. The frequency-dependent EM properties of both structures are also illustrated to depict the MM nature. To understand the absorption mechanism, the surface current, E-field, and H- field distributions of both structures are also demonstrated in this chapter. Finally, both structures are fabricated to evaluate the effectiveness of designs. The measured results from the fabricated prototypes are in close agreement with the simulated results, suggesting the effectiveness of the structures for real electromagnetic applications.

CHAPTER 4

DESIGN AND DEVELOPMENT OF ACTIVE MICROWAVE ABSORBING STRUCTURE

In this chapter, an efficient tunable absorber based on an AFSS utilizing p-i-n diode is presented. Initially, the AFSS has been designed, simulated and analyzed using the CST studio. Futher, the design of the active absorber which is based on AFSS is also presented. Another study is executed on AFSS loaded absorber with diode and without diode, to know its effect on the absorption chracteristics. To obtain the tunability AFSS loaded absorber with different values of resistance has been evaluated. The normalized impedance, surface current, **E** field, and **H** field distributions are also presented. Finally, the proposed prototype has been fabricated to evaluate the measured result. The free-space microwave measurement setup is used for the performance evaluation of the fabricated prototype.

4.1 INTRODUCTION AND MOTIVATION

FSSs which have variable frequency response is known as active FSS, whereas the passive FSS having static frequency response. The active and passive FSSs have their own merits and demerits. The frequency response that is either reflection or transmission characteristics of passive FSS can not be modified, without redesigning the process of the geometry. This is the major drawback of the passive FSSs and also restrict for some practical applications. Active FSSs provide more bandwidth and freedom to operate at different frequencies simultaneously. In recent years, active absorbers have attracted much attention as compared to the CMAs [80-81]. CMA provides no flexibility after fabrication, whereas, active absorber provides tunability over a wide frequency range with the help of external biasing circuits [82]. The polarization insensitive behavior and broad bandwidth of absorber can also be obtained by non-linear active devices. The basic configuration of the tunable absorber is illustrated in Figure 4.1. The tunable absorber is similar to the conventional absorber, although in the unit cell of the tunable absorber has the active component. The researchers have introduced the transistor, p-i-n diode, and varactor diode as an active component in the development of the active absorbers [83-84]. Three ways are suggested to generate tunability behavior in FSS viz. electronic, mechanical, and magnetic [81]. By changing the shape of FSSs element, mechanically tunability can be achieved. The magnetically tunable FSSs are realized by changing the permeability property of the ferrite substrate [81].

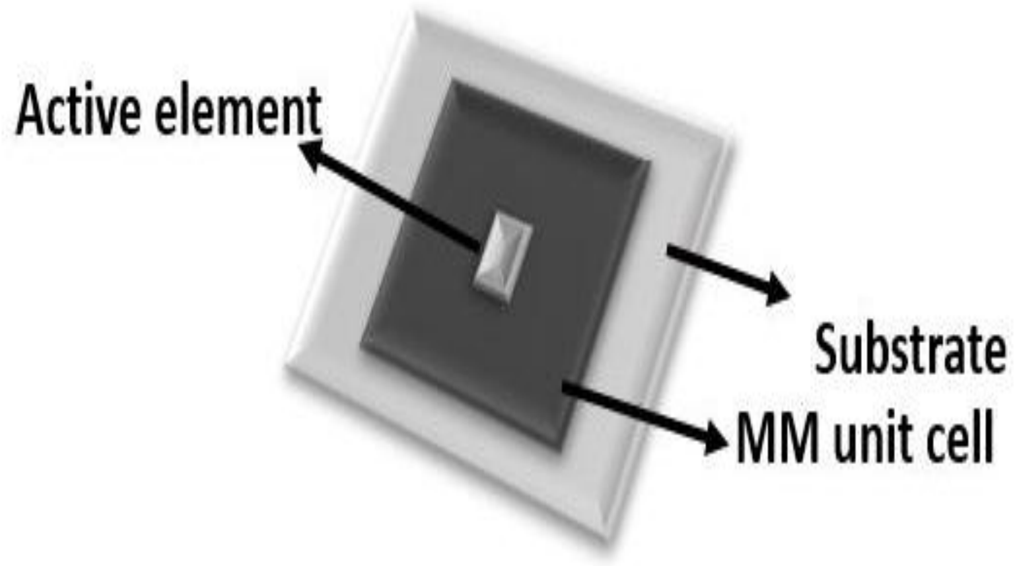

Figure 4.1. Basic configuration of the active absorber.

Graphene-based tunable absorbers are also reported in the literature, but it enhances its cost and it is a strenuous job to manage the surface conductivity [85]. Liquid crystals can also be used to achieve tunability in FSS structures, but the limitation of this technique is the limited tuning range [86]. The mechanical and magnetic tunable FSSs have a small range and low speed of tuning. Electronic tunable FSSs use active electronic devices like barium-strontium-titanate varactor [87], p-i-n diode [88], and varactor diode [89], etc. In electronically tunable absorbers there is a need to provide the biasing circuit, which increases the complexity during fabrication of the prototype. Therefore, a simple biasing circuit is needed to reduce the complexity of the circuit, and isolation between the unit cells of the prototype needs to be carefully achieved. To obtain the broadband absorption and the switchable mechanism, authors have used the multilayer geometry and p-i-n diodes, respectively.

4.2 DESIGN METHODOLOGY

A tunable, single layer, and wideband AFSS based absorber is presented, which demonstrates the tunability in the range of 9.2 to 11.2 GHz. AFSS demonstrates the tunable performance with a 1.1 GHz and 2.0 GHz bandwidth in ON and OFF states, respectively. The p-i-n diode with a unique biasing technique is used to obtain the tunability performance, which reduces the complexity. A similar design of AFSS has been used to construct an efficient tunable microwave absorber, in which the bandwidth with forward resistance of 30Ω has been achieved. Additionally, the critical analysis has also been investigated to know the effect of dimensions on AFSS loaded tunable absorber. Finally, the prototype is fabricated and measured for the validation of simulated results.

4.2.1 DESIGN OF AFSS BASED TUNABLE MICROWAVE ABSORBER

This section describes the designing part of the tunable microwave absorber, which is based on AFSS absorber. A schematic view of AFSS unit cell structure is shown in Figure 4.2. The unit cell is composed of two reverse 'G' shaped patterns with the biasing line at the center of the structure, in which p-i-n diode is connected.

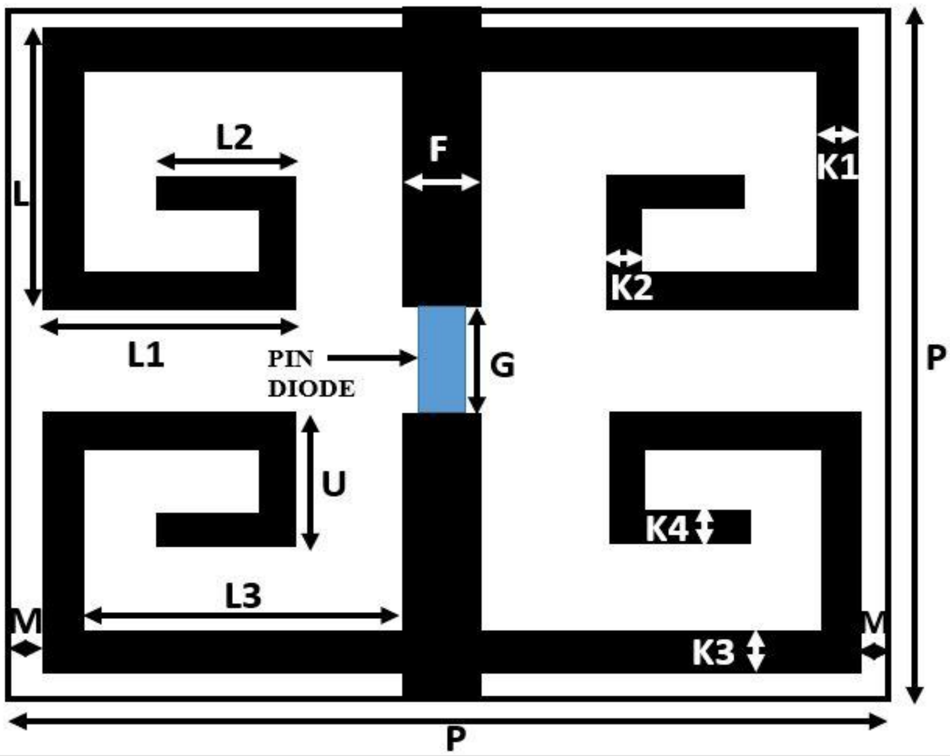

Figure 4.2. Schematic view of AFSS unit cell structure.

The proposed AFSS geometry has been printed on one side of the FR4 substrate (relative permittivity, ε_r=4.3, and dielectric loss tangent, tan δ= 0.025) with a thickness of 1.0 mm, whereas the other side of the FR4 substrate is entirely etched. The optimal geometrical design variables of the unit cell are listed in Table 4.1.

Table 4.1. Optimal design variables of AFSS unit cell.

Parameters	Value (mm)	Parameters	Value (mm)
P	20.0	F	2.0
L	9.0	K1	1.5
L1	5.0	K2	1.0
L2	2.5	K3	1.5
L3	7.0	K4	1.0
G	1.0	U	2.5
M	0.5	-	-

The structure has been designed and simulated using the CST software in frequency domain solver. The periodic boundary conditions and Floquet port have been employed along the x- **y-**axis and z-axis, respectively. During the simulation, p-i-n diode has been considered equivalent to the pure resistor in both 'on' and 'off' states. During the on state, the value of resistance is 10 **Ω**, which means the diode is in forward biasing condition. To make the diode in reverse biasing condition, the value of resistance set to 10MΩ, this state is called off state. To design the tunable absorber based on AFSS, an air gap 'A' of 8.0 mm is introduced in between the copper plate and FSS. The 3 dimensional (D) topology is depicted in Figure 4.3.

4.2.2 CRITICAL ANALYSIS AND SIMULATED RESULTS

Foremost, the transmission coefficient graph of AFSS in both states is elucidated in Figure 4.4. It has been found that during the "on" state, the resonance frequency of 6.8 GHz with a transmission coefficient of -24.5 dB is acquired. The overall bandwidth of 1.1 GHz is obtained in the range of 6.4 GHz to 7.5 GHz. While in "off" state condition, AFSS exhibits a bandwidth of 2.0 GHz in the range of 6.9 GHz to 8.9 GHz. The resonating peak is observed at 7.8 GHz with a transmission coefficient of -33.2 dB. Further, an extensive study is performed on AFSS to know the effect of different variables on the TC response of FSS structure. Here, the first study is performed on the width of the feed line 'F' in the range of 1.0 mm to 3.0 mm with a step size of 0.5 mm. Figures 4.5 (a) and (b) illuminate the effect of the width of the feed line in "on" and "off" states, respectively.

The optimal value of this variable is 2.0 mm. It can be evaluated from figure 4.5 (a) that as the value of the variable goes increases, the resonance shifts towards the higher frequency. An identical effect has been observed in Figure 4.5 (b). Similarly, the size of the unit cell 'P' is varied from 19.0 mm to 21.0 mm. The study of this variable is shown in Figures 4.6 (a) and (b) for "on" and "off" conditions, respectively. In this graph, five samples have been considered with a step size of 0.5 mm.

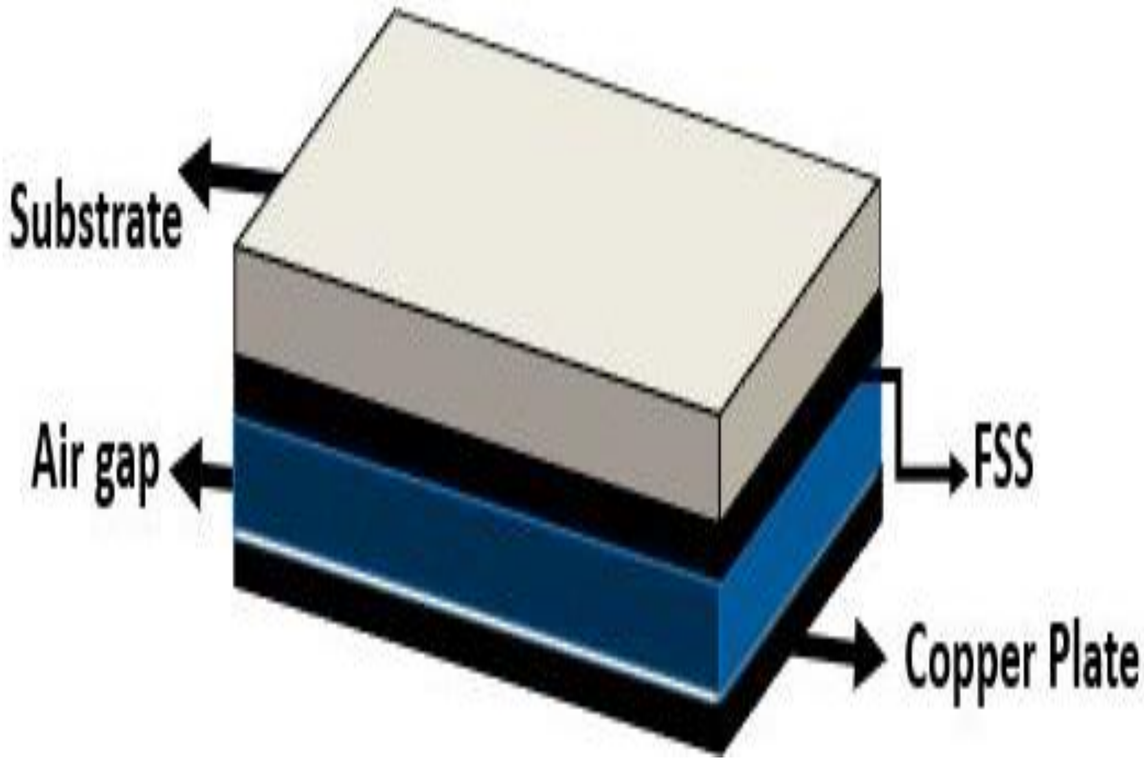

Figure 4.3. 3D view of the tunable absorber.

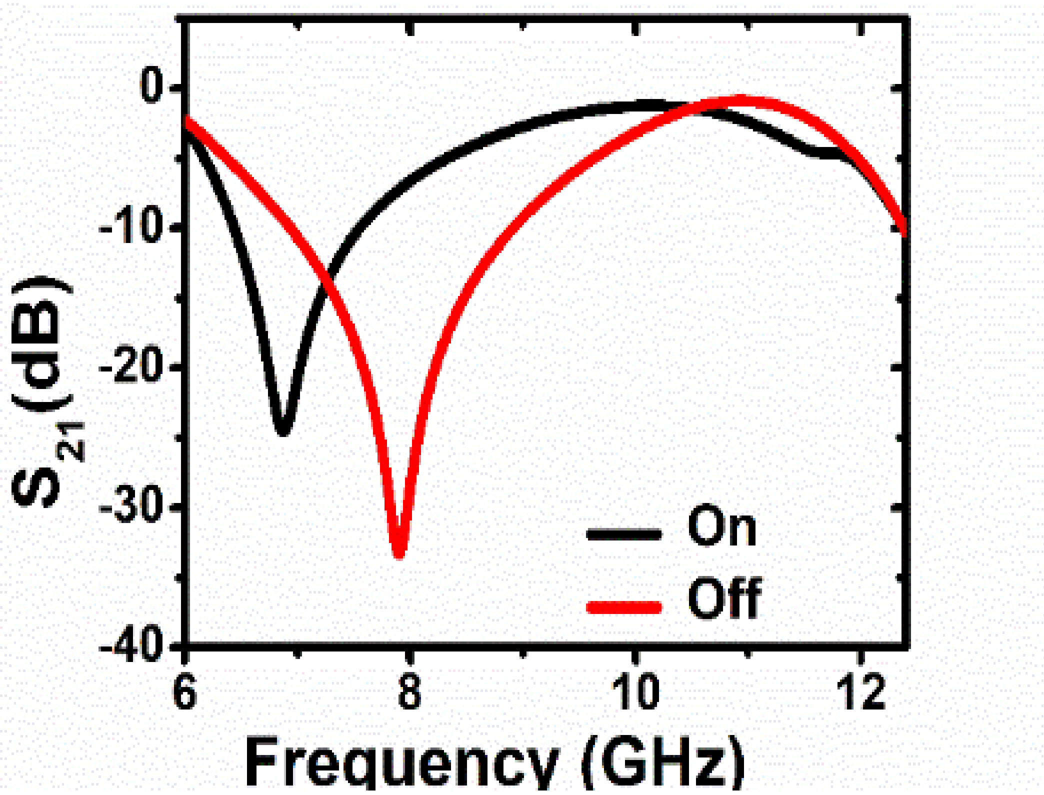

Figure 4.4. Simulated transmission coefficient spectra in on and off states of PIN diode.

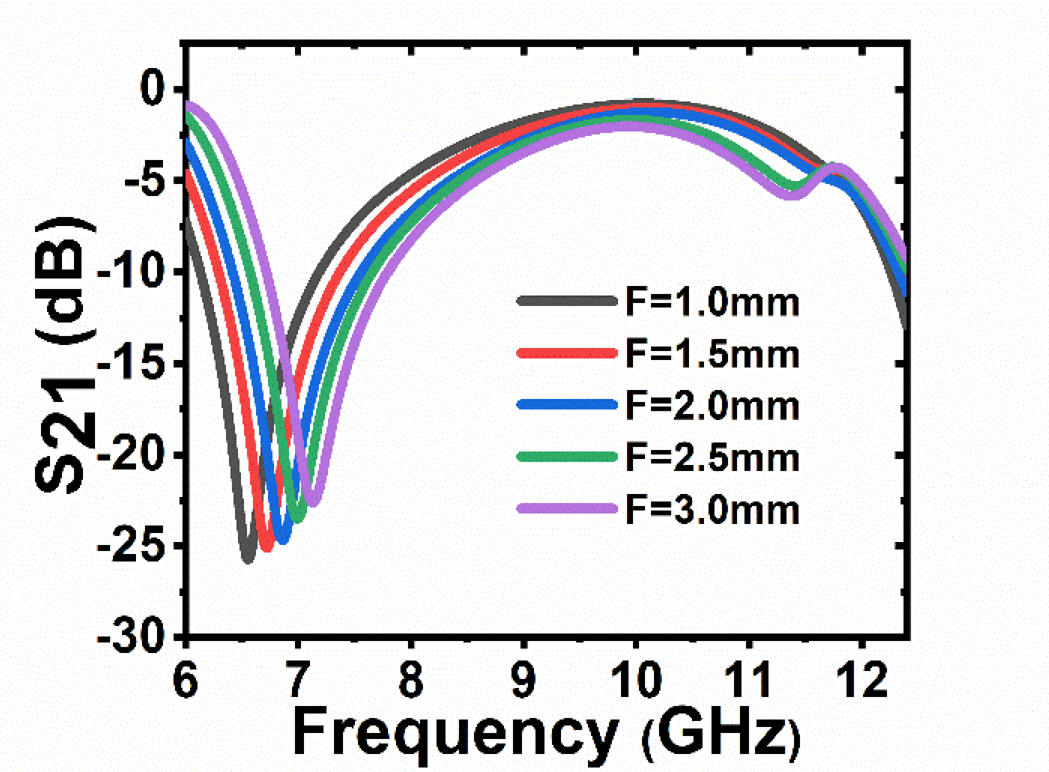

(a)

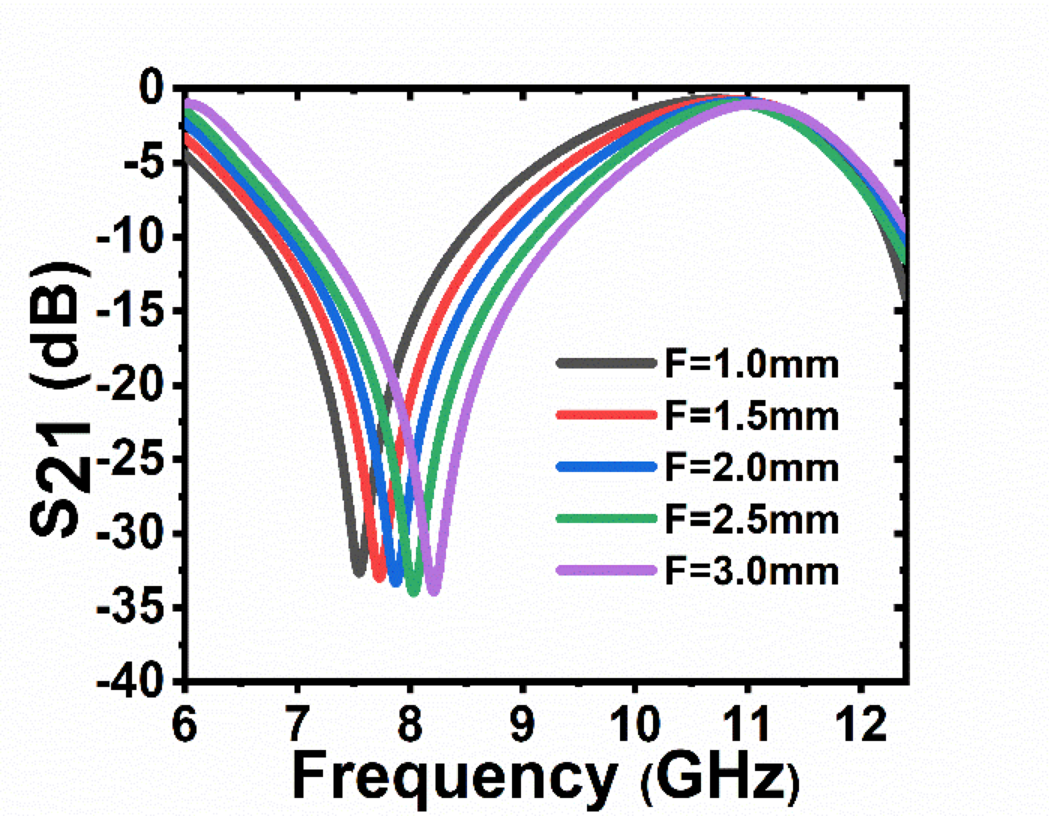

(b)

Figure 4.5. Effect of the width of feed line on AFSS (a) on state, and (b) off state.

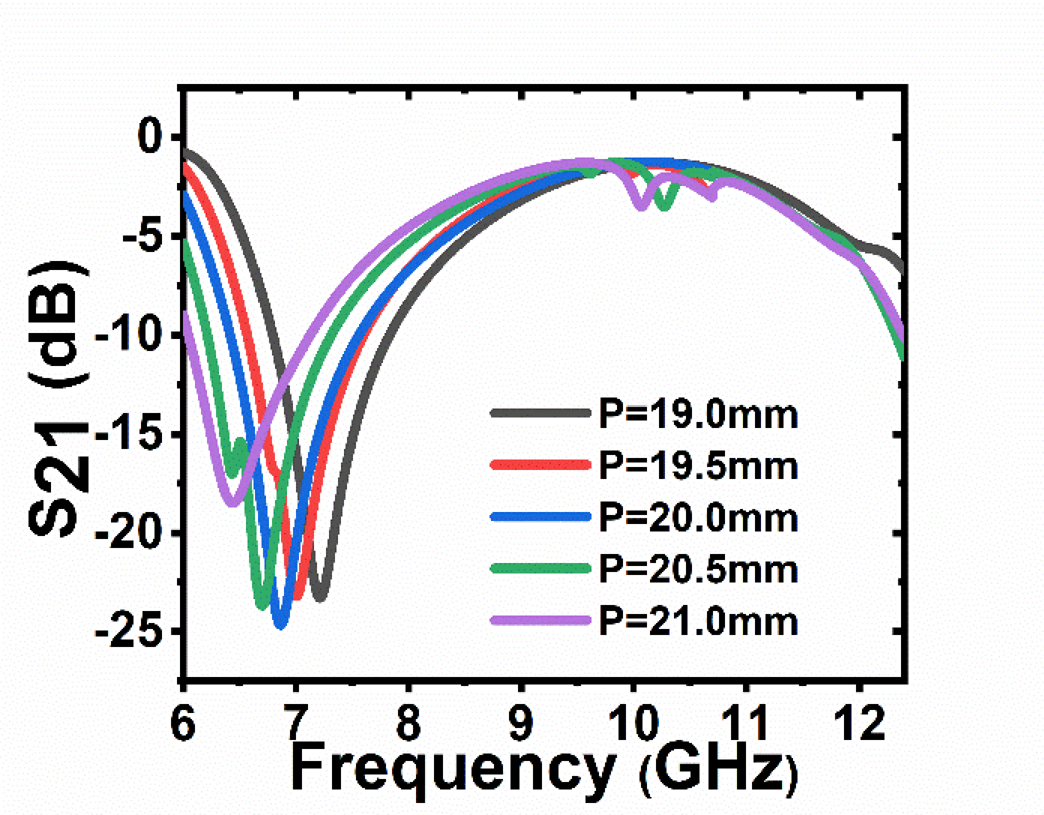

(a)

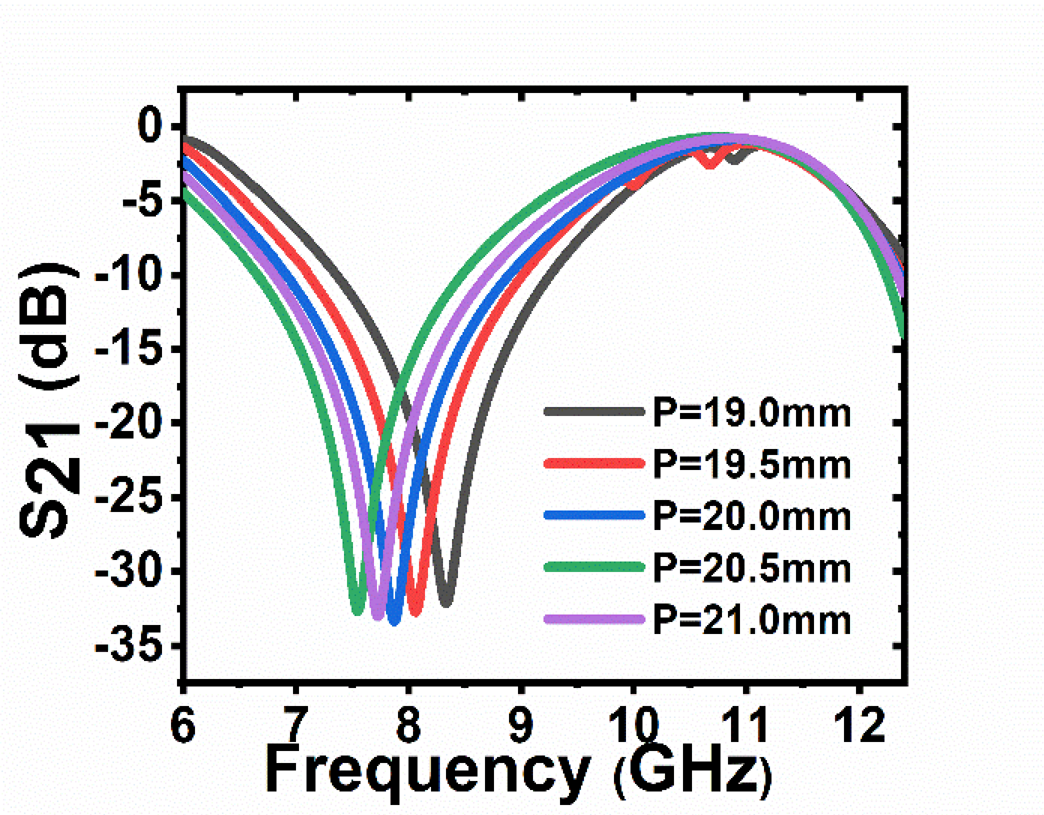

(b)

Figure 4.6. Effect of size of the unit cell on AFSS in (a) on state and (b) off state.

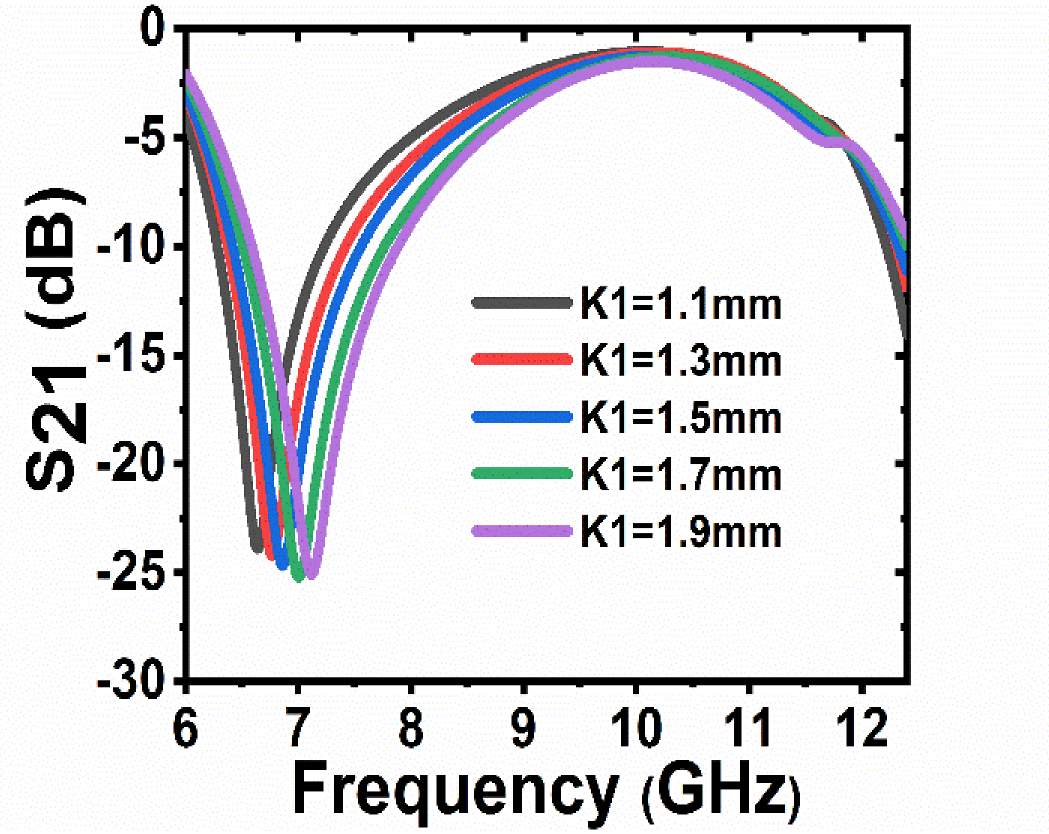

(a)

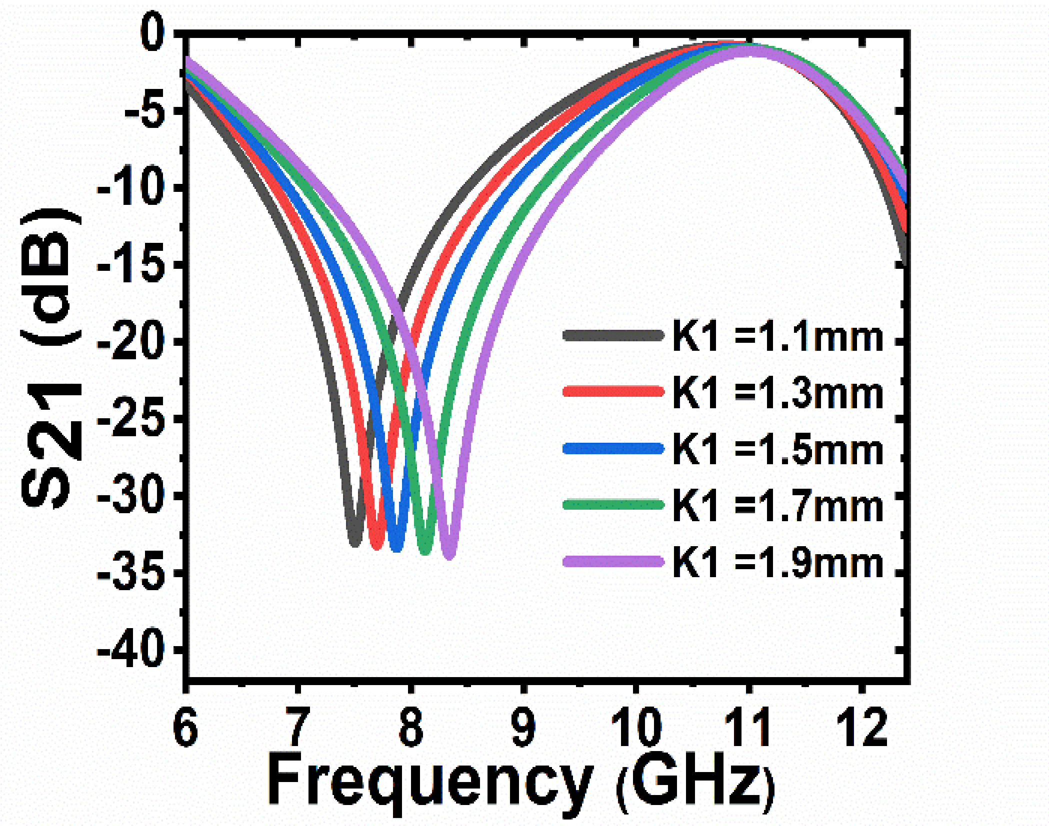

(b)

Figure 4.7. Effect of ‘K1’ variable on AFSS structure in (a) on state and (b) off state.

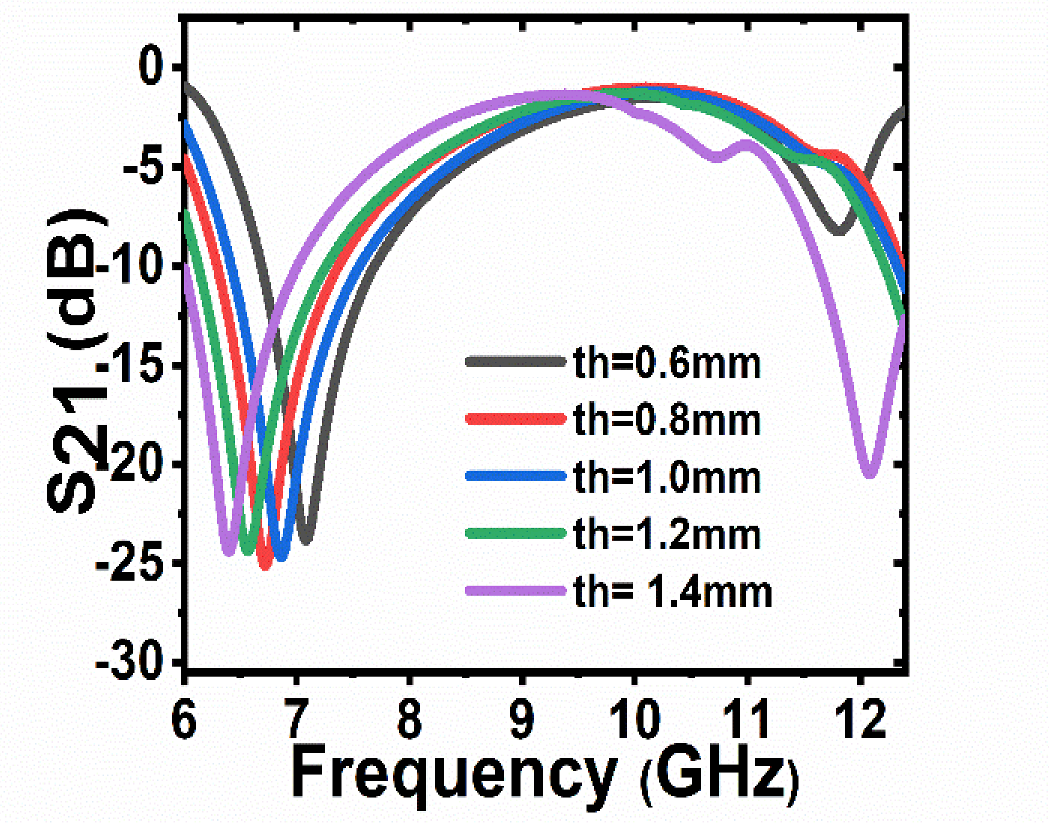

(a)

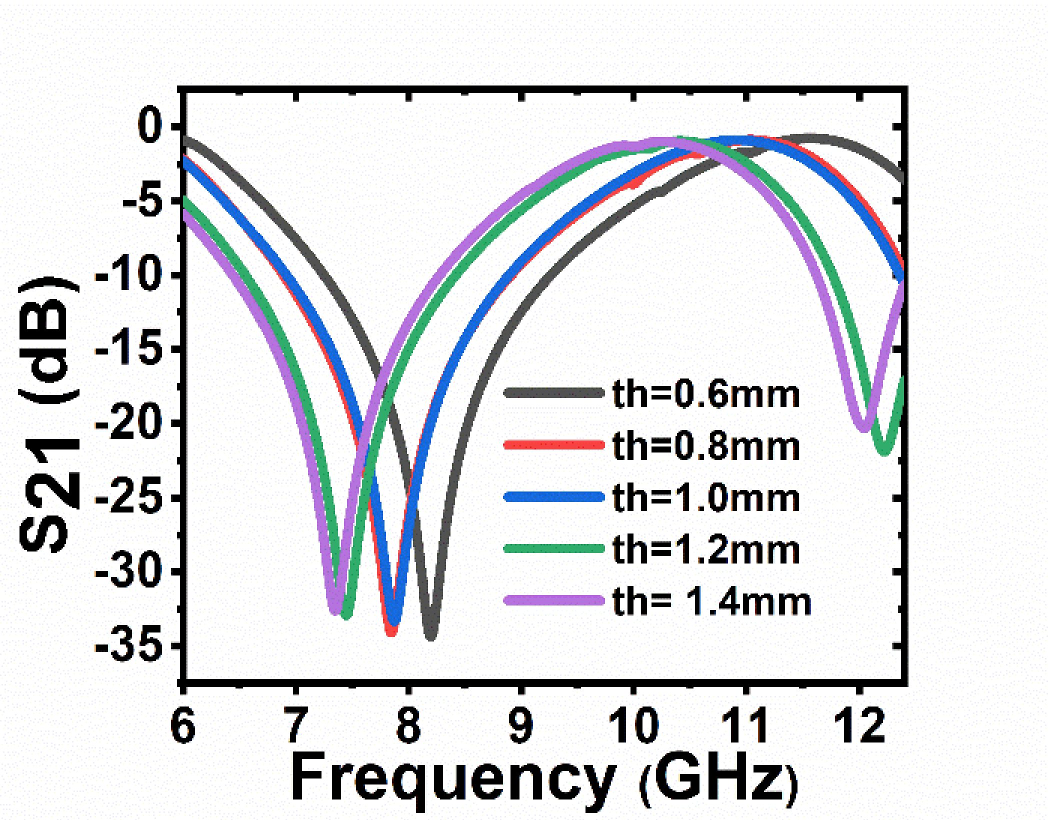

(b)

Figure 4.8. Effect of thickness of the substrate in (a) on state and (b) off state.

It has been observed in Figure 4.6 (a) that as the size of the unit cell increases, the resonance frequency shifts towards the lower frequency region. It is clearly shown in Figure 4.6 (a) that the bandwidth of the structure decreases, as ‘p’ increases beyond its optimal value. The optimal value of ‘P’ variable is 20.0 mm. It has been observed from Figures 4.7 (a) and (b) that as the value of ‘K1’ variable is increased, the resonant peak shifts towards the lower frequency. The next study is carried out on the thickness ‘th’ of the substrate of AFSS structure. The corresponding results with varied substrate layer thickness are presented in Figures 4.8 (a) and (b) for “on” and “off”, respectively.

The same effect has been observed in Figure 4.6 (b) for “off” state, as the value of ‘P’ increases the resonant peak shifts towards the lower frequency regime. Similarly, the variable ‘K1’ of the AFSS structure is varied from 1.1 mm to 1.9 mm with a step size of 0.2 mm. The study on ‘th’ is evaluated ranging from 0.6mm to 1.4 mm with a step size of 0.2mm while keeping the other parameters constant. The broad bandwidth has been obtained with 1.0 mm thickness of the substrate. As the thickness of the structure increases beyond optimal value, the more bandwidth has been obtained in a higher frequency regime as portrayed in Figures 4.8 (a) and (b). However, it is well known that the bandwidth is strongly influenced by the substrate thickness, as the thickness of the substrate increases, the more bandwidth will attain. But we cannot consider the higher value of thickness because of a tradeoff between thickness and bandwidth [Panwar, 2015]. Meanwhile, one other study has been executed to know the effect of the diode on the AFSS based absorber structure. RC characteristics of the absorber are illustrated in Figure 4.9, which shows that without diode there is no RC bandwidth below -10 dB. Whereas, 2 GHz bandwidth below -10 dB has been obtained with diode. Six different values of resistance have been taken to perceive the response of RC as depicted in Figure 4.10. The variation in peak RC has been observed as the value of resistance changes. The remarkable maximum bandwidth of 2.0 GHz with a resistance of 30Ω is perceived. Whereas the resonating peak is acquired at 9.7 GHz with a transmission coefficient of -30.8 dB. As the value of resistance increases from 15 Ω to 90Ω, the resonance frequency shifts from 11.1 GHz to 10.5 GHz. Further, when the value of resistance increases, resulting in poor impedance matching, therefore no resonant peak is observed. Additionally, a critical parametric analysis is also performed on the dimensions of AFSS loaded tunable absorber.

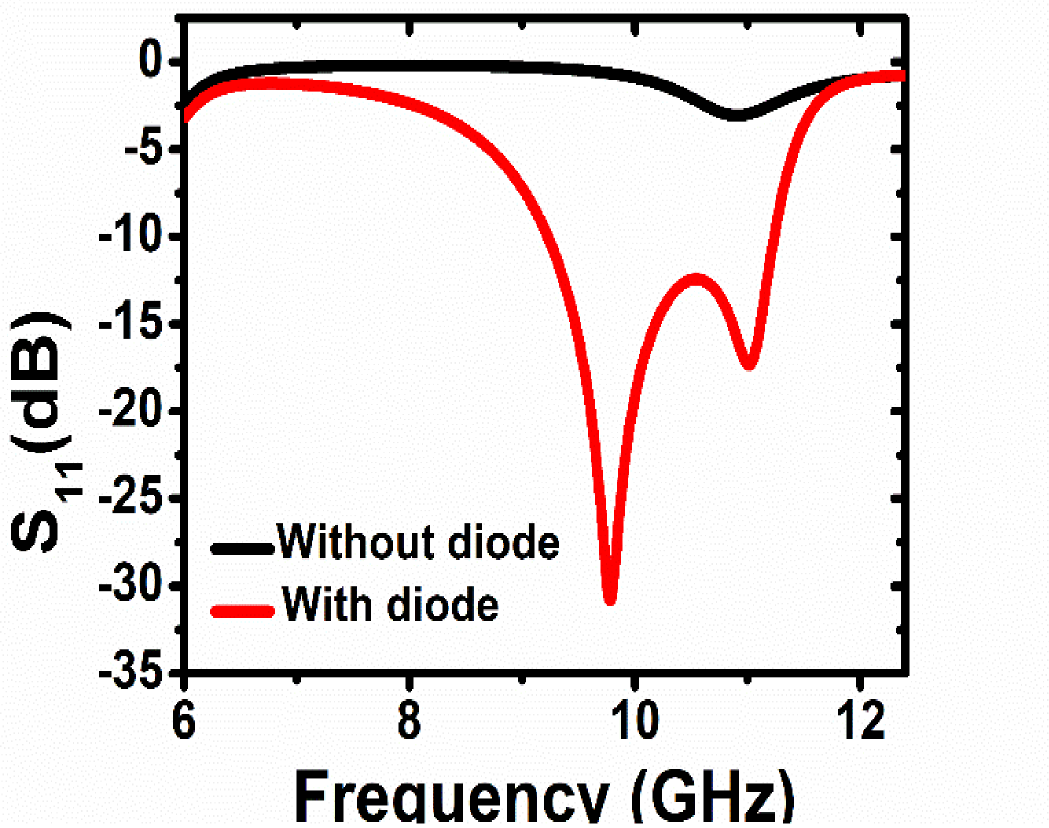

Figure 4.9. Simulated RC spectra of AFSS loaded absorber with diode and without diode.

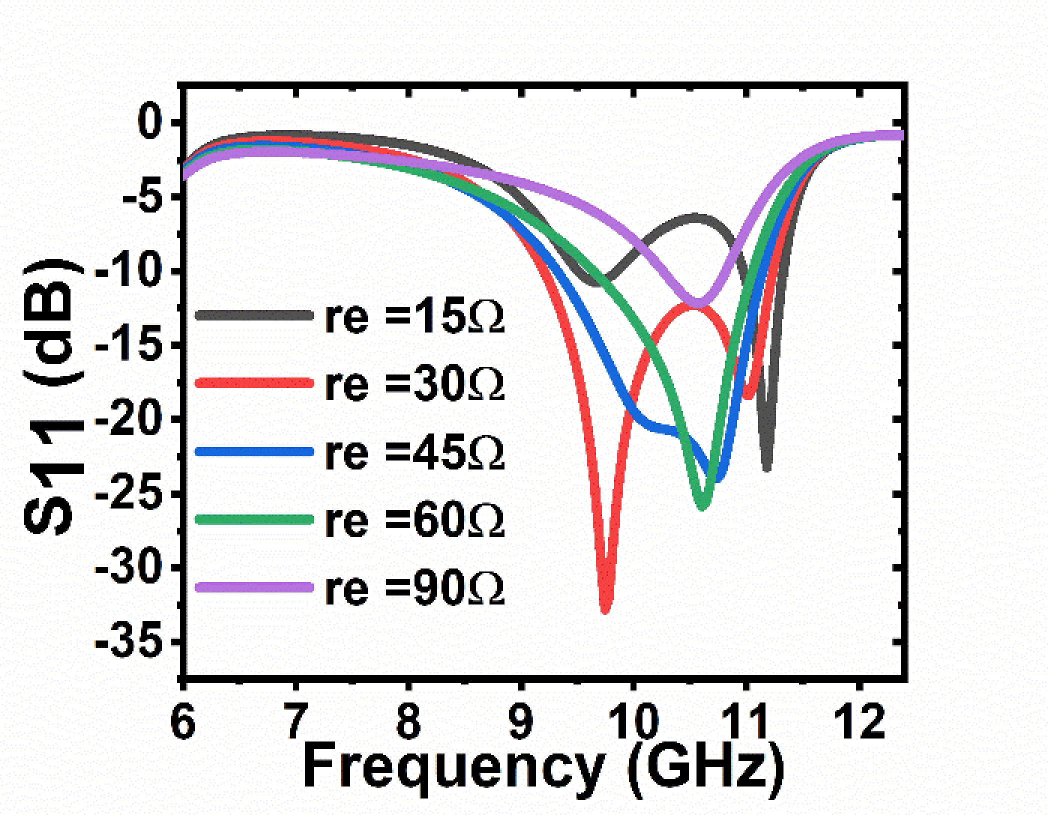

Figure 4.10. Simulated RC spectra of AFSS loaded absorber with different values of resistance.

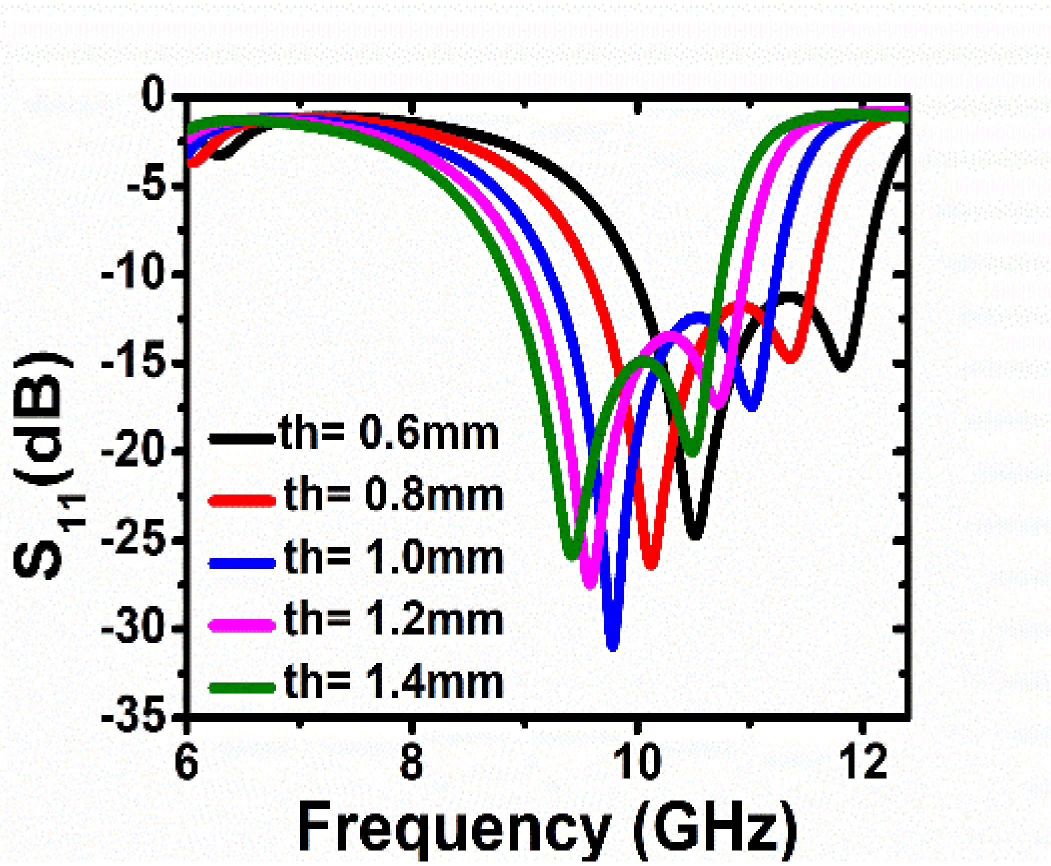

0
-5
-10
-15
-20
-25
-30
-35
6
8
10
12
S_{11}(dB)
Frequency (GHz)
th= 0.6mm
th= 0.8mm
th= 1.0mm
th= 1.2mm
th= 1.4mm

(a)

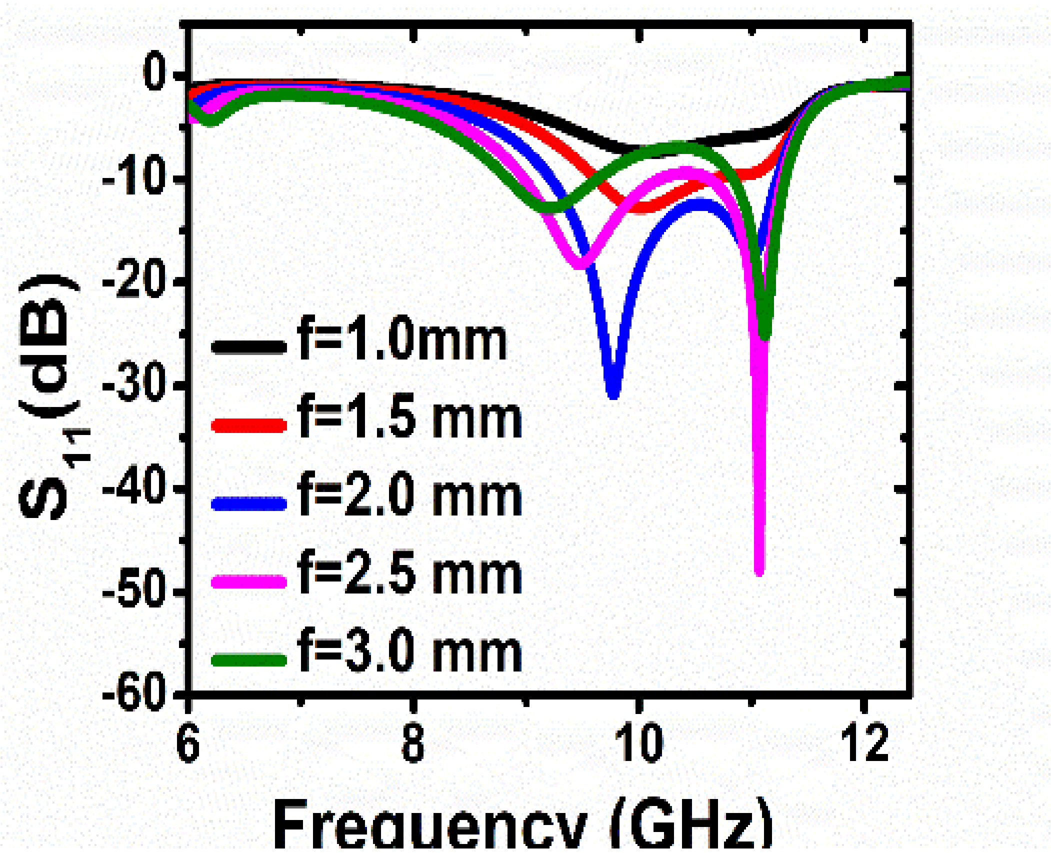

0
-10
-20
-30
-40
-50
-60
6
8
10
12
S_{11}(dB)
Frequency (GHz)
f=1.0mm
f=1.5 mm
f=2.0 mm
f=2.5 mm
f=3.0 mm

(b)

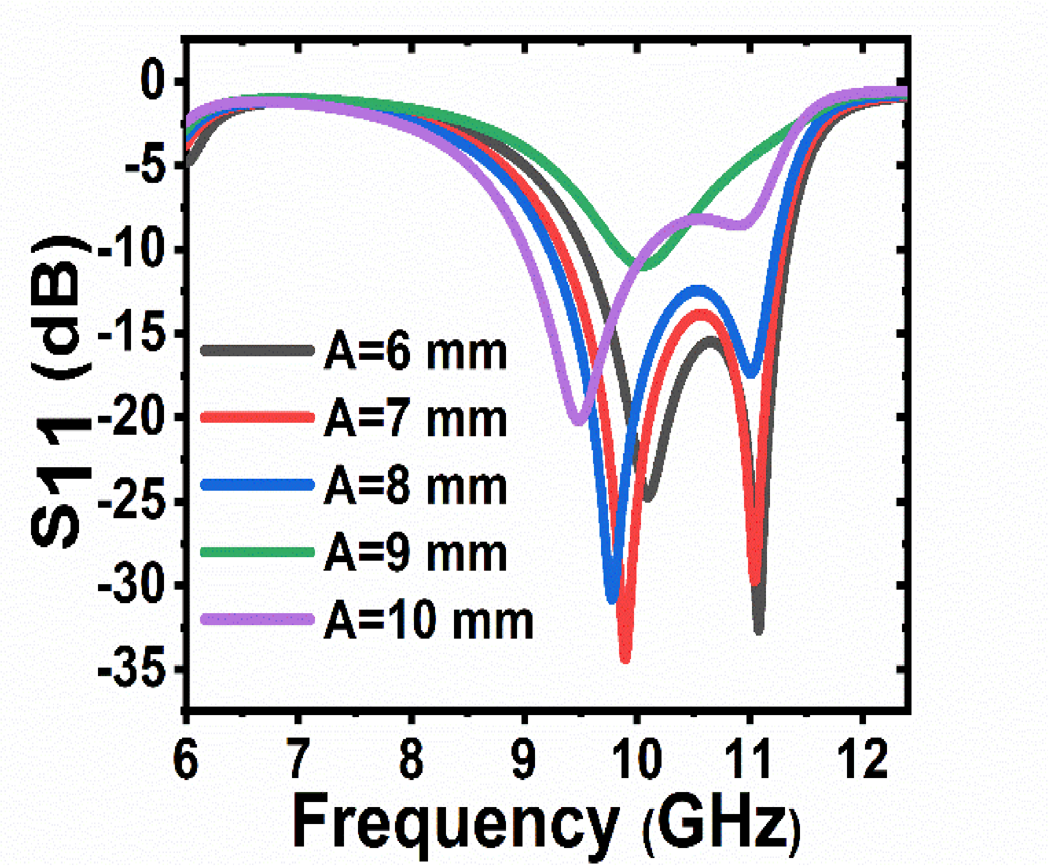

(c)

Figure 4.11. Effect of design variables (a) thickness of the substrate (th), (b) width of feeding line (f), and (c) air gap (A).

The first study is performed to examine the effect of substrate thickness (th) on the absorption properties of AFSS loaded tunable absorber as shown in Figure 4.11 (a). This parameter is varied from 0.6 mm to 1.4 mm with a step size of 0.2 mm. Interestingly, as the value of thickness increases, the resonant frequency shifts towards lower frequency. Also, the value of RC reaches below -10 dB with a corresponding increment in the value of substrate thickness. Next, the width of the feed 'f' is varied from 1.0 mm to 3.0 mm with a step size of 1.0 mm.A wide absorption bandwidth is noticed for an optimal feed width of 2.0 mm, as shown in Figure 4.11 (b). The effect of the air gap on AFSS is portrayed in Figure 4.11 (c). 'A' variable is ranging from 6 to 10mm with a 1.0 mm gap in-between. The broad bandwidth is obtained with 'A'= 8 mm. The bandwidth is reduced, as the value of 'A' goes high or low beyond the optimal value of 'A'. Furthermore, the frequency-dependent normalized impedance values of the proposed structure are extracted, to explicate the primary condition of an absorber. The value of the real part is almost equal to 1, whereas the imaginary part is nearly equal to zero from 9.2 to 11.2 GHz as illustrated in Figure 4.12. The maximum absorption is acquired in a similar frequency range, which proves the absorption mechanism with impedance matching. To examine the physical insight behind the absorption of AFSS, surface current distribution plots are illuminated in Figure 4.13. As evident from Figure 4.13 (a) the maximum surface Current is distributed around the horizontal lines of the 'G' shaped structure along with the biasing line. While at 11.0 GHz, the surface current is distributed similarly as shown in Figure 4.13 (a) together with, at the corners of the biasing line as illustrated in Figure 4.13 (b). Similarly E field distribution is illustrated in Figures 4.14 (a) and (b) at 9.7 and 11.0 GHz. At 9.7 GHz maximum E field is distributed upon the biasing line, whereas some E field distribution is also observed on the horizontal lines of the 'G' shaped structure. Howbeit, at the higher resonant frequency, i.e., 11.0 GHz, the E field distribution is more on the horizontal lines of the 'G' shaped structure as shown in 4.14 (b).

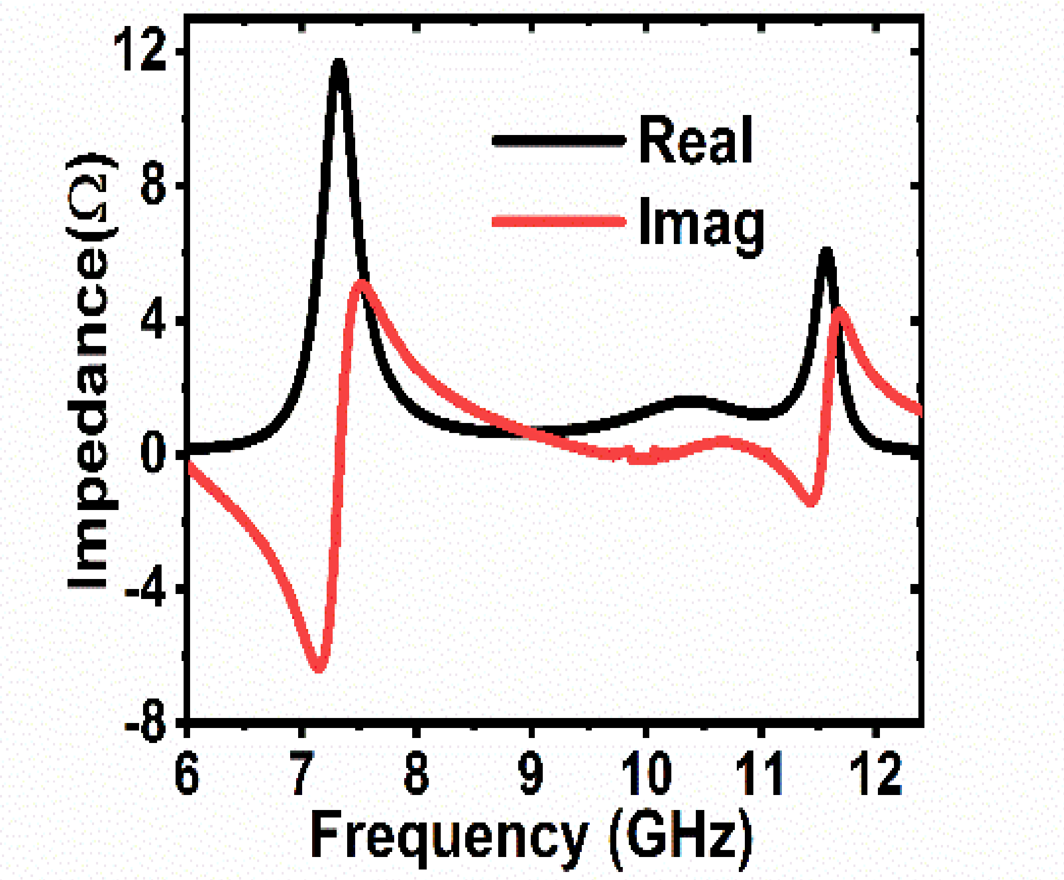

Figure 4.12. Frequency-dependent normalized impedance of AFSS loaded absorber with a resistance value of 30 Ω.

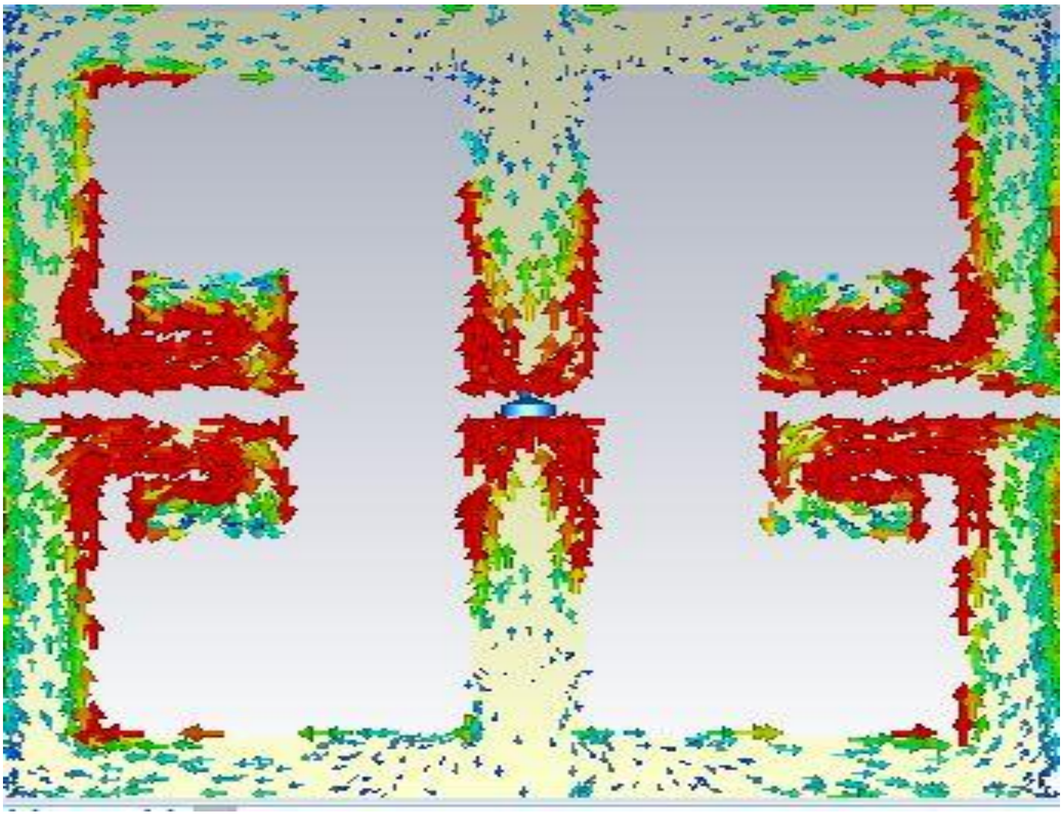

(a)

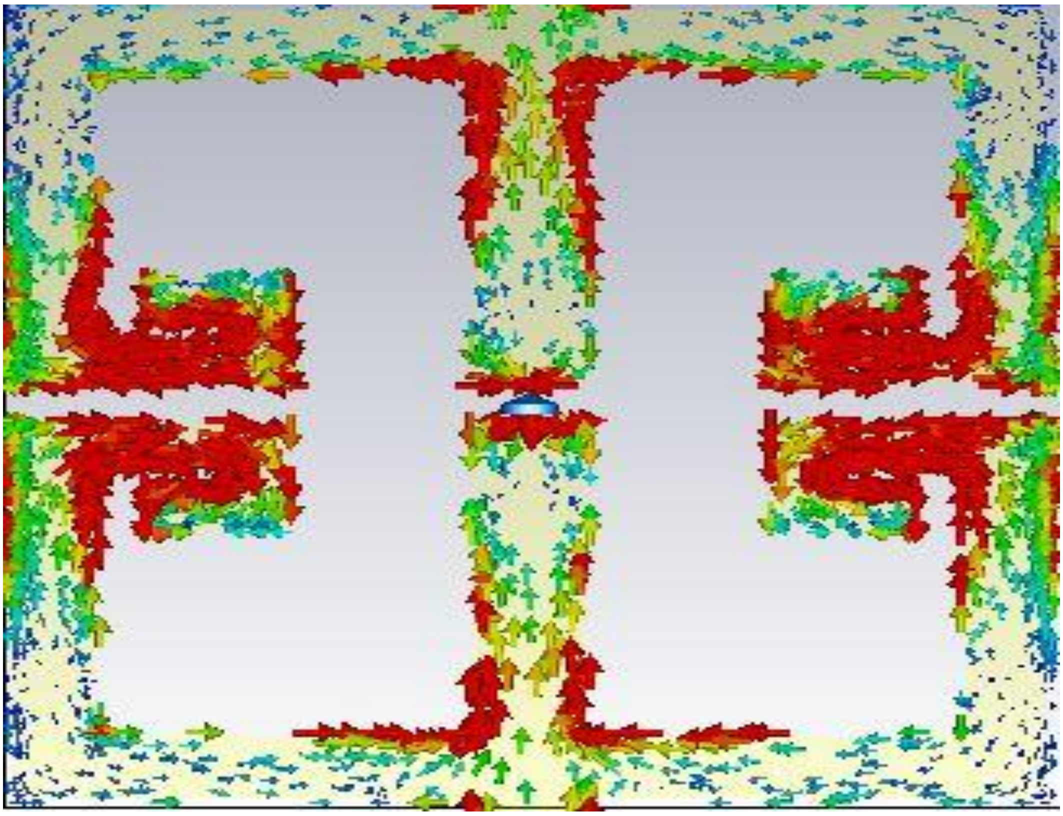

(b)

Figure 4.13. Surface current distribution at absorption frequencies (a) 9.7 GHz, and (b) 11.0 GHz.

Identically, H filed distribution is also manifested in Figures 4.15 (a) and (b) for both resonating peaks. After analyzing the results it has been observed that H field distribution is similar to the surface current distribution at both resonating peaks.At the resonant frequencies, high absorption has been observed, because with the top metallic patch the electrical resonance is coupled and the surface current makes the circulating loops around the incident magnetic field, therefore creating strong magnetic resonance.

4.2.3 FABRICATION AND EXPERIMENTAL VERIFICATION

To validate the simulated results, AFSS loaded tunable radar wave absorber with dimensions of 200 × 200 mm^2 has been fabricated using a standard PCB method. The proposed structure contains an array of 10 × 10 AFSS unit cells loaded with an equal number of PIN diodes (BAP 70-03) using the hand-soldering technique. The fabricated sample and it’s enlarging view are presented in Figure 4.16 (a). Figure 4.16 (b) depicts the non-destructive free space measurement setup utilized for the performance evaluation of the fabricated prototype. The measurement setup consists of a pair of broadband horn antennas connected to a vector network analyzer (Keysight VNA E5063A). To achieve tunability, an external voltage has been provided with the help of a DC power source, and the performance evaluation of the fabricated structure was carried out in an anechoic chamber. The fabricated prototype has been kept in front of the transmitting and receiving antennas, satisfying the far-field condition in the anechoic chamber. A detailed description of the aforementioned experimental measurement setup and procedure is provided in [73] and is not repeated here for conciseness. The absorption capability of the sample has been measured based on frequency-dependent minimum reflection coefficient values. Figure 4.17 (a) illustrates the measured RC of the proposed absorber for different values of bias voltages. The remarkable 3.0 GHz bandwidth with a resonating peak at 8 GHz has been obtained in on state. While in the off state, absorption bandwidth of 1.8 GHz has been perceived with a resonating peak at 6.8 GHz. The measured RC characteristics with different values of bias voltage are illuminated in Figure 4.17 (b). It can be observed that as the biasing voltage increases, the resonating frequency shifts towards lower frequency.

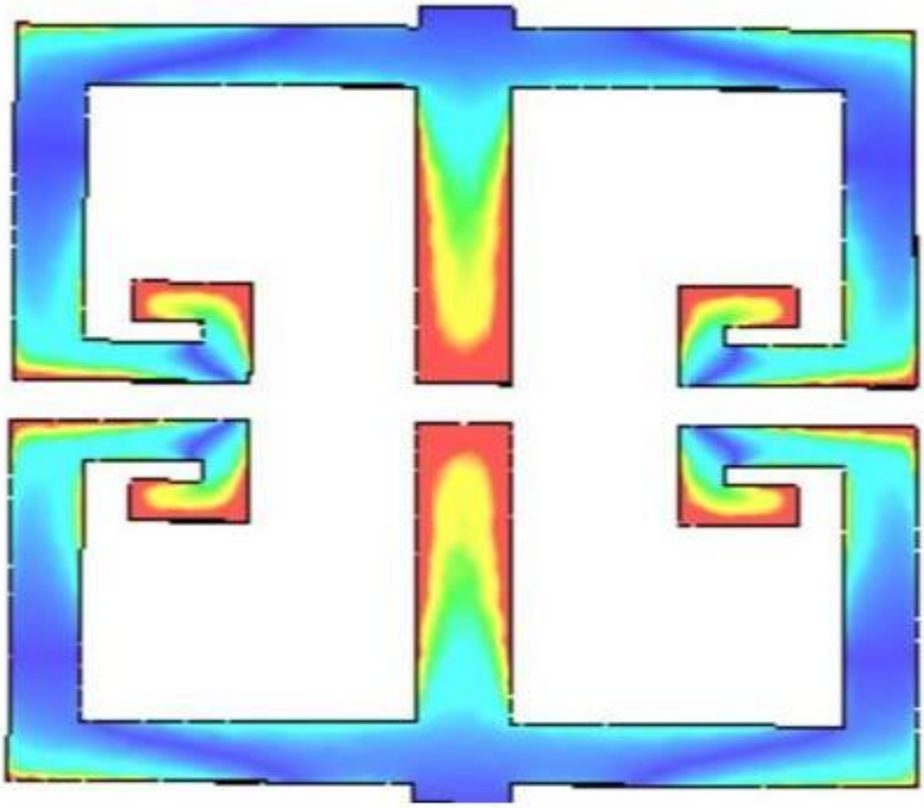

(a)

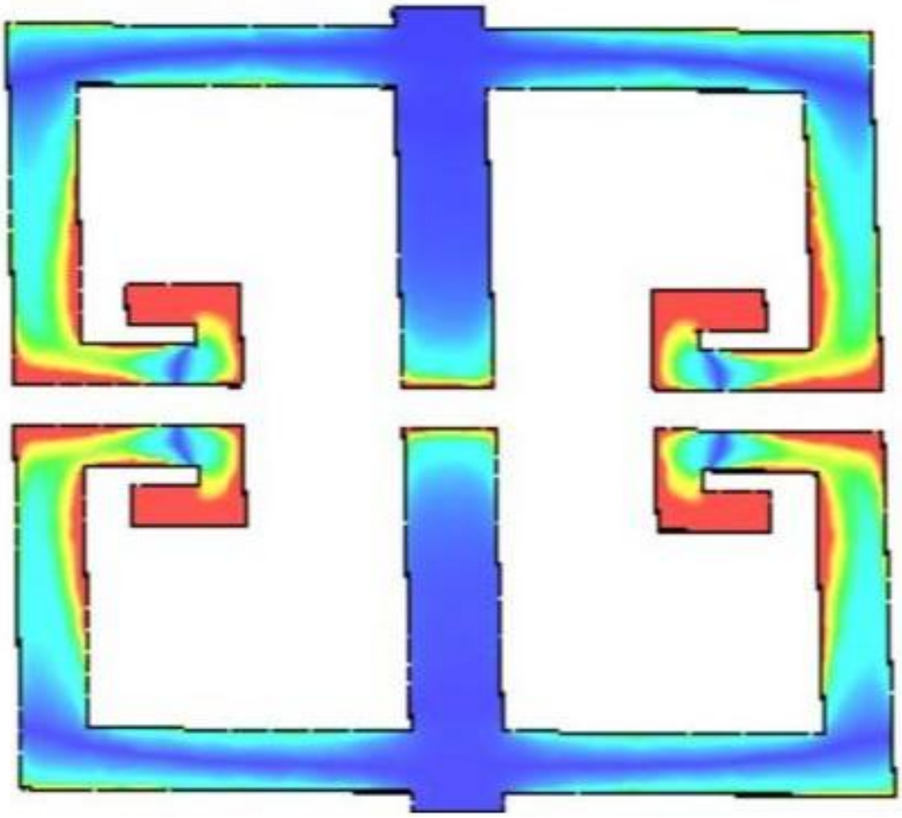

(b)

Figure 4.14. E field distribution at absorption frequencies (a) 9.7 GHz, and (b) 11.0 GHz.

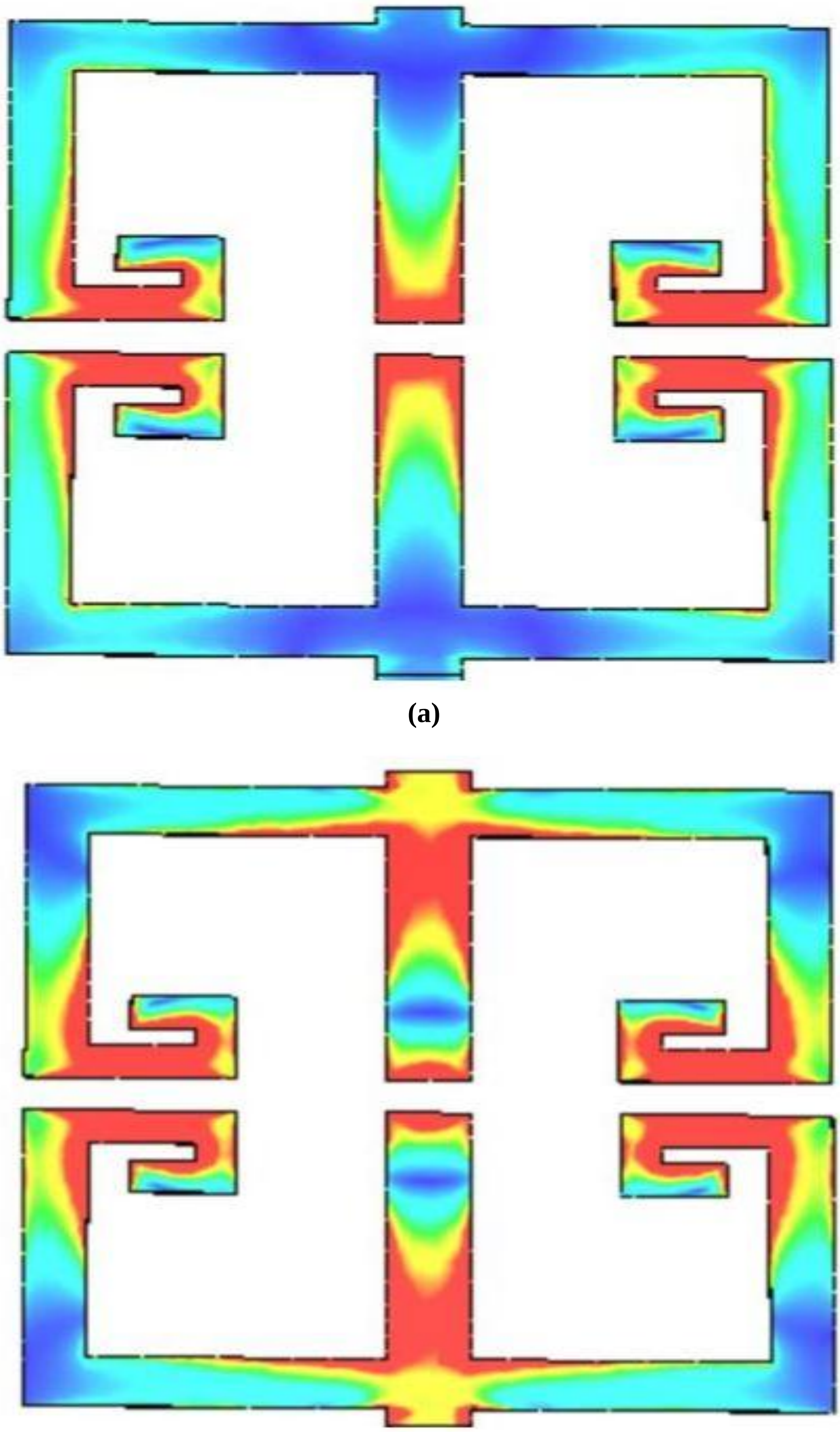

(a)

(b)

Figure 4.15. H field distribution at absorption frequencies (a) 9.7 GHz, and (b) 11.0 GHz.

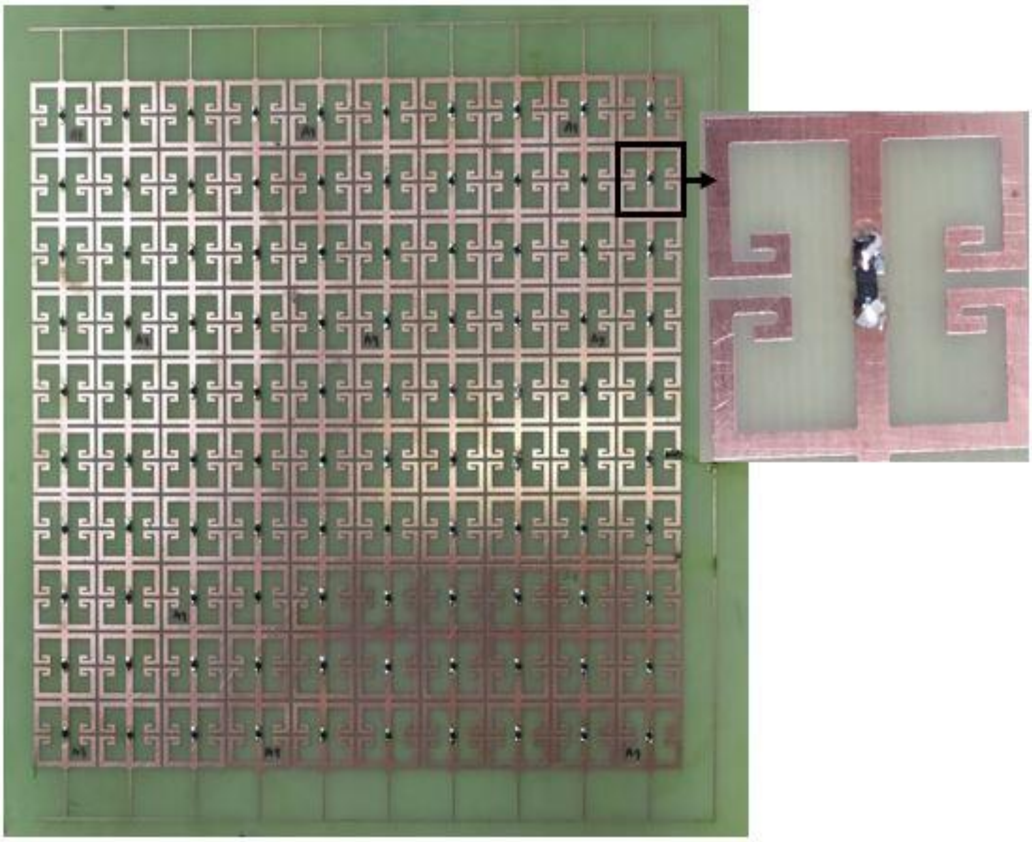

(a)

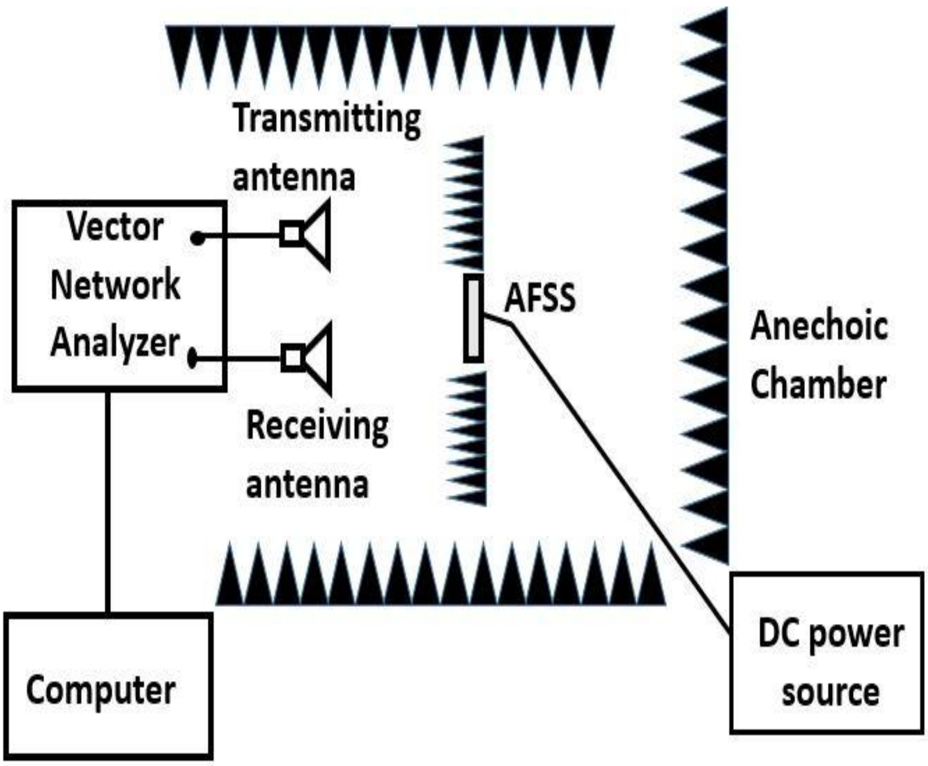

(b)

Figure 4.16 (a) Fabricated prototype of AFSS loaded absorber and (b) Free-space microwave measurement setup.

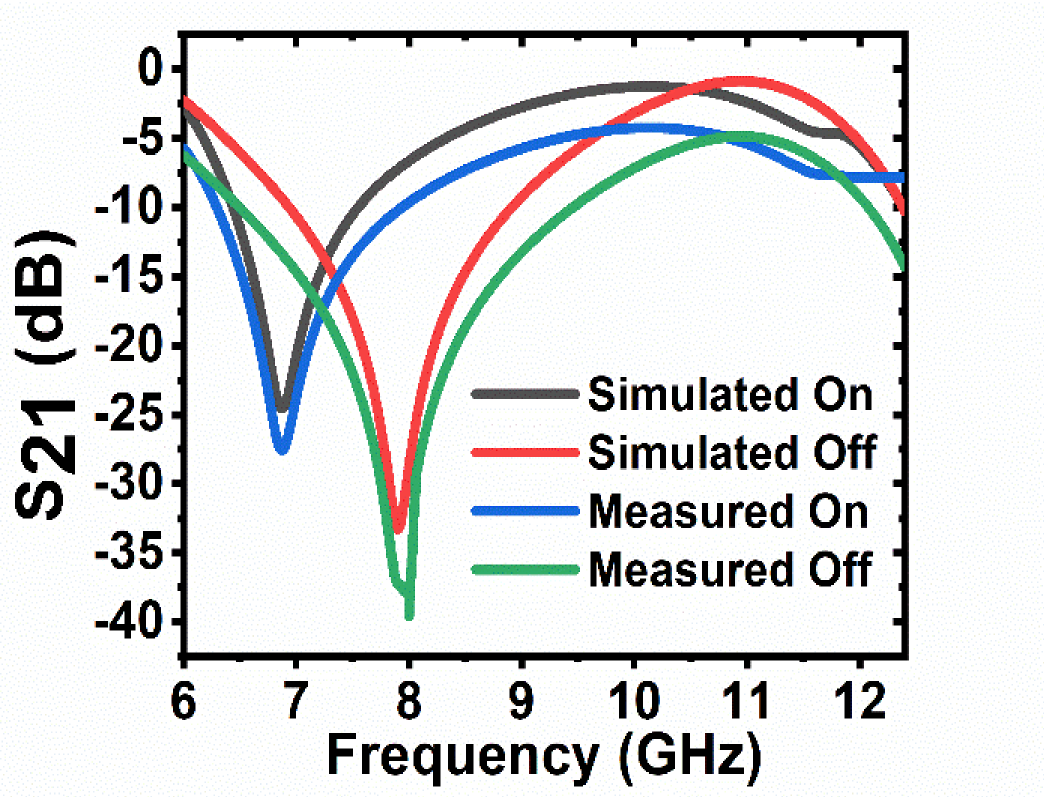

(a)

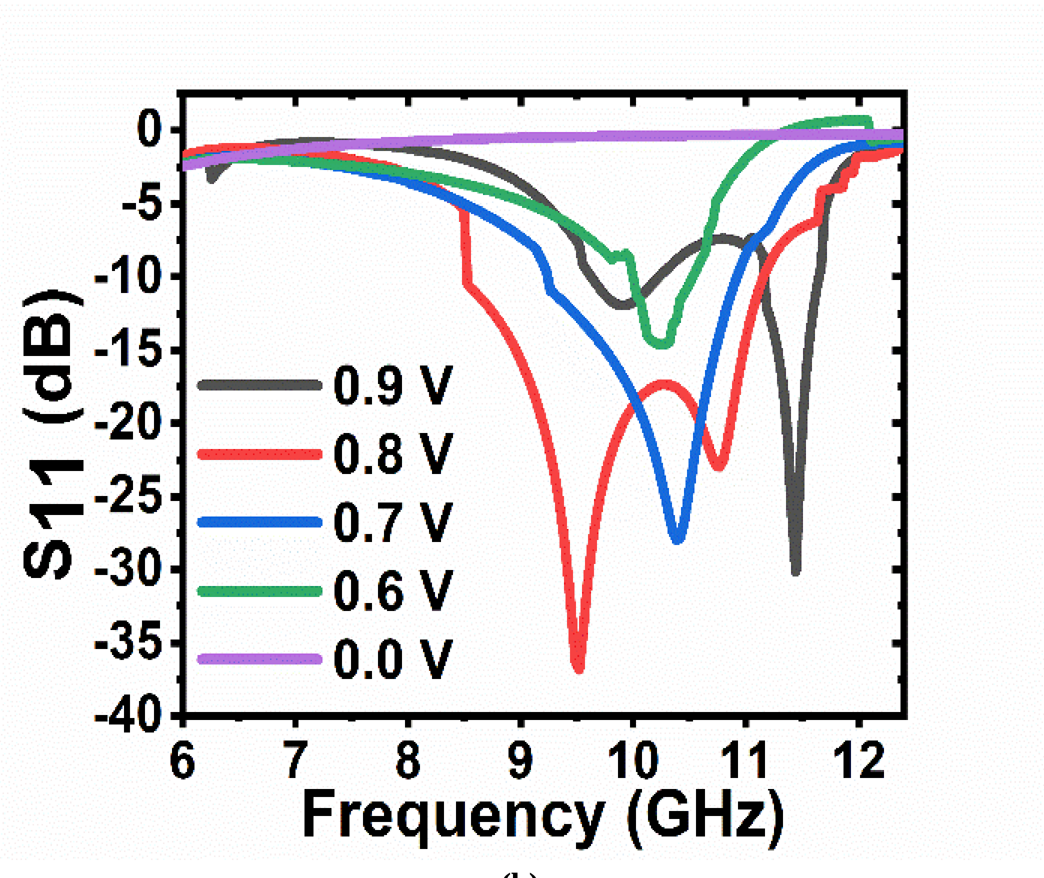

(b)

Figure 4.17. (a) Measured transmission coefficient spectra in on and off states and (b) Measured RC characteristics with different values of bias voltage.

A 0.82 V of biasing voltage demonstrates the maximum bandwidth, whereas the minimum bandwidth has been observed at 0.67 V of biasing voltage. The measured results are well matched with simulated ones. The small discrepancies arise due to the fabrication tolerances like the soldering process and finite fabricated structure. It may also be because of the ohmic losses, parasitic inductance, and capacitance effect of p-i-n diode [23].

4.3 CONCLUSION

In this chapter, a single-layered, tunable, and wideband AFSS based absorber is presented, which demonstrates the tunability in the range of 9.2 GHz to 11.2 GHz. Whereas, AFSS structure demonstrates the tunable performance with 1.1 GHz and 2.0 GHz bandwidth in ON and OFF states, respectively. The p-i-n diode and unique biasing technique are used to obtain the tunability performance, which reduces the complexity. Further, an extensive study is performed on AFSS to know the effect of different variables on the TC response of FSS structure. A similar design of AFSS has been used to construct an efficient tunable microwave absorber, in which the maximum bandwidth with forward resistance of 30Ω has been achieved. Similarly, a critical analysis of the dimensions of AFSS loaded tunable absorber has been also presented. The surface current, E field, and H field distribution are also manifested to understand the absorption mechanism. The measured results from a fabricated prototype are in close agreement with the simulation, suggesting the effectiveness of the structure for actual electromagnetic applications.

CHAPTER 5

DEVELOPMENT OF A MM INSPIRED ANTENNA WITH LOW RCS

In this chapter, low RCS antennas are developed, which are based on MM techniques. The first one is MM inspired antenna and the second one is flexible MM-based superstrate coupled MPA, which enhances the gain along with RCSR of the MPA. To evaluate the optimized values of the distinct dimensions, parametric studies have been performed on both the structures. Finally, the proposed prototypes have been fabricated to evaluate the measured results. The performance evaluation of the fabricated antennas has been carried out using a microwave measurement setup. A comparison between proposed structures with other reported works is also presented in this chapter.

5.1 MOTIVATION AND INTRODUCTION

RCSR has been extensively studied by researchers, for military tactics [48], [73]. LO technology or stealth technology is one of the parts of military tactics. LO technology concept is based on making sensitive targets like airborne vehicles and naval ships invisible to different detection devices such as sonar, radar, etc. In stealth technology, antenna plays the dominant role, as it is a part of the communication system, which transmit and receive EM wave. Therefore, it is to say that the stealth property could be reduced because of the high RCS of an antenna. That means, it is mandatory to reduce the RCS of an antenna. Mainly, there are two methods to reduce RCS, first one is the shaping technique, in which the target configuration is modified for reduction and the other is the application of RAM [90]. Recently, another method has been reported to reduce the RCS, by using MM structures and FSS [91-94] [53]. MM is an artificial composite structure, which shows remarkable property like a negative index of refraction, which is not found in natural materials [95-96].Many other ways have been also reported to reduce RCS from the last few years, such as AMC [58], [60], [97] and EBG [98-99], [69]. MM can also be used to reduce the mutual coupling between antenna elements of MIMO systems [100]. Several pioneer research studies on low RCS and high gain antennas have been carried out by researchers worldwide, but the simultaneous achievement of low RCS and high gain antenna is a difficult task. Therefore, it is of great importance to identify an efficient approach to resolve the aforementioned issue. In this direction, an effort has been made to couple a new MM superstrate to MPA for the broadband RCS reduction and gain improvement.

5.2 MM INSPIRED ANTENNA

An efficient approach is presented, to reduce RCS of MPA, without affecting other radiation characteristics by the application of a novel hybrid MM structure. The MPA is designed to operate at 4.2 GHz. Three different configurations of MM structures (i.e., CB_1, CB_2, and hybrid) with splitted square and ring-shaped two non- identical MM cells are designed and critically analyzed in the range of 2 GHz to 18 GHz. A hybrid MM configuration is chosen for the design and implementation of a low RCS antenna due to its exceptional performance as compared to CB_1 and CB_2. The hybrid MM is organized in chessboard configuration, comprised of splitted square and ring-shaped MM unit cells. The results show that the proposed antenna gives substantially out of band RCSR from 6 GHz to 18 GHz and the proposed antenna has a lower RCS than the reference antenna. The proposed antenna attains wideband bandwidth around 7.4 GHz (ranging 2.0 GHz to 4.4 GHz, 7.8 GHz to 9.1 GHz, and 14.3 GHz to 18 GHz). The maximum reduction of -30.1 dB at 16.4 GHz is achieved in the hybrid MM structure impinged MPA. Finally, the fabrication and performance evaluation of MM loaded antenna is carried out. Moreover, the measured results of the fabricated samples are closely matched with simulated results, which proves the effectiveness of the adopted approach for practical applications.

5.2.1 DESIGN OF MM INSPIRED ANTENNA

This section presents and discusses the design of MM unit cell, design of reference, and proposed antennas. Different MM configurations are analyzed and results are discussed to choose the best configuration.

5.2.1.1 DESIGN AND SIMULATED RESULTS OF MM UNIT CELL

The front view of the unit cell of MM#1 and MM#2 is shown in Figures 5.1(a) and (b). MM#1 and MM#2 are made up of a conductor backed by a grounded dielectric substrate. A 2.0 mm thick FR4 material (relative permittivity, ε_r=4.3, and dielectric loss tangent, tan δ= 0.025) has been chosen as a dielectric substrate material. Table 5.1 presents the optimal design variables of the proposed MM unit cells. MM#1 consists of a splitted square, whereas MM#2 is made up of a splitted ring geometry. In

Figure 5.1, the black color represents the copper layer, while the white portion represents the dielectric substrate. One step further, the surface current distribution of the MM#1 and MM#2 is shown in Figures 5.2 (a) and (b).

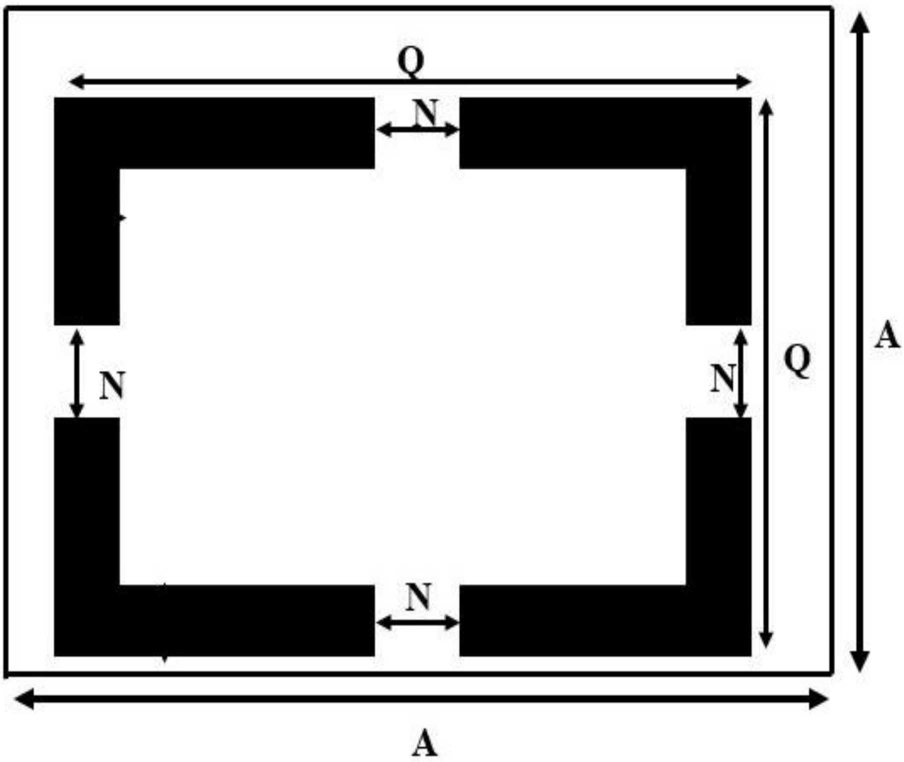

(a)

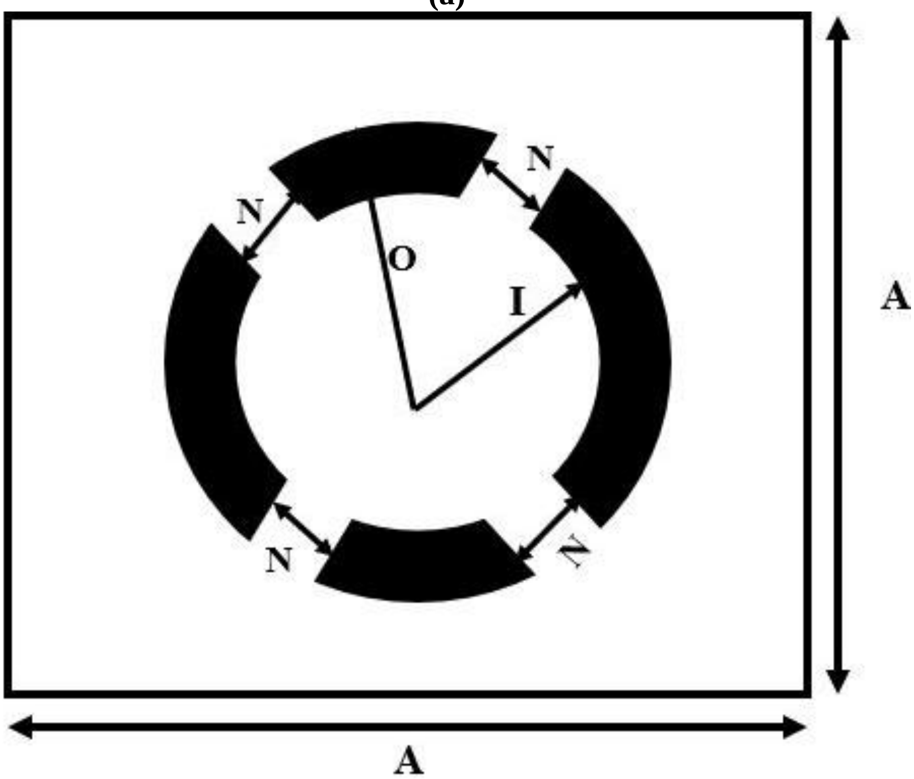

(b)

Figure 5.1. Front view of the proposed unit cell (a) MM#1 (b) MM#2.

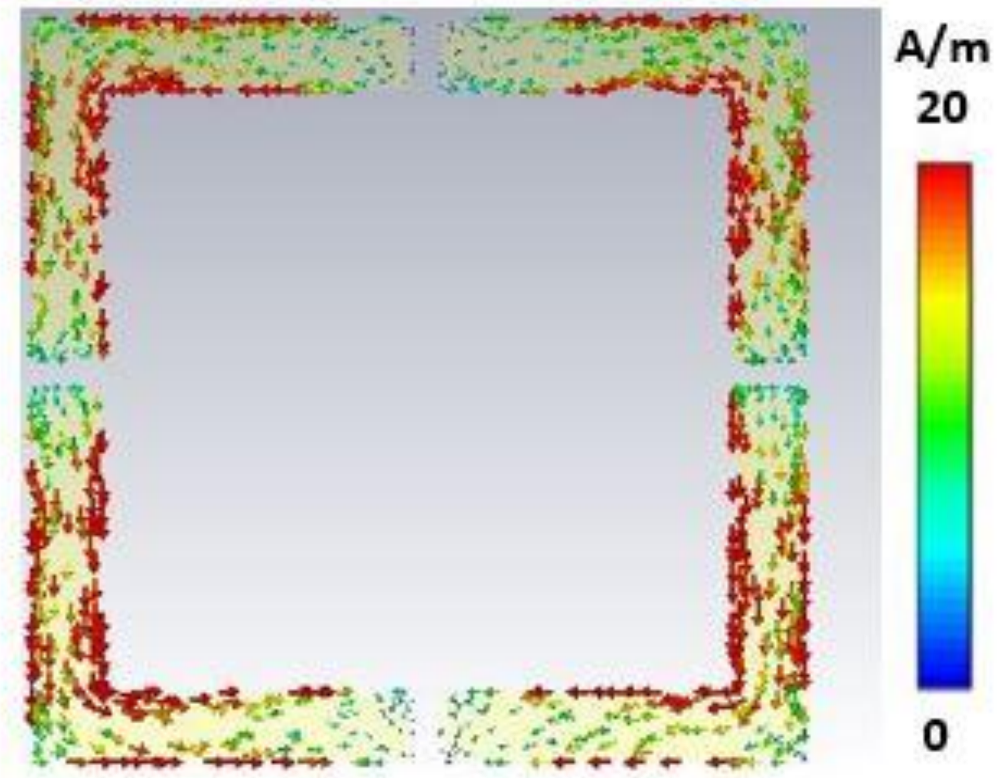

(a)

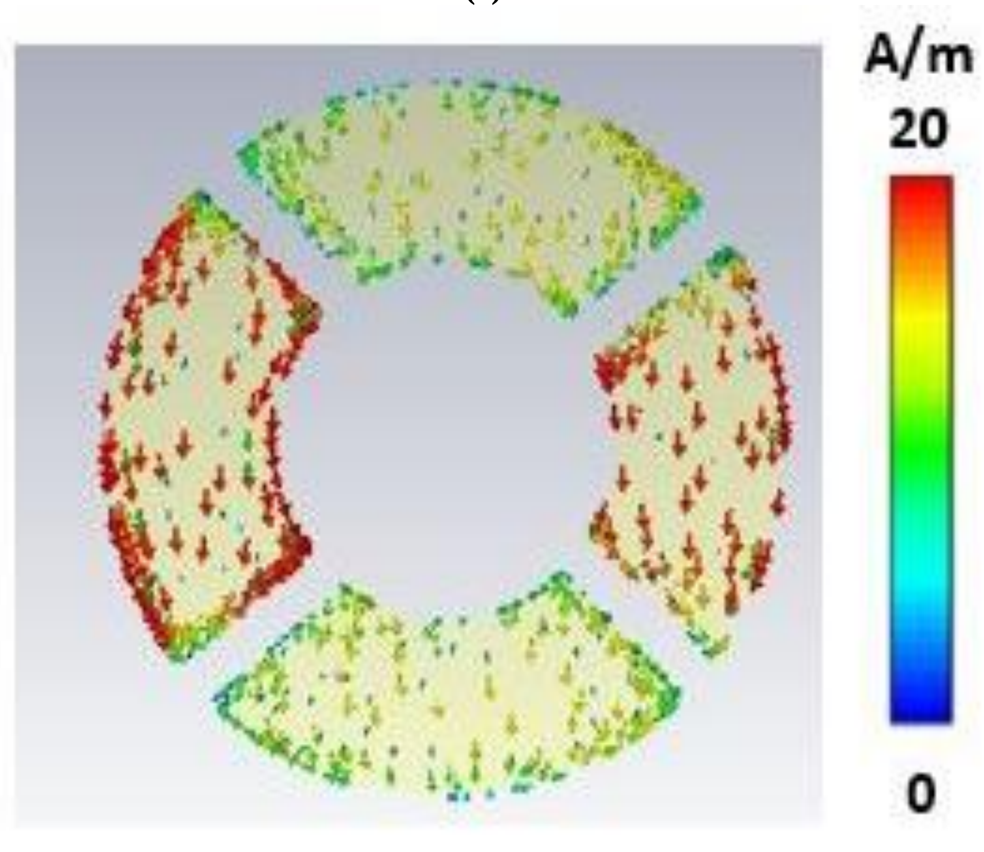

(b)

Figure 5.2. Surface current of unit cell (a) MM#1 (b) MM#2.

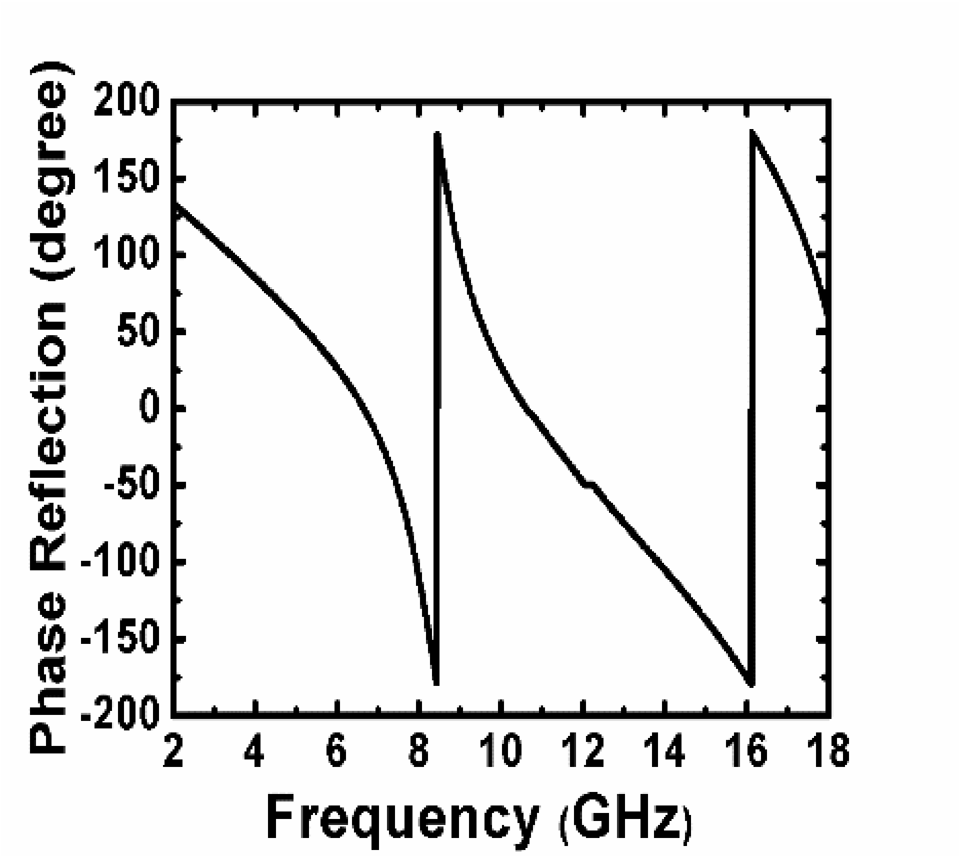

(a)

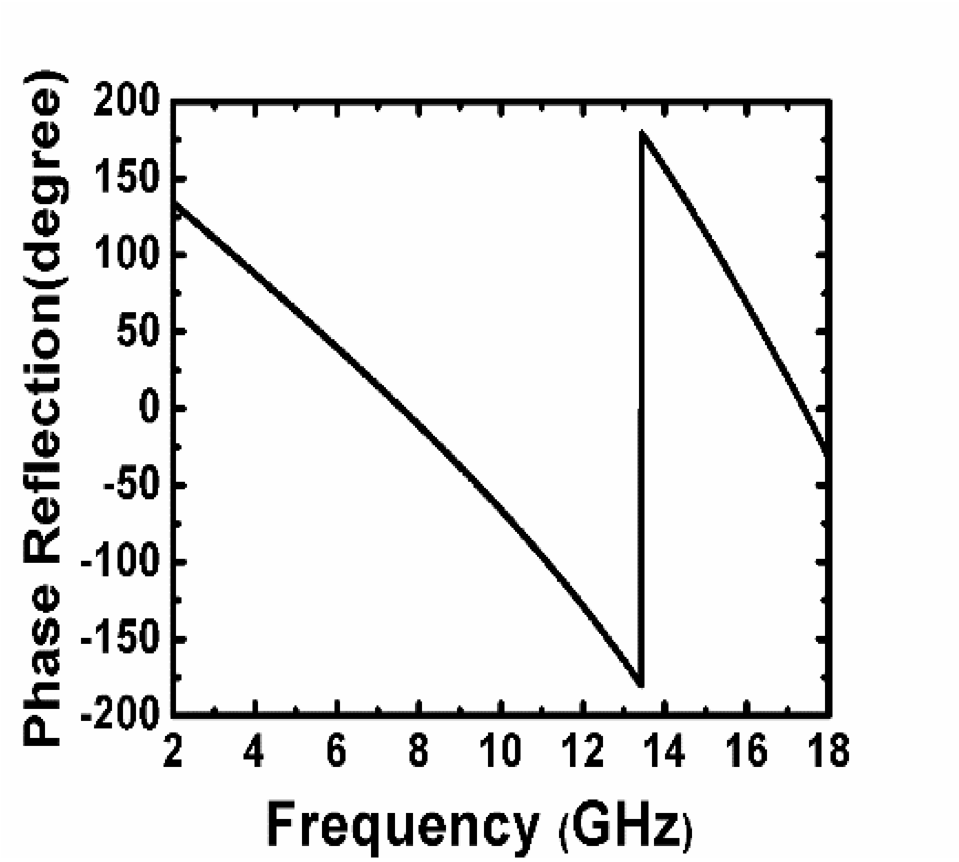

(b)

Figure 5.3. Phase reflection of unit cell (a) MM#1 (b) MM#2.

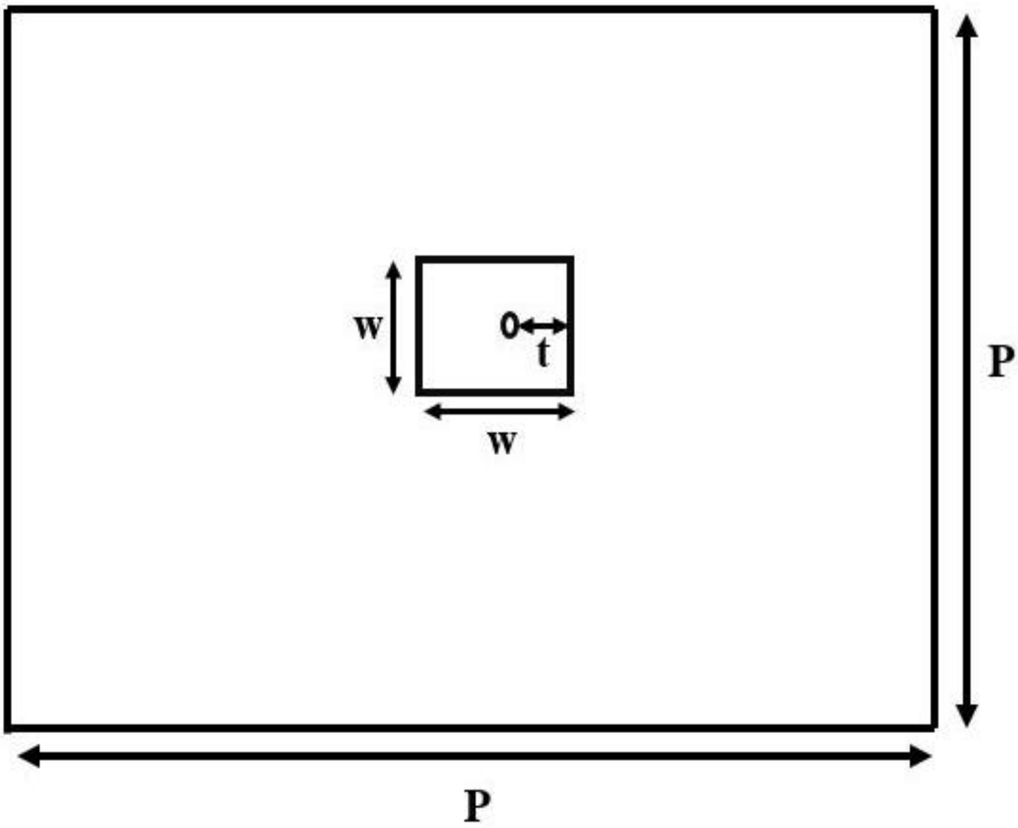

(a)

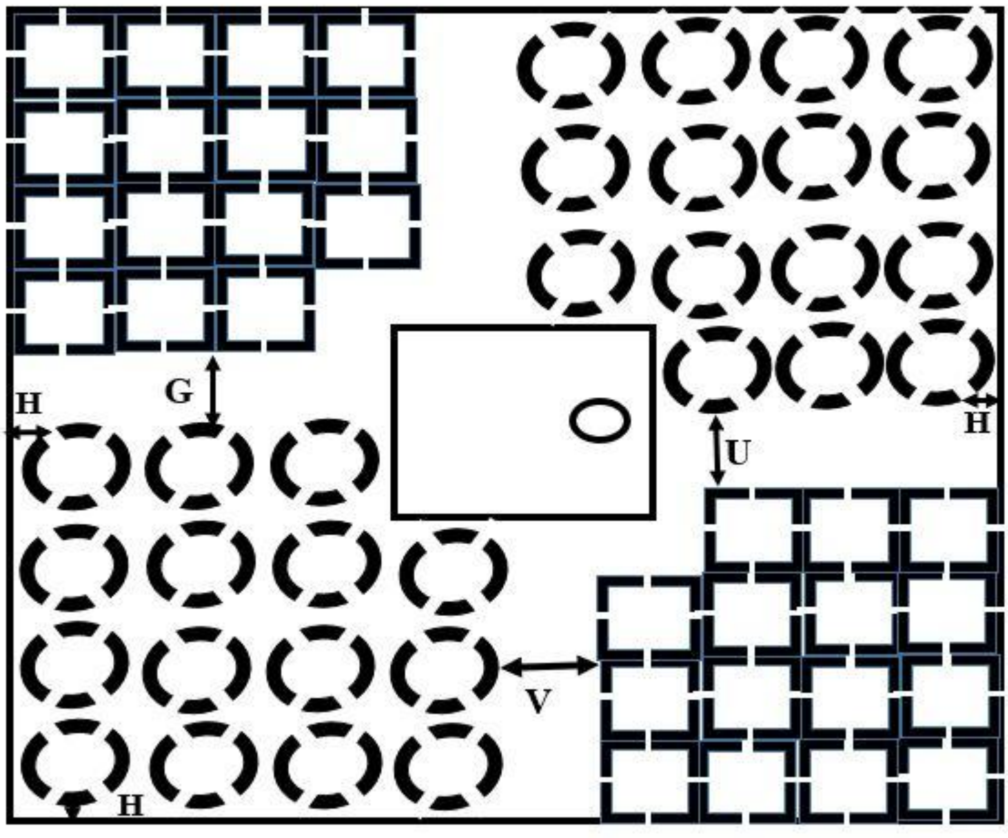

(b)

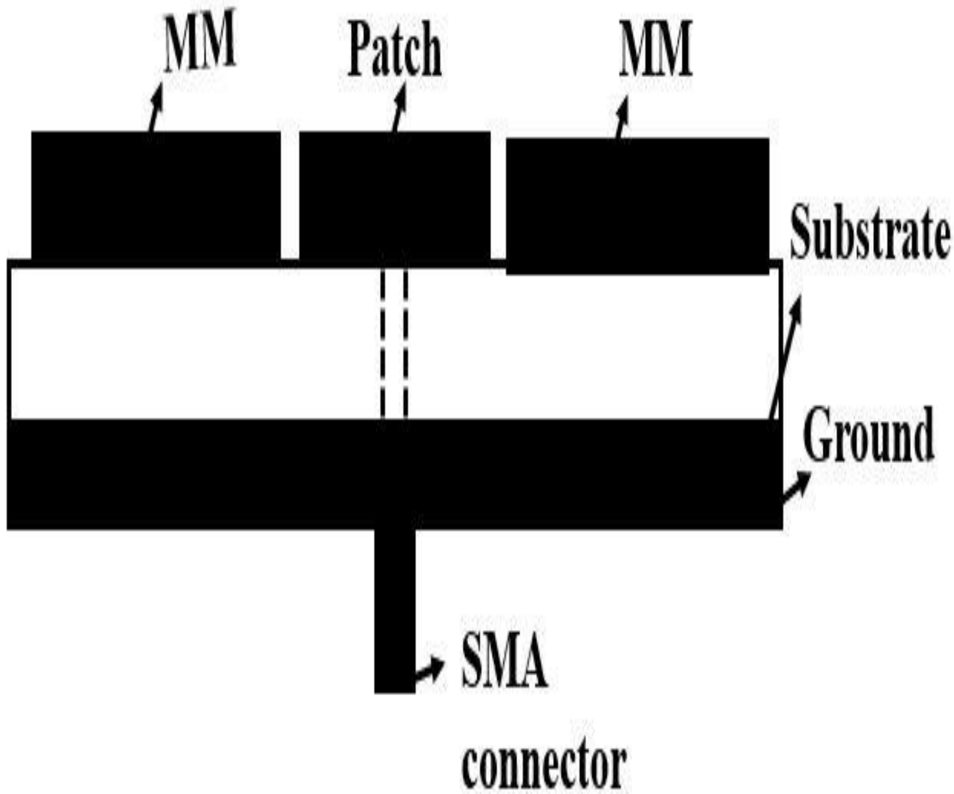

(c)

Figure 5.4. Configurations of (a) reference antenna (b) hybrid MM loaded antenna (c) side view of the hybrid MM loaded antenna structure.

Table 5.1. Optimal design variables of the proposed MM unit cells.

Parameter	**Value (mm)**	**Parameter**	**Value(mm)**
A	9.5	N	0.4
D	0.8	O	2.5
I	1.3	Q	9.2

Figures 5.2 (a) and (b) shows that maximum current flows at the edges of the inner square in MM#1 and in MM#2 horizontal arms of split ring carry more current as compared to the vertical arms. The opposite current direction is observed on the MM layer and ground plane, which generates the magnetic flux and results in magnetic resonances. Therefore it is concluded that surface current distribution is directly proportional to the magnetic field intensity, which means in places where the maximum surface current distribution has been observed, the magnetic field intensity will be higher. However, the current density distribution and electric field intensity are inversely proportional to each other. CST Microwave Studio software has been used for the designing of these structures. Along with the x and y directions, the

periodic boundary conditions have been applied and the Floquet port has been used to electrify incident wave in the z-direction. The phase reflection versus frequency graph of MM#1 and MM#2 is shown in Figures 5.3(a) and (b). The phase reflection of MM#1 and MM#2 is in the range of $180^\circ \pm 30^\circ$ has been obtained in the range of 2 GHz to 18 GHz. Therefore, a good monostatic RCS reduction can be expected in this frequency range. To justify this behavior, the chessboard structure and the proposed hybrid structure with the same total dimension of 80 mm × 80 mm has been simulated.

5.2.1.2 DESIGN OF REFERENCE AND PROPOSED MPA

The configuration of the reference antenna with a dimension of 80×80 mm and the hybrid MM loaded antenna with the same dimension is shown in Figures 5.4 (a) and (b), respectively. MM cells are distributed around the radiating patch to achieve the low RCS of an antenna as depicted in Figure 5.4 (b). The operating frequency range of the reference antenna is 4.2 GHz. The side view of the hybrid MM loaded antenna is shown in Figure 5.4 (c). The design parameters of reference and MM impinged antennas are described in Table 5.2.

CB_1 and CB_2 configurations are also simulated to know the effect of the structure on the monostatic RCS. However, CB_1 and CB_2 surfaces differ in the shape of the unit cell and arrangement of unit cells, as shown in Figures 5.5 (a) and 5.5(b), while the other design parameters of CB_1 and CB_2 are the same with a hybrid antenna. Figure 5.5(c) illustrates the design of the hybrid MM structure. CB_1, CB_2, and hybrid configurations are compared with respect to bandwidth, resonant frequency, and monostatic RCS value as depicted in Table 5.3. At the resonant frequencies, a phase shift has been observed because of MM structure, which leads to a reduction of RCS. Compared to the hybrid structure, CB_1 and CB_2 are showing high RCS as manifested in Figure 5.6.

Table 5.2. Design parameter of proposed antennas.

Parameter	Value (mm)	Parameter	Value(mm)
P	80	G	5.0
W	15.6	V	4.5
T	4.0	U	6.5
H	2.5	Y	9.75

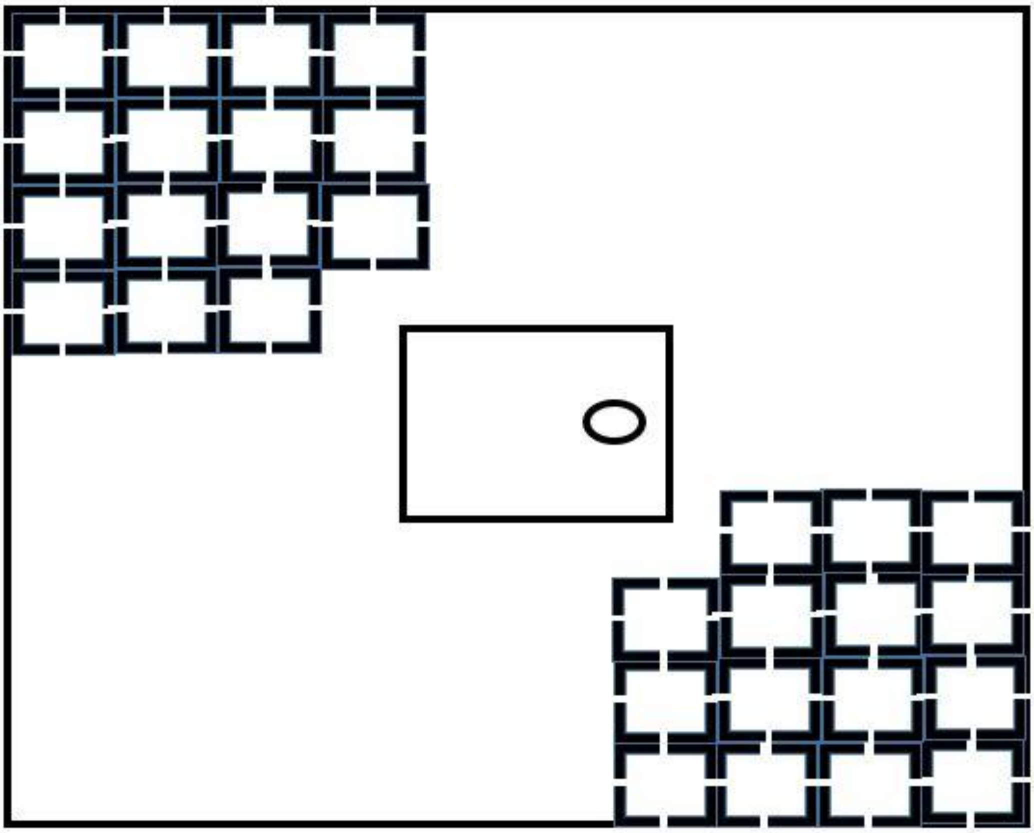

(a)

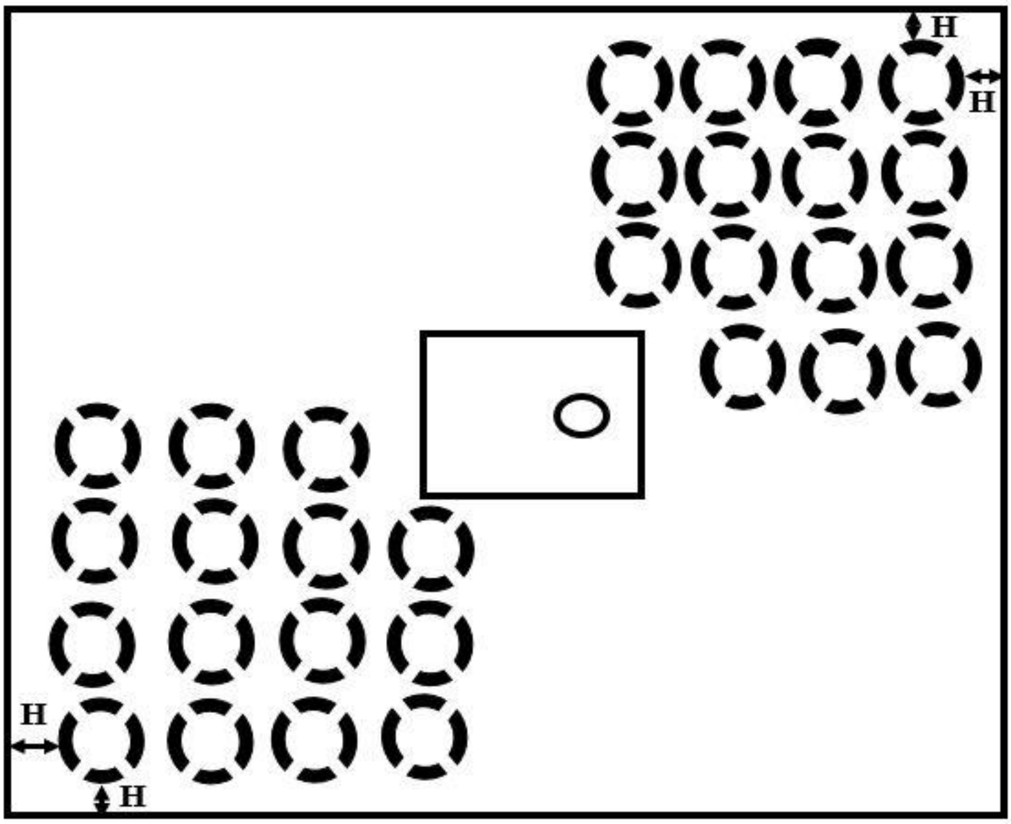

(b)

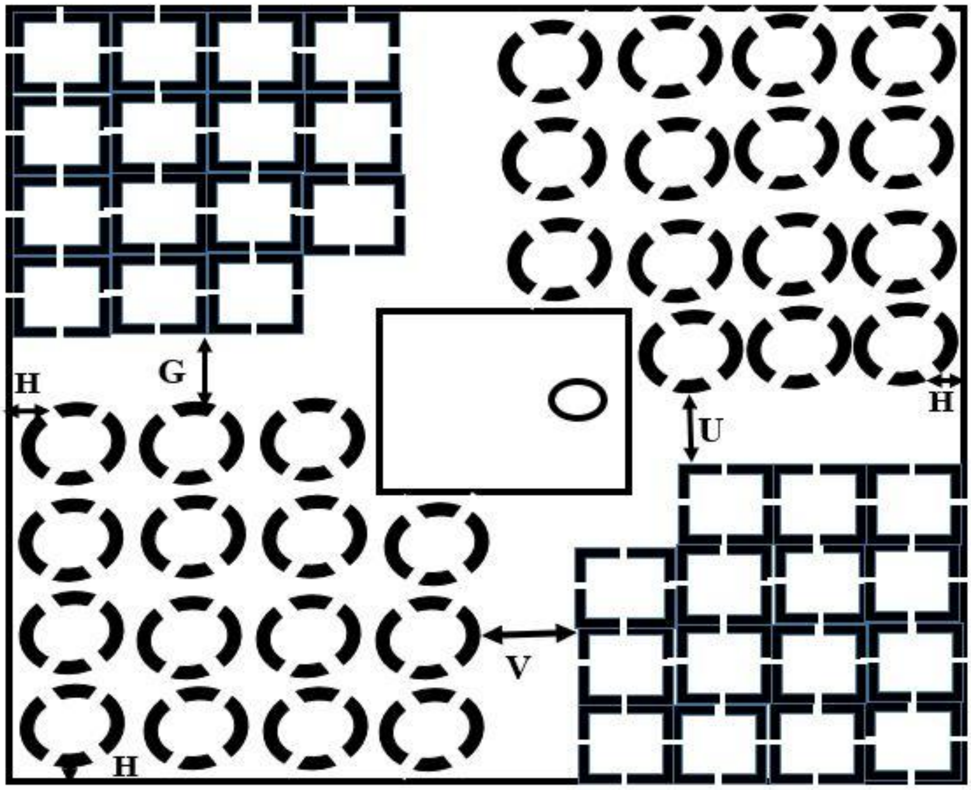

(c)

Figure 5.5. Configurations of (a) CB_1 (b) CB_2 and (c) hybrid MM geometry.

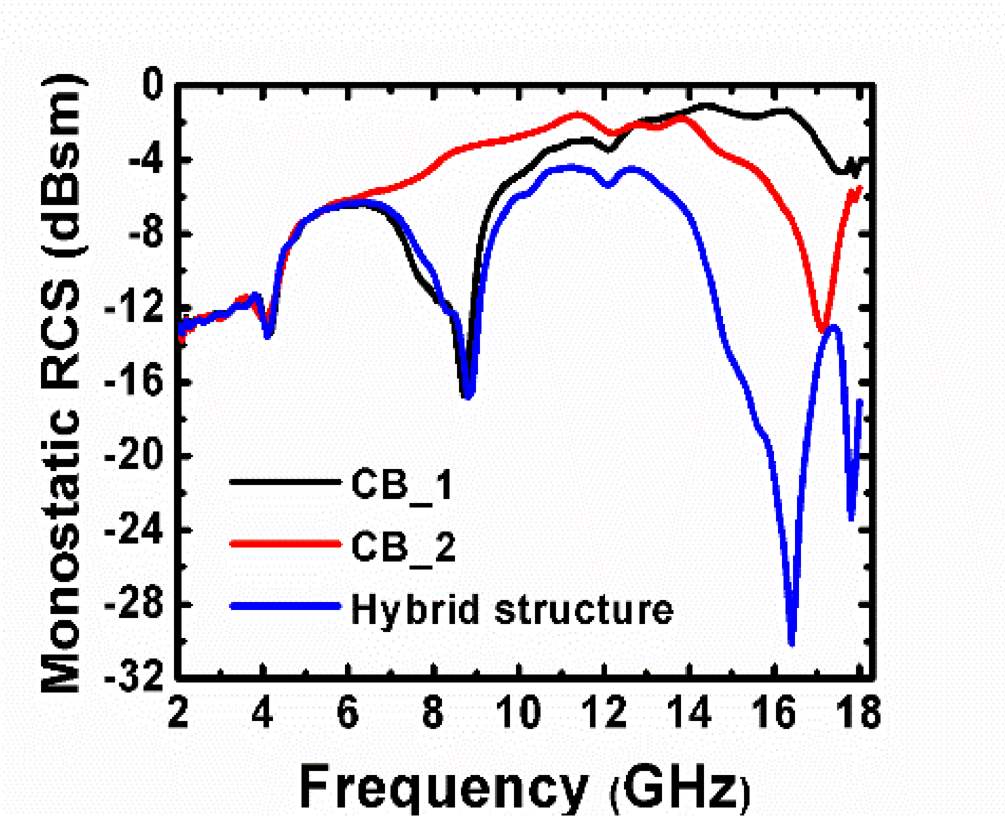

Figure 5.6. Comparison of proposed MM geometries (i.e., CB_1, CB_2, and hybrid) in terms of their monostatic RCS.

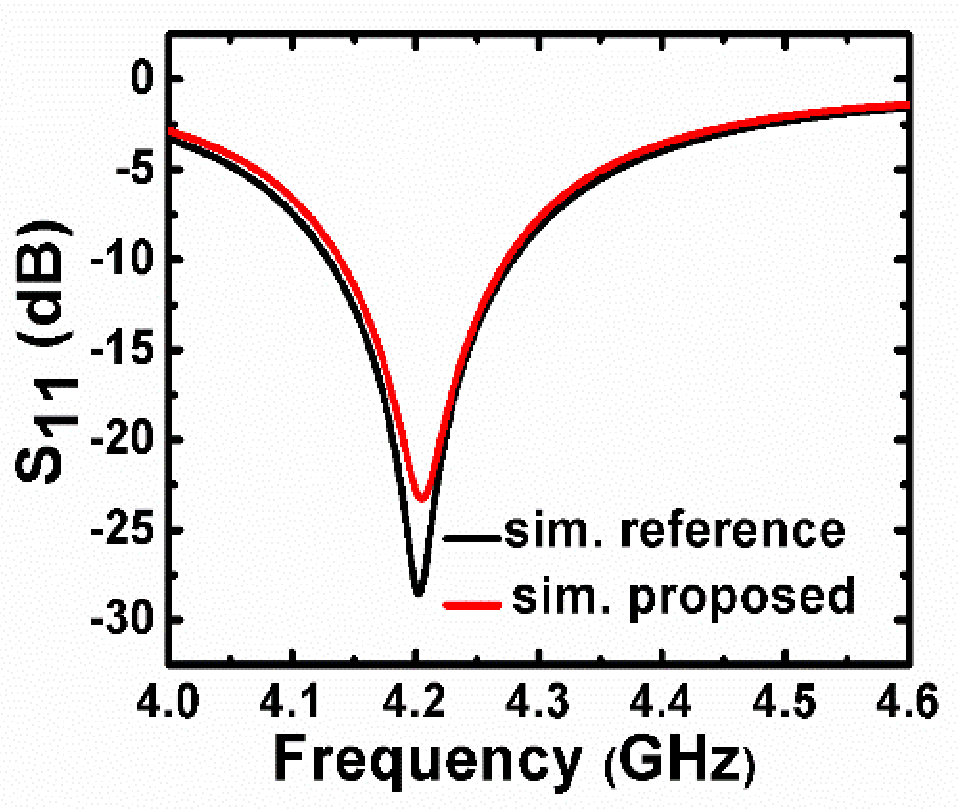

(a)

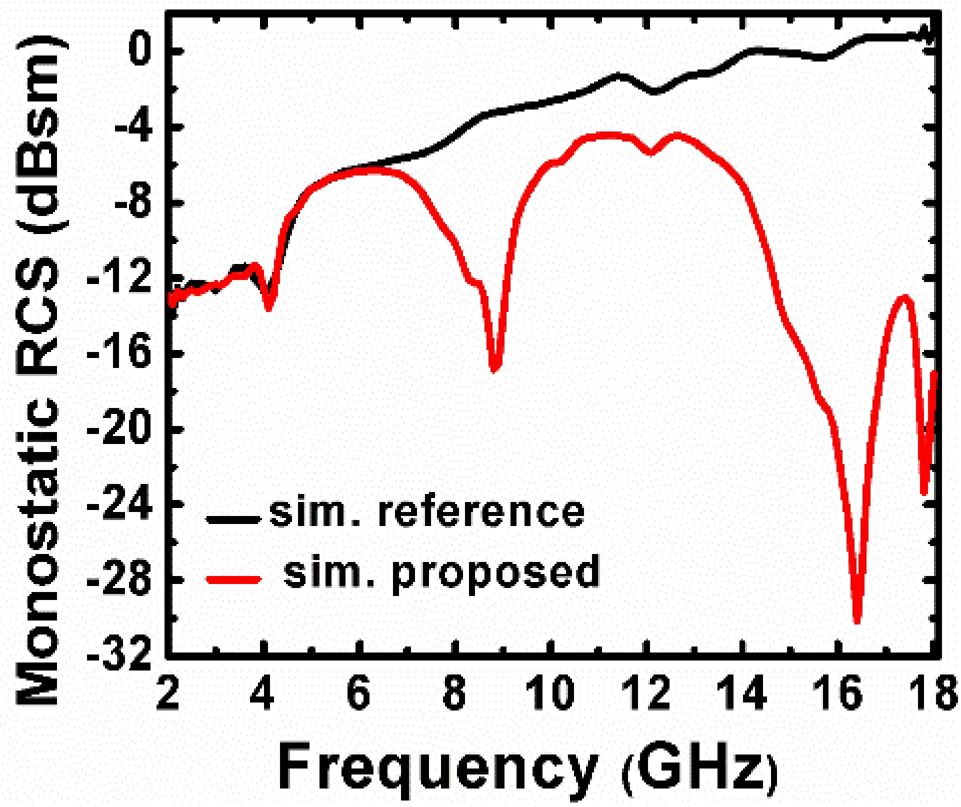

(b)

Figure 5.7. Comparison of reference and proposed antennas (a) RC characteristics and (b) RCS characteristics.

Table 5.3. Comparison of RCS characteristics of CB_1, CB_2, and hybrid geometries.

Configuration	Bandwidth (GHz)	Resonant frequency (GHz)	Monostatic RCS value (dB)
CB_1	5.9	4.0 and 8.7	-13.3 and -16.6
CB_2	3.1	4.0 and 17.0	-12.2 and -13.3
Hybrid	7.4	4.0, 8.7, 16.4 and 17.7	-13.3, -16.9, -30.1 and -23.3

5.2.2 SIMULATED RESULTS

For an extensive study, the scattering and radiation properties of the reference antenna and the hybrid structure have been simulated. A comparison of simulated RC-frequency spectra's of reference antenna and the proposed antenna is shown in Figure 5.7 (a). It has been observed that the peak RC value of the reference antenna is -28.5 dB at 4.2 GHz, while the peak RC value of the proposed antenna is -19.6 dB at 4.19 GHz. The difference between both resonant frequencies is 0.01%, which is an acceptable value. Using the hybrid MM structure, out of band RCS reduction is possible. To validate this, a monostatic reduction versus frequency graph of the reference antenna and the proposed antenna is shown in Figure 5.7 (b).

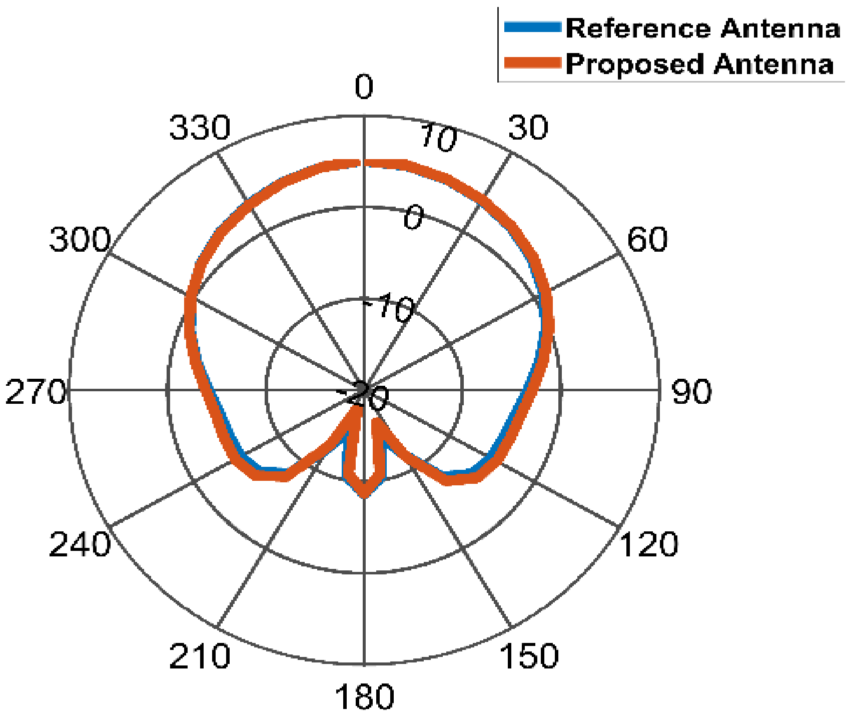

(a)

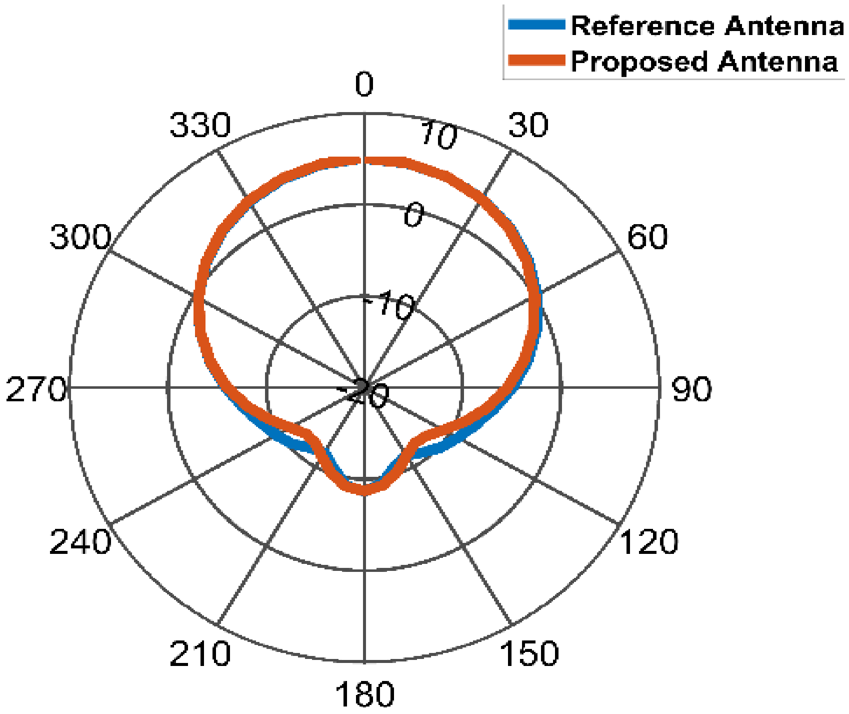

(b)

Figure 5.8. Radiation pattern of reference and proposed antenna (a) E plane (b) H plane.

A noticeable out of band RCS reduction is achieved with a maximum RCSR value of -30.1 dB at 16.4 GHz as clear from Figure 5.7(b).The comparison of xoz (**E** plane) and yoz (**H** plane) of the radiation patterns in terms of gain of reference and proposed antennas are plotted in Figures 5.8 (a) and (b). It can be observed that in both antennas, the change in gain value is almost negligible. Means, the radiation properties of an antenna are not degraded by the application of a hybrid structure. Meanwhile, the parametric studies are also performed on the hybrid structure to examine the effect of parameters on the monostatic RCS characteristics. Figure 5.9 shows the frequency-dependent monostatic RCS characteristics of the hybrid structure whose range is from 2 GHz to 18 GHz. The study has been carried out to know the effect of the gap between inner Square and the outer square (d), which is illustrated in Figure 5.9(a). The value of 'd' varies from 0.4 mm to 1.2 mm with a step size of 0.2 mm. Before 0.8 mm, the value of RCS reducing, but after 0.8 mm the value of RCS increases, therefore, the optimal value of 'd' is 0.8mm. In this study, the value of 'd' is varied from 0.4 mm to 1.2 mm. In Figure 5.9(b), the inner radius (i) of the split ring is varied from 1.1 mm to 1.5 mm.

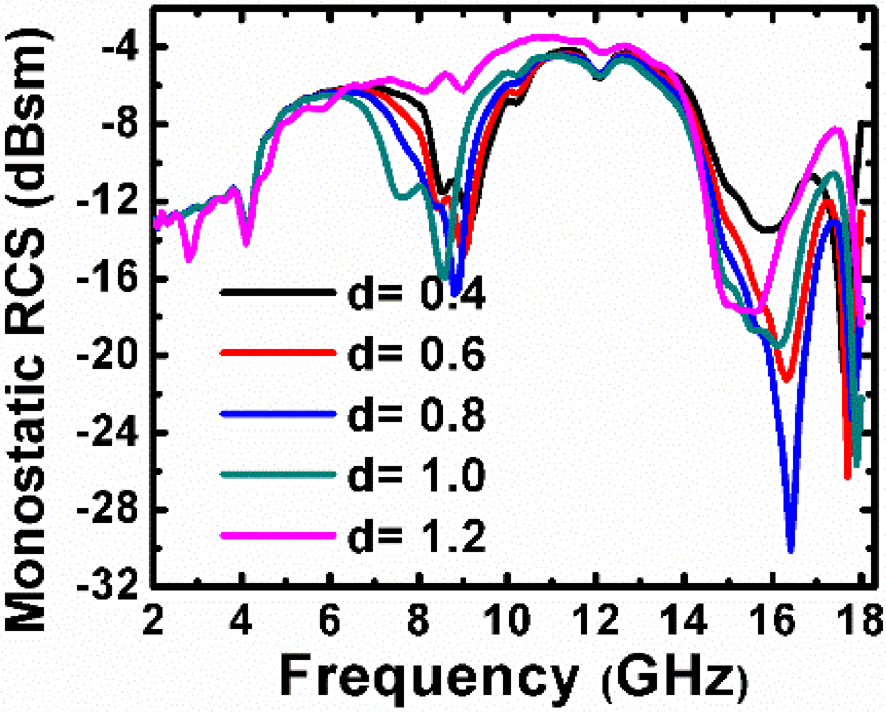
Monostatic RCS (dBsm)
-4
-8
-12
-16
-20
-24
-28
-32
2
4
6
8
10
12
14
16
18
Frequency (GHz)
d= 0.4
d= 0.6
d= 0.8
d= 1.0
d= 1.2

(a)

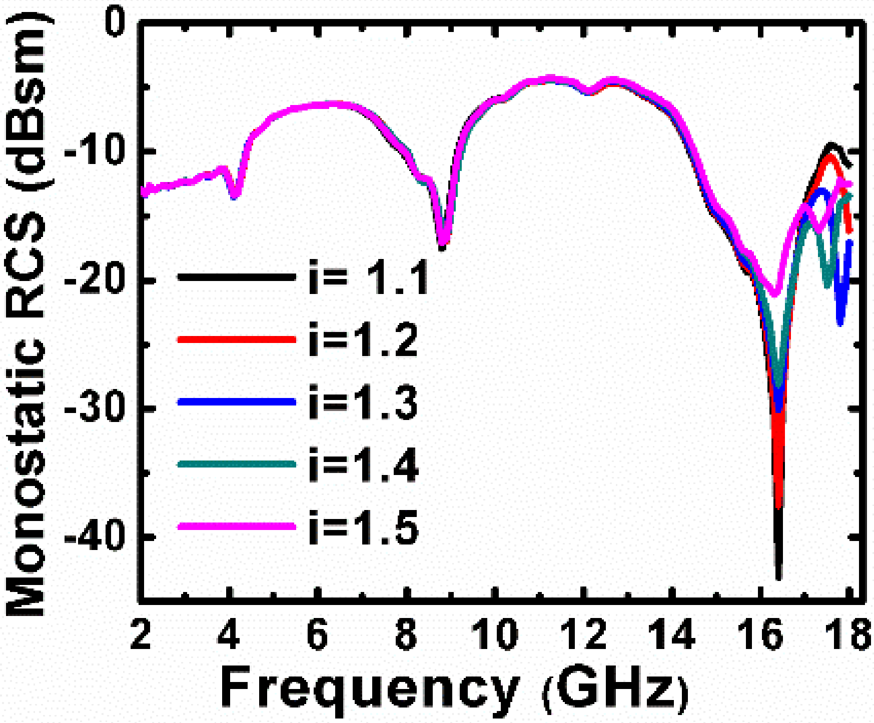
Monostatic RCS (dBsm)
0
-10
-20
-30
-40
2
4
6
8
10
12
14
16
18
Frequency (GHz)
i= 1.1
i=1.2
i=1.3
i=1.4
i=1.5

(b)

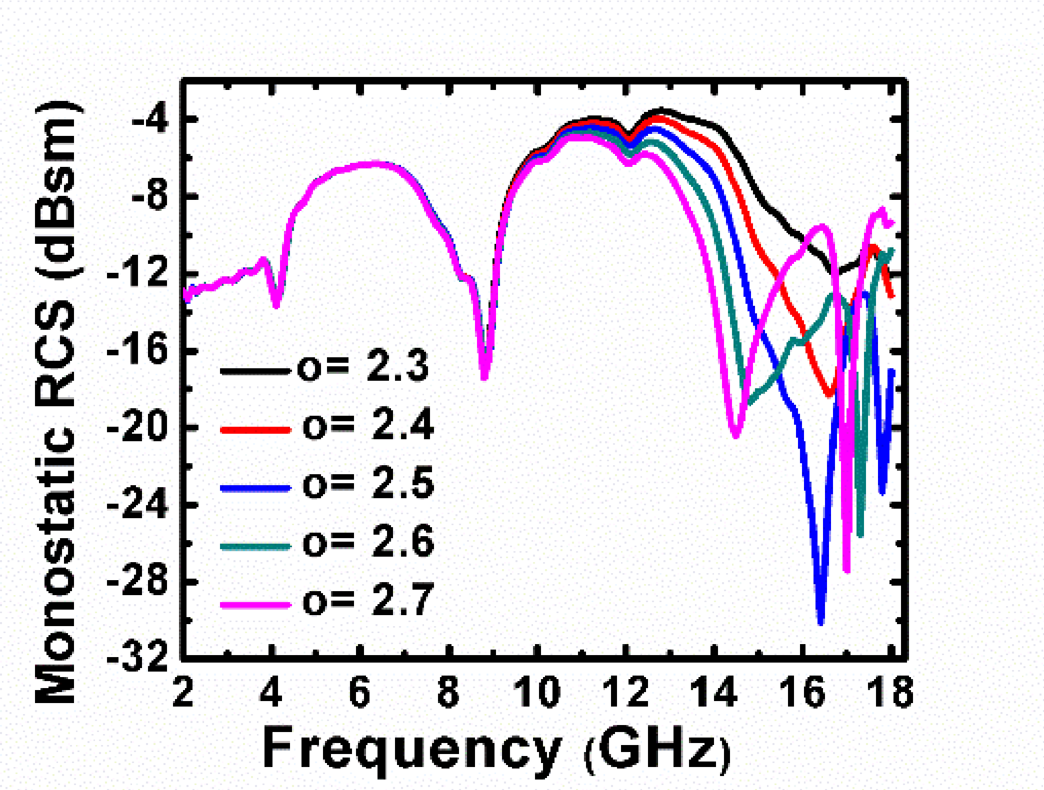

(c)

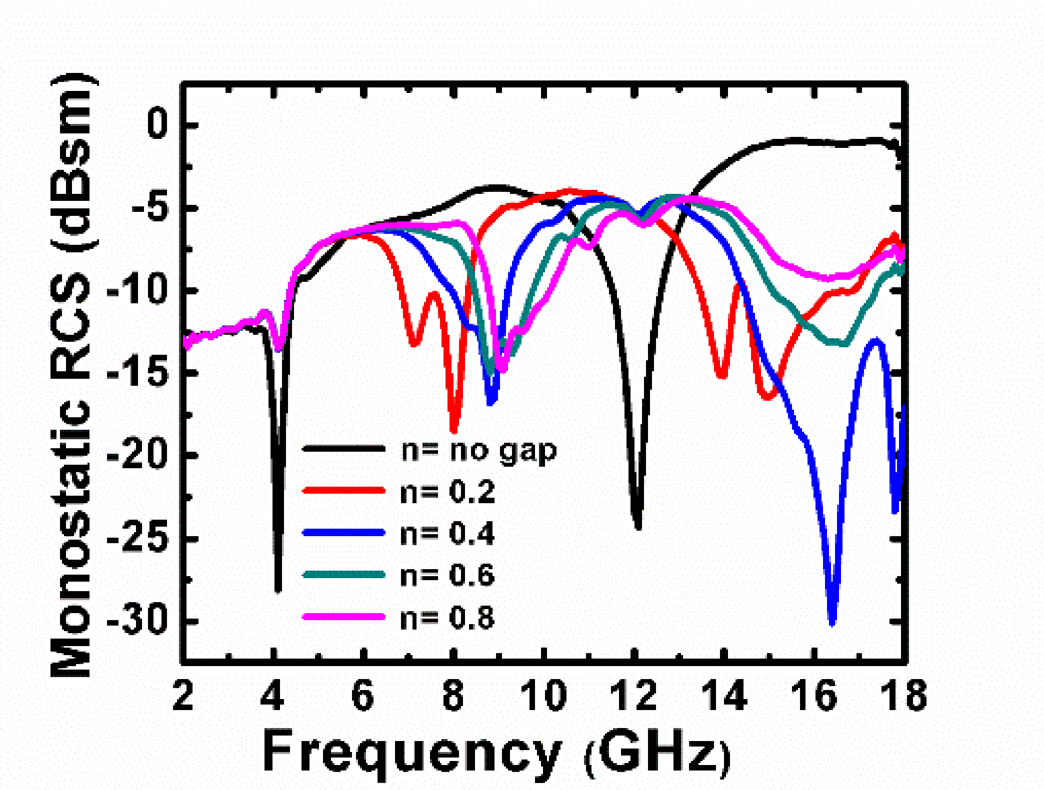

(d)

Figure 5.9. Effect of design variables (a) gap between inner square and outer square (b) inner circle radius, (c) outer circle radius and (d) gap between split ends.

As mentioned earlier, the split ring is responsible for the high-frequency RCS reduction, the value of the inner circle radius increasing the peak shifts towards upside almost at 16 GHz. The optimal value of the inner circle is 1.3 mm. Identically, the outer radius (o) of the split ring is differed from 2.3 mm to 2.7 mm, as illustrated in Figure 5.9(c). The resonant frequency shifts towards the lower side of the spectrum, when the outer radius increases, which also results in wideband response. The optimal value of the outer radius of the split ring is 2.3 mm. To investigate the effect of the gap between split ends (n), the value of n has been varied from 0.2 mm to 0.8 mm with 0.2 step size as shown in Figure 5.9(d). In the first case, the value of n is equal to zero means that there is no gap between the circle and square. For every value of 'n', a completely different response is obtained, due to changes in the value of capacitance leading to a change in the gap.

5.2.3 FABRICATION AND COMPARISON WITH MEASURED DATA

The reference and the hybrid antennas were fabricated using PCB technology to validate the theoretical results. Figures 5.10 (a) and (b) illustrate the images of the fabricated samples of the reference and proposed antennas. The performance evaluation of the fabricated antennas has been carried out using a microwave measurement setup, which consists of a broadband horn antenna (1 GHz to 18 GHz) and a vector network analyzer (VNA Keysight E5063A).

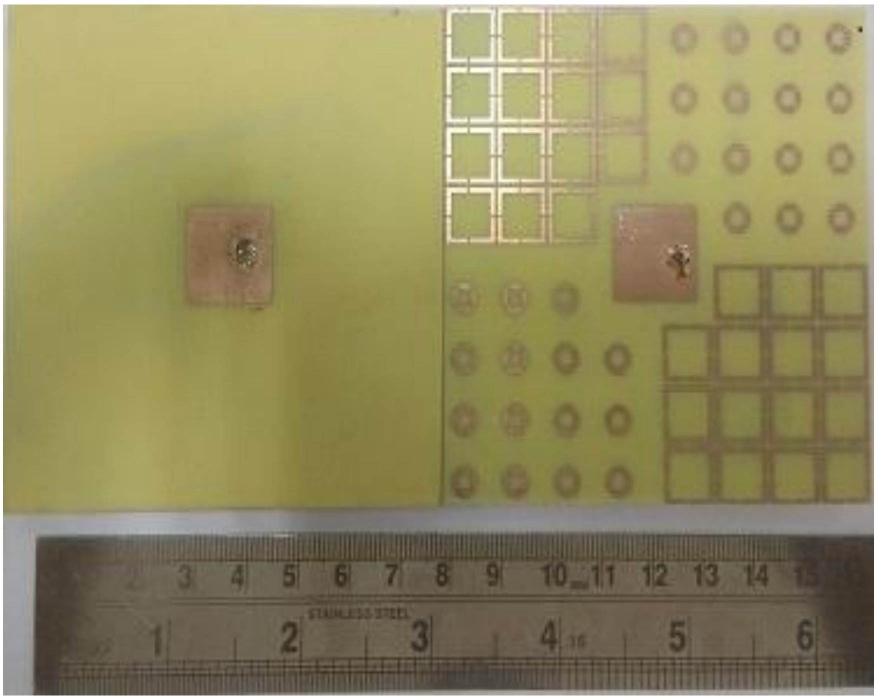

(a)

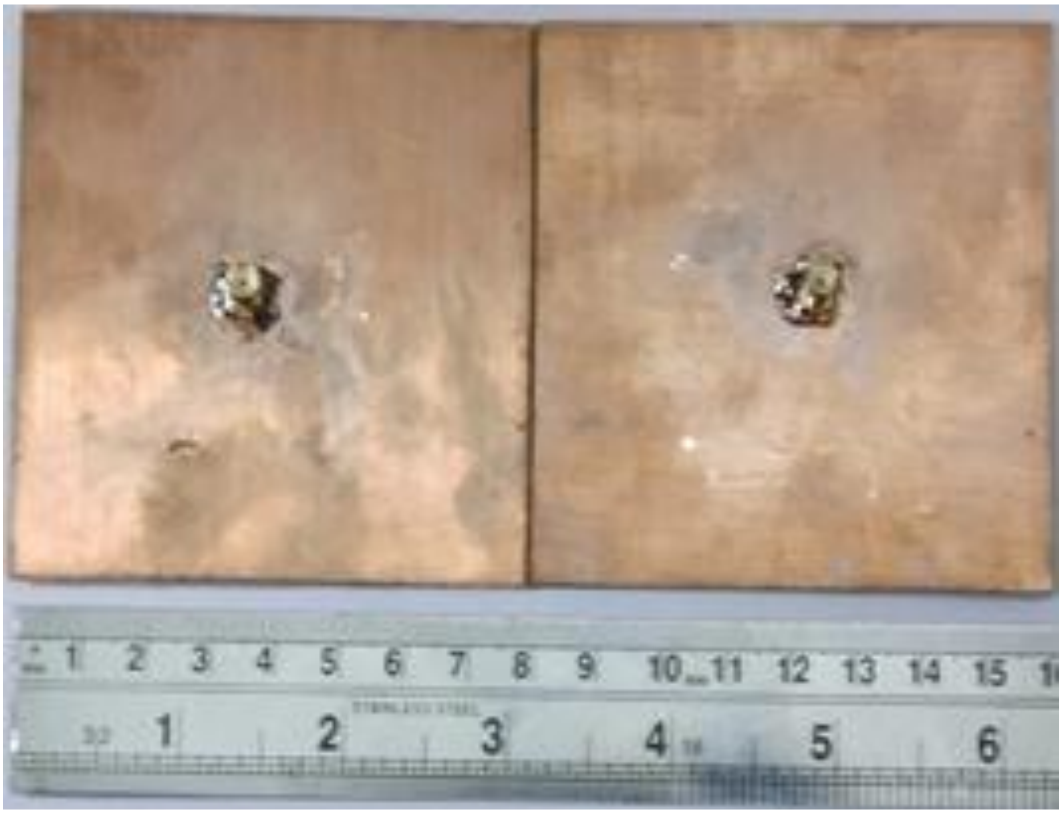

(b)

Figure 5.10. Fabricated sample of reference and proposed antennas (a) top view and (b) bottom view.

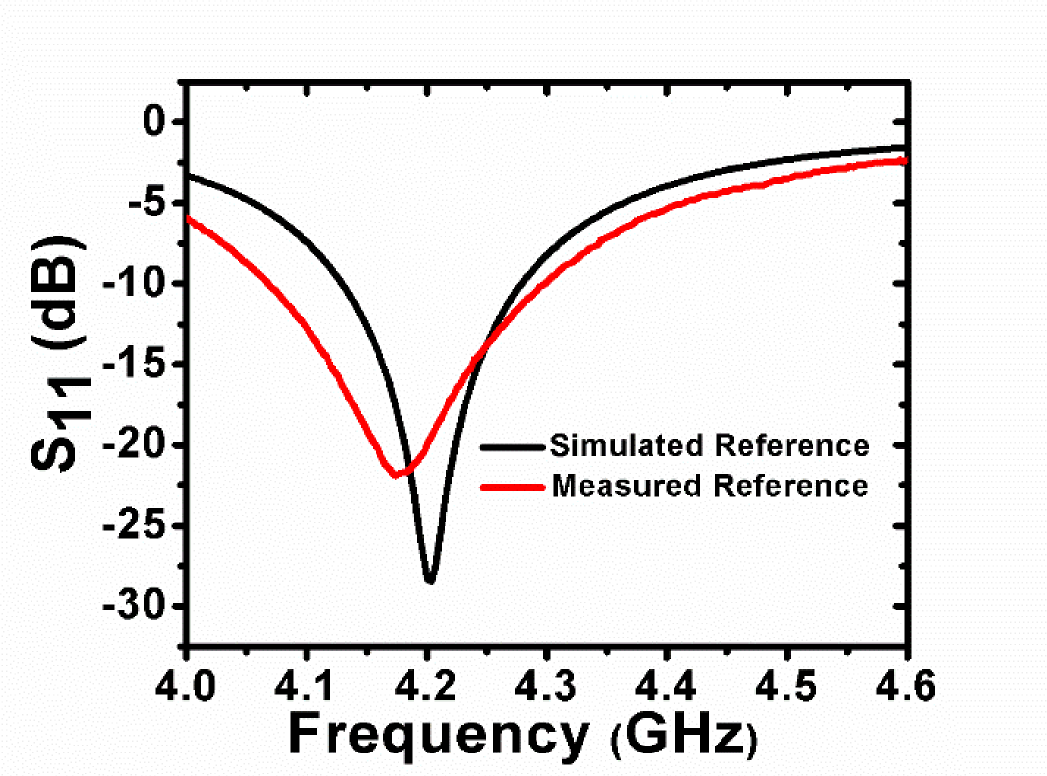

(a)

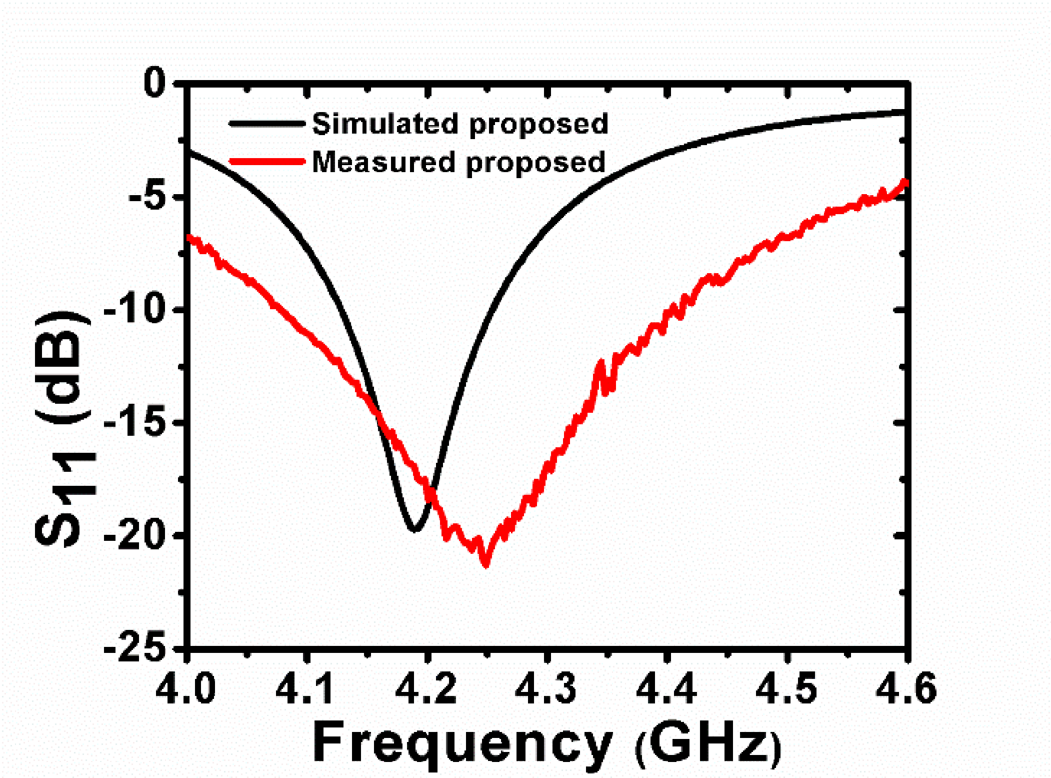

(b)

Figure 5.11. Frequency dependent measured and simulated RC characteristics of (a) reference (b) proposed antennas.

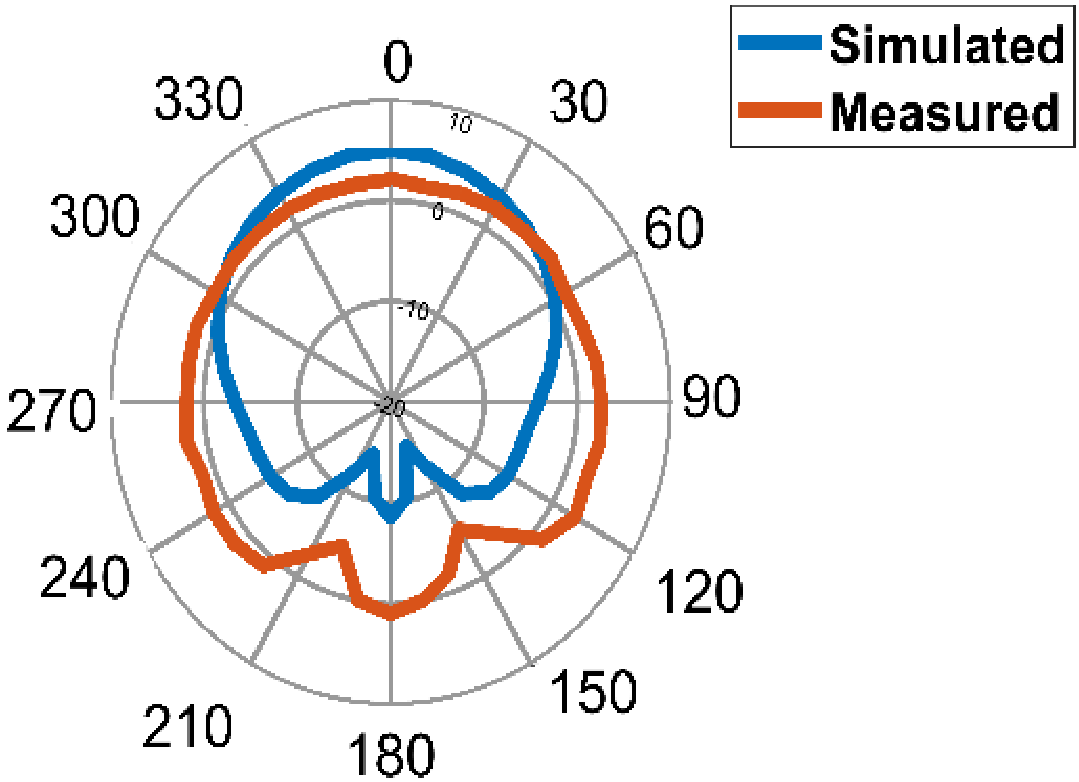

(a)

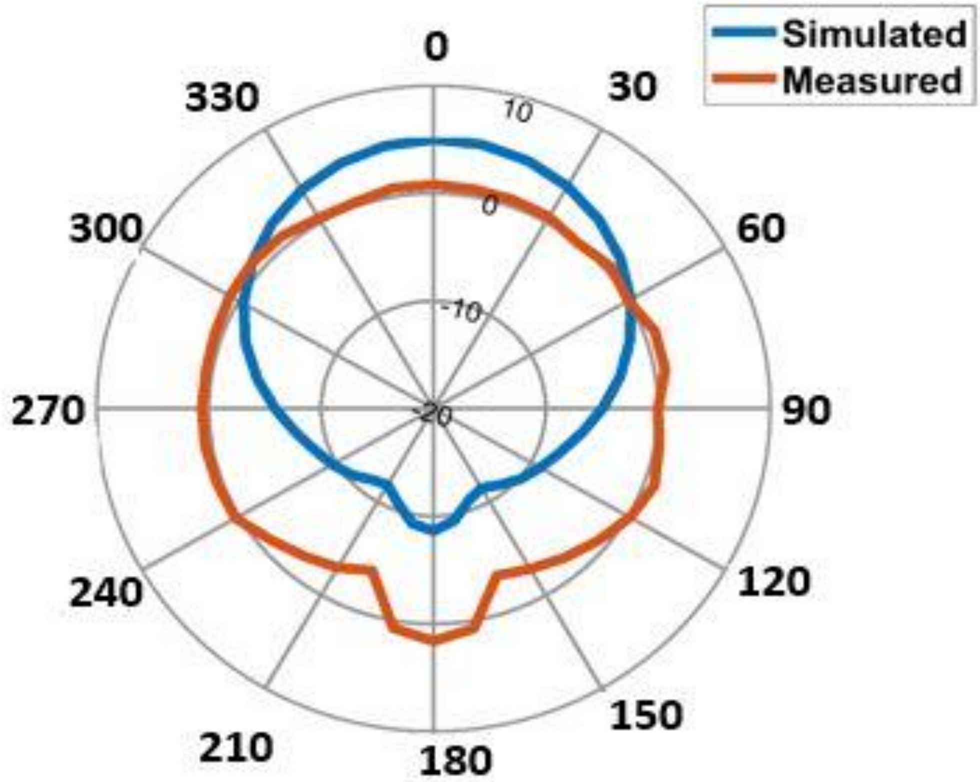
Simulated
Measured
0
30
60
90
120
150
180
210
240
270
300
330
10
0
-10
-20

(b)

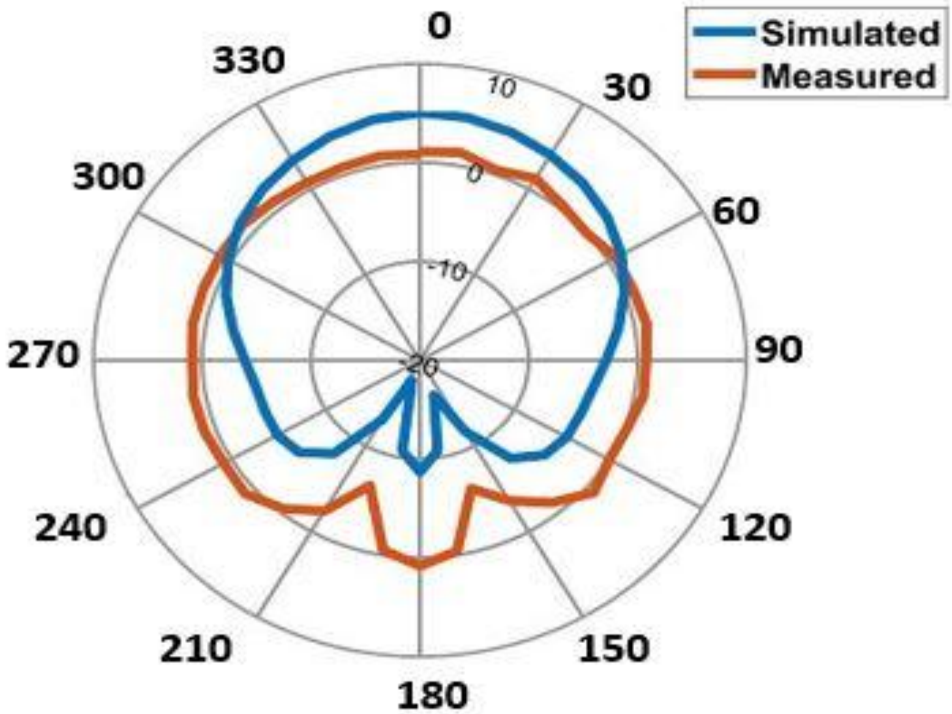
Simulated
Measured
0
30
60
90
120
150
180
210
240
270
300
330
10
0
-10
-20

(c)

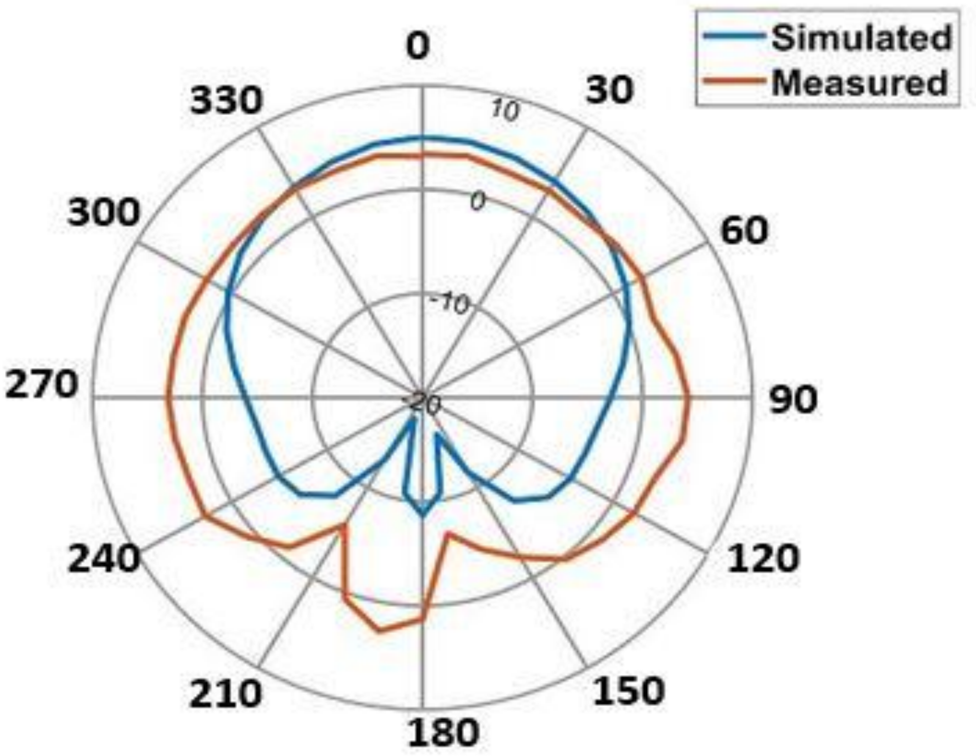

(d)

Figure 5.12. Radiation pattern of reference antenna (a) E plane (b) H plane and proposed antenna (c) E plane (d) H plane.

To estimate the similarity and dissimilarity between the measured and simulated S-parameter of the reference and hybrid antennas, the comparison has been reported in Figures 5.11 (a) and (b) and in Table 5.4. It has been observed that the measured peak RC value of the reference antenna is -22.0 dB at 4.1 GHz, while the peak measured RC value of the proposed antenna is -24.6 dB at 4.2 GHz.

Table 5.4. Comparison between simulated and measured results of the primary and proposed antenna.

Antenna	**Simulated resonant frequency (GHz)**	**Simulated RC value (dB)**	**Measured resonant frequency (GHz)**	**Measured RC value (dB)**
Primary antenna	4.2	-28.5	4.1	-22.0
Proposed antenna	4.19	-19.6	4.2	-24.6

To measure the radiation pattern in terms of gain of the fabricated sample, a signal generator with a transmitter broadband horn antenna (15 dB gain) has been used on one end of the anechoic chamber [101]. The antenna under test (AUT) was placed on the other end of the anechoic chamber, connected to the VNA. Sigma generator has been set to provide a signal of 4.2 GHz and power level 0 dBm, on the other side VNA marker was also positioned at 4.2 GHz (resonating frequency). The measurement has been performed using software, which controls the antenna rotator and also plots the data from VNA in polar plot form. A comparison between measured and simulated radiation pattern of reference and proposed antennas at E Plane and H plane is illustrated in Figures 5.12 (a) - 5.12(d). The maximum radiation of proposed and reference antennas are towards the front side of the structure, and also the backward radiation is quite less, as shown in Figures 5.12 (a) -5.12 (d). The measured data is marginally varied as a result of the fabrication tolerance and the loss due to the sub-miniature version A (SMA) connector.

5.3 FLEXIBLE MM BASED SUPERSTRATE COUPLED MPA

In this section, the effect of a superstrate layer coupled with an MPA for the RCSR is described. The primary and proposed MPAs are designed to operate in C-band. The two distinct MM unit cells, namely FSS#1 and FSS#2, are designed and simulated in the range of 2 to 12 GHz. The EM properties of these structures are estimated to reflect their MM nature. Five different configurations loaded with MM structures are designed and compared in terms of their RCSR characteristics in the range of 2 to 12 GHz. An optimal MM configuration is found to possess a maximum RCSR of an antenna along with an increment in gain. Besides, the primary and proposed antennas are fabricated and measured to authenticate the accuracy of the simulation. A quite good agreement has been obtained among theoretical and measured results. The proposed design approach simultaneously meets the requirement of a low RCS and high gain antenna, which reflects its potential for low observable applications.

5.3.1 DESIGN OF HYBRID MM SUPERSTRATE COUPLED MPA

This section including three parts, the first part describes the designing of the primary antenna. The second part explicates the design of MM unit cell, and the MM structure loaded patch antenna is presented in the third part.

5.3.1.1 DESIGN OF PRIMARY ANTENNA

MPA with a 2.0 mm thick FR4 substrate (dielectric loss tangent, tan δ= 0.025 and relative permittivity, ε_r=4.3) is designed as a primary antenna as depicted in Figure 5.13. The proposed antenna configuration has been simulated using CST, Darmstadt, Germany microwave studio software, in the time domain solver. To excite the antenna, a waveguide port, and coaxial feed are used. Table 5.5 presents the geometrical design variables with corresponding values for MPA, which are illustrated in Figure 5.13. Here, P is the width and the length of the antenna's substrate, L and W are the length and width of the patch, respectively. T is the thickness of the antenna substrate.

Table 5.5. Geometrical design variables of the patch antenna.

Parameter	Value (mm)	Parameter	Value (mm)
P	80.0	A	7.0
W	14.2	T	2.0
L	14.2	-	-

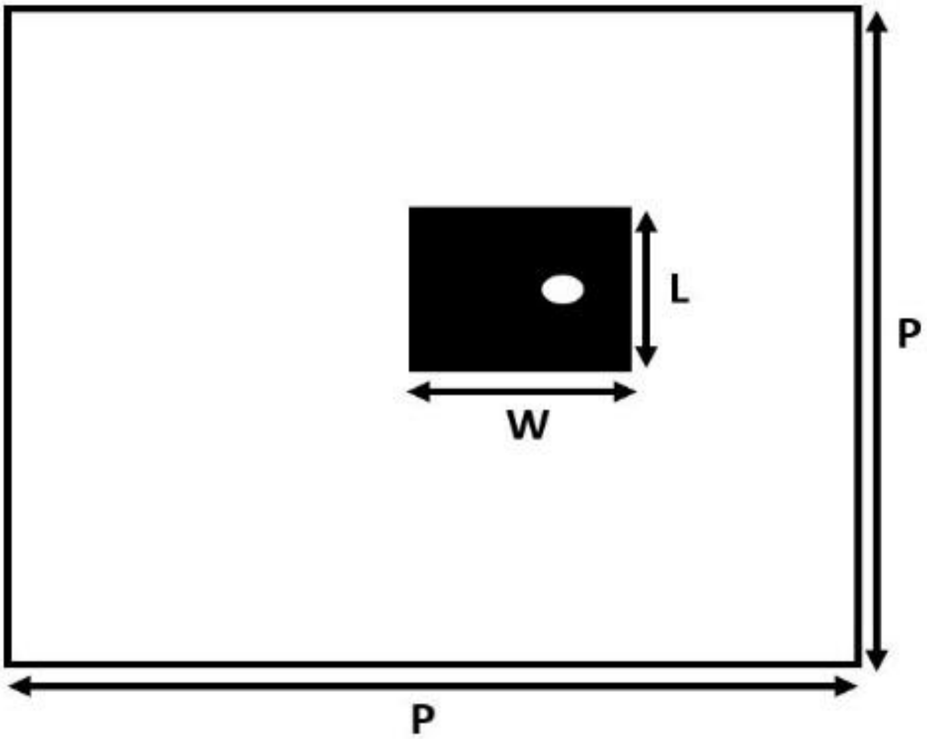

Figure 5.13. Front view of the primary MPA utilized for this study.

5.3.1.2 DESIGN OF FSS BASED MM STRUCTURES

The two-unit cells of FSS have been designed and simulated, namely FSS#1 and FSS#2. FSS#1 consists of a square geometry surrounded by a circle as illustrated in

Figure 5.14 (a). The radius of the circle in FSS#1 is defined by R, and S is the length and width of the square. 'E' is designated as the gap between the two circles as elucidated in Figure 5.14 (b). MM unit cell has been simulated in the frequency domain solver, using CST microwave studio software by employing periodic boundary conditions. MM consists of a copper layer printed on a dielectric substrate FR4 with a thickness of 0.2 mm. MM geometrical design variables with corresponding values are shown in Table 5.6. Here, 'z' is the periodicity of the unit cell, and 'u' is the dimension of the unit cell. FSS based MM configurations, i.e., DG#1, DG#2, DG#3, DG#4, and DG#5 are designed and simulated and compared in the terms of RCSR. There are (n+1-i) elements of FSS#1 and FSS#2 in a row of each iteration, where 'n' are the total number of elements at the beginning and 'i' is the iteration number. The repetition factor of the unit cell in a row is 10.6 mm, whereas the dimension of u is 10 mm. In each iteration, one row of FSS#1 and FSS#2 was added on the upper and lower side of their respective positioning in the previous configuration. The first hybrid MM superstrate structure i.e. DG#1 comprised of first-order iterated five FSS elements (i.e. n=5). Similarly, second-order four FSS elements are arranged, resultant in second MM superstrate structure i.e. DG#2. Similarly, the combinations have been carried out up to DG#5 configuration. The evolutions of various configurations are illustrated in Figure 5.15.

Table 5.6. Geometrical design variables of MM unit cell.

Parameter	**Value (mm)**	**Parameter**	**Value (mm)**
R	4.8	L1	9.60
E	0.8	L2	9.60
R2	3.5	U	10.0
S	4.2	K	0.80
H	1.2	G	16.2
H2	1.2	G2	1.20
Z	10.6	T1	0.2
P	80.0	-	-

5.3.1.3 DESIGN OF MM STRUCTURE (MMS) LOADED PATCH ANTENNA

MM superstrate designed in section 5.3.1.1 is loaded on the primary patch antenna designed in section 5.3.1.2, and the general configuration of the same is shown in

Figure 5.16. A higher iterated hybrid MM geometry (i.e., DG #5) has been loaded on the top of the primary patch antenna with a 7.0 mm air gap in between for the design of MM superstrate antenna. The overall dimension of the structure, including primary MPA and impinged hybrid MM layer was 80 × 80 mm. Finally, MM superstrate antenna (composite of the primary patch antenna and hybrid MM) was simulated to estimate the reflection characteristics (RC) and the RCS response of the structure.

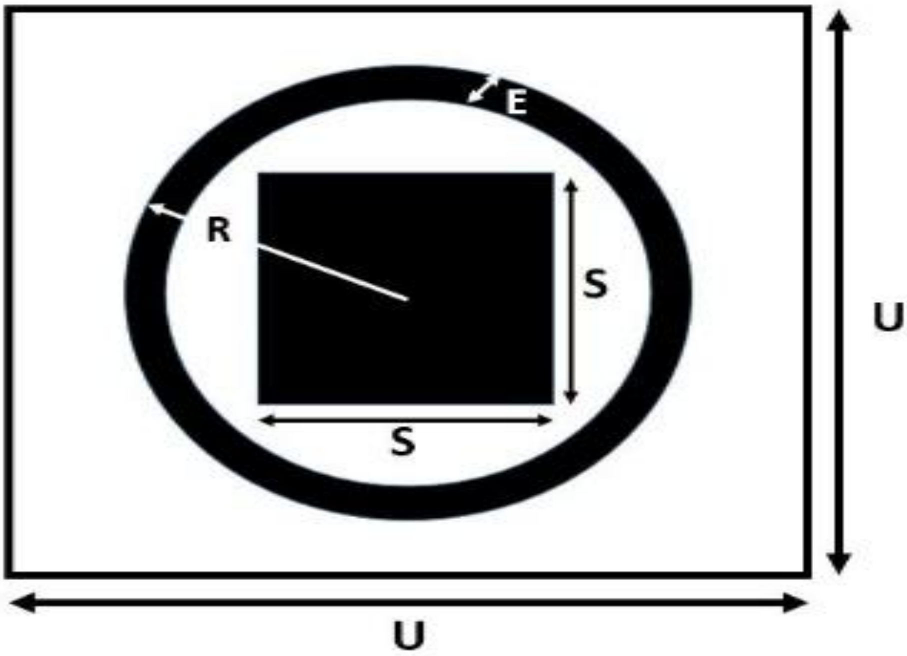

(a)

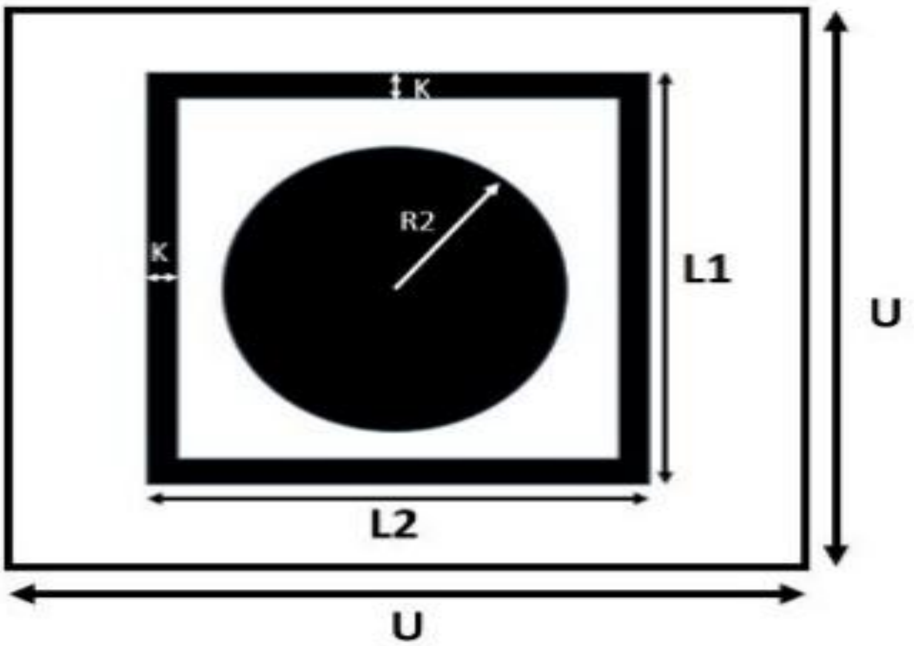

(b)

Figure 5.14. Front view of (a) FSS#1 and (b) FSS#2 with corresponding design parameters.

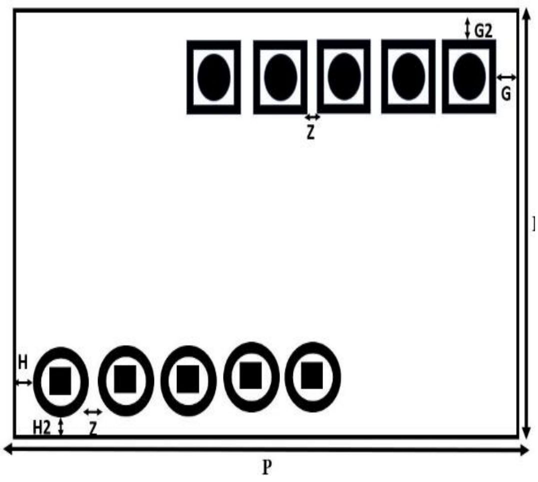

(a)

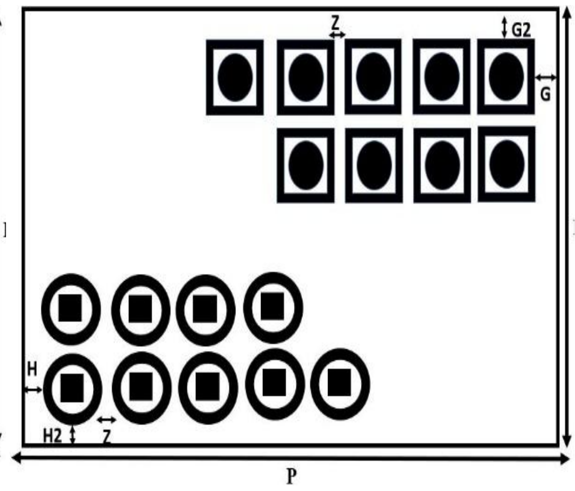

(b)

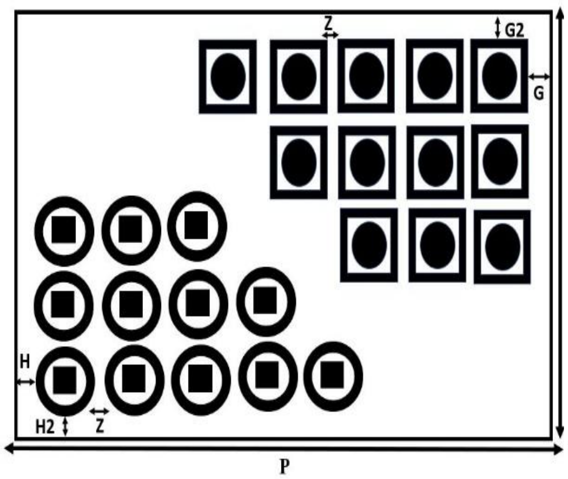

(c)

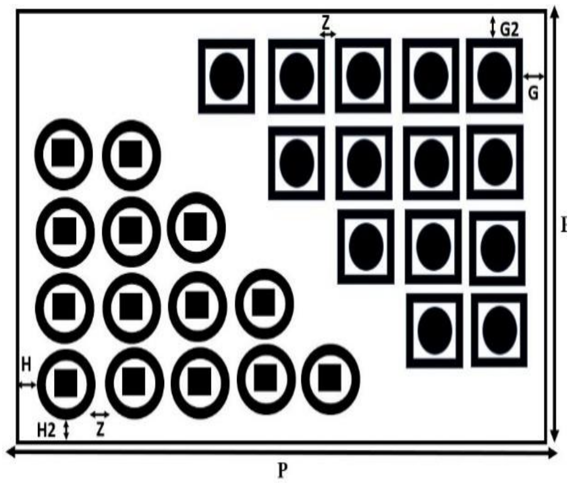

(d)

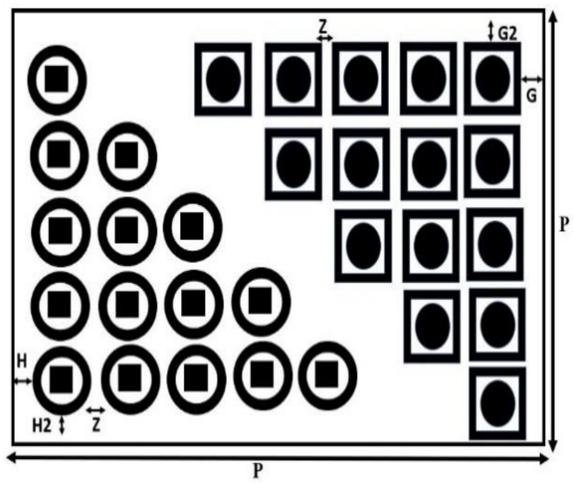

(e)

Figure 5.15. Different configurations of MM layer (a) DG#1, (b) DG#2, (c) DG#3, (d) DG#4 and (e) DG#5.

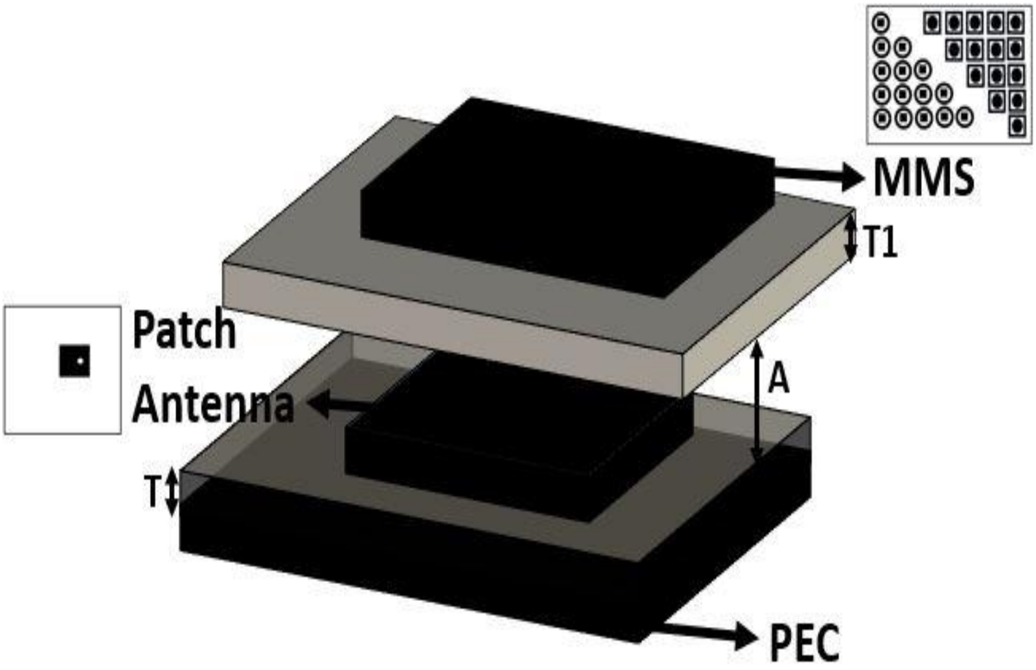

Figure 5.16. 3D topology of hybrid MM inspired antenna comprises of a patch antenna, MMS, air gap, and PEC.

5.3.2 CRITICAL ANALYSIS AND SIMULATED RESULTS

Figures 5.17 (a) and (b) illustrate the Scattering parameters (S-parameters) in terms of the co and cross-polarization of FSS#1 and FSS#2, respectively, which proves that the structure is acting purely as an absorber. The unit cells are designed to operate at X-band, to minimize the RCSR in X-band especially. It has been analyzed that the resonance of $\square_{11}$ of FSS#1 appears at 10.44 GHz, whereas the resonance of $\square_{21}$ is observed at 6.82GHz.Similarly, $\square_{11}$ resonance of FSS#2 is observed at 7.69 GHz and $\square_{21}$ resonance of FSS#2 is observed at 4.73 GHz.

The real part of the permittivity and permeability of FSS#1 and FSS#2 are shown in Figure 5.18, which proves that both structures are MM structures. As, FSS#1 has the negative value of epsilon, while the permeability of the FSS#1 shows the positive value, which means FSS#1 falls in the single negative index MM category. While the FSS#2 falls in the double negative index MM category because its permittivity and permeability both reflect the negative values. Figure 5.19 (a) illuminates the maximum gain over the frequency graph of primary and proposed antennas in the range of 2 GHz to 12 GHz. It shows that the maximum gain attained by the primary antenna is equal to 6.6 dB, where the maximum gain of the proposed antenna is equal to 7.2 dB, which proves the gain enhancement by the proposed structure.

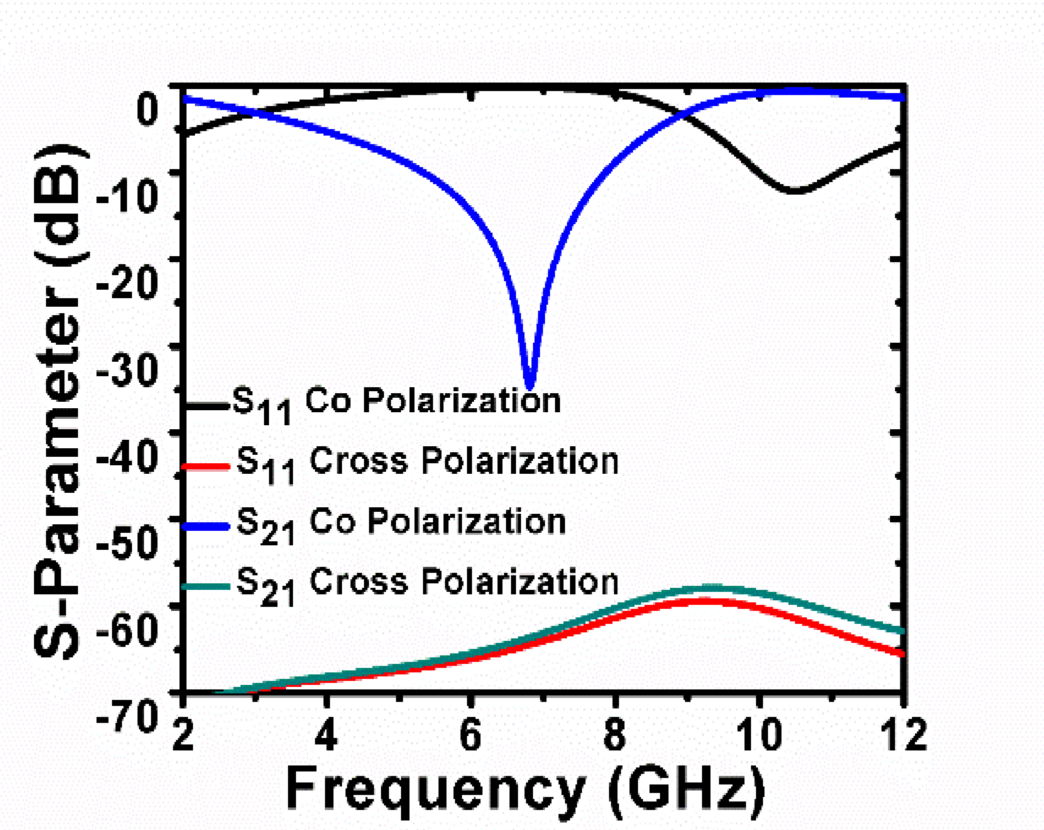

(a)

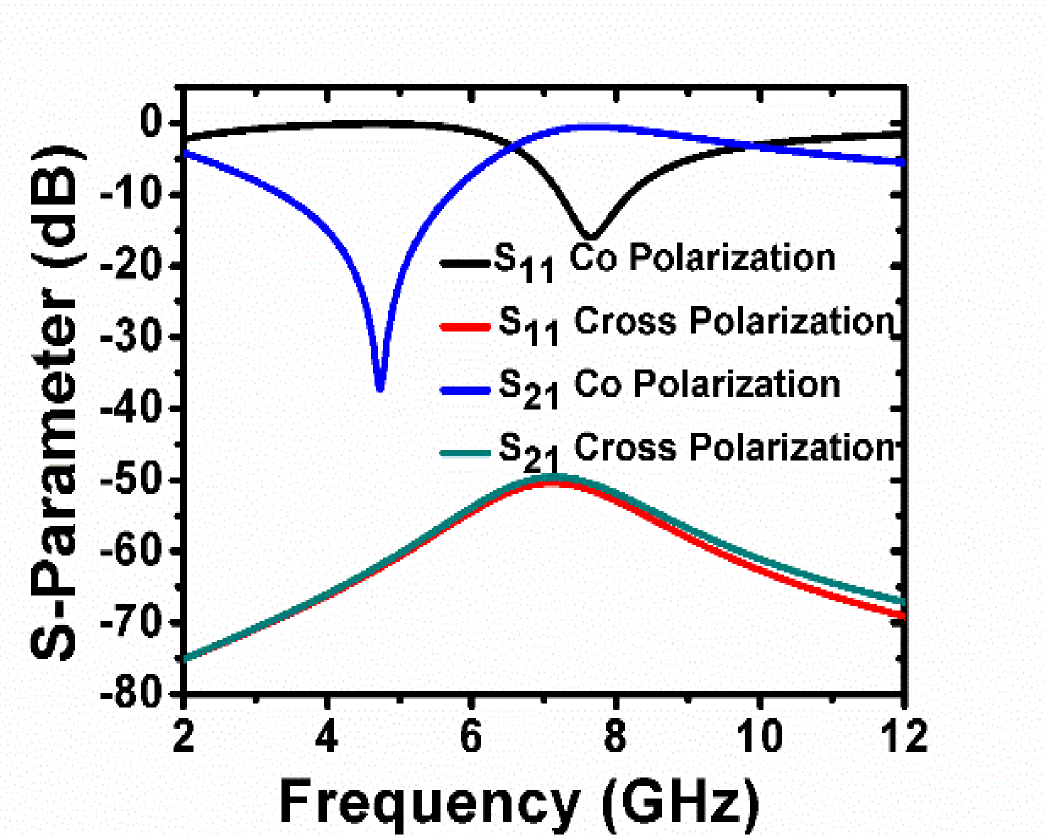

(b)

Figure 5.17. S-parameters in terms of co and cross polarization of (a)UC#1 and (b) UC#2.

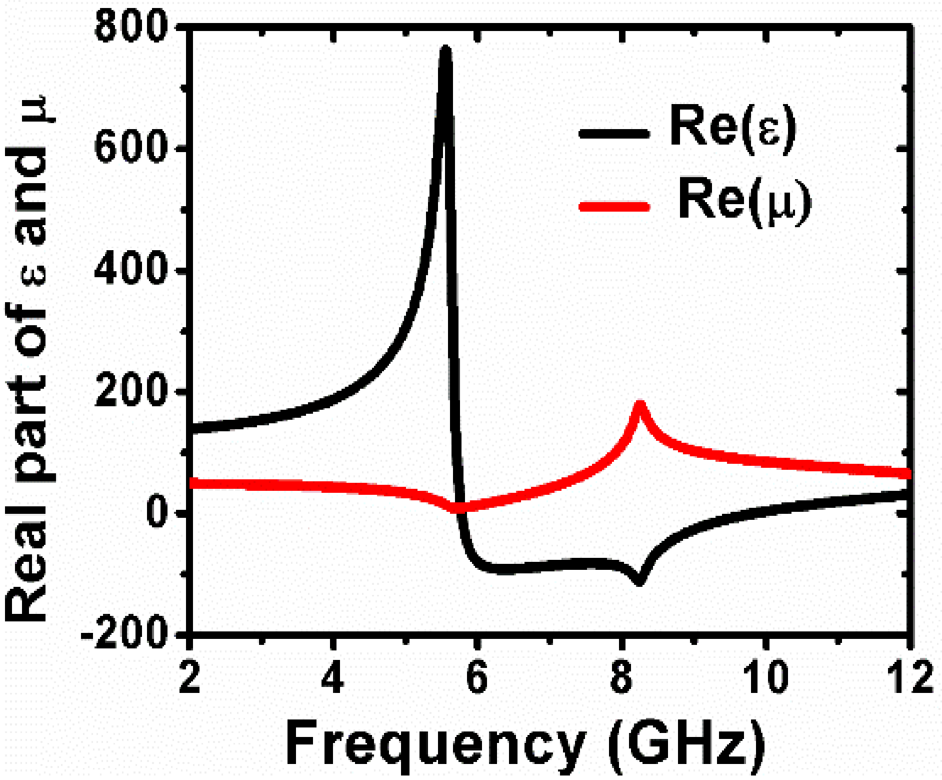

(a)

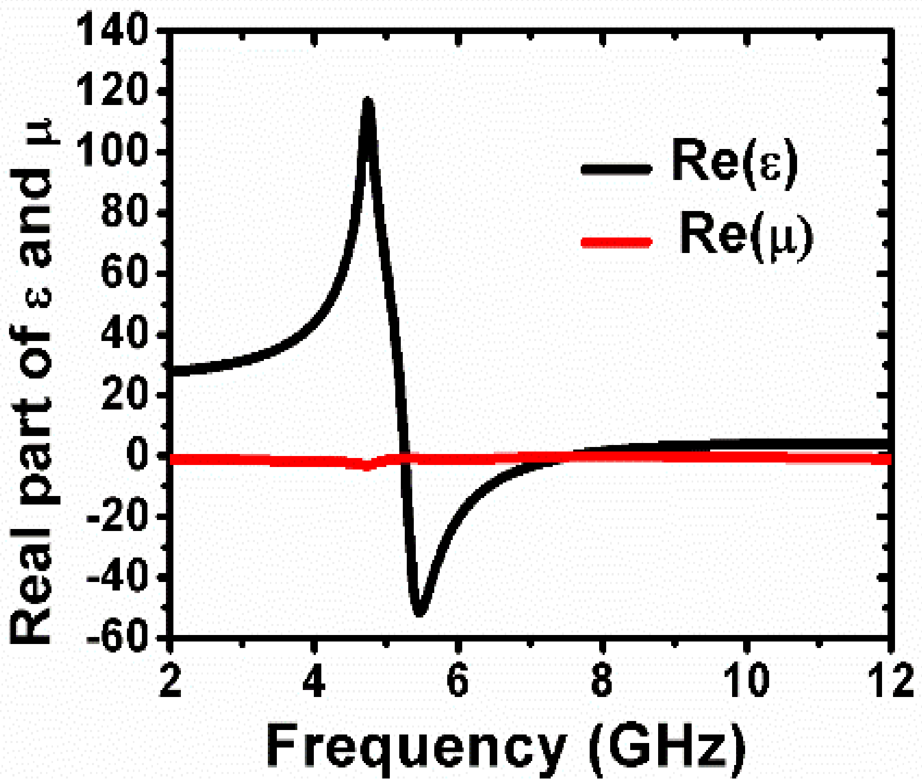

(b)

Figure 5.18. Frequency dependent permittivity and permeability graph of (a) FSS#1 and (b) FSS#2.

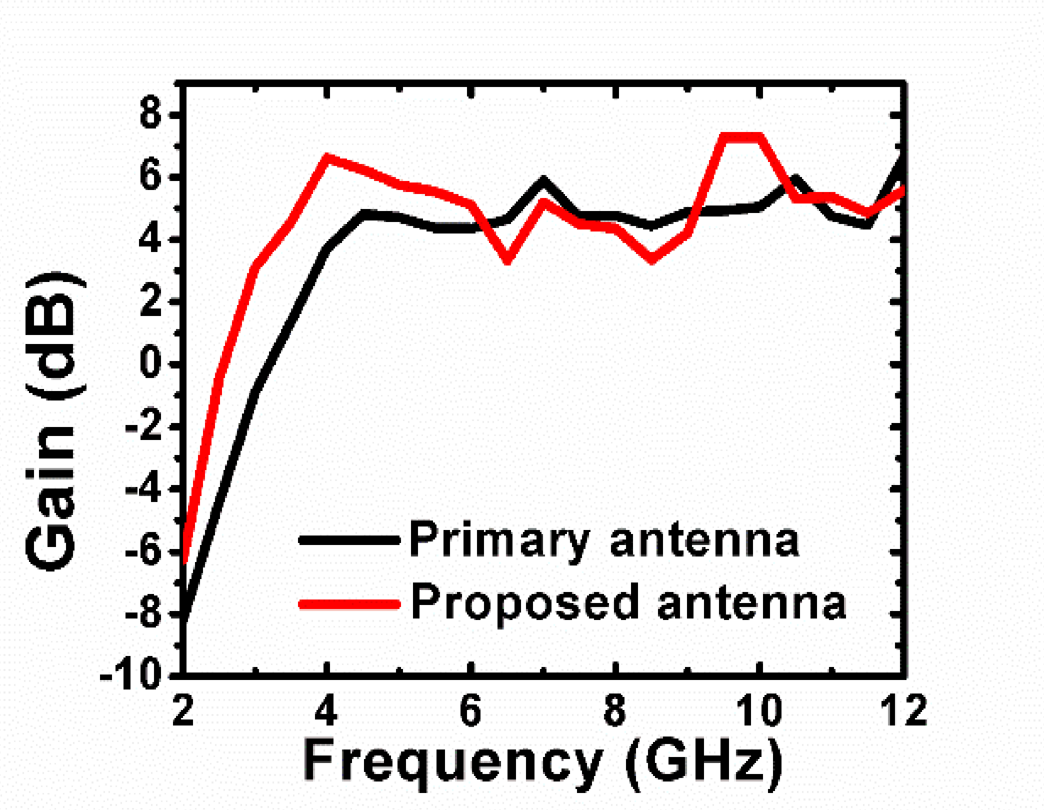

(a)

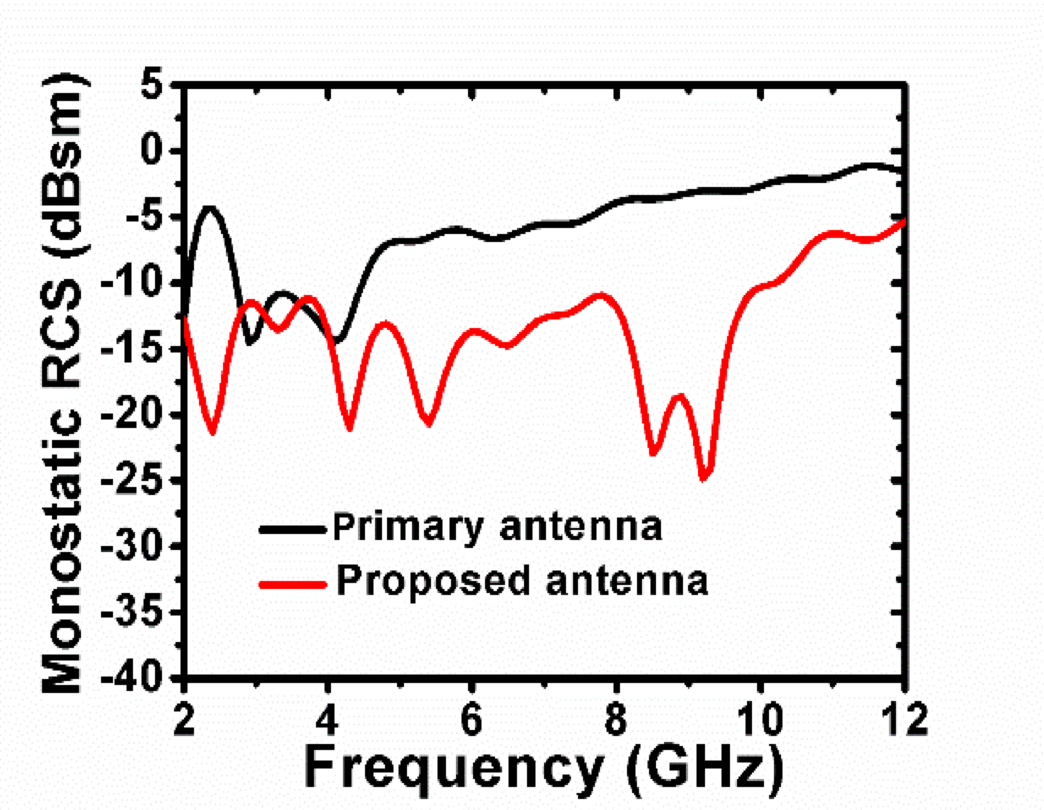

(b)

Figure 5.19. Comparison between primary and proposed antenna in terms of (a) gain (dB) and (b) RCS characteristics.

Figure 5.19 (b) manifested the RCS characteristics of the primary and proposed antenna, in which it is observed that in the band as well as out of band RCSR is achieved with the proposed antenna. The comparison among DG#1, DG#2, DG#3, DG#4, and DG#5 in terms of RCS is shown in Figure 5.20, in which it has been observed that the maximum RCSR has been achieved with DG#5 configurations. The reflection coefficient bandwidth of primary and proposed antennas is the same (i.e., 800MHz), though the RCS bandwidth of the primary antenna is 1.7 GHz and the RCS bandwidth of the proposed antenna is 8.1 GHz. A comparison between primary and proposed antenna in terms of bandwidth, gain and RCS bandwidth is illustrated in Table 5.7.

Table 5.7. Comparison between primary and proposed antenna.

Antenna	S_{11} Bandwidth	RCS Bandwidth	Maximum Gain
Primary	800 MHz	1.7 GHz	6.6 dB
Proposed	800 MHz	8.1 GHz	7.2 dB

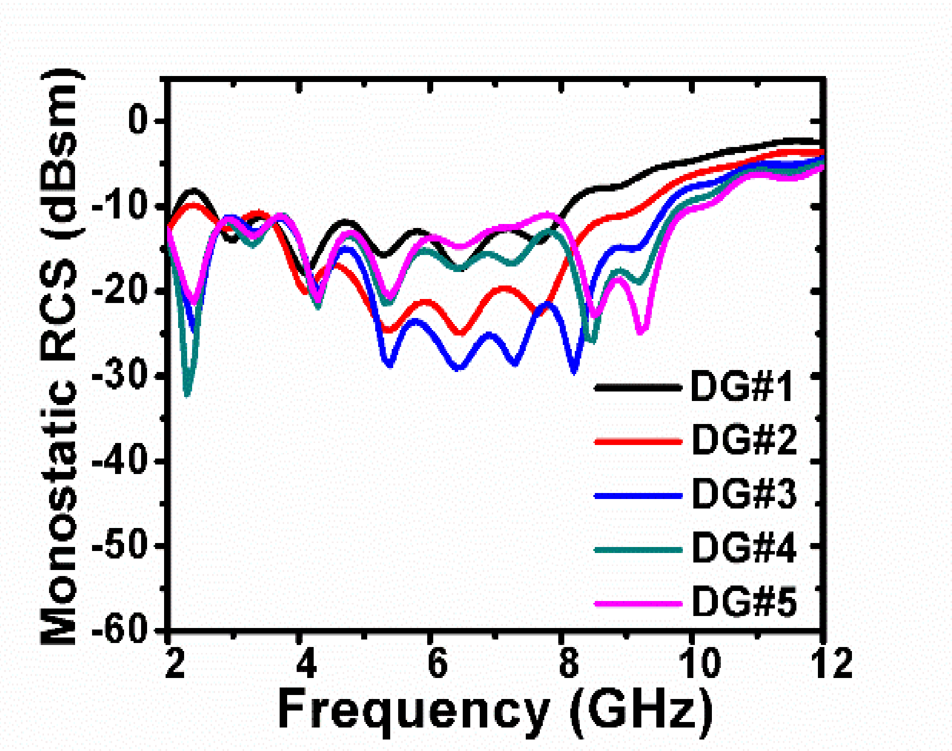

Figure 5.20. Comparison between DG#1, DG#2, DG#3, DG#4 and DG#5 configurations.

Next, the simulated radiation patterns in term of gain of the primary and proposed antenna at 4.6 GHz frequency for E and H planes is manifested in Figures 5.21 (a) and (b), respectively.

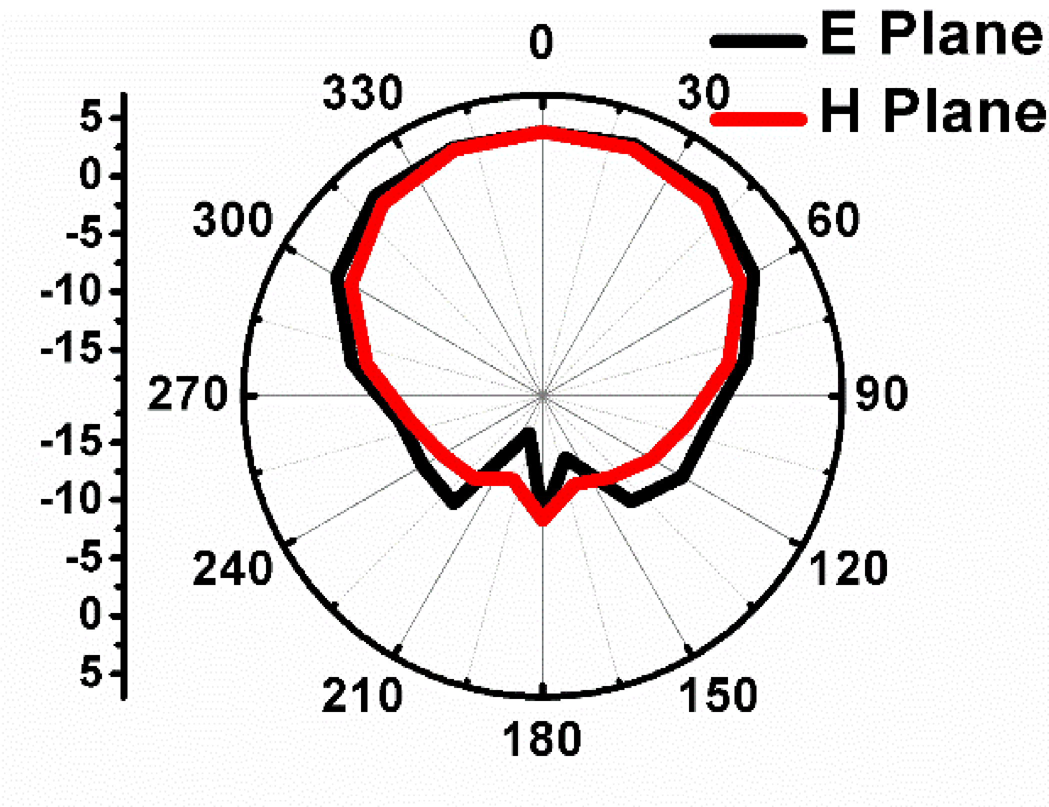

(a)

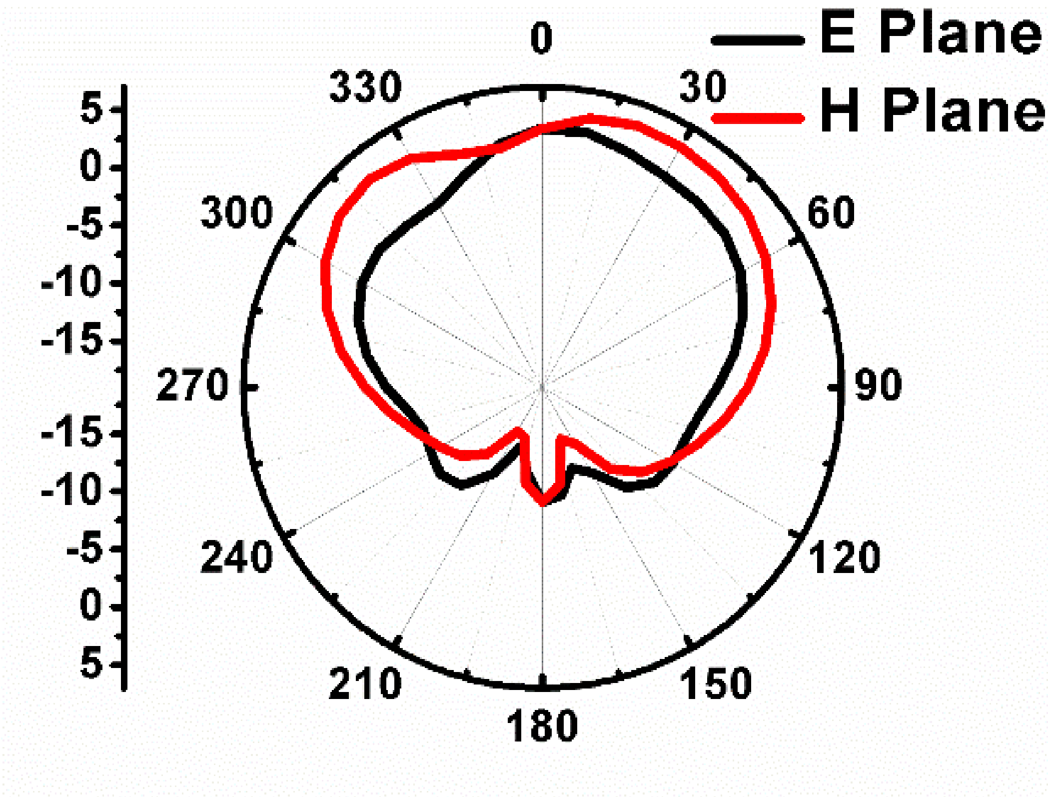

(b)

Figure 5.21. Simulated radiation pattern of E and H plane at 4.6 GHz of (a) primary antenna and (b) proposed antenna.

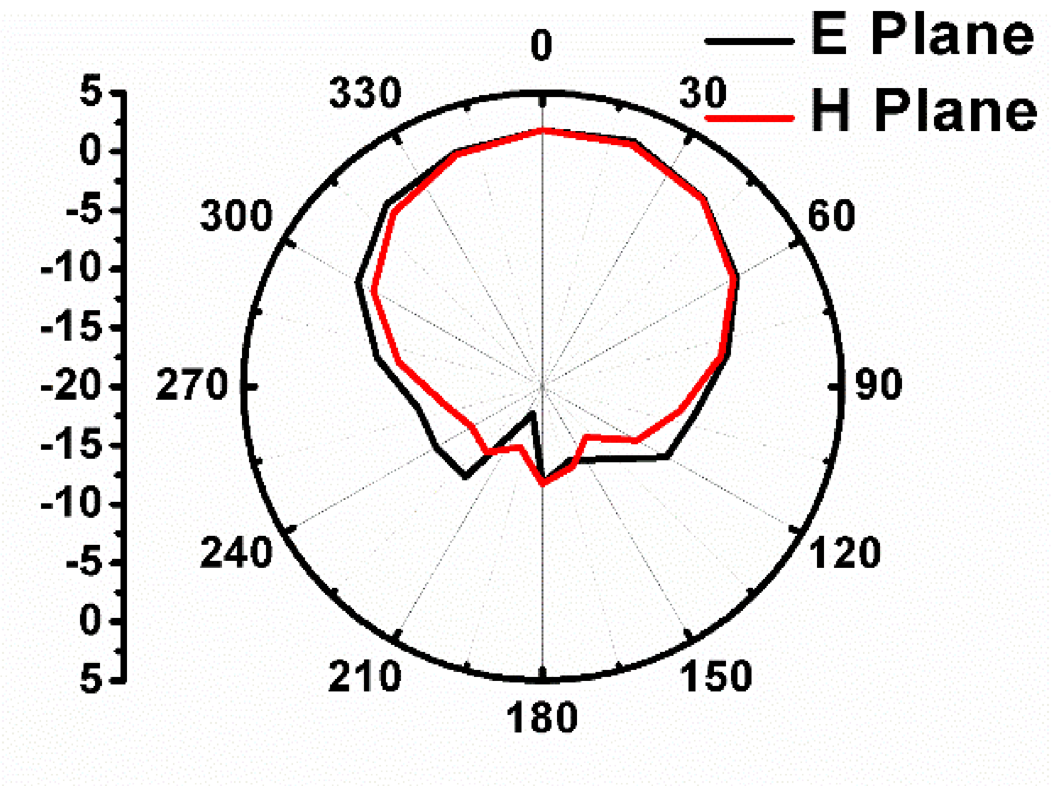

(a)

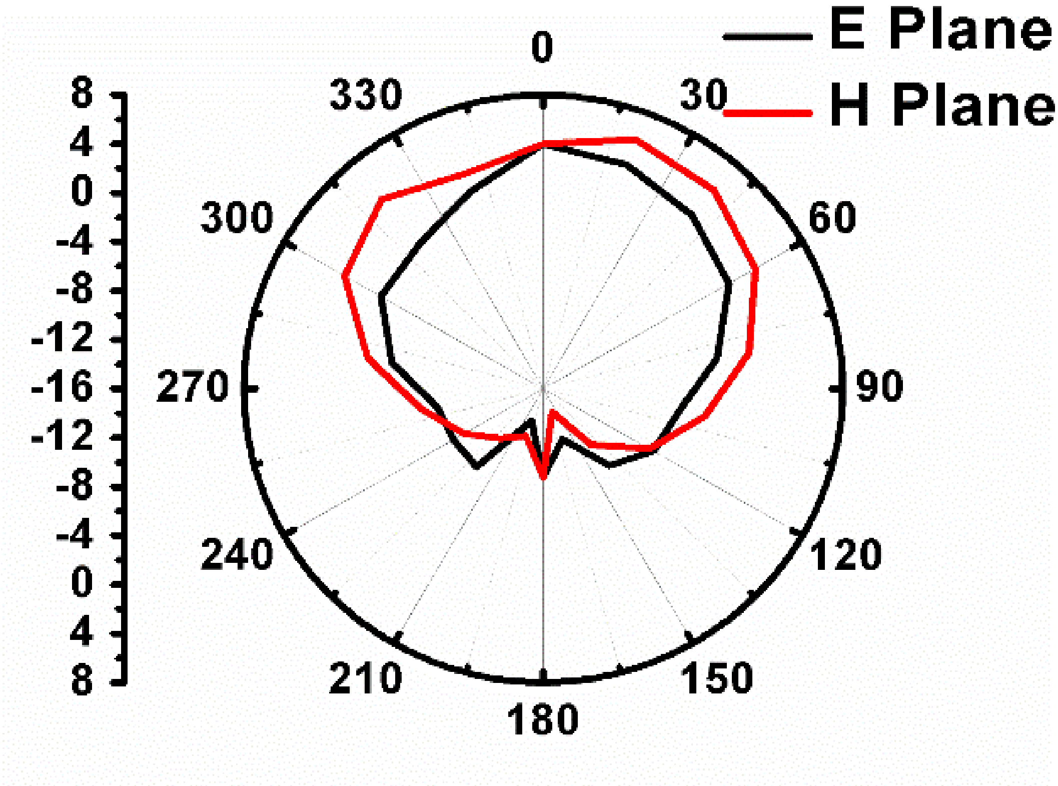

(b)

Figure 5.22. Measured radiation pattern of E and H plane at 4.6 GHz of (a) primary antenna and (b) proposed antenna.

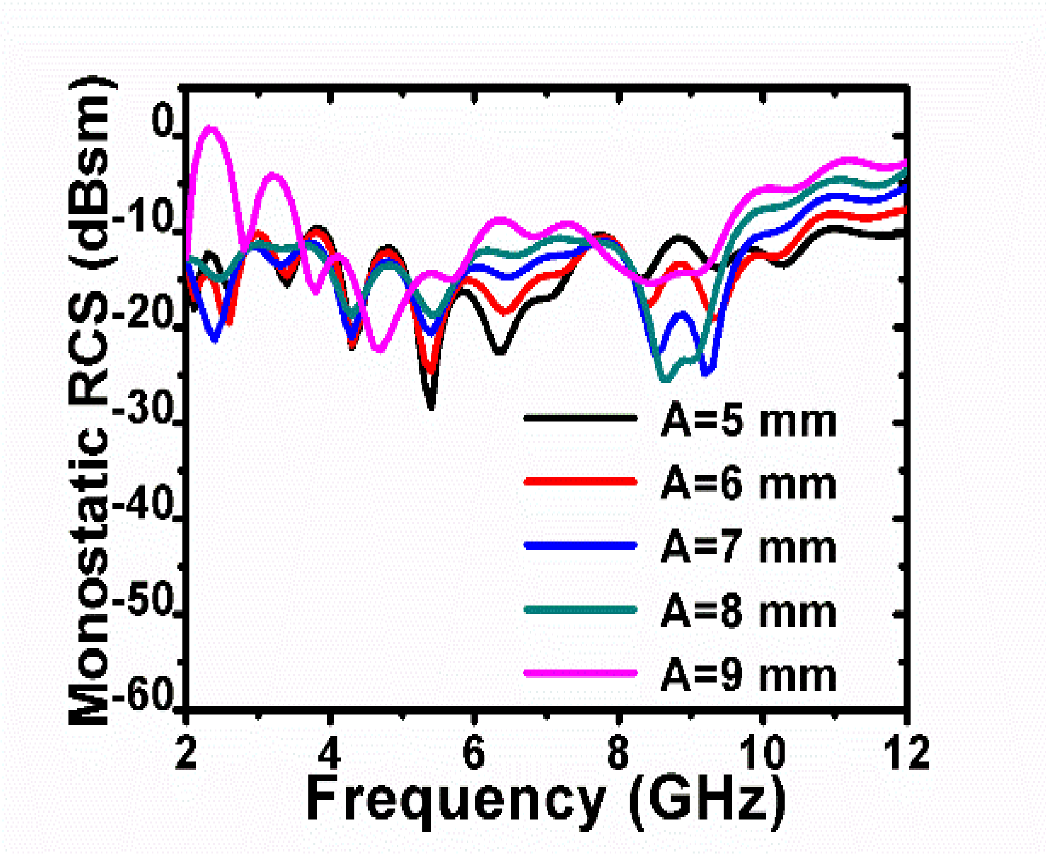
Monostatic RCS (dBsm)
Frequency (GHz)
A=5 mm
A=6 mm
A=7 mm
A=8 mm
A=9 mm

(a)

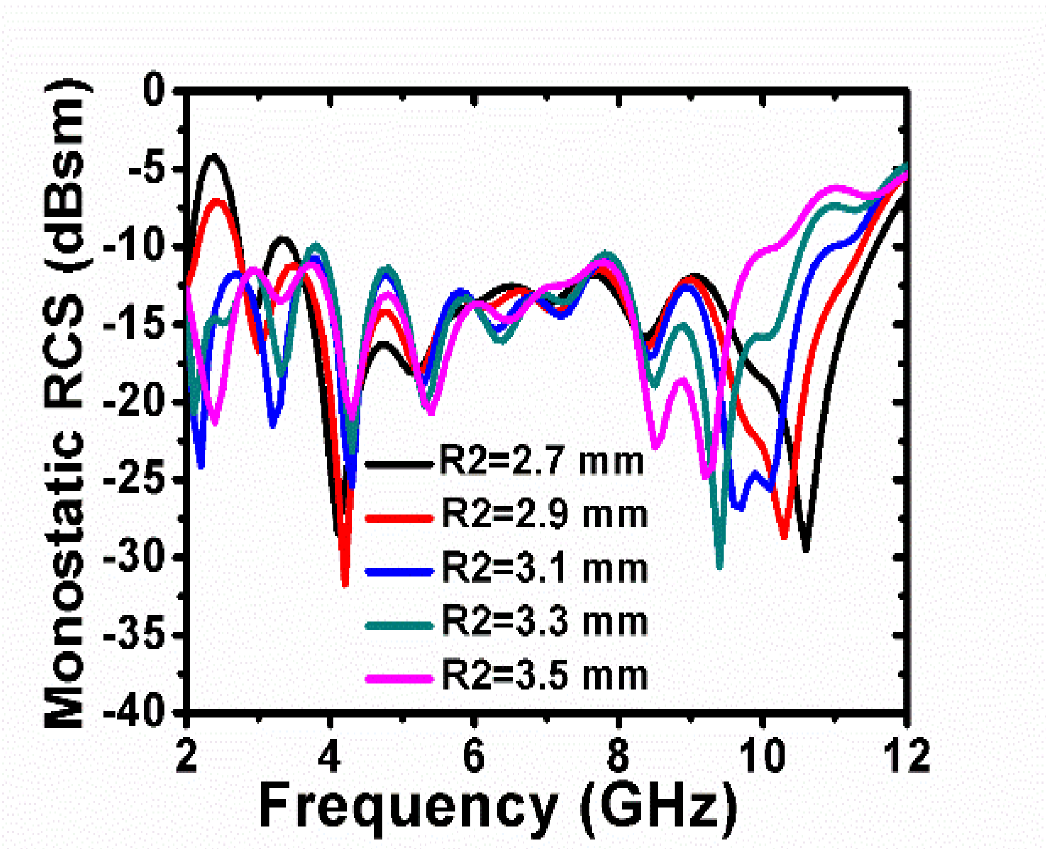
Monostatic RCS (dBsm)
Frequency (GHz)
R2=2.7 mm
R2=2.9 mm
R2=3.1 mm
R2=3.3 mm
R2=3.5 mm

(b)

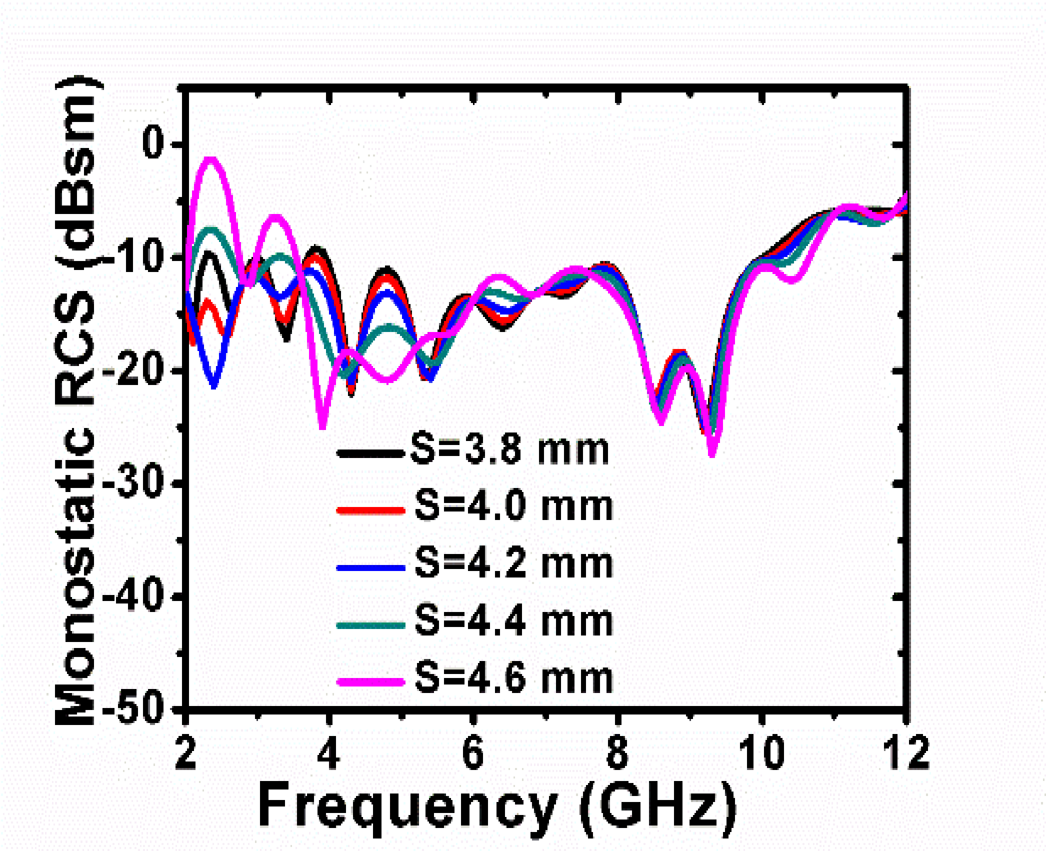

(c)

Figure 5.23. Effect of design variables over RCS characteristics (a) air gap (A), (b) radius of the circle (R2), and (c) dimension of square (S).

Figures 5.22 (a) and (b) illustrate the measured simulated radiation patterns of the primary and proposed antenna at 4.6 GHz frequency for E and H planes. It is observed that no significant changes occur in both simulated and measured results for both the primary and proposed antennas. The parametric studies are performed to realize the consequences of different geometrical design variables (i.e., air gap (A), circle radius (R2), and square dimensions (S) on RCS characteristics of the antenna. The air gap (A) between the antenna and MM superstrate is varied from 5.0 mm to 9.0 mm, with a step size of 1.0 mm. It has been observed from Figure 5.23 (a) that the best results of monostatic RCSR have been achieved for an optimal air gap (A) of 7.0 mm. The radius of the circle (R2) is varied from 2.7 mm to 3.5 mm as shown in Figure 5.23 (b), and it is noticed that the optimal value of R2 is 3.5 mm. Meanwhile, the square dimensions (S) is also studied to recognize its effect on the monostatic RCSR. Here, S is varied from 3.8 mm to 4. 6 mm with a step size of 0.2 mm. It can be observed from Figure 5.23 (c) that the maximum reduction with a wide bandwidth of RCS has been attained at 4.2 mm.

5.3.3 SAMPLE FABRICATION AND CORRESPONDING MEASURED RESULTS

To validate the simulated results, the primary and proposed antennas have been fabricated on FR4 substrate using PCB technology. Figure 5.24 (a) shows an image of the fabricated primary antenna. To excite the MPA, the coaxial feeding technique (with Sub Miniature version A connector) is used. The measurement of the return loss for primary and proposed antennas has been carried out using a vector network analyzer (Keysight E5063A). Figure 5.25 (a) and (b) illustrates the measured simulated radiation patterns of the primary and proposed antenna at 4.6 GHz frequency for E and H plane. It has been observed that no significant changes occur in primary and proposed antennas in both simulated and measured results. To observe the difference between the measured and simulated S-parameter of the primary antenna and superstrate antenna, the comparison is presented in Figures 5.26 (a) and (b). It is analyzed that the measured resonant frequency of the primary antenna is shifted by 300 MHz, whereas the measured resonant frequencies of the proposed antenna is shifted towards the left and downwards.

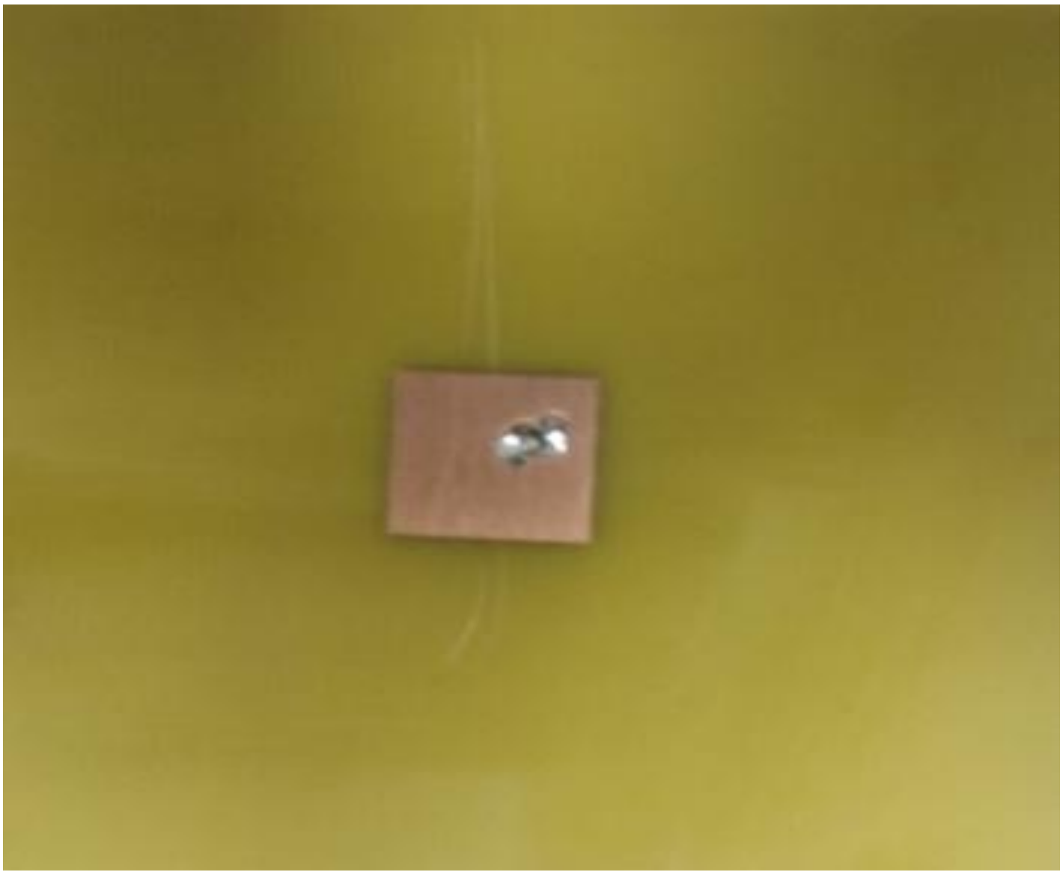

(a)

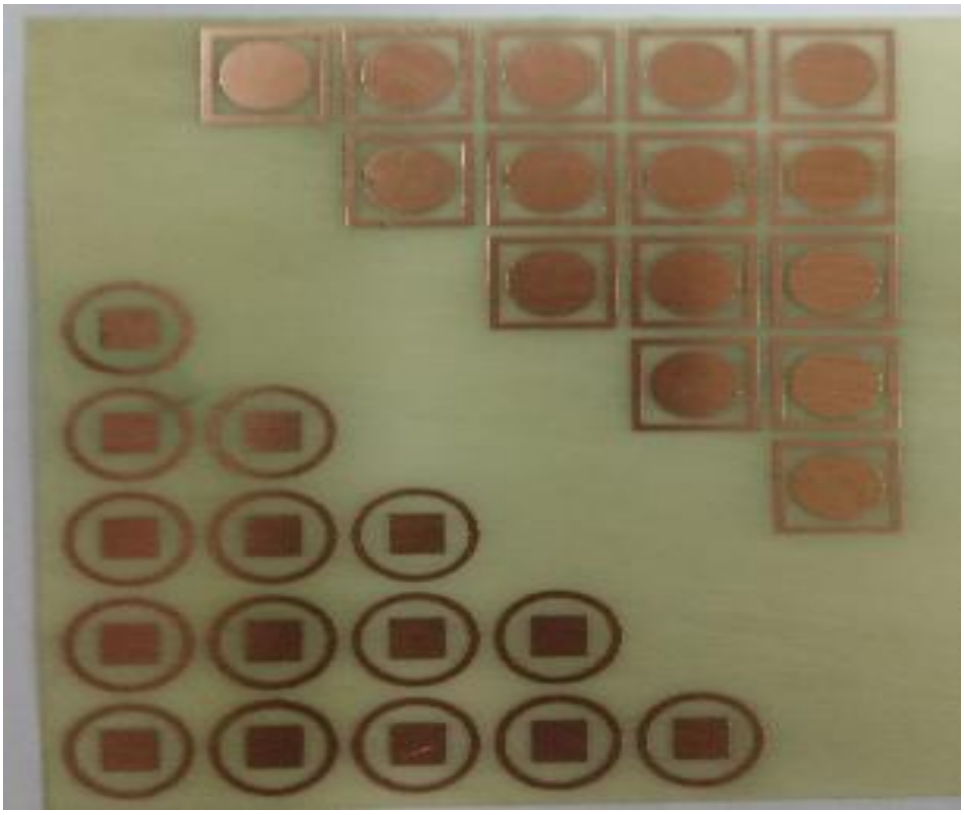

(b)

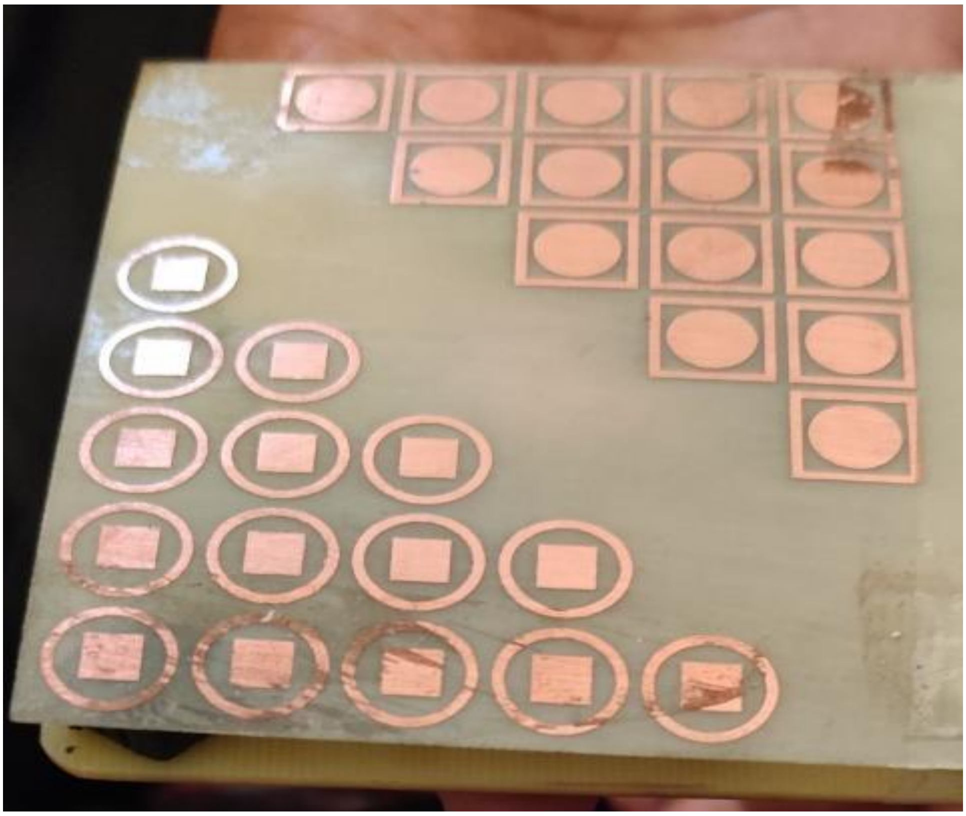

(c)

Figure 5.24. Fabricated prototype (a) primary antenna (b) superstrate layer (c) proposed antenna.

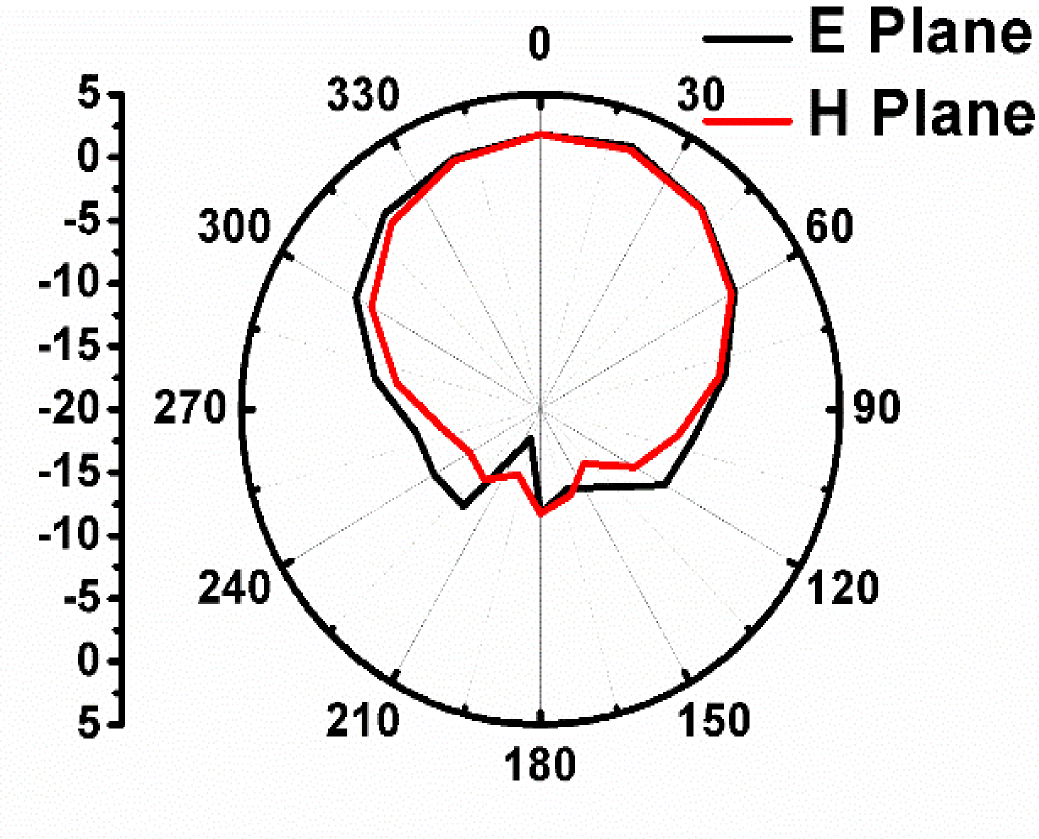

(a)

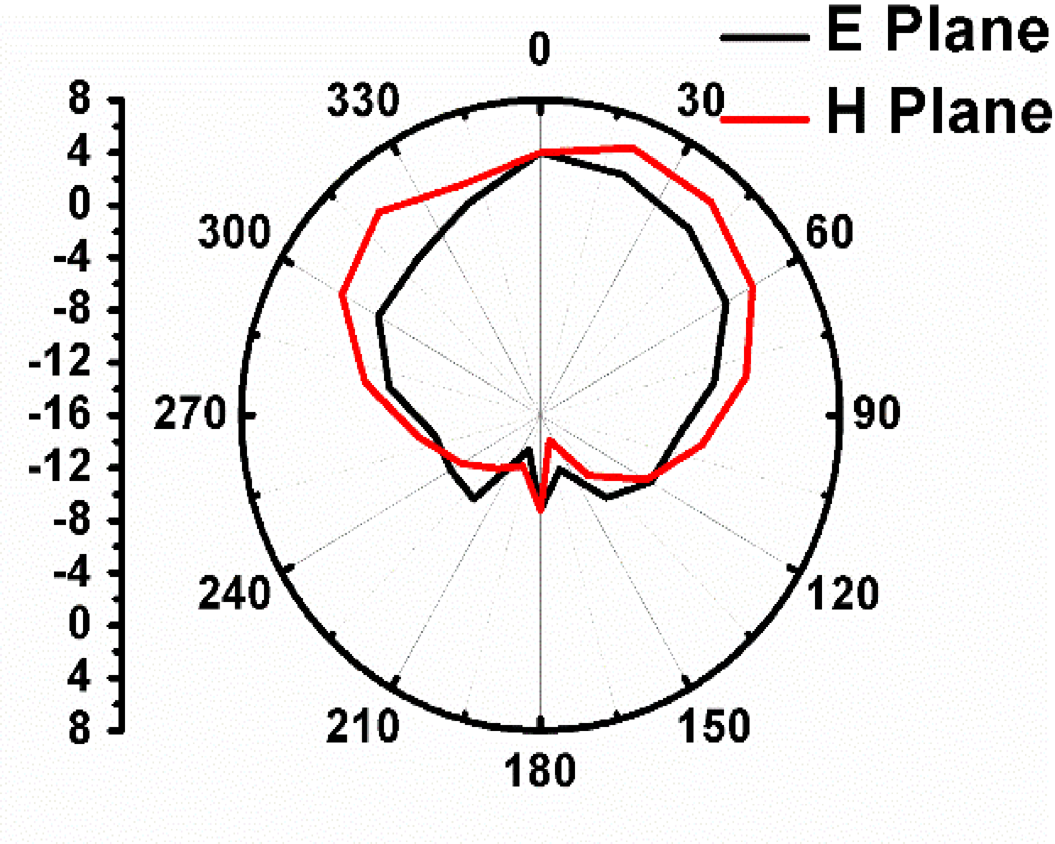

(b)

Figure 5.25. Measured radiation pattern of E and H plane at 4.6 GHz of (a) primary antenna and (b) proposed antenna.

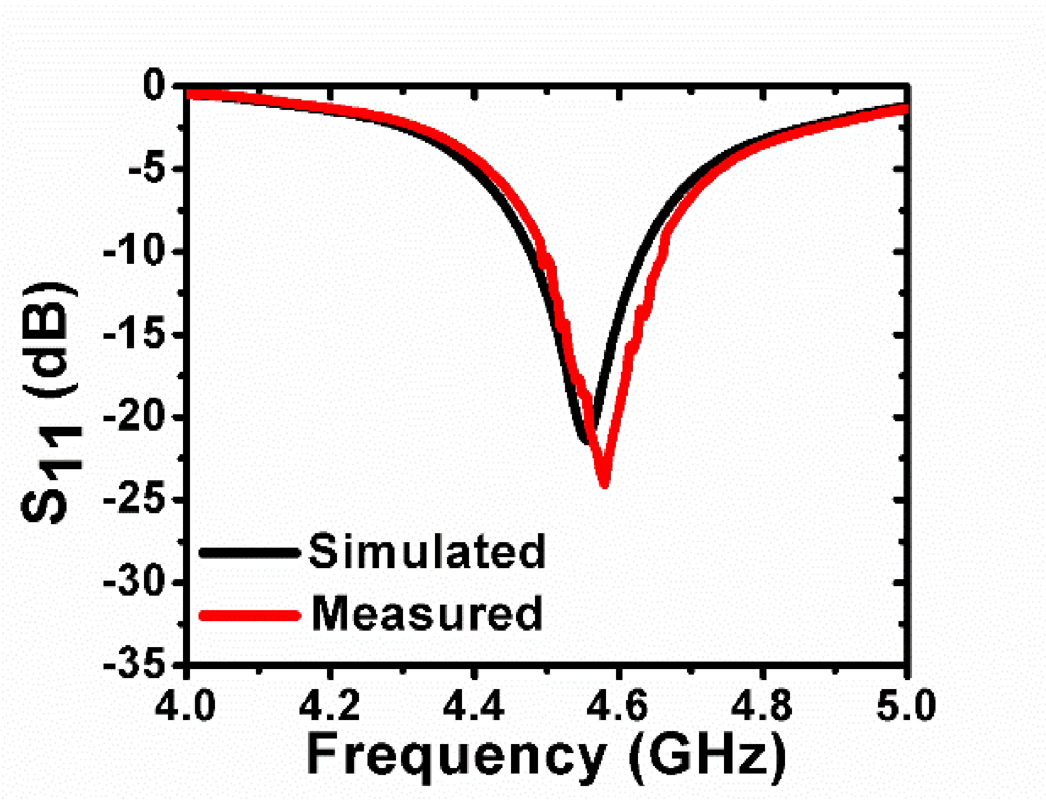

(a)

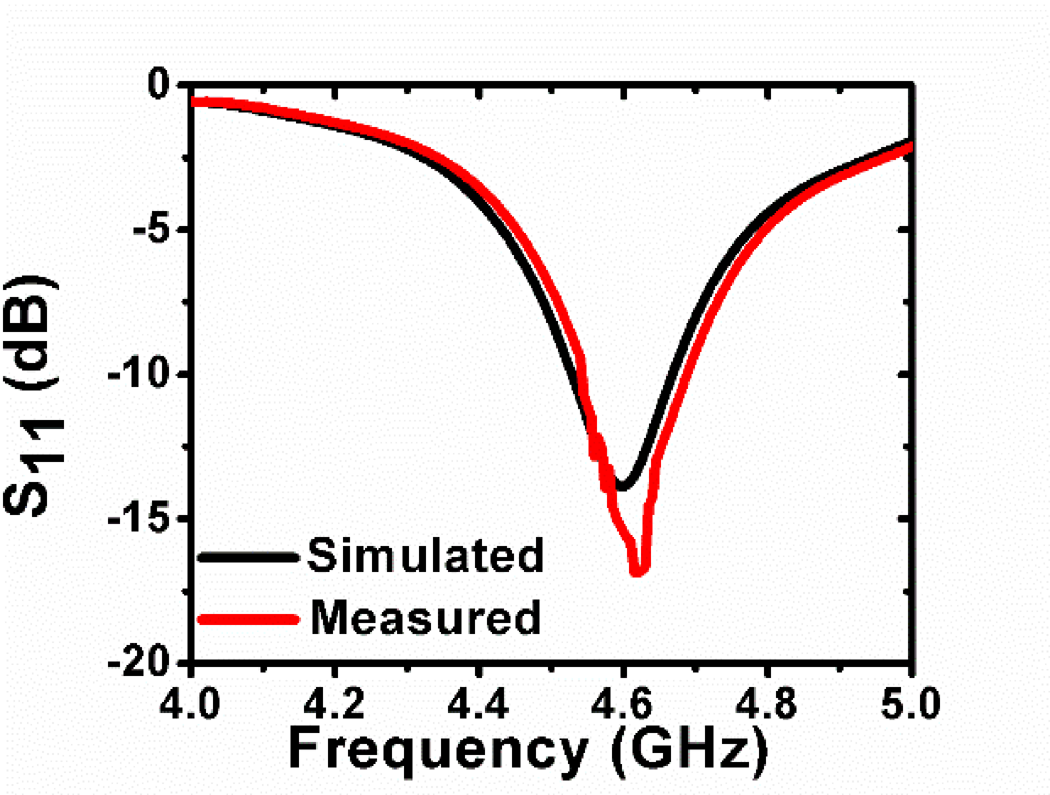

(b)

Figure 5.26. Measured and simulated return loss curve of (a) primary antenna (b) proposed antenna.

The variation between simulated and measured return loss is due to the losses caused by the sub-miniature version A connector, fabrication error, and measurement tolerance. The measured results keep the good agreement with the simulated results, which confirms the feasibility of the primary and proposed antennas. In Table 5.8, a comparison between proposed structures and other structures reported in references is given, which proves that large RCSR has been achieved with a smaller overall dimension of an antenna.

Table 5.8. Comparison table with proposed structures and other structures reported in the literature.

ID	Antenna geometry	Antenna Dimension	RCSR band (GHz)	Peak value of RCSR (dB)
MM inspired antenna	Square MPA	80×80×2	7.5-18	-30.1
Superstrate antenna	MPA with superstrate layer	80×80×2.2	2-10	-24.7
[102]	Slot antenna with square patch metasurface	120×120×3	4.9 -7.18	-30
[103]	Square MPA with shared aperture metasurface	30×30×15.36	9-17	-43
[104]	Slot antenna with horizontal and vertical strip based patch	80×80×2.76	9-19	-27
[105]	Slot antenna with rectangular patch superstrate layer	66×66×13.5	6 -14	-24
[62]	Slot antenna with orthogonally arranged stair shape patches	77.6×77.6×3.5	3.5-7	-30.9

5.4 CONCLUSION

Based on the literature survey, this chapter gives insight into two low RCS MM based MPAs. First MPA exhibits broadband RCSR by using hybrid configuration consist of two unique structures. Whereas, second MPA reveals the wideband RCSR along with high gain by the application of a hybrid MM superstrate structure. A critical analysis of both proposed MPAs has been implemented to study the effect of design variables over the monostatic RCS. A good agreement has been observed between simulated and measured data of both MPAs. Broad RCSR bandwidth has been obtained than the work mentioned in the literature, as a result, the research we have done is remarkable and important to attract more researchers.

CHAPTER 6

CONCLUSION AND FUTURE SCOPE

In this chapter, the contributions of this thesis are summarized. A, few directions for future research work are also proposed.

6.1 CONCLUSION

To achieve stealth technology, it is necessary to design absorber structures which can absorb the incident wave, so that the object becomes invisible to the radar range. To enhance the properties like absorption characteristics, thickness reduction of absorbers, MMs are used. The RCS of the antenna also plays a significant role in stealth technology. Therefore, it is also important to reduce the RCS of the antenna. For this purpose, the MM can be employed. The main contribution of this dissertation is to design compact, lightweight, broadband MM absorbers, and low RCS antennas.

The development of new hybrid MM based microwave absorbing structures are discussed in chapter 3. The two different MM based absorbers are designed, simulated, and measured in the range of 2 to 18 GHz. The first MMA is a hybrid structure that comprises of a cross-loaded split ring. The first MMA show the RC is less than -10 dB from 8.5 to 16 GHz for the hybrid structure, which covers 7.5 GHz bandwidth. The peak RC values of the hybrid geometry are -20.2 dB, -17.5 dB, -29.0 dB, and -21.0 dB at 8.9, 9.3, 12.2, and 15.5 GHz, respectively. An optimal sample of the cross-loaded split ring with an overall size of 200 × 200 mm^2 has been fabricated using standard PCB technology, to verify the simulated results. A close agreement has been observed among simulated and measured data. It has been noticed that the proposed absorber shows minimum RC from 8 to 16 GHz in measured plots. The other proposed structure comprises eight sectors loaded circle inside the square. This structure exhibits the four resonant peaks of -25.9 dB, -18.9 dB, -16.1 dB, and -21.3 dB are noticed at 4.4 GHz, 6.0 GHz, 14.1 GHz, and 16.0 GHz, respectively. The maximum absorption is observed of 94% and 92% at 4.4 GHz and 16.0 GHz, respectively. It is analyzed that the second proposed structure exhibit polarization-insensitive characteristics from 2 to 18 GHz. Finally, the structure is fabricated using PCB technology. The proposed structure exhibits a polarization-insensitive response from 0^o to 60^o. A quite good agreement is noticed among simulated and measured results. So, it can be concluded that the first MMA exhibits broadband RC characteristics with 2mm thickness of the substarte and simple geometry,whereas the angular stable and polarization insensitive respone is obtained from the second proposed absorber with multiband RC characteristics .

The structure demonstrated in chapter 4, is designed to provide tunability over a wide frequency range with the help of external biasing circuits. A single layer, tunable, and wideband AFSS based absorber provides the tunability in the range of 9.2 to 11.2 GHz. It has been found that during the “on” state, the resonance frequency of 6.8 GHz with a transmission coefficient of -24.5 dB is acquired. While in “off” state condition, AFSS exhibits a bandwidth of 2.0 GHz in the range of 6.9 GHz to 8.9 GHz. Firstly, a tunable AFSS unit cell with a 1.1 GHz and 2.0 GHz bandwidth in ON and OFF states, respectively is developed. An air gap of 8.0 mm is introduced in between the copper plate and AFSS layer to construct the tunable absorber. One other study is performed to know the effect of diode on absorber characteristics which shows that without diode there is no RC bandwidth below -10 dB. Whereas, 2 GHz bandwidth has been obtained with diode. Six different values of resistance have been taken to perceive the response of RC. As the value of resistance increases from 15 Ω to 90Ω, the resonance frequency shifts from 11.1 GHz to 10.5 GHz. The remarkable maximum bandwidth of 2.0 GHz with a resistance of 30Ω is perceived. Additionally, a critical parametric analysis is also performed on the dimensions of AFSS loaded tunable absorber. The surface current, E field, and H field distribution are also manifested to understand the absorption mechanism. To validate the simulated results, AFSS loaded tunable radar wave absorber with dimensions of 200 × 200 mm^2 has been fabricated using a standard PCB method. It can be observed that as the biasing voltage increases, the resonating frequency shifts towards lower frequency. A 0.82 V of biasing voltage demonstrates the maximum bandwidth, whereas the minimum bandwidth has been observed at 0.67 V of biasing voltage. A quite good agreement is noticed among simulated and measured results.

The two distinct low RCS antennas are discussed in chapter 5. The first one is MM inspired antenna and the second one is flexible MM-based superstrate coupled MPA, which enhances the gain along with RCSR of the MPA. The two novel unit cells are designed for the MM inspired antenna. The primary MPA is designed to operate at 4.2 GHz. The hybrid MM is organized in a chessboard configuration in the proposed

MPA. The results show that the proposed antenna gives substantially out of band RCSR from 6 GHz to 18 GHz and the proposed antenna has a lower RCS than the reference antenna. The maximum reduction of -30.1 dB at 16.4 GHz is achieved in the hybrid MM structure impinged MPA. The proposed antenna attains wideband bandwidth around 7.4 GHz (ranging 2.0 GHz to 4.4 GHz, 7.8 GHz to 9.1 GHz, and 14.3 GHz to 18 GHz). Finally, the fabrication and performance evaluation of MM loaded antenna is carried out. Moreover, the measured results of the fabricated samples are closely matched with simulated results. In the proposed MM impinged MPA it can be concluded that the structure provide RCSR, without affecting the other radiation properties and volume of the antenna. The second structure is a superstrate layer coupled to an MPA is designed in the second part. The primary and proposed antennas resonate at 4.6 GHz. The reflection coefficient bandwidth of primary and proposed antennas is the same (i.e., 800MHz), though the RCS bandwidth of the primary antenna is 1.7 GHz and the RCS bandwidth of the proposed antenna is 8.1 GHz. The increment in gain is observed in the proposed antenna. It can be observed that the maximum gain attained by the primary antenna is equal to 6.6 dB, where the maximum gain of the proposed antenna is equal to 7.2 dB. So, it can be concluded that the superstrate layer coupled MPA reduces the RCS and improves the gain of the antenna.

6.2 FUTURE SCOPE

In near future, the multilayered and cascaded metamaterial absorbing structure can be explored in the development of other efficient classes of the absorber. Besides, a graphene-based absorber can also be designed to achieve tunability. In this thesis, we have used p-i-n diode to achieve tenability, in the future, the tunability characteristics of the absorber can also be studied with other devices like varactor diode and MEMS. The equivalent circuit model of the proposed absorber can also be derived to study the impedance behavior of the absorber. In this thesis, MM inspired antenna with coaxial feeding technique has been designed, the other feeding technique can also be explored in the future. Another future research area is to reduce the volume of the MM inspired antenna. The present work deals in the development of MM inspired structures in the microwave regime, in the future millimeter and terahertz wave structures may be developed.

REFERENCES

1. W. Cai, V. Shalaev, "Optical metamaterials: *Fundamentals and applications*," Springer, 2010.
2. F. Capolino "Metamaterials Handook vol 1 *Theory and Phenomena of Metamaterials,"*
Boca Raton, FL: CRC Press, 2009.
3. F. Capolino "Metamaterials Handook vol 2 *Applications of Metamaterials,"* Boca
Raton, FL: CRC Press, 2009.
4. V.M Shalaev, "Optical negative index metamaterials," Nature Photonics, pp. 141-48,
2007.
5. J. Y. Chung, K. Sertel, J.L. Volakis, A non-invasive metamaterial characterization system using synthetic Gaussian aperture," IEEE transactions on antennas and propagation, Vol.57, no.7, pp. 2006-13, 2009.
6. V. G. Veselago, "The electrodynamics of substances with simultaneously negativevalues of ε and μ," Soviet Physics Uspekhi, Vol. 10, pp. 509-514, 1968.
7. A. Alu, N. Enghetal, A. Erentok, and R. W. Ziolkowski, "Single-Negative, Double-Negative, and Low-index Metamaterials and their Electromagnetic Applications," IEEE Antennas and Propagation Magazine, Vol. 49, no. 1, 2007.
8. T K Wu and S W Lee, "Multiband frequency selective surface with multiring patch elements", IEEE Transactions on Antennas and Propagation, Vol.42, No.11, pp.1484-90, 1994.
9. D H Werner and D Lee, "Design of dual-polarised multiband frequency selective surfaces using fractal elements", Electronic Letters, Vol.36, No.6, pp. 487–488, 2000.
10. A L Joumayly et al. "Low-profile, highly-selective, dual-band frequency selective surfaces with closely spaced bands of operation", IEEE Transactions on Antennas and Propagation, Vol. 58, No.12, pp. 4042-4050, 2010.

11. F Costa, A Monorchio, “A frequency selective radome with wideband absorbing properties”,IEEE Transactions on Antennas and Propagation, Vol. 60, No.6, pp.2740-2747, 2012.
12. F Costa, A Monorchio and G Manara, “Analysis and Design of Ultra-Thin Electromagnetic Absorbers Comprising Resistively Loaded High Impedance Surfaces,” IEEE Transactions on Antennas and Propagation, vol. 58, no. 5, May 2010.
13. S Bhattacharyya, S Ghosh, D Chaurasiya and K V Srivastava, “Wide-angle Broadband MicrowaveMetamaterial Absorber with Octave Bandwidth,” IET Microwaves, Antennas & Propagation, vol. 9, no. 11, pp. 1160-1166, 2015.
14. A Bhattacharya, S Bhattacharyya, S Ghosh, D Chaurasiya, and K V Srivastava, “An Ultrathin Penta-band Polarization-Insensitive Compact Metamaterial Absorber for Airborne Radar Applications,” Microwave and Optical Technology Letters, vol. 57, no. 11, Nov 2015.
15. Dong Wan, ShaoweiBie, Jie Zhou, HaibingXu, YongshunXu, and Jianjun Jiang, “A Thin and Broadband Microwave Absorber Based on MagneticSheets and Resistive FSS,” Progress In Electromagnetics Research C, vol. 56, pp. 93-100, Feb 2015.
16. Devkinandan Chaurasiya, Saptarshi Ghosh, Somak Bhattacharyya, Anamiya Bhattacharya and Kumar Vaibhav Srivastava, “Compact multi-band polarisation-insensitive metamaterial absorber,” IET Microwaves, Antennas & Propagation, vol. 10, no.1, pp. 94-101, 2016.
17. S Ghosh, et al. “Triple-band polarization-independent metamaterial absorber using destructive interference,” IEEE European Microwave Conference (EuMC), pp. 335-338, 2015.
18. S Bhattacharyya and K V Srivastav, “Triple band polarization-independent ultra-thin metamaterial absorber using electric field-driven LC resonator,” Journal of Applied Physics, Vol. 115, No. 6, pp.064508, 2014.
19. R Panwar, et al. “Fractal frequency-selective surface embedded thin broadband microwave absorber coatings using heterogeneous composites,” IEEE Transactions on Microwave Theory and Techniques, Vol. 63, No. 8, pp.2438-2448, 2015.

20. C. Yong-Zhi et al. “A wideband metamaterial absorber based on a magnetic resonator loaded with lumped resistors,” Chinese Physics B, Vol.21, No.12, pp. 127801, 2012.
21. H. Xiong et al. “An ultrathinand broadband metamaterial absorber using multilayer structures,” Journal of Applied Physics, Vol. 114, pp. 064109, 2013.
22. Y Zhi Cheng, et al. “Design, fabrication and measurement of a broadband polarization-insensitive metamaterial absorber based on lumped elements,” Journal of Applied Physics, Vol. 111, No.4, pp.044902, 2012.
23. H Li, et al. “Ultrathin multiband gigahertz metamaterial absorbers,” Journal of Applied Physics, Vol. 11, No.1, pp.014909, 2011.
24. S. Çimen, “Novel closely spaced planar dual-band frequency-selective surface,” IET Microwaves, Antennas & Propagation, Vol. 7, No.11, pp.894-899, 2013.
25. D. Li et al. “Applications of split-ring resonances on multi-band frequency selective surfaces,”Journal of Electromagnetic Waves and Applications, Vol.21, No.11, pp.1551-63, 2007.
26. R A Sekar and S R Inabathini, “An Ultra-thin Compact Wideband Metamaterial Absorber,” Radioengineering, Vol.27, No.2, pp.365, 2018.
27. S Fan and Y Song, “Bandwidth-enhanced polarization-insensitive metamaterial absorber based on fractal structures,” Journal of Applied Physics, Vol. 123, No. 8, pp. 085110, 2018.
28. Y Cheng et al. “Compact Ultra-Thin Seven-Band Microwave Metamaterial Absorber Based on a Single Resonator Structure,” Journal of Electronic Materials, Vol.48, No.6, pp.3939-3946, 2019.
29. S Tan et al. “Broadband terahertz metamaterial absorber with two interlaced fishnet layers,” AIP Advances, Vol. 8, No.2, pp.025020, 2018.
30. Sy Tuan et al. “Defect induced co-polarization broadband metamaterial absorber,” AIP Advances. Vol. 9, No.5, pp.055321, 2019.
31. N T Hoa et al. “Facile design of an ultra-thin broadband metamaterial absorber for C-band applications,” Scientific reports, Vol. 9, No.1, pp.468, 2019.

32. T Beeharry et al. “A dual layer broadband radar absorber to minimize electromagnetic interference in radomes,” Scientific report, Vol.8, No.1, pp.382, 2018.
33. M Yoo and S Lim, “Polarization-independent and ultrawideband metamaterial absorber using a hexagonal artificial impedance surface and a resistor-capacitor layer,” IEEE transactions on antennas and propagation. Vol.62, No.5, pp. 2652-2658. 2014.
34. D Sood and C C Tripathi, “A wideband ultrathin low profile metamaterial microwave absorber,” Microwave and Optical Technology Letters. Vol.57, No.12, pp.2723-2728, 2015.
35. M Bakir et al. “U-shaped frequency selective surfaces for single-and dual-band applications together with absorber and sensor configurations,” IET Microwaves, Antennas & Propagation, Vol.10, No.3, pp.293-300, 2016.
36. J Zhou, S Bie, D Wan, Ha Xu, Y Xu, and J Jiang, “Realization of Thin and Broadband Magnetic Radar Absorption Materials with the Help of Resistor FSS,” IEEE Antennas and Wireless Propagation Letters, vol. 14, Jan 2015.
37. F. Costa and A. Monorchio, “Multiband electromagnetic wave absorber based on reactive impedance ground planes,” IET Microwaves, Antennas and Propagation, vol. 4, no. 11, pp. 1720-1727, Jan 2010.
38. S Ghosh and K V Srivastava, “Polarization-Insensitive Single- and Broadband Switchable Absorber/Reflector and Its Realization Using a Novel Biasing Technique,” IEEE Transactions on Antennas and Propagation, vol. 64, no. 8, Aug 2016.
39. X Zeng et al. “Tunable and Broadband Radar Absorber Based on PIN Diodes Controllable FSS,” IEEE 11th International Symposium on Antennas, Propogation and Theory, pp.720-722, Oct2016.
40. Y Fan et al. “An Active Wideband and Wide-Angle Electromagnetic Absorber at Microwave Frequencies,” IEEE Antennas and Wireless Propagation Letters, vol. 15, pp.1913-1916, 2016.
41. M. Safari et al. “X-band tunable frequency selective surface using MEMS capacitive loads,” IEEE transactions on antennas and propagation, Vol. 63, No. 3, pp.1014-1021, 2014.

42. F Costa et al. “Low-cost metamaterial absorbers for sub-GHz wireless system,” IEEE Antennas and Wireless Propagation Letters, Vol.13, pp.27-30, 2013.
43. C U Sabah et al. “Metamaterial absorber-based sensor embedded into X-band waveguide,” Electronics letters, Vol.50, No.15, pp.1074-6, 2014.
44. D.M. Pozar, “RCS reduction for a microstrip antenna using a normally biased ferrite substrate,” IEEE Microwave Guided Wave Letters, Vol. 2, pp. 196 - 198, 1992.
45. Paquay M et al. “Thin AMC structure for radar cross-section reduction,” IEEE Transactions on Antennas and Propagation, Vol.55, No.12, pp.3630-3638, 2007.
46. Li, Y., et al. “Microstrip antenna using ground-cut slots and miniaturization techniques with low RCS,” Progress in Electromagnetics Research, Vol.1, pp.211-220, 2008.
47. M E de Cos et al. “A novel approach for RCS reduction using a combination of artificial magnetic conductors,” Progress In Electromagnetics Research, Vol.107, pp.147-59, 2010.
48. M Z Joozdani, et al. “Wideband RCS reduction of patch array antenna with miniaturized FSS,” Microwave and Optical Technology Letters, Vol.58, No. 4, pp.969-973, 2016.
49. S Genovesi et al. “Low-profile array with reduced radar cross section by using hybrid frequency selective surfaces,” IEEE Transactions on Antennas and Propagation, Vol. 60, No. 5, pp.2327-2335, 2012.
50. H K Jang et al. “Design and fabrication of a microstrip patch antenna with a low radar cross section in the X-band,” Smart Materials and Structures, Vol.20, No.1, pp.015007, 2010.
51. F W Wang et al. “RCS reduction of array antennas with radar absorbing structures”, Journal of Electromagnetic Waves and Applications, 2011 Vol.25, No. (17-18), pp.2487-2496.
52. Wang WT et al. “RCS reduction of array antenna by using bandstop FSS reflector,” Journal of Electromagnetic Waves and Applications, Vol.23, No. (11-12), pp.1505-1514, 2009.

53. J.P Turpin et al. “Absorbing ground planes for reducing planar antenna radar cross-section based on frequency selective surfaces,” IEEE Antennas and Wireless Propagation Letters, Vol.12, pp.1456-1459, 2013.
54. J.K Zhang, “Low radar cross section microstrip antenna based on left- handed material,” Microwave and Optical Technology Letters, Vol.61, No.6, pp.1559-1565, 2019.
55. C Zhang et al. “Low scattering microstrip antenna array using coding artificial magnetic conductor ground,” IEEE Antennas and Wireless Propagation Letters, Vol. 17, No. 5, pp.869-872, 2018.
56. Y Zhao et al. “Broadband low-RCS circularly polarized array using metasurface-based element,” IEEE Antennas and Wireless Propagation Letters, Vol. 16, pp.1836-1839, 2017.
57. T Liu et al. “RCS reduction of waveguide slot antenna with metamaterial absorber,” IEEE Transactions on Antennas and Propagation, Vol.61, No.3, pp.1479-1484, 2012.
58. Y Fu et al. “Wideband composite AMC surfaces for RCS reduction,” Microwave and Optical Technology Letters, Vol. 53, No. 4, pp.712-715, 2011.
59. M Paquay et al. “Thin AMC structure for radar cross-section reduction,” IEEE Transactions on Antennas and Propagation, Vol.55, No.12, pp.3630-3638, 2007.
60. M Mighani and G. Dadashzadeh, “Broadband RCS reduction using a novel double layer chessboard AMC surface,” Electronics Letters, Vol.52, No.14, pp.1253-1255, 2016.
61. Q R Zheng et al. “High impedance ground plane (HIGP) incorporated with resistance for radar cross section (RCS) reduction of antenna,” Progress In Electromagnetics Research, Vol.84, pp.307-319, 2008.
62. Q Zheng et al. “Wideband and low RCS planar circularly polarized array based on polarization conversion of metasurface,” Microwave and Optical Technology Letters, Vol.60, No.3, pp.784-789, 2018.
63. Y Liu et al. “Wideband RCS reduction of a slot array antenna using polarization conversion metasurfaces,” IEEE Transactions on Antennas and Propagation, Vol. 64, No.1, pp. 326-331, 2015.

64. A Edalati, and K Sarabandi, "Wideband, wide angle, polarization independent RCS reduction using nonabsorptive miniaturized-element frequency selective surfaces," IEEE transactions on antennas and propagation, Vol. 62, No. 2, pp.747-754, 2013.
65. Y Liu et al. "Radar cross section reduction of a microstrip antenna based on polarization conversion metamaterial," IEEE Antennas and Wireless Propagation Letters, Vol. 15, pp.80-83, 2015.
66. H B Baskey et al. "Design of metamaterial based structure for the radar cross section reduction of a microstrip antenna," IEEE International Microwave and RF Conference (IMaRC), pp. 104-107, 2014.
67. Y Liu, "RCS reduction of a patch array antenna based on microstrip resonators," IEEE Antennas and Wireless Propagation Letters, Vol. 14, pp.4-7, 2014.
68. Y Q Li, et al. "RCS reduction of ridged waveguide slot antenna array using EBG radar absorbing material," IEEE Antennas and Wireless Propagation Letters, vol. 7, pp.473-476, 2008.
69. J Zhang "RCS reduction of patch array antenna by electromagnetic band-gap structure," IEEE Antennas and Wireless Propagation Letters, Vol.11, pp.1048-51, 2012.
70. M Gustafsson, "RCS reduction of integrated antenna arrays and radomes with resistive sheets," IEEE Antennas and Propagation Society International Symposium, pp. 3479-3482, 2006.
71. G Singh and A Marwaha, "A review of metamaterials and its applications," International Journal of Engineering Trends and Technology, Vol. 14, pp. 305-310, 2015.
72. R.K. Jaiswal, N. Pandit, N.P. Pathak, "Design of multiple band-notch ring resonator filter based on plasmonic metamaterial at microwave frequency," IEEE International Conference on Antenna Innovations & Modern Technologies for Ground, Aircraft and Satellite Applications (iAIM), pp. 1-5, 2017.
73. R Panwar and J R Lee, "Performance and non-destructive evaluation methods of airborne radome and stealth structures," Measurement Science and Technology, Vol. 29, 062001, 2018.

74. M Li et al. “An ultrathin and broadband radar absorber using resistive FSS,” IEEE Antennas and Wireless Propagation Letters, Vol. 11, pp. 748-751, 2012.
75. F, Sakran et al. “Absorbing frequency-selective-surface for the mm-wave range,” IEEE Transactions on Antennas and Propagation, Vol.56, pp.2649-2655, 2008.
76. N I Landy et al. “Perfect metamaterial absorber,” Physics Review Letters, Vol. 100, 207402, 2008.
77. S Fan, and Y Song, “Bandwidth-enhanced polarization-insensitive metamaterial absorber based on fractal structures,” Journal of Applied Physics,” Vol. 123, 085110, 2018.
78. S Ghosh et al. “An ultrawideband ultrathin metamaterial absorber based on circular split rings,” IEEE Antennas and Wireless Propagation Letters, Vol. 14, pp. 1172-1175, 2015.
79. J Chen et al. “High-Impedance Surface-Based Broadband Absorbers with Interference Theory, ” IEEE Transactions on Antennas and Propagation, Vol. 63, pp. 4367-4374, 2015.
80. K L Ford and B Chambers, “Smart microwave absorber,” Electronics Letters, Vol.36, No.1, pp.50-52, 2000.
81. X G Huang et al. “Tunable 3-D bandpass frequency-selective structure with wide tuning range, ” IEEE Transactions on Antennas and Propagation, Vol. 63, No.7, pp.3297-3301, 2015.
82. H Yuan et al. “A frequency and bandwidth tunable metamaterial absorber in X-band, ” Journal of Applied Physics, Vol.117, No.17, pp. 173103, 2015.
83. B Q Lin et al. “A varactor-tunable high impedance surface for active metamaterial absorber, ” Progress In Electromagnetics Research, Vol. 43, pp.247-254, 2013.
84. A Li et al. “High-power transistor-based tunable and switchable metasurface absorber, ” IEEE Transactions on Microwave Theory and Techniques, Vol.65, No.8, pp.2810-2818, 2017.
85. C Mias, “Varactor tunable frequency selective absorber, ” IET Electronics Letters, Vol. 39, No.14, pp.1060-1062, 2003.
86. A Ebrahimi, et al. “Interlayer tuning of X-band frequencyselective surface using liquid crystal,” in Proc. Asia–Pacific Microwave Conference proceedings, pp. 1118–1120, Nov. 2013.

87. M Haghzadeh and A Akyurtlu, “All-printed, flexible, reconfigurable frequency selective surfaces,” Journal of Applied Physics, Vol.120, No.18, pp.184901, 2016.
88. A Tennant and B Chambers, “A single-layer tuneable microwave absorber using an active FSS,” IEEE Microwave and Wireless Components Letters, Vol. 14, No. 1, pp.46-7, 2004.
89. J Zhao et al. “A tunable metamaterial absorber using varactor diodes,” New Journal of Physics, Vol.15, No.4, pp.043049, 2013.
90. E. Knott et al. “Radar Cross Section,” (Boston, MA: Artech House1993 2nd edition)
91. M E Cos et al. “Novel broadband artificial magnetic conductor with hexagonal unit cell,” IEEE Transaction on Antennas and Propagation, Vol. 10, pp. 615-618, 2011.
92. A Foroozesh and L Shafai, “Effects of artificial magnetic conductors in the design of low-profile high-gain planar antennas with high permittivity dielectric superstrate,” IEEE Transaction on Antennas and Propagation letters, Vol. 8, pp. 10–13, 2009.
93. Y Liu et al. “Low RCS Microstrip Patch Antenna Using Frequency-Selective Surface and Microstrip Resonator,” IEEE Antennas and Wireless Propagation Letters, Vol. 14, pp. 1290-1293, 2015.
94. R Panwar and J R Lee, “Progress in frequency selective surface-based smart electromagnetic structures: A critical review,” Aerospace Science and Technology Vol. 66, pp. 216-234, 2017.
95. N Enghetaand R W Ziolkowski, “Metamaterials: physics and engineering explorations,” John Wiley & Sons, 23 Jun 2006.
96. A Sharma et al. “Experimental validation of a frequency-selective-surface-loaded hybrid metamaterial absorber with wide bandwidth,” IEEE Magnetic Letters, Vol. 10, pp. 1-5, 2019.
97. A. Azarbar and M. Mashhadi, “Broadband RCS Reduction using a Composite AMC Structure,” Majlesi Journals of Telecommunication Devices, Vol. 4, No. 3. pp.107-111, 2015.
98. H Jiang et al. “Low-RCS High-Gain Partially Reflecting Surface Antenna With Metamaterial Ground Plane,” IEEE Transactions on Antennas and Propagation, Vol. 64, pp.4127-4132, 2016.

99. W Xu, et al. "A novel microstrip antenna with composite patch structure for reduction of in-band RCS," IEEE Antennas on Wireless Propagation Letters, Vol. 14, pp.139–142, 2014.
100. M M Bait-Suwailam et al. "Mutual coupling reduction between microstrip patch antennas using slotted-complementary split-ring resonators," IEEE Antennas and Wireless Propagation Letters, Vol.9, pp. 876-8, 2010.
101. J. Malik and M.V. Kartikeyan, "Metamaterial inspired patch antenna with L-shape slot loaded ground plane for dual band (WiMAX/WLAN) applications," Progress In Electromagnetics Research, Vol. 31, pp.35-43, 2012.
102. Y Zhao et al. "A low-RCS and high-gain slot antenna using broadband metasurface," IEEE Antennas on Wireless Propagation Letters, Vol. 15, pp.290-293, 2015.
103. L Zhang and T Dong, "Low RCS and high-gain CP microstrip antenna using SA-MS," Electron Letters, Vol.53, pp.375-376, 2017.
104. A Sharma et al. "RCS reduction and gain enhancement of SRR inspired circularly polarized slot antenna using metasurface," International Journal of Electronics and Communication, Vol. 91, pp.132-142, 2018.
105. K Li et al. "A circularly polarized high-gain antenna with low RCS over a wideband using chessboard polarization conversion metasurfaces," IEEE Transactions on Antennas and Propagation, Vol.65, pp.4288-4292, 2017.